Advanced Rheological Characterization of Nanofilled Materials for Automotive Applications

by

Jianyi Du

B.S., Shanghai Jiao Tong University (2016)
B.S., Purdue University (2016)
S.M., Massachusetts Institute of Technology (2018)

Submitted to the Department of Mechanical Engineering
in partial fulfillment of the requirements for the degree of

Doctor of Philosophy in Mechanical Engineering

at the

MASSACHUSETTS INSTITUTE OF TECHNOLOGY

February 2022

Author .....
Department of Mechanical Engineering
January 7, 2022

Certified by .....
Gareth H. McKinley
School of Engineering Professor of Teaching Innovation
Thesis Supervisor

Accepted by .....
Nicolas Hadjiconstantinou
Graduate Officer Department of Mechanical Engineering

This page is intentionally left blank.

Advanced Rheological Characterization of Nanofilled Materials for Automotive Applications

by

Jianyi Du

Submitted to the Department of Mechanical Engineering
on January 7, 2022, in partial fulfillment of the
requirements for the degree of
Doctor of Philosophy in Mechanical Engineering

Abstract

Nanofilled polymer composites and lubricants have gained significant attention in fuel-efficient vehicle designs due to the superior material properties and economic potentials with minimal filler loadings. However, mass-market applications are impeded by a lack of understanding of the complex rheological behavior arising from addition of nanofillers, especially in strong shear and extensional flows. In this thesis, these challenges are addressed through design of a rapid characterization protocol for the extensional rheology of such material systems, as well as a comprehensive rheological study of a prototypical graphene-derived nanocomposite with the development of a robust constitutive model framework to provide more insights into the microstructural variations that are induced through large deformations and strong flows during material processing and manufacturing operations.

In the first part of this thesis, an improved version of capillary breakup extensional rheometry (CaBER) is presented, with a special focus on quantifying the filament thinning dynamics which are governed by multiple contributions to the total tensile stress in the fluid. An Inelastic Rate-Thickening (IRT) constitutive model is proposed to characterize the weakly rate-dependent response of commercial synthetic motor oils. The evolution of the full-dimensional filament profiles is quantified through analytical and numerical calculations from which an explicit empirical expression is developed based on the magnitude of each stress contribution. Finally, a statistical strategy is proposed to select the best-fit model with regularized parameters on the basis of the Bayesian information criterion, paving the path for an automated industrial process to extract accurate and meaningful constitutive parameters from CaBER measurements.

The second part of this thesis focuses on the filament thinning dynamics of entangled polymer systems based on two modern tube models derived from reptation theory. One-dimensional numerical solutions of the governing equations are demonstrated to accurately capture a number of key observations reported in previous studies of concentrated polymer solutions, including rate-thinning behavior near filament breakup, and markedly different relaxation time constants in shear and extensional flows. An analytical expression for the ratio of these two relaxation times is obtained as a function of the polymer concentration and the number of entanglements, which shows excellent agreement with the experimental results from a number of polymer systems

with no additional fitting parameters. As a case study, the material response predicted from the Rolie-Poly (Rouse-Linear-Polymer) model is used to interpret the rheology and dynamics of concentrated cellulose/ionic liquid systems, which are beginning to find application in fabric recycling and regeneration operations through a wet-spinning process. To obtain an accurate set of constitutive parameters, the material response in nonlinear shear and extensional flows are fitted to the model in order to obtain a universal set of constitutive parameters and scalings that can describe the rheology of these complex nanocomposite solutions as the concentration, temperature and degree of polymerization are varied.

The final part of this thesis presents a comprehensive study of the rheology of a graphene oxide (GO)/polyvinyl alcohol (PVA) system. Distinct features of the low-frequency dynamic moduli indicate the formation of a fractal nanofiller microstructure as the GO concentration is increased. A nonlinear fractional K-BKZ constitutive framework is used to develop a comprehensive rheological equation of state for this nanocomposite system in both the linear and non-linear regimes. In extensional flow the observed rheological behavior is similar to the prediction from the tube models due to the structural similarity of the materials, and the nanofiller orientation can be readily described in terms of the model parameters. The sensitivity of the nanofiller structural variations to the flow kinematics inspires the design of a new rheometric method to optimize nanofiller dispersion by using a periodic exponential shear flow. General principles for the design of the required flow profiles are provided and are justified via proof-of-concept experiments.

Thesis Supervisor: Gareth H. McKinley
Title: School of Engineering Professor of Teaching Innovation

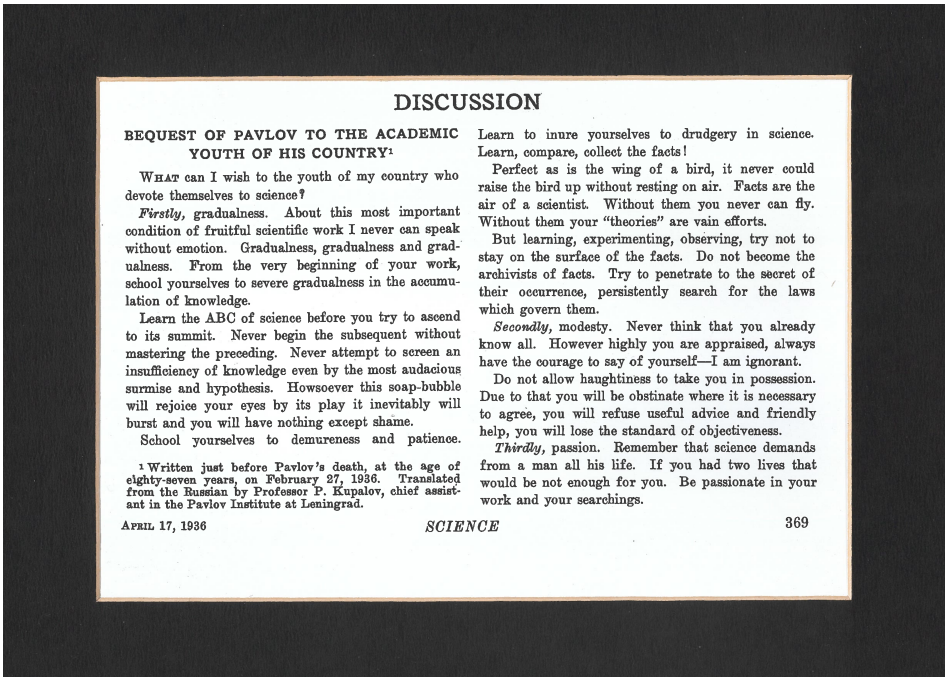

DISCUSSION

BEQUEST OF PAVLOV TO THE ACADEMIC YOUTH OF HIS COUNTRY[1]

WHAT can I wish to the youth of my country who devote themselves to science?

Firstly, gradualness. About this most important condition of fruitful scientific work I never can speak without emotion. Gradualness, gradualness and gradualness. From the very beginning of your work, school yourselves to severe gradualness in the accumulation of knowledge.

Learn the ABC of science before you try to ascend to its summit. Never begin the subsequent without mastering the preceding. Never attempt to screen an insufficiency of knowledge even by the most audacious surmise and hypothesis. Howsoever this soap-bubble will rejoice your eyes by its play it inevitably will burst and you will have nothing except shame.

School yourselves to demureness and patience. Learn to inure yourselves to drudgery in science. Learn, compare, collect the facts!

Perfect as is the wing of a bird, it never could raise the bird up without resting on air. Facts are the air of a scientist. Without them you never can fly. Without them your "theories" are vain efforts.

But learning, experimenting, observing, try not to stay on the surface of the facts. Do not become the archivists of facts. Try to penetrate to the secret of their occurrence, persistently search for the laws which govern them.

Secondly, modesty. Never think that you already know all. However highly you are appraised, always have the courage to say of yourself—I am ignorant.

Do not allow haughtiness to take you in possession. Due to that you will be obstinate where it is necessary to agree, you will refuse useful advice and friendly help, you will lose the standard of objectiveness.

Thirdly, passion. Remember that science demands from a man all his life. If you had two lives that would be not enough for you. Be passionate in your work and your searchings.

[1] Written just before Pavlov's death, at the age of eighty-seven years, on February 27, 1936. Translated from the Russian by Professor P. Kupalov, chief assistant in the Pavlov Institute at Leningrad.

Bequest of Pavlov to the Academic Youth of His Country,
from Dr. J. William Boley, my undergraduate research mentor upon his departure from Purdue University in 2015, originally from Science, 83:2155, April 1936.

This page is intentionally left blank.

Acknowledgments

It was as if yesterday that this 1866-day journey of self-discovery started and time really flies. Looking back at all the joy and tears over the past five years, this work would not have been possible without the help and love from many.

I would like to express my deepest gratitude to Prof. Gareth H. McKinley, my thesis advisor. He is not only an admirable figure in science, with whom I feel enlightened and how much I still need to learn in our discussions and communications, but also a gentleman (as implied from his first name of "gwaredd") of passion for life who constantly inspires me through my ups and downs. I still treasured the birthday card from him when I turned "1/4 century" old, and I feel truly grateful of working with him at the 0.25 ± 0.03-th century of my life.

I would also like to thank Prof. Peko Hosoi, Prof. Irmgard Bischofberger and Prof. Gang Chen for being in my thesis committee and providing me with all the help and guidance throughout my research journey. I wish all the best for Prof. Gang Chen.

I would like to thank Ford Motor Company for the financial and technical support to make my research project possible. In particular, if allowing me to quote *The Hitchhiker's Guide to the Galaxy*, I want to thank all the *hoopy* colleagues, mentors and friends I met - Kevin, Hiroko, Alper, Sandeep, Andy, Bala among many others - for the insightful discussions and generous help, as well as the hospitality during my two visits to Dearborn, Michigan. I would also like to thank Aaron and Joydip from the Greenfield Labs for a wonderful summer internship!

I would like to thank Sean for his fantastic job with the lab management, as well as for the cherished memories of twinkling Christmas lights and holiday parties, which makes me feel home. I would like to thank Leslie for her decades of passion for our department and the Institute, as well as her care for every student, which will keep inspiring me in my future career.

I would like to thank Edgerton House, where I called home during my whole MIT career of studying and living. I would like to thank Dave and Pam for your devotion to the management of this residence house, and your care for every resident. I want to thank Trudy, Katina, Lee and Sonam for your warmest welcome when I first arrived in Boston and for the five years of love and care. I would also like to thank all the friends and colleagues, especially Bethany, Cameron, Jerry and Mohammad for their help when I served in the Edgerton House Association as a Social Chair, the co-President and a member on the Student Advisory Board. I am proud of contributing to this lovely

community where I call home.

I would like to thank all my friends. I cherish my time with many members and alumni of NNF and HML - Amir, Anoop, Bavand, Caroline, Crystal, Divya, George, Igor, Ippolyti, Jae, Jake, Josh, Michela, *Ninja*, Pablo, Philippe, Qing, Sami, Sean, Setareh, Sijie, Youzhi, Yonatan. I thank Lenan, with whom we sticked together in need of support. I thank Jiliang, Baoliang and Sijie, who I am so fortunate to meet here to have your love and care. I thank Weixiang and Changxin and many others, who live in different places around the world though, for your consistent accompanying throughout this fantastic journey.

In particular, I would like to thank my family. I would not have ended up being here today without the devoting love from my parents, and you are always the heroes of my life. I would also like to thank my grandparents and all the members of my big family for the warmth and support since my childhood.

Finally, I would like to thank the members of my to-be little family, Ivy and Cookie. I am glad to have you to constitute all the lovely memories of my graduate study and to accompany me through the life of my graduate study. I am fortunate to have you in my life, and I cannot wait to explore the future with lovely you and fluffy you.

Contents

List of Figures

This page is intentionally left blank.

List of Tables

List of Symbols

Here are listed the symbols that will be later used in the body of this thesis. Symbols in square brackets are dimensionless variables.

Constants [Dimensionless]

k	Boltzmann constant, 1.38×10^{-23} J/K
$[\mathrm{Ec}^*_{\text{V-E}}]$	Critical elasto-capillary number to distinguish weakly rate-thickening and strongly viscoelastic filament thinning, with the value of approximately 4.7
g	Gravitational acceleration $g = 9.81\,\mathrm{m/s^2}$
$[X_{\mathrm{EC}}]$	Asymptotic solution of the geometric correction factor solely from the polymer contribution in the Oldroyd-B model, with the value of 1
$[X_{\mathrm{N}}]$	Geometric correction factor for a Newtonian fluid under a visco-capillary balance with the value of approximately 0.7127
$[X_{\mathrm{RT}}]$	Asymptotic solution of the geometric correction factor solely contributed from the rate-thickening stress in the IRT model, with the value of approximately 0.5778

Variables [Dimensionless]

$[\xi]$	Characteristic aspect ratio of nanofillers
$[\mathrm{Bo}_0]$	Initial Bond number based on the lengthscale of R_0
c^*	Overlapping concentration
c_{e}	Entangled concentration
$[\mathrm{Ec}_0]$	Intrinsic elasto-capillary number with the lengthscale of R_0 (expression slightly varies for different constitutive models)

$[\mathrm{Ec}_{\text{V-E}}]$	Elasto-capillary number with the lengthscale evaluated at $t = t_{\text{V-E}}$
$[\nu]$	Excluded volume parameter
Γ	Surface tension
$\mathrm{II}_{\dot{\gamma}}$, $\mathrm{III}_{\dot{\gamma}}$	Second and third invariants of the strain rate tensor
I_1	First invariant of a tensor, with optional subscripts of "s" and "e" indicating shear and extensional flows
I_2	Second invariant of a tensor, with optional subscripts of "s" and "e" indicating shear and extensional flows
K $[\hat{K}]$	Mean curvature of an axisymmetric liquid filament $R(z,t)$.
l_{cap}	Capillary length
G', G''	Storage and loss modulus
[Oh]	Ohnesorge number
δ	Phase angle
λ_{D}	Disengagement time
λ_{e}	Extensional relaxation time
λ_{R}	Rouse time
λ_{s}	Shear relaxation time
λ_{Z}	Zimm time
G_{N}	Plateau modulus
M_{e}	Molecular weight between entanglements
Z	Number of entanglements per polymer chain
$[\phi_{\text{C}}]$	Percolation threshold (volume fraction)
$H(\lambda)$	Relaxation time spectrum
R_0	Disc radius or initial radius of a liquid filament (in CaBER)
R_{mid} $[\hat{R}_{\text{mid}}]$	Filament radius at the symmetry plane (mid-plane) [nondimensionalized by R_0]
$[\eta_{\text{r}}]$	Relative viscosity
$[\mathscr{R}(\zeta)]$	Self-similar function for the shape profile in filament thinning
$[\mathscr{V}(\zeta)]$	Self-similar function for the axial velocity profile in filament thinning
$[\zeta]$	Self-similar variable as a function of $\hat{z}$ and $\hat{t}$ to describe the filament thinning profile
$\dot{\epsilon}$ [Wi]	Extensional rate [Weissenberg number]
$\dot{\gamma}$	Shear rate
ϵ	Hencky strain

$[\boldsymbol{S}]$	Averaged orientation tensor for tube segments
$[\Lambda]$	Ensemble strain on polymer chain segments within the tubes
$[\Lambda_{\mathrm{m}}]$	Maximum extensibility of polymer chain segment within the tube
$[\theta]$	Structural variable
τ	Time distance to filament breakup $t - t_{\mathrm{C}}$
T_0	Absolute temperature in the unit of K
t_{C}	Filament breakup time
t_{M}	Motor actuation time (in CaBER)
$t_{\mathrm{V\text{-}E}}$	Crossover time at which the filament radii predicted by the visco-capillary (V) and the elasto-capillary (E) thinning are equal
η	Shear viscosity
η_0	Zero-shear viscosity
η_{app}	Apparent shear viscosity obtained from the linear decaying region in a filament thinning process
$\eta_{\mathrm{e,app}}$ $[\mathrm{Tr}_{\mathrm{app}}]$	Apparent extensional viscosity [apparent Trouton ratio]
η_{e} [Tr]	Extensional viscosity [Trouton ratio]
$[X]$	Geometric correction factor (in CaBER)

This page is intentionally left blank.

1 Introduction

1.1 Research background and thesis structure

Until 2019, the transportation sector has become the largest contributor (29%, or 1902 Mt/yr) to the annual emission of CO_2 in the United States, in which 85-90% of the emission comes from direct consumption of petroleum-based fuels [36, 37]. Despite progressive engineering efforts over the past century, the energy efficiency of modern automotive vehicles remains as low as 12% to 30% due to the energy losses from various subsystems (*e.g.*, power to wheels, parasitic losses and engine losses, etc) and the thermodynamic limit of internal combustion engine [38–41]. The worldwide conviction for reducing carbon footprints has significantly promoted innovations in automotive manufacturing for more advanced fuel-economy technologies [42]. Meanwhile, the burgeoning industries of electric vehicles and autonomous driving have brought new inspirations and opportunities in the designing and manufacturing of automotive vehicles that accord with the aim of improved driving and passenger experiences [43]. These trends in the automotive industry result in an increasing demand for the development of advanced materials that feature lightweight, tunable material properties (mechanical, thermal, electrical, tribological, chemical, etc), compatibility with various existing or innovative manufacturing processes, as well as cost and ecological efficiencies [42, 44]. Among numerous candidates of new materials, graphene-derived nanocomposites (GDNC) have gained especial attention in recent decades due to its superior properties and great potentials in the enhancements of material performance with minimal loadings of nanofillers. Despite abundant studies on various chemical formulations of GDNC over the past two decades [45–48], exploratory applications of such materials to commercial automotive vehicles are observed recently in the production of Ford Mustang and Ford F-150 [49, 50]. Compared with the conventional foam materials used for pump and front engine covers, new designs using GDNC materials have exhibited outstanding performance with 17% noise reduction, 30% im-

provement in heat resistance and 20% increase in mechanical strength [49, 51]. As the supply chain of nanofillers steadily matures, more applications of GDNC materials are being demonstrated and envisioned in different automotive subsystems. Examples include the reinforcement of car bodies with abrasive resistance [37, 52], interior decorations with enhanced toughness, and the optimization of engine and transmission systems with better thermal management and collision performance [37, 43]. Notably, recent progression in autonomous driving has motivated an extensive application of smart sensors on the exterior car body for real-time perception and decision-making, such as LiDARs, high-definition cameras and ultrasonic detectors [53]. A properly functional autonomous-driving system is expected to interact seamlessly and robustly under various weather conditions in a timely and accurate manner with minimal efforts for maintenance. Such unattended nature has proposed higher standards for the exterior sensors not only on the life time of electronic devices, but also on the durability of materials to accommodate extreme working conditions with additional capabilities of self-deicing, self-cleaning, anti-scratching and defrosting by heating [43]. The GDNC materials with tunable mechanical, thermal and electrical properties have become potential solutions for such applications, with a handful of proof-of-concept studies available recently [54–57]. The more recent emergence of additive manufacturing techniques, such as fused filament fabrication provides additional versatility to the customization of GDNC materials with engineered hierarchical structures at smaller lengthscales (10 μm to 1000 μm) [58] and thus enables the manufacturing of more functional devices [59, 60].

However, mass-market applications of GDNC materials in the automotive industry have been so far inhibited by numerous challenges that arise from increased structural and dynamical complexities in these materials [47, 50].

First, a comprehensive study of the complex fluid rheology and flow dynamics of GDNC materials is absent. In particular, advanced techniques for rapid rheological characterizations of these materials in varying flow types are less accessible. In addition, a robust constitutive framework to quantify the multiphase interactions in both linear and nonlinear regimes is desired to enhance the understanding of structural variations induced in large extensional deformation, which is expected in various manufacturing processes for automotive vehicles (*e.g.*, extrusion, spinning, stamping, forging, spraying, etc). As a result, these fundamental understandings of complex nanocomposite materials can provide insightful guidance from a rheological perspective to induce desired material properties with an optimal manufacturing cost.

Beyond a lack of understanding in the rheology of GDNC materials and their flow dynamics in real manufacturing processes, the other major limitation that hampers mass-

market applications of these materials lies in material processing, or to be more specific, an optimal dispersion of graphene-derived nanofillers [59]. By virtue of the layered structure of graphene-derived nanofillers, a large surface-volume ratio arises and promotes unwanted nanofiller aggregations at smaller lengthscales, which adversely impact the property enhancement due to spatial heterogeneity and an increased percolation threshold that diminish nanofiller connectivity [61,62]. The existing compounding processes that primarily rely on a steady-shear process are far from optimized for handling such anisotropic nanofillers [63]. Innovative compounding protocols based on a profound understanding of the complex structure-rheology relationship of the GDNC materials are desired to introduce beneficial structural variations to the nanofiller aggregation and dispersion that can be accessed on a generic compounding device with additional flexibility and improved performance.

To address the remaining challenges that impede large-scale applications of GDNC materials in automotive industry, this thesis is aimed at providing deeper insights into the non-linear rheology of GDNC materials exhibited under large shear and particularly extensional deformations experienced in real manufacturing processes. The thesis work is primarily comprised of the construction of an improved capillary breakup extensional rheometer based on the author's master's thesis [64], which is subsequently applied to a series of numerical and experimental studies on dilute and concentrated polymer solutions, as well as prototypical nanocomposite systems that feature complex material responses arising from multiphase interactions. These results further inspire a systematic workflow that can be readily applied for rapid and accurate rheological characterizations and identifications of constitutive models through the measurements of extensional rheology. In addition, the detailed knowledge obtained through the aforementioned measuring techniques is further demonstrated to inspire the development of a rheology-assisted protocol to assist in the dispersion of graphene-derived nanofillers, which will greatly benefit practical applications in manufacturing the material processing.

The structure of this thesis is outlined as follows.

Chapter 1 introduces the background of graphene-derived nanocomposites (GDNC) with especial focus on the applications in automotive industry and primary challenges in the rheological characterizations and material processing that delay large-scale implementation. The structure of this thesis is subsequently outlined, and a list of the publications from this thesis is presented.

Chapter 2 provides a review of previous studies on the dynamics and applications of GDNC materials. This chapter is laid out in three sections, covering the structures and

properties of GDNC materials, the generic characterizing techniques, and the state-of-the-art material processing techniques to improve the nanofiller dispersion. In addition, the fundamentals of non-linear shear and extensional rheology and structure-rheology relationship, as well as a number of definitions of dimensionless variables are presented as the theoretical dimensions for the following chapters.

Chapter 3 presents a comprehensive study of the extensional rheology for multiple types of complex fluids. The construction of a customized capillary breakup extensional rheometer (CaBER) is briefly introduced, followed by a series of experimental and numerical studies to establish a comprehensive understanding of the complex capillarity-driven thinning dynamics resulted from multiple stress contributions. A temporally-evolving geometric correction factor is incorporated into the data fitting process, and a statistics-based protocol is applied to obtain a more robust model identification, from which accurate rheological constitutive parameters can be obtained.

Chapter 4 extends the study from the preceding chapter on extensional rheology to concentrated polymer solutions in entangled regimes. A constitutive framework is proposed based on reptation theory, aiming at capturing key features of flow-dependent relaxation times and non-monotonic trends in viscosities that have been observed from previous experimental measurements. A case study that applies the proposed constitutive framework is presented on a benchmark cellulose/ionic liquid system near the entangled regime that finds practical applications in fabric recycling through a wet-spinning process. The rheological measurements in both shear and extensional flows are compared with the model predictions at varying degrees of polymerization, concentrations and temperatures, from which constitutive parameters can be obtained and described by more general scaling laws.

Chapter 5 describes the shear and extensional rheology for a prototypical GDNC material, graphene-oxide (GO) nanofillers dispersed in aqueous polyvinyl alcohol (PVA) solutions. A number of rheological techniques are demonstrated to describe the material responses in shear and extensional flows, from which a robust non-linear constitutive framework is proposed. The flow-induced morphological variation of nanofillers exhibited from the rheological characterizations inspires a new protocol using periodical exponential shear flows to assist in nanofiller dispersion by generating augmented tensile stresses in principal directions to break down large aggregates. The efficacy of this protocol is justified through the application to a viscoelastic polymer solution, in which the material responses exhibit significant strain-hardening responses that resemble the behavior in an extensional flow. A proof-of-concept experiment is conducted on a "less-well-dispersed" nanofilled system, and an improved state of dispersion can be identified by measuring the low-frequency elastic response.

Chapter 6 summarizes the key outcomes from this thesis. A brief discussion is given on the potential opportunities and remaining challenges of the techniques developed in this thesis, as well as an outlook for the future works.

1.2 Publications from this thesis (including manuscripts in preparation)

[1] **J. Du**, H. Ohtani, C. E. Owens, L. Zhang, K. Ellwood, and G. H. McKinley. An improved Capillary Breakup Extensional Rheometer to characterize weakly rate-thickening fluids: Applications in synthetic automotive oils. *Journal of Non-Newtonian Fluid Mechanics*, 291:104496, May 2021.

[2] **J. Du**, H. Ohtani, K. Ellwood, and G. H. McKinley. *Macromolecules*. In preparation.

[3] **J. Du**, H. Ohtani, K. Ellwood, and G. H. McKinley. *Journal of Non-Newtonian Fluid Mechanics*. In preparation.

[4] **J. Du**, P. B. Sanchez, C. E. Owens, G. H. McKinley. *ACS Sustain. Chem. Eng*. In preparation.

[5] P. B. Sanchez, C. E. Owens, **J. Du**, G. H. McKinley. *Biomacromolecules*. In preparation.

This page is intentionally left blank.

2 | Literature Review on GDNC Rheology and Applications

2.1 Graphene-derived nanocomposites (GDNC)

2.1.1 Graphene-derived nanofillers

Graphene-derived nanofillers, while commonly sharing a layered honeycomb structure, may differ slightly in their molecular conformation and microscopic behavior due to distinct chemical compositions, states of exfoliation that arise from different synthesis methods, as well as external conditions such as temperature and humidity, thus showing different degrees of property enhancement in practice [45,62,65,66]. In principle, two routes of production of graphene-derived nanofillers are widely adopted. The first route is chemical synthesis, from which small quantities and sizes of nanofillers with well-controlled single or few-layered structures and minimal structural defects can be produced [62]. A number of techniques are currently available for the synthesis of superlative graphene structures, including self-assembly methods [67], chemical vapor deposition (CVD) [68], reduction of carbon monoxide [69] and arc discharge [70]. Evidently, a mass application of chemical synthesis for the production of nanofillers is less likely due to the relatively low production rates with high costs. As a result, the second route of production, mechanical or chemical exfoliation, is more widely applied in industry. Such exfoliation process, commonly performed on easily-accessible graphite, graphite intercalation compounds (GIC) or graphite oxides [62], is more applicable for scaled-up productions of larger quantities of graphene-derived nanofillers that can be readily used for nanocomposites [71]. For graphite, common exfoliation methods include micromechanical cleavage [72], ultrasonication [73], and electrochemical exfoliation [74]. Compared with graphite, GIC is more commonly used as a precursor due to its larger layer spacing that arises from the additional alkali metals and min-

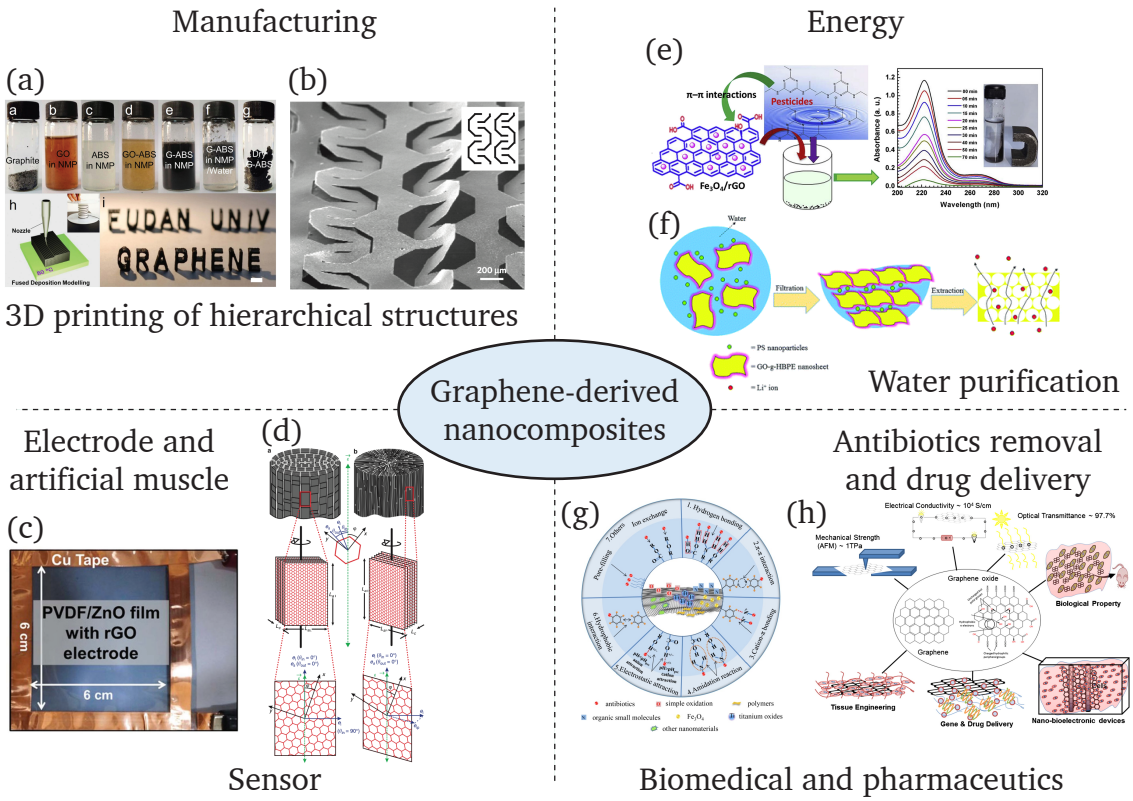

Figure 2-1: A brief overview of applications of graphene-derived nanocomposites in various fields, including advanced manufacturing, smart sensors, energy harvesting and water purification and biomedical solutions. Images reproduced from: (a) Ref. 1; (b) Ref. 2; (c) Ref. 3; (d) Ref. 4; (e) Ref. 5; (f) Ref. 6; (g) Ref. 7; (h) Ref. 8.

eral acids in the intercalation [75], which assists in the exfoliation process by virtue of a weakened layer-to-layer van der Waals attraction [75]. In recent studies, expanded graphite (EG) with an expanding volume ratio of approximately 300 has been obtained through rapid heating (thermal shocking) of GIC dispersed in sulfuric and nitric acid mixtures [76–78]. This expanded graphite can be further exfoliated through ultrasonication or pulverization to form graphene nanoplatelets (GNP) with an averaged thickness of 5 nm to 10 nm and a lateral width of 15 μm [76, 79–81]. Similar to graphite-derived precursors, graphene oxides (GO) are multi-layered oxidized graphenes with an averaged interlayer spacing of 6 Å to 10 Å that is sensitive to humidity [82–84]. GO can be used to produce well-exfoliated few-layer or monolayer graphenes through chemical and thermal reductions [10, 85–89]. In practice, large-scale synthesis of GO

is possible through variations of the Staudenmaier [90] or Hummers [91] methods that oxidize graphites using permanganates, chlorates and nitrite salts with nitric/sulfuric acids. Unlike the well-established molecular structure of pristine graphenes, a putative model for the chemical structure of GO had been an ongoing research topic for decades [92]. To this point, the Lerf-Klinowski model [9] is recognized as the most realistic description. As shown in Figure 2-2(a), this model describes a single GO molecule as a lamellar backbone mostly comprised of aromatic components, epoxy and hydroxyl groups, with carboxyl groups decorated on the periphery [82, 93]. The C/H/O ratio for a typical GO molecule is approximately 2:0.8:1 [82, 94, 95]. Because of the additional functional groups, GO is readily hydrophilic and can be easily dispersed in protic solvents due to the enhanced repulsion of negative charges induced by the carboxyl groups [82].

Previous studies have verified the existence of stable single-layer GO platelets in aqueous dispersions [96, 97]. However, the excessive amount of oxygen (C/O ratio of 2:1) inhibits the electron and phonon mobility, resulting in poor electrical and thermal conductivities [82]. These physical properties can be partially restored through a reduction of the C/O ratio, resulting in what is commonly known as reduced GO (rGO) by the application of strong reducing agents such as hydrazine [85, 98], titanium dioxide (TiO_2) [99], sodium borohydride [82] and more recently benzyl alcohol [100]. These chemically reduced GO platelets have been characterized with a higher C/O ratio in the range of 10 to 29.9:1 [95, 101], which results in a higher electrical conductivity up to 4600 S/m [102]. More recently, high temperature heating is applied to initiate the reduction process in an inert-gas environment [88], in which the epoxy and hydroxyl bonds can be readily decomposed, resulting in a C/O ratio of 10:1 (which can be further increased with extended heating time or higher temperature) [103]. This reduction process can potentially reach a state of nearly complete exfoliation for GO platelets due to the generation of small molecules such as CO and CO_2 from decomposition that increases the internal pressure in the nanofiller intercalation [10]. Notably, the exfoliation method through thermal expansion is well-known to result in a crumpled shape for the GO nanofillers attributed to the intertwining of nanofillers during the expansion process, as shown in Figure 2-2(b). Such crumpled shapes decrease the averaged contact area with the neighboring nanofillers, thus are beneficial in minimizing the nanofiller interaction and preventing the nanofillers from restacking. The reduced GO platelets have a high surface area of 700 m^2/g to 1500 m^2/g [88], which is close to the theoretical bound for pristine graphenes at 2600 m^2/g. The resulting electrical conductivity of rGO has been measured as 1000 S/m to 2000 S/m [95], and Young's moduli ranging from 208 GPa to 650 GPa [96, 104]. The thermal shocking can also be practically performed using microwave radiation, leading to a slightly lower C/O ratio

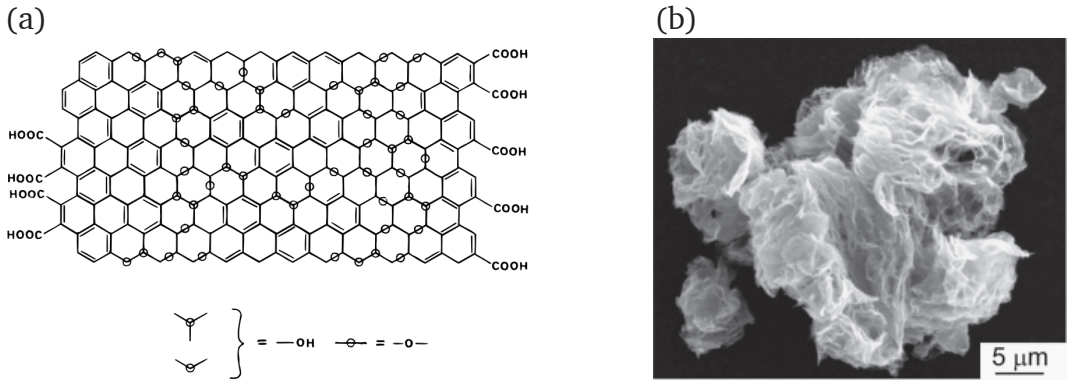

Figure 2-2: (a) Lerf-Klinowski model for the chemical structure of a single graphene oxide (GO) molecule. Reproduced from Ref. 9. (b) Scanning electron microscope image of thermally expanded GO platelets, showing a crumpled shape due to the intertwining during the expansion process. Reproduced from Ref. 10.

of 3:1 and a satisfactory electrical conductivity at approximately 270 S/m [105].

Despite the poor electrical and thermal properties of untreated GO, its high C/O ratio introduces additional reactive functional groups that motivate a variety of chemical, biomedical and mechanical applications [100, 106, 107]. In addition, the hydrophilic nature of GO and relatively monodisperse size assist in the formation of a benchmark well-dispersed system in water-soluble polymer matrices, while keeping the mechanical and geometrical fidelity of a layered nanofiller structure with the pristine graphene [18, 107]. Compared with nanocomposites filled with graphenes or few-layered GNPs, the GO dispersion has a notably lower percolation threshold with reversible flocculated network in dispersion [18, 107]. As a result, GO is widely used as a prototypical material to study the rheology of graphene-derived nanocomposites, or more generally, nanocomposite systems with high-aspect-ratio nanofillers.

2.1.2 Structure and rheology

Aspect ratio and percolation threshold

Addition of a small amount of well exfoliated nanofillers can lead to significant enhancement in the material properties of GDNC materials. The underlying mechanism arises not only from the superior properties of the nanofillers, but also from an increased surface area (more than 1000 m^2/g [88]) due to a high nanofiller aspect ratio [45]. The conformation of nanofillers dispersed in polymer melts or solutions can

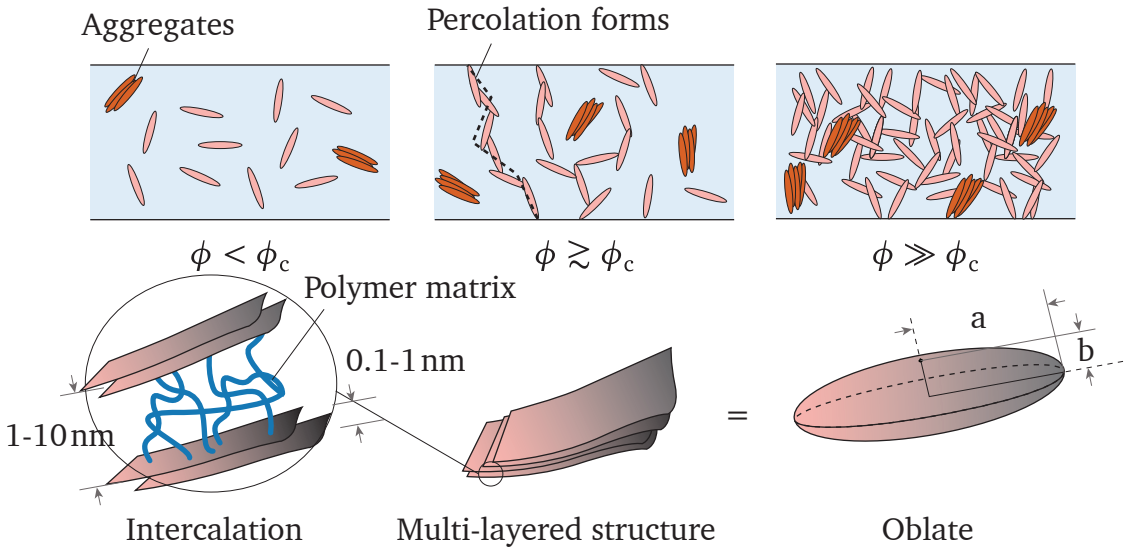

Figure 2-3: Schematic of the nanofiller conformation in a polymer matrix. The stacked nanofillers, generally in the form of a few-layered structure, can be simplified as an oblate spheroid with a semi-major axis a and a semi-minor axis b. The interlayer spacing is primarily characterized by two lengthscales ranging from 0.1 nm to 10 nm, depending on the state of exfoliation and the conformation of polymer chains in the intercalation. When the nanofiller concentration increases above a percolation threshold ϕ_C, an elastic backbone (dashed line) forms and substantially alters the macroscopic properties. Notably, aggregates of the layered structures (in orange color) are serendipitous due to the persistent van der Waals attraction.

be illustrated in the schematic of Figure 2-3, in which monolayer nanosheets stack in the [002] direction and form few-layered structures (known as "platelets") with possible polymer chains in the intercalation. In practice, completely exfoliated nanofillers in a continuous phase are less accessible due to the persistent van der Waals attraction between nanosheets. As a result, the interlayer spacing within the stacked structure depends on the local state of exfoliation, the chemical compositions, the method of synthesis as well as exterior conditions, and can be generally characterized by two lengthscales [45]: If no polymer chains exist in the intercalation, the interlayer spacing is solely governed by the interaction between two adjacent nanosheets and falls within a range of 0.1 nm to 1 nm (*e.g.*, 0.36 nm for graphenes and 0.6 nm to 0.8 nm for graphene oxides [45]). In contrary, polymer chains in the intercalation can increase the interlayer spacing by a factor of 3 to 10 due to reduced nanosheet attraction as

well as additional intermolecular repulsion arising from the polymer thermal motion (*e.g.*, 2.2 nm for polyvinyl alcohol intercalated in graphene oxide [108]). At even larger lengthscales, the van der Waals interactions become weak, and the integrity of stacked structures is subject to the variations of nanofiller concentration and macroscopic dynamics, thus does not conform to a fixed topology. Consequently, the few-layered structure with an interlayer spacing between 0.1 nm and 10 nm can be treated as a unit structure to study the nanofiller morphology and its impact on the macroscopic properties. In light of its stacked geometry, this unit component can be simplified as an oblate spheroid quantified by its semi-major axis a and semi-minor axis b. The aspect ratio of this structure can be readily defined as

$$\xi \equiv \frac{a}{b}. \tag{2.1}$$

The nanofiller morphology at larger lengthscales ($>$ 10 nm) can be subsequently determined by the oblate geometry as well as the concentration. As Figure 2-3 illustrates, at small nanofiller concentrations, dynamics of the nanocomposite system are primarily governed by the continuous phase as well as the hydrodynamic interactions arising from individual oblate structures. As more nanofillers are added to the system, there is a critical volume fraction ϕ_C, above which a sample-spanning filler network forms through an elastic backbone and substantially alters the macroscopic properties. The value of ϕ_C, defined as the percolation threshold, can be connected with the aspect ratio ξ [109] as

$$\phi_C \approx \frac{1.5}{\xi} = \frac{1.5b}{a}. \tag{2.2}$$

As a result, nanofillers with high aspect ratios are more likely to form a lower fractal dimensional network through the edge-to-edge or face-to-edge interactions [33]. Extensive studies have found evident enhancement in the material properties beyond the percolation threshold, which commonly follows a power-law trend with the quantity $(\phi - \phi_C)$ [45, 62]. Consequently, the approach to the percolation threshold is critical in practice, if significant property improvement is desired. Equation (2.2) readily rationalizes the application of graphene-derived nanofillers due to their large aspect ratios, which typically range from 50 to 1000 [45]. As a hallmark of the percolated network, the electrical percolation threshold has been measured for various GDNC materials, including GNP/polymethyl methacrylate (PMMA) at 1 vol% [110] and GNP/Nylon-6 at 1.8 vol% [111]. These values are notably lower than those for the nanocomposites filled with carbon blacks, which normally range from 8 vol% to 9 vol% [65, 112, 113]. During the processing of GDNC materials, restacking of nanofillers is spontaneous due to persistent van der Waals attractions, resulting in a decreased effective aspect ratio

due to an increased layer thickness, thus increasing the percolation threshold proportionally according to Equation (2.2) [62, 114]. Due to high aspect ratios of graphene-derived nanofillers, factors that alter the percolation threshold also include external deformation imposed on the bulk material that reorients or migrates the anisotropic nanofillers due to convection [69, 115]. A non-trivial averaged particle orientation can increase the percolation threshold because of a decreased fractal dimension of the filler network [116]. Such particle reorientation is particularly common in a number of manufacturing processes that involve large shear or extensional deformation, which can adversely impact the resulting properties of the processed materials [116, 117]. As a result, long-time annealing is commonly performed above the glass transition temperature [45] at the end of material processing. The morphology of nanofillers is thus a combined result of the dispersion state induced by the exfoliation process, the affinity of nanofillers to the surrounding nanofillers and polymer matrices, as well as the external deformation imposed on the bulk nanocomposites. As a result, it is critical to understand the morphological variations under various flow conditions in order to maintain a good dispersion state of nanofillers for effective property enhancement with minimal filler loadings.

Nanofiller dispersion and rheology

As shown in previous sections, a well-dispersed state for the nanofillers is critical to induce desired material properties of the bulk nanocomposites, and is highly subject to variations in the nanofiller geometry, rigidity, and its affinity with different phases in the material system. As a result, it is prerequisite to justify a satisfying dispersion state of nanofillers for optimal property enhancement, and it is necessary to seek a connection between the dispersion state and the micro- or macroscopic measures [17].

In general, the dispersion state of nanofillers in a typical nanocomposite system can be evaluated either through direct, optical observation of the nanofiller morphology (*e.g.*, electron microscopic and spectroscopic studies) or indirect measurements of the nanocomposite properties (*e.g.*, thermal, electrical, rheological or dynamical analysis). Transmission electron microscopy (TEM) is one of the most-used instruments to provide a direct visualization of the layered nanofiller structure and to measure the interlayer spacing accurately, from which a local dispersion state can be accessed [73, 118–122]. Figure 2-4(a) and (b) show two examples of the TEM micrographs obtained from individual graphene oxide sheets and exfoliated graphenes in a polymer matrix, in which the number of layers, aspect ratio and layer spacing can be readily measured and used to justify their dispersion states [11, 12]. However, challenges remain in the observation of highly-deformed or single-layer nanosheets due to the

limited resolution [62, 119]. In addition, measurements from TEM are highly localized (with an observation window from 0.1 μm to 10 μm) and can result in biased characterizations if the system is non-homogeneous [62]. To obtain structural information on a lengthscale closer to bulk nanocomposites, X-ray diffraction (XRD) is applied to examine the averaged layer spacing, which is a practical measure to infer the state of intercalation and stacking [13, 121]. Here, an example is shown in Figure 2-4(c) for a GO/PMMA nanocomposite system with optional addition of microazoinitiator (MAI) [13], and an increased layer spacing is captured from the shift of 2θ peak value due to the presence of MAI in the intercalation. However, valid measurements of XRD require sufficient amounts of crystalline structures, which are less accessible for a nanocomposite system with nearly complete exfoliation [62]. Besides the two major observation techniques, local nanosheet topology can also be probed accurately through atomic force microscopy (AFM). An example is shown in Figure 2-4(d), where the AFM image of functionalized graphene sheets is captured in a contact mode, and the thickness of a single-layer graphene sheet can be read out from the stepped height along the microscopic tip path [14].

More recently, scattering techniques have been widely applied to obtain more comprehensive information of the nanofiller morphology in bulk nanocomposites over a wide range of lengthscales [123]. The intensity profile plotted as a function of wavenumber is captured from scattering at different lengthscales and can be used as a measure to infer the structural information, including the layer spacing (at a wide scattering angle) and the fractal dimension (at a small scattering angle) [124]. As shown in Figure 2-4(e), the intensity profile obtained from x-ray scattering techniques is plotted for graphite and functionalized graphite sheets in polyethylene naphthalate (PEN) [15]. The top and middle subfigures show the intensity profiles at wide scattering angles to characterize the structural information at a smaller lengthscale (0.1 nm to 10 nm). The peak of the scattering intensity disappears at $q \approx 18.4\,\mathrm{nm}^{-1}$ for the functionalized graphite sheets (middle subfigure), which corresponds to an interlayer spacing for graphite of approximately 0.34 nm, justifying an exfoliated state with better dispersion. At smaller scattering angle, small-angle X-ray scattering (SAXS) and ultra-small-angle X-ray scattering (USAXS) techniques can be used to measure the fractal dimension d_f. This fractal dimension quantifies the connectivity of the percolated network and provides a more complete knowledge of the nanofiller morphology, which has been directly connected to the bulk material properties [45]. An example is shown at the bottom of Figure 2-4(e) with a notably small wavenumber range of $0.01\,\mathrm{nm}^{-1}$ to $1\,\mathrm{nm}^{-1}$ (corresponding to a characteristic lengthscale of 6.28 nm to 628 nm). Via the intensity profile at low wavenumbers, the fractal dimension d_f can be obtained by examining the power-law exponent, where the scattering intensity scales as $I(q) \sim 1/q^{d_\mathrm{f}}$ [17, 125, 126].

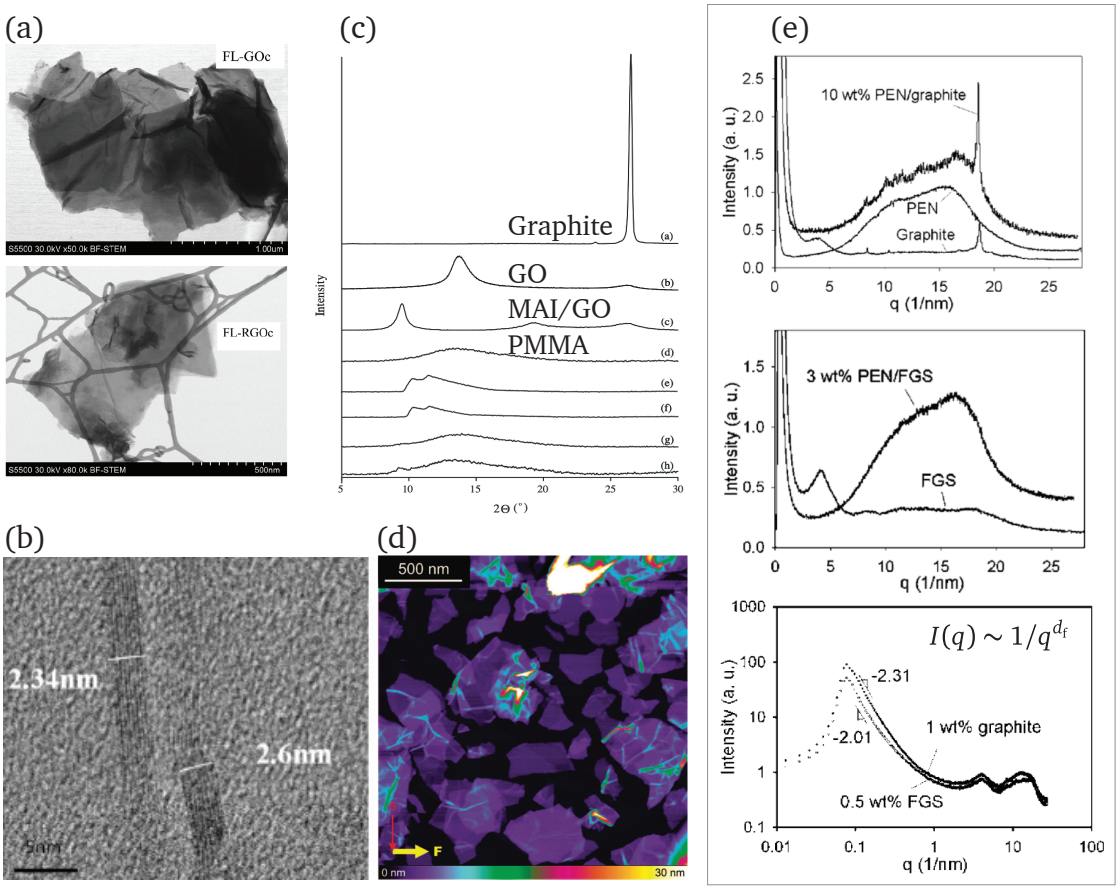

Figure 2-4: Examples of direct observations of graphene-derived nanofillers via a number of techniques. (a) TEM micrograph of commercial graphene oxide (FL-GOc, top) and better exfoliated reduced graphene oxide (FL-RGOc, bottom) platelets. Reproduced from Ref. 11. (b) TEM micrograph of Py-PGMA-graphene/epoxy nanocomposites. Reproduced from Ref. 12. (c) XRD measurement of GO/PMMA with optional addition of macroazoinitiators in the intercalation. Reproduced from Ref. 13. (d) AFM image of functionalized graphene sheets. Reproduced from Ref. 14. (e) X-ray scattering intensity profile for graphite (top) and functionalized graphite sheets (middle) in PEN. The bottom figure is obtained from small angle X-ray scattering (SAXS), from which a fractal dimension can be obtained. Reproduced from Ref. 15.

Admittedly, the direct observations by microscopic and scattering techniques provide clear visualizations of the nanofiller morphology. A more practical (and possibly more "direct" in the context of property enhancement) method to probe the dispersion state

is through examining the resulting bulk-phase material properties. In particular, a number of rheological techniques are available that permit versatile protocols to characterize the material responses under small and large deformations that are consistent with the working conditions in real manufacturing processes, from which a comprehensive picture of the bulk structure-rheology relationship can be established [17,45].

The results from previous studies have provided rich rheological information for a variety of nanocomposites with high-aspect-ratio nanofillers [15,17,45,62,69,127–132]. General rheological studies primarily focus on both the linear and nonlinear regimes. Linear rheology characterizes the dynamic responses resulted from the material structure and nanofiller morphology, whereas non-linear rheology characterizes the morphological variations that are subject to large material deformation. The most prominent observation for a percolated nanocomposite system from linear rheology is the progressive formation of a non-trivial low-frequency storage modulus G_0' as the concentration increases, which can be attributed to the additional elasticity arising from the percolated backbone. Figure 2-5(a) shows an example for the nanocomposite system filled with graphite and functionalized graphite sheets (FGS), in which the storage moduli of both material systems progressively flatten as the concentration reaches the percolation threshold [15]. Notably, a smaller concentration at which the storage modulus flattens can be identified for the FGS (orange lines), indicating an improved state of dispersion [15]. The detection of G_0' can be assisted by a number of alternative plots, including the van Gurp-Palmen plot (*i.e.*, the phase angle δ against $|G^*|$) and Han plot (G' against G''), in which the convergence of G' in the low-frequency limit can be more clearly visualized [133]. Figure 2-5(b) shows an example of the van Gurp-Palmen plot for multi-walled carbon nanotubes (MWCNT) suspensions, from which the value of G_0' was readily determined by extrapolating to a vanishing phase angle, or $\delta = 0$ [16]. The low-frequency storage modulus G_0' is a measure of the percolated network elasticity, and its value commonly scales with the volume fraction as $G_0' \sim (\phi - \phi_C)^\alpha \sim \phi^\alpha$ in the limit of $\phi \gg \phi_C$, as exemplified in Figure 2-5(c) for two clay/polypropylene nanocomposites [17]. The exponent α can be further connected to the bulk structural information of the fractal dimension [17,109,134] as

$$\alpha = \frac{3+x}{3-d_f}, \tag{2.3}$$

where d_f is the fractal dimension of the percolated network, and x is a shape factor that is dependent on the number of particles in the oblate structure as illustrated in Figure 2-3. Equation (2.3) thus constructs a practical relationship between the measured rheology and the nanofiller structure, which can be readily used to evaluate the

dispersion state.

Because of a plateau storage modulus at low frequencies, nanocomposites with $\phi \geq \phi_C$ feature a non-zero yield stress, which can be obtained through steady flow tests. Figure 2-5(d) shows an example steady flow curve for aqueous GO dispersions, where the shear stress plateaus at low shear rates (corresponding to Peclet numbers $Pe \ll 1$) and high concentrations [18]. This trend of the steady shear stress can be practically described by the Herschel-Bulkley model [135] as

$$\sigma(\dot{\gamma}) = \sigma_0 + k\dot{\gamma}^n, \tag{2.4}$$

where σ_0 is the yield stress, and k and n describe the shear-thinning behavior at high shear rates in a power-law manner. The yield stress σ_0 can be connected to the low-frequency storage modulus G_0' by $\sigma_0 = G_0'\gamma_{0,c}$, where $\gamma_{0,c}$ is the critical oscillatory strain beyond which non-linear behavior arises [136]. In light of the high-aspect-ratio nature, a flow-induced nanofiller orientation can alter the bulk rheology as well, as a result of the induced anisotropy that effectively reduces the structural dimension [62]. This change in the fractal dimension is evident in the limit of low nanofiller concentrations, when the increase in the shear viscosity is mainly attributed to the hydrodynamic interactions between the nanofillers and the continuous phase. As a result, classical semi-empirical expressions of the Einstein-Batchelor (E-B) [137, 138] or the Krieger-Dougherty (K-D) [139] equations are applicable, which can be expressed as

$$\text{E-B: } \eta_r = 1 + 2.5\phi + 6.2\phi^2, \tag{2.5a}$$

$$\text{K-D: } \eta_r = \left(\frac{1}{1-\phi/\phi_m}\right)^{[\eta]\phi_m}, \tag{2.5b}$$

where $\eta_r = \eta/\eta_{con}$ is the dimensionless relative viscosity and η_{con} is the viscosity of continuous phases. Here, $[\eta]$ is the intrinsic viscosity and ϕ_m is the maximum packing fraction. In an ideal scenario of spherical monodisperse fillers, the value of ϕ_m is 0.64 [20, 140]. Figure 2-5(f) shows an example for the evolution of relative viscosity as a function of the volume fraction for low- and high-aspect-ratio nanofillers, both of which can be well described by the K-D equation, thus justifying the viscosity increase arising from the hydrodynamic interactions at low nanofiller concentrations [19, 20]. However, discrepancies in the viscosity between the two shapes of nanofillers mainly arise from a decreased maximum packing fraction due to the anisotropic nature of nanofillers with high aspect ratios, which broadly scales inversely with the nanofiller aspect ratio [19, 114].

This relation can be similarly interpreted from the perspective of the percolation threshold according to Equation (2.2). Taking carbon nanofibers as an example, the percolation threshold can be reduced to 0.05 [20]. The filler-induced microstructures at varying nanofiller concentrations, while exhibiting different behavior in the bulk rheology as a result of distinct filler-filler (percolated network) or filler-matrix (hydrodynamic) interactions, still share similar rheological trends. Such similarity can be described through time-concentration superposition (TCS) [127]. The development of a robust superposition model remains an ongoing research topic. Recently, phenomenological models have been proposed to construct the TCS for a number of material systems [127, 141–145], from which modulus and frequency shifting factors as well as other rheological parameters such as the yield stress can be extracted. Despite a number of studies on the TCS of nanoparticle filled systems, the application of TCS to GDNC systems has been scarce so far. Figure 2-5(f) shows the collapsed storage moduli through TCS for a number of different nanocomposite systems [21]. The collapsed moduli data exhibit similar material responses shared by different nanofillers to describe the interplay between the continuous and nanofiller phases in dominating the resulting linear rheology over a wide frequency range. Consequently, a practical TCS model can promote better understanding for the origins of the rheological behavior from a material perspective [21, 127].

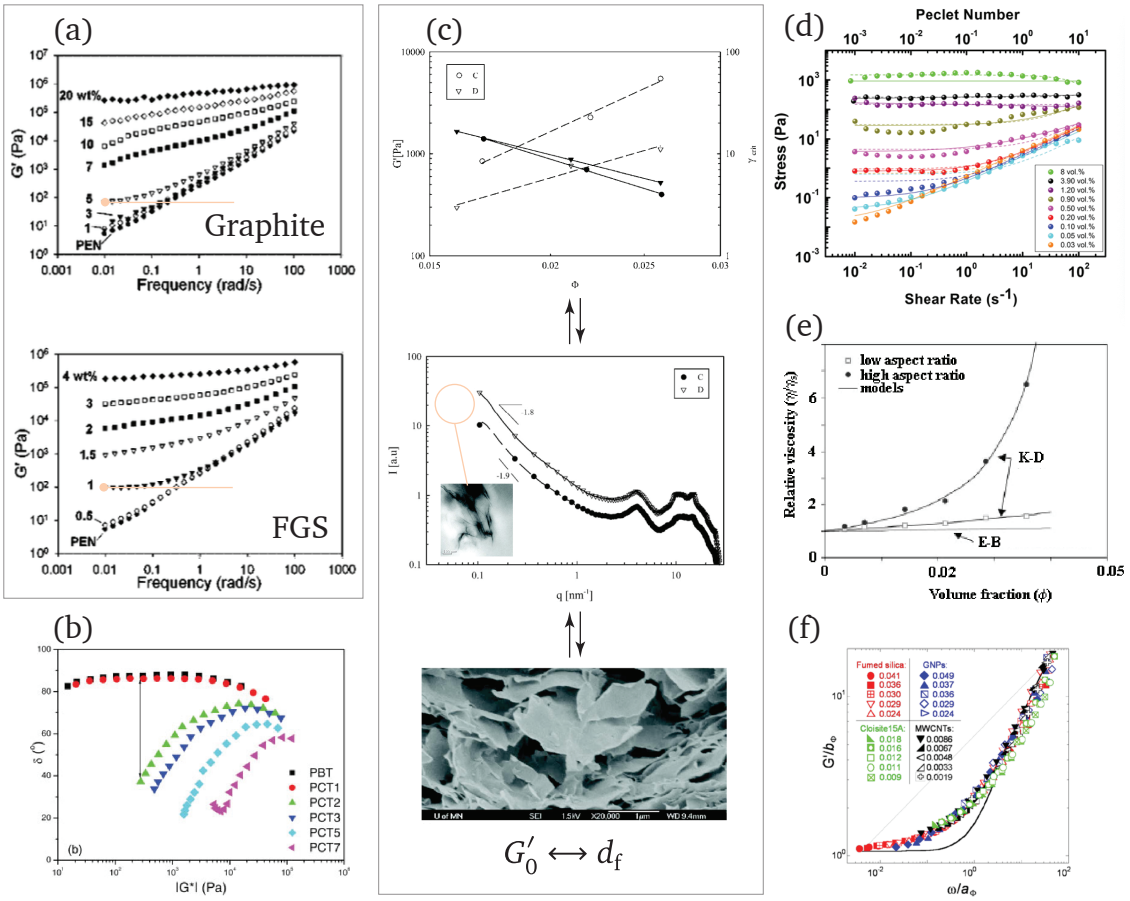

Figure 2-5: Typical rheological characterizations for various nanocomposite systems. (a) Dynamic moduli of graphite and functionalized graphite sheets (FGS) through small amplitude oscillatory shear. An estimated G_0' is marked in orange at the percolation threshold. Reproduced from Ref. 15. (b) van Gurp-Palmen plot for multi-walled carbon nanotubes. Reproduced from Ref. 16. (c) Top: Low-frequency plateau storage modulus and critical strains for clay/polypropolene nanocomposites. Middle and bottom: SAXS and TEM results to characterize the fractal dimension. The rheological and scattering information are combined to determine the dispersion state. Reproduced from Ref. 17. (d) Steady shear flow curve of GO dispersions, fitted with the Herschel-Bulkley model (solid lines). Reproduced from Ref. 18. (e) Relative viscosity for low- and high-aspect-ratio nanofillers fitted with the Einstein-Batchelor (E-B) and Krieger-Dougherty (K-D) equations. Reproduced from Ref. 19 and originally from Ref. 20. (f) Reduced storage moduli through both modulus and frequency shifting for the nanocomposite systems with various types of nanofillers. Reproduced from Ref. 21.

Methods to improve dispersion

In order to improve the state of nanofiller dispersion to optimize property enhancement, different processing methods have been applied, depending on the state of precursors and the compatibility with various manufacturing processes. In general, these dispersion methods can be subsumed into two categories.

The first category, as introduced previously for the production of nanofillers, is to break down large agglomerates or to delaminate the nanofiller layers [62]. While this process occurs concomitantly in the exfoliation process induced by chemical reactions or thermal shocking as briefly introduced previously, the most common protocol, applied in both lab and industry, is through solution or melt blending to induce non-covalent dispersions. In this protocol, dried nanofillers, readily exfoliated nanofiller suspensions or solutions are added to the desired polymer matrix and subsequently mixed under high-shear deformation. For solution mixing, the nanocomposites can be obtained through either precipitation with a non-solvent, or by mold casting and subsequent removal of solvent [45]. Ultrasonication can be also subsumed into this category because of a similar mechanism. The method of blend mixing has been widely adopted for exfoliated graphene-derived platelets due to its compatibility with a variety of polymers [45], including polystyrene [146], polyimides [147], polymethyl methacrylate (PMMA) [148] and polyvinyl alcohol (PVA) [149]. In addition, thermal or chemical methods have been recently used to reduce or screen the platelet interactions for better dispersion. Examples include the application of surfactants [150], lyophilization [151] and phase transfer [152].

The second category of the dispersion methods is through *in situ* polymerization, which generally renders a better dispersion state without the application of extremely high-shear conditions [45]. The polymerization process can result in delaminated layers with improved exfoliation through the intercalation of monomers with relative rigid structures and consequently a more homogeneous system [62]. An evident advantage of this technique is tunable nanofiller-matrix interactions through the reactive functional groups on the nanofiller surface that readily react with the monomers, which enable the nanofillers to be grafted with long polymer chains through physical of chemical bonds. Such grafting can be either covalent [153, 154] or non-covalent (*e.g.*, hydrogen bonding) [13, 81, 108, 155–158]. A number of previous studies have demonstrated an increased interlayer spacing with *in situ* polymerization, which results in significantly improved dispersion [76, 111, 155, 159]. However, the *in situ* polymerization technique has so far been limited to the monomers that can be simultaneously polymerized in solvents and are compatible with a selected range of nanofillers. In addition,

the filler-monomer suspension needs to maintain a low-to-medium viscosity to achieve homogeneous polymerization in the bulk phase [45]. These limitations have inhibited the application of this technique for mass productions.

In industry, melt blending is deemed a cost-efficient and scalable method for the mass production of thermoplastic polymer nanocomposites [15,69,121,124,160]. The large stress resulting from a vigorous shearing process as well as high viscosity of the polymer melts has proven to assist in direct exfoliation of layered silicate nanocomposites [161]. Studies have also found generally higher alignment of the nanofillers than the solution mixing method at same nanofiller loadings due to a confined geometry and higher shear rates [162]. Previous studies on the melt-blending technique have focused on thermally expanded GO and GNP particles dispersed in various polymer matrices that are directly fed into a compounding process for industrial applications, as exemplified by polypropylene [110,163], polyethylene [164], polyethylene naphthalate (PEN) [15] polyurethane [162], polycarbonate [69] and natural rubbers [160]. However, it remains challenging for the melt-blending technique to reach the same level of dispersion for graphene-derived nanofillers as obtained from solution mixing [45, 162]. In addition to the relatively poor level of dispersion, challenges that barricade the approach to an optimal dispersion state also include proper handling of low-density nanofillers and biotoxicity that arises from these nanofillers during the loading process [165, 166].

In general, the performance of a compounding process primarily depends on the design of flow kinematics, which are critical in altering the nanocomposite morphology, especially for nanofillers with high aspect ratios [167]. In practice, the design of flow kinematics for a melt blending process is limited by the material properties, such as the thermal instability of polymer matrices or even nanofillers at high temperature, and the drastic density difference between the matrix and dried nanofillers that result in large aggregations prior to the dispersion process [168]. As a result, an effective protocol is desired to induce optimal dispersion without impairing the structural integrity of nanocomposite systems.

More recently, a number of studies have proposed innovative designs to improve the conventional twin-screw extrusion process with the introduction of strong extensional flow to break down the aggregates and optimize the pulverization and dispersion of fillers in the nanocomposites [168, 169]. The idea of using extensional flow originally came from Grace [22] in the study of dispersing an immiscible fluid-fluid emulsion system. As shown in Figure 2-6 reproduced from the original paper, an extensional flow, here labeled as an “irrotational shear” flow (dashed line) showed superior advantages over the shear counterpart (solid line) in effectively breaking up small drops (area above the lines) when the viscosities of the two phases significantly contrast,

whereas a maximum viscosity ratio of $\mu_D/\mu_C \approx 4$ is identified for shear flow, beyond which drops become unbreakable regardless of the magnitude of input shear stress[1].

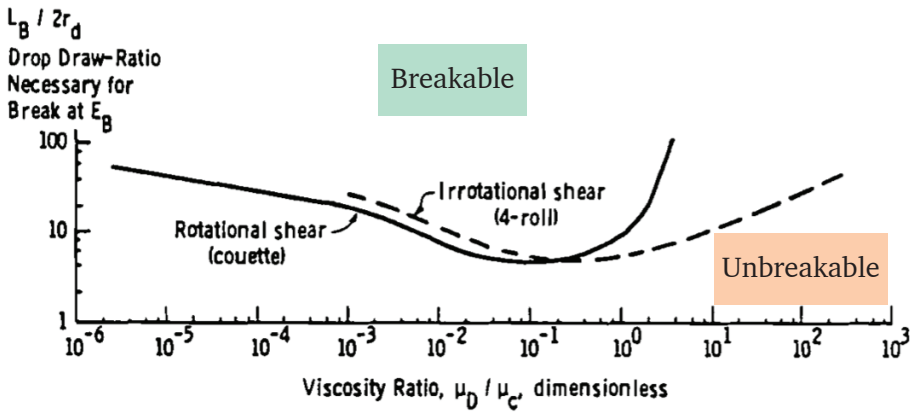

Figure 2-6: Critical drop draw-ratio against viscosity ratio of the two phases. The critical drop value for rotational shear flow (solid lines) is bounded at a viscosity ratio of approximately 4, beyond which the drops are unbreakable through shear flow, whereas an extensional flow (dashed line) shows the capability to break up large drops even at high viscosity ratios, providing that a sufficient stress is imposed. Reproduced from Ref. 22.

A number of prototypes have since been available that enable a strong extensional flow to the existing compounding process, either as standalone devices (*e.g.*, extensional flow mixer [170] and elongational flow reactor & mixer [171]), or as attachments to a commercial compounder (*e.g.*, extensional mixing element [169, 172]). The extensional flow has been proved to be effective in dispersing graphites and carbon blacks in a number of polymer matrices, such as polystyrene [173], PMMA [173], ethylene propylene diene monomer (EPDM) rubber [171] and polylactic acid (PLA) [174]. Nevertheless, the new compounding devices or attachments bring engineering challenges for durability and maintenance in the context of mass production, as well as extra costs for the update of existing compounding lines. In addition, the extensional deformation, commonly induced by a hyperbolically converging channel, is driven by a large pressure gradient, and the accumulated Hencky strain is primarily set by the geometry,

[1]The "irrotational shear" flow essentially specifies an extensional flow, and the terminology was used in the original paper to refer to the 4-roll system, from which the flow was generated.

which may not suffice to break up smaller aggregates. As a result, new protocols based on existing compounding instruments with increased flexibility are desired and being actively explored.

Due to the simple configuration and optimal scalability for mass production, flow-induced dispersion methods have gained increased attention by automotive industries [169, 172, 175]. In many contexts, large deformation of polymer composites is inevitable in a number of applicable manufacturing processes, such as blow molding, fiberspinning and 3D printing [17, 62]. However, a comprehensive understanding of the non-linear rheology for the composite systems with anisotropic nanofillers is still absent, which inhibits further optimization of the material synthesis, design of dispersion protocols and manufacturing processes [62]. In light of the remaining limitations, this thesis is aimed at understanding the rheology of graphene-derived nanocomposite and probing the structural variation under strong shear and extensional flows in the non-linear regime.

2.2 Techniques for rheological characterizations

2.2.1 Shear rheology

Shear rheology can be characterized by a commercial shear rheometer. In the most common experimental set-up on a rotary rheometer, a sample is placed between two precisely manufactured coaxial conic or plate geometries, and one geometry axially rotates to impose shear motion to the interstitial fluid. The temporal evolution of the shear rate and shear stress is obtained by the angular velocity and torque measured from the embedded encoder and force transducer. The linear rheology is probed primarily through small amplitude oscillatory shear (SAOS), where a sinusoidal shear motion with a small oscillatory strain is imposed to the sample, and a sinusoidal stress response is expected with modified amplitudes and phases due to viscous and elastic responses. The storage and loss moduli, G' and G'', obtained from the sinusoidal histories reveal the viscoelastic dynamics of the tested sample in the linear region, from which the structural information arising from the complex material components and their interactions can be implied. By plotting G' and G'' in the van Gurp-Palmen form (δ or $\tan(\delta)$ against $|G^*|$, as introduced previously in this chapter), the liquid-to-solid transition can be captured as the filler loading increases and the phase angle progressively vanishes, and the low-frequency storage modulus G'_0 as introduced in the previous sections can be obtained from extrapolation.

The dynamic moduli are further fitted into a number of well-established constitutive models to extract meaningful physical parameters. Alternatively, the complex linear viscoelastic response can be clearly visualized through inspecting the relaxation time spectrum. As Figure 2-7(a) illustrates, the Maxwell model, as a well-known benchmark, is comprised of a spring (with a modulus G_0) and a dashpot (with a viscosity η_P) connected in series, which gives rise to a single relaxation time $\lambda = \eta_P/G_0$, and the resulting constitutive equation can be expressed as

$$\sigma + \lambda\dot{\sigma} = \eta_P\dot{\gamma}, \tag{2.6}$$

where σ and $\gamma = \gamma_1 + \gamma_2$ are the stress and strain imposed on either end of the spring-dashpot structure. By taking Fourier transform on both sides of Equation (2.6), the storage and loss moduli can be obtained as

$$G'(\omega) = \frac{G_0(\lambda\omega)^2}{1+(\lambda\omega)^2}, \tag{2.7a}$$

$$G''(\omega) = \frac{G_0(\lambda\omega)}{1+(\lambda\omega)^2}, \tag{2.7b}$$

$$\tag{2.7c}$$

as plotted in Figure 2-7(b) as thin solid and dashed lines. For a complex viscoelastic fluid, multiple relaxation modes may exist, and a continuous relaxation time spectrum $H(\lambda)$ can be defined based on the results from the single-mode Maxwell model, such that the storage and loss moduli can be expressed [136] as

$$G'(\omega) = \int_0^\infty H(\xi)\frac{(\xi\omega)^2}{1+(\xi\omega)^2}\mathrm{d}\ln\xi, \tag{2.8a}$$

$$G''(\omega) = \int_0^\infty H(\xi)\frac{\xi\omega}{1+(\xi\omega)^2}\mathrm{d}\ln\xi. \tag{2.8b}$$

To incorporate multiple relaxation modes in the constitutive model, the spring-dashpot structure for Maxwell model illustrated in Figure 2-7(a) can be aligned in parallel with individual sets of parameters $(\eta_{P,i}, G_{0,i})$, resulting in a series of discrete relaxation modes $H(\lambda) = \sum_{i=1}^{n} G_{0,i}\lambda_i\delta(\lambda-\lambda_i)$, where $\delta(t)$ is the Dirac delta function, and $\lambda_i \equiv \eta_{P,i}/G_{0,i}$. In this thesis, the concept of a fractional "springpot" (as a semantic combination of "spring" and "dashpot") is implemented to derive a more compact description for a broad relaxation time spectrum [23, 176]. Under a special circumstance

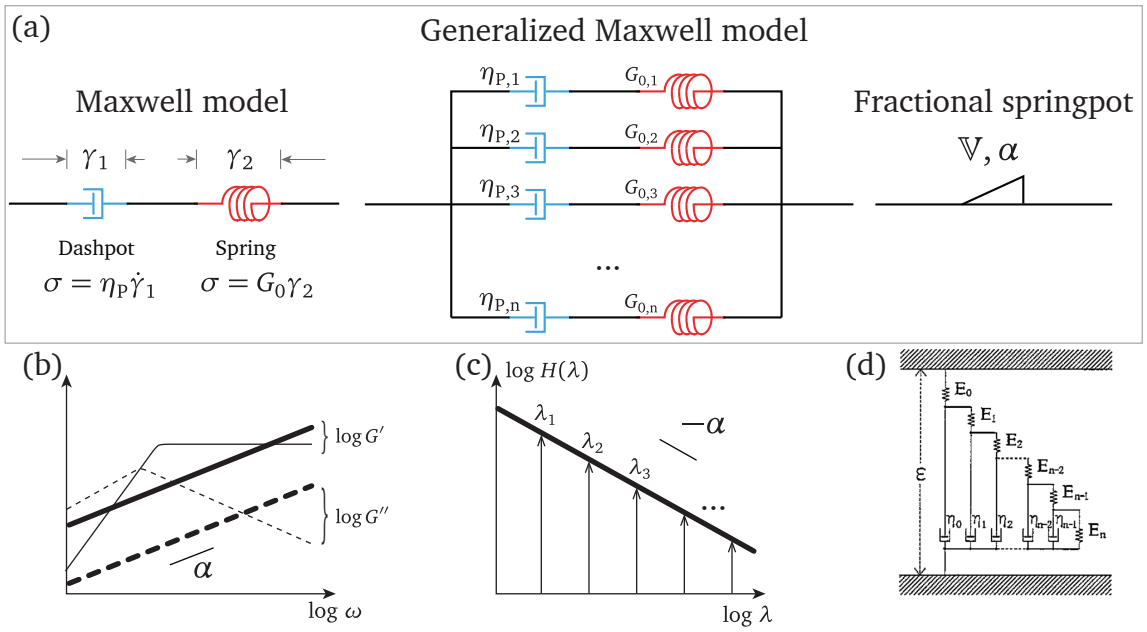

Figure 2-7: Derivations and characterizations of a fractional springpot. (a) Spring-dashpot analogy of the Maxwell model, the generalized Maxwell model and notation of a springpot parameterized by a quasiproperty $\mathbb{V}$ and fractional exponent α. (b) Frequency responses of the dynamic moduli for the Maxwell model (thin lines) and a fractional springpot (thick lines). Solid and dashed lines correspond to storage modulus G' and loss modulus G''. (c) Continuous relaxation time spectrum for the generalized Maxwell model (series of Direc delta functions) and a fractional springpot (continuous power-law function). (d) Spring-dashpot analogy for a fractional springpot. Reproduced from Ref. 23.

when the discrete time spectrum shows a broad power-law trend, the constitutive equation can be written in a simple form using the fractional derivative [177] as

$$\sigma = \mathbb{V}\frac{\mathrm{d}^\alpha \gamma}{\mathrm{d}t^\alpha} \equiv \frac{\mathbb{V}}{\Gamma(1-\alpha)}\int_0^t (t-\xi)^{-\alpha}\dot{\gamma}(\xi)\mathrm{d}\xi, \tag{2.9}$$

where $\mathrm{d}^\alpha/\mathrm{d}t^\alpha$ is the fractional derivative operator, and $\Gamma(x)$ is the gamma function. In the limit of $\alpha = 0$ and $\alpha = 1$, Equation (2.9) is reduced to the constitutive relations for a spring and a dashpot, respectively. The single springpot can be equally represented by an infinite series of springs and dashpots, which has been demonstrated previously [23] as shown in Figure 2-7(d). The resulting storage and loss moduli can be similarly

calculated from Equation (2.9) as

$$G'(\omega) = \mathbb{V}\omega^{\alpha}\cos\left(\frac{\pi\alpha}{2}\right), \tag{2.10a}$$

$$G''(\omega) = \mathbb{V}\omega^{\alpha}\sin\left(\frac{\pi\alpha}{2}\right), \tag{2.10b}$$

both of which show power-law trends with frequency with an identical exponent α, as illustrated in Figure 2-7(b) in thick solid and dashed lines. By combining multiple springpot components, a more complex time spectrum can be generated. It will be shown in later sections that this model provides a compact, however, accurate description of the linear rheological behavior for a range of materials.

The non-linear shear rheology can be probed through the transient flow response by either imposing a step strain, a step-up strain rate or a constant stress and monitoring the resulting dynamics [136]. For a complex fluid with a broad relaxation time spectrum, the material response can exhibit distinct rheological behavior at different timescales. When the input strain or stress is sufficiently large, the resulting material response can substantially deviate from the linear behavior, and the nanocomposite morphology is subject to variations. An enhanced understanding of the non-linear rheology constitutes a practical measure of the flow-induced material properties, which in turn provides insights into the beneficial modifications to the nanofiller morphology with possibly improved structural and rheological performance. In this thesis, a K-BKZ constitutive framework combining the linear viscoelasticity using the fractional models and damping functions [177] will be applied to produce a robust model for the GDNC systems to describe the microstructural variations under large deformation for multiple phases in the system, and more detailed will be provided in Chapter 5.

2.2.2 Extensional rheology

In addition to the rheological characterization in shear flow, material responses in an extensional flow are less focused for the GDNC systems, however, of paramount importance in real manufacturing processes. In an extensional flow, a fluid deforms in an irrotational manner. Mathematically, its kinematics can be described by a strain-rate tensor with only diagonal terms as

$$\dot{\boldsymbol{\gamma}} = \begin{bmatrix} -\dot{\epsilon} & 0 & 0 \\ 0 & -\dot{\epsilon} & 0 \\ 0 & 0 & 2\dot{\epsilon} \end{bmatrix}. \tag{2.11}$$

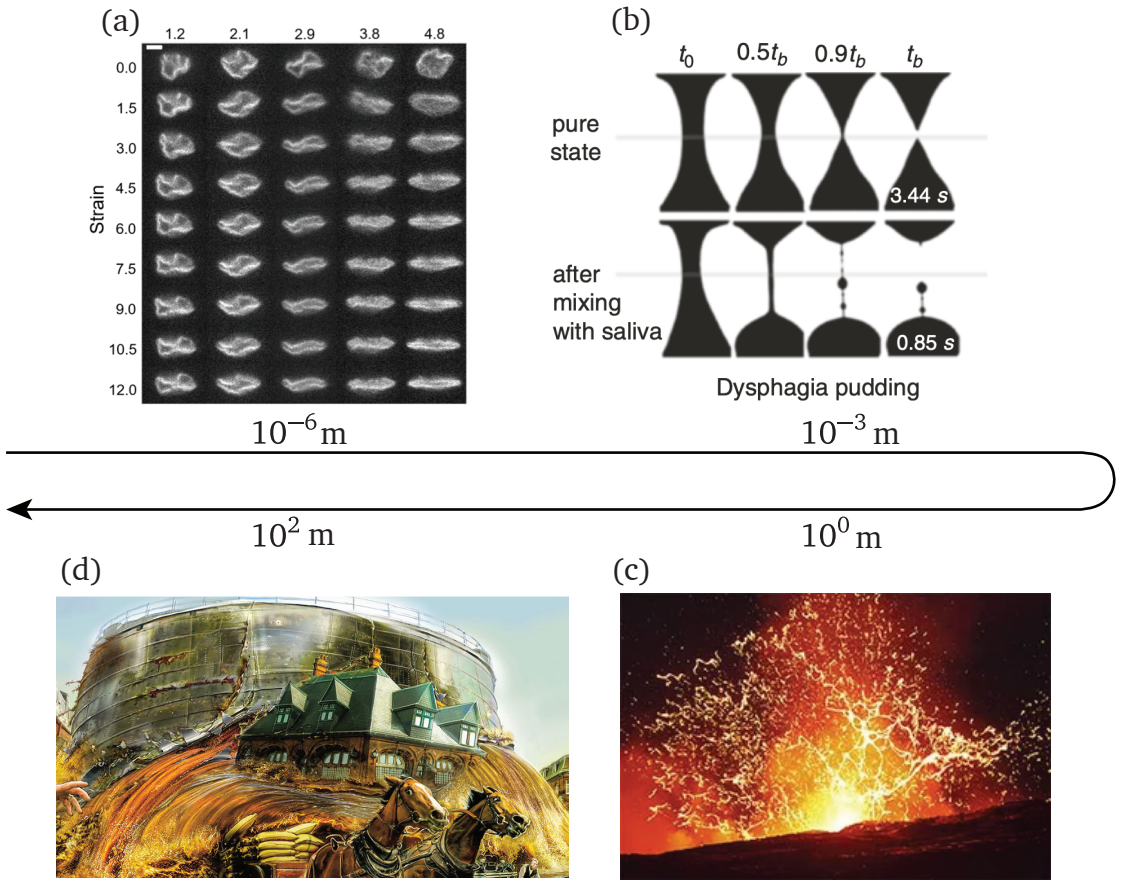

Figure 2-8: Examples of extensional flows at different lengthscales. (a) Kinetoplast deformed in a planar extensional flow. Reproduced from Ref. 24. (b) Pudding samples before and after contact with human saliva under extensional flow. Reproduced from Ref. 25. (c) Lava splashing during active volcano eruption[2]. (d) Illustration in memory of the *Great Molasses Flood* that occurred in the North End neighborhood of Boston, 1919, depicting the moment of explosion of the molasses tank[3].

Extensional flow is prevalent in real life over a wide range of lengthscales. As shown in Figure 2-8, a number of examples are illustrated over a lengthscale range from 1 ×

[2]T. Sasaki, *Getty Images*. [Online]. Available: `https://science.howstuffworks.com/nature/natural-disasters/single-volcanic-eruption-destroy-all-life.htm`, Accessed on: Aug. 30, 2021.

[3]B. Walker, *Scholastic News*. [Online]. Available: `https://sn4.scholastic.com/issues/2018-19/010719/the-great-molasses-flood.html`, Accessed on: Aug. 30, 2021.

10^{-6} m to 1×10^{2} m, including the deformation of kinetoplasts [24] and the mixture of pudding and human saliva [25], lava splashing during volcano eruption and the explosion of molasses tank in memory of the *Great Molasses Flood* that took place in Boston, 1919[4].

Unlike shear flow, the steady extensional flow is deemed a strong flow due to its exponentially increasing principal elongational ratio, $\lambda_1 = \exp(\dot{\epsilon}t/2)$, where $\dot{\epsilon}$ is the magnitude of the extensional rate [136]. Therefore, the rheological response in extensional flow is noticeably different from that in shear flow. To describe the material response in extensional flow, an extensional viscosity can be defined using the first normal stress difference as

$$\eta_e = \frac{\sigma_{11} - \sigma_{22}}{\dot{\epsilon}}, \tag{2.12}$$

where σ_{11} and σ_{22} are the first and the second normal stress component of the stress tensor. For a Newtonian fluid in uniaxial extension, this corresponds a constant extensional viscosity of $\eta_e = 3\eta$, where η is the shear viscosity [178].

Because of the nature of irrotational deformation, the rheological behavior in extensional flow cannot be captured directly by a shear rheometer. Unlike a rotary shear flow where a steady state can be readily obtained, pure extensional flow is commonly transient, and special care in the data processing is necessary to justify the obtained measurements. The dynamics of extensional deformation greatly diversify as the rheological complexity of the tested sample varies. In addition, measurements in extensional flow can be potentially modified by additional factors, such as the fluid inertia, gravity and the surface tension, while these factors are relatively easy to handle with in the shear flow. As a result, a universal instrument to quantify extensional rheology is hardly accessible, and existing extensional rheometers are generally applicable to a certain operating spaces bounded by viscosities or characteristic strain rates [26, 35]. Figure 2-9 provides an overview of the existing extensional rheometers with their operating regimes [26]. Based on the imposed strain rates, common extensional rheometers can be fitted into three categories, and they are briefly introduced as follows.

The first category is filament stretching rheometer. This type of extensional rheometer operates in the similar principle as a commercial shear rheometer by imposing a constant strain rate, but in extensional flow. A sample is placed between two coaxial discs, which are separated in a pre-programmed profile in order to induce the desired flow kinematics. The material response is quantified by the normal stress measured from the

[4]Regretfully, even though the explosion of the molasses tank that induced a strong extensional flow was characterized by a lengthscale of 1×10^{2} m, the disastrous shear flow of the molasses that followed affected an area with a lengthscale of more than 1×10^{3} m.

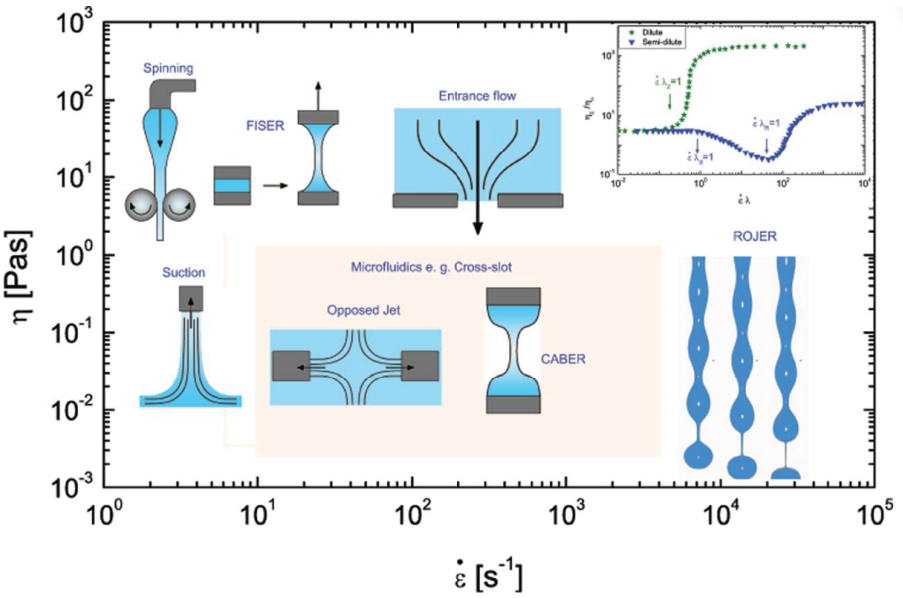

Figure 2-9: Existing extensional rheometers and their applicable ranges of viscosity and strain rates. Reproduced from Ref. 26.

end of the discs, commonly by force or stress sensors, and the material properties can be calculated subsequently. The major advantages of this type of extensional rheometer include no necessary *a priori* knowledge of the constitutive equation, and customizable kinematic profiles to investigate more complex rheological behavior. However, unlike the shear rheometer on which a steady state can be reached by imposing a constant rotational speed, a steady extension requires an exponentially increasing disc separation. Such rapidly increasing actuation cannot last long due to the limitations in the instrument size, motor acceleration and sensor resolution as the filament approaches pinch-off. In addition, the transient measurements can be susceptible to surface tension due to the non-trivial filament curvature as well as gravity, when the material response is altered profoundly. To alleviate the measuring bias induced by unwanted environmental factors, advanced control strategies need to be implemented, adding up to the complexity of the instrument design and operation [179]. In light of these limitations, the filament stretching technique is found useful for the measurements of highly viscous complex fluids, such as polymer melts or rubber-like liquids [178]. Examples of this type of extensional rheometer include the Münstedt creepmeter [180], the Meissner's rheometer with rotary clamps [181], the Reotens tensile test [182], the SER device [183] and a number of filament stretching extensional rheometers

(FiSER) [183–185].

The second category is capillarity-driven extensional rheometer. In this type of extensional rheometer, a similar geometrical configuration as in filament stretching rheometers is identified with a liquid sample (approximately 10 μL to 50 μL) placed between two coaxial discs. Instead of a pre-programmed profile to induce a constant strain rate in the first category, a sufficiently large step-strain is imposed to the liquid sample beyond its Rayleigh-Plateau limit, subsequently initiating a transient filament thinning process [35]. The filament kinematics are primarily resulted from a balance between the driving capillary pressure and the resistance from the viscous and elastic stresses described by the constitutive equation. The constitutive parameters can be obtained by fitting the measured filament thinning profile with the prediction line from the specified constitutive model. Compared with the first category of extensional rheometer, the instability-induced rheometer requires less stringent control of the instrument actuation, thus simplifying the instrument design and experimental procedures with improved robustness in the measurements. However, *a priori* knowledge of the constitutive equation is necessary to calculate a reference prediction of the filament thinning profile in order to obtain valid constitutive parameters through fitting and data processing. As a result, the instability-induced extensional rheometry is not suitable for constructing new constitutive models for an unknown complex fluid, but to obtain meaningful constitutive parameters based on an appropriately selected constitutive model. In practice, this constitutive model is selected empirically from the measured filament thinning profile. However, if the capillarity-driven thinning dynamics are complex, the model selection can be heavily biased, and the subsequent fitting of the measured filament thinning profile may lead to biased understanding of the rheological behavior that only applies to a particular range of strain rates. It is undoubtedly an ongoing work to introduce new constitutive equations to the arnesal of model candidates for more accurate and comprehensive measurements of the material properties [35], but it remains a challenge so far to choose the best-fit model with a parsimonious set of parameters [29]. Over the past few decades, a number of different extensional rheometers that adopt the instability-driven mechanism have been designed, and representative examples include the microfilament rheometer [186], the capillary breakup extensional rheometer and its variations [35, 187, 188], and the jetting-based extensional rheometer (free jet elongation rheometer [189], Rayleigh-Ohnesorge jetting extensional rheometer [190]), and dripping-on-substrate devices [191]).

The third category is microfluidic-based rheometer. This type of extensional rheometer utilizes precisely fabricated microfluidic channels to induce a well-defined planar extensional flow. Because of the channel flow in the absence of free surface, a steady-

state extensional flow can be achieved to obtain more accurate characterizations with additional *in situ* measurements, such as microscopic or birefringence observations to probe the structure-rheology relationship. It also creates a miniature extensional-flow environment that is increasingly applied to enhance the understanding of the material responses to the external mechanical deformation for a number of bioactive matters, such as bacteria, single cells and single DNA strands [24, 192]. The primary challenges that barricade the application of this type of extensional rheometer are in the design and fabrication of the flow channels, as well as a precise control of the flow rate or pressure at each in- and outlet to induce the desired flow field. In addition, a relatively large volume of fluid samples is needed to maintain the steady state, and the allowed viscosity of the tested sample is limited ($\lesssim 1\,\mathrm{Pa\,s}$) by the flow actuator capability and the mechanical strength of the flow circuit, due to the inversely proportional relation between the millimeter-scaled channel size and the channel pressure difference, $\Delta P \sim 1/R^4$ (at a fixed flow rate) according to the Hagen–Poiseuille equation [193]. Examples of this type of extensional rheometer include the E-VROC [194] microfluidic chip and the cross-slot geometry with the addition of birefringence measurements [195].

As Figure 2-10 shows, extensional flow is observed in various manufacturing processes, with typical examples of melt blowing, molding and spinning, as well as extrusion in food processing [196]. However, a profound knowledge for the extensional rheology of the raw materials in these applications, as well as rapid measuring protocols are yet to be attained [196, 197]. For polymer melts or entangled polymer solutions, rheological characterizations in extensional flow are mostly obtained from the filament stretching technique [178, 198], while applications of the capillarity-driven thinning technique are limited in dilute or semi-dilute regimes [35, 199–201]. Previous studies on the extensional rheology of polymer nanocomposites are mostly phenomenological, with a number of exploratory works focusing on simplified subsystems such as aqueous dispersions [202], yield stress fluids [203–205] and emulsions [206], while their rheological fidelity to the more complex real nanocomposites is yet to be justified in the absence of morphological information.

Capillary breakup extensional rheometry

The capillary breakup extensional rheometer (CaBER) is a typical measuring instrument of the second category as introduced above, which has been extensively used to characterize the rheological behavior of various complex fluids in an effective and accurate manner [35]. As shown in Figure 2-11, in a typical geometrical configuration, a cylindrical fluid sample (approximately $60\,\mu\mathrm{L}$) is placed between two coaxial discs

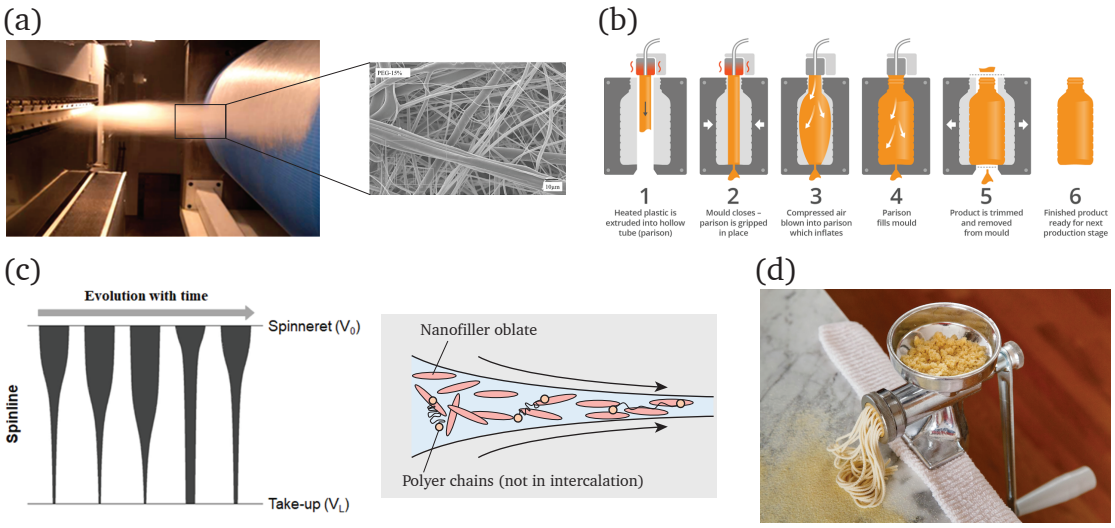

Figure 2-10: Examples of industrial applications featuring extensional deformation. (a) Melt blowing process for the production of surgical masks[5]. Zoom-in view: Non-woven structure from melt-blown polypropylene/polyethylene glycol copolymers. Reproduced from Ref. 27. (b) Extrusion blow molding process[6]. (c) Schematic of melt spinning process. Reproduced from Ref. 28. (d) Pasta extruded from semolina flour[7].

of radius R_0 with an initial separation of L_0. The two discs are separated axially by a rapid step-strain to a distance of L_f beyond the Rayleigh-Plateau limit. As the discs separate, a liquid filament forms and subsequently undergoes a self-thinning process, which is governed by the visco-elasto-capillary interactions. The temporal evolution of the minimum filament radius $R(t)$ is recorded by an optical device such as a laser micrometer or a high-speed camera. The measurements are fitted to the prediction from a suitable selection of the constitutive model for the extraction of material parameters.

In the data processing of CaBER measurements, the inertial and gravitational effects

[5]Wikipedia contributors, *Melt Blowing*. [Online]. Available: `https://en.wikipedia.org/wiki/Melt_blowing`, Accessed on: Aug. 30, 2021.

[6]Alison, *Injection Blow Molding vs Extrusion Blow Molding*. [Online]. Available: `https://e2global.com/injection-blow-molding-vs-extrusion-blow-molding`, Accessed on: Aug. 30, 2021.

[7]Lucy Vaserfirer, *More Adventures in Extruded Pasta*. [Online]. Available: `http://www.hungrycravings.com/2014/02/more-adventures-in-extruded-pasta.html`, Accessed on: Aug. 30, 2021.

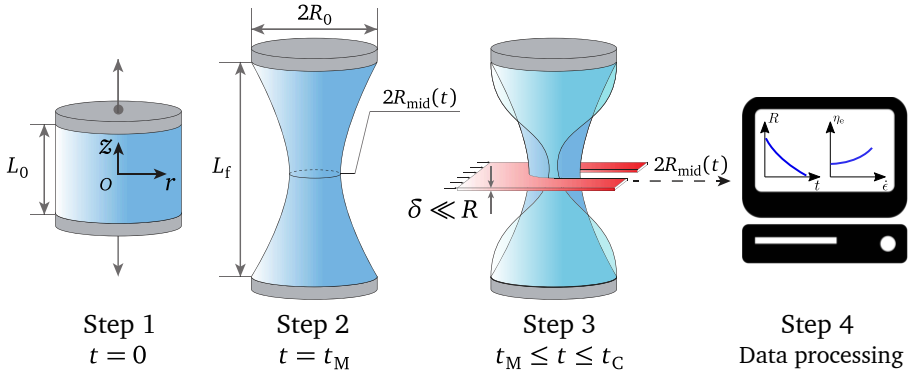

Figure 2-11: Steps of a generic CaBER measurement. Reproduced from Ref. 29.

are commonly negligible to simplify the calculation. These conditions are often justified through the dimensionless Ohnesorge number Oh and the initial Bond number Bo_0, which are expressed [35] as

$$\text{Oh} \equiv \frac{\eta}{\sqrt{\rho \Gamma R_0}} \gtrsim 0.1, \tag{2.13a}$$

$$\text{Bo}_0 \equiv \frac{\rho g R_0^2}{\Gamma} \ll 1, \tag{2.13b}$$

where η, ρ, Γ are the characteristic shear viscosity, density, and surface tension of the liquid sample, respectively. Finally, the temporal evolution of the filament radius can be solved analytically from the stress balance in the axial direction of the filament as

$$\frac{F_a(t)}{\pi R^2} - \Gamma K = \sigma_{zz} - \sigma_{rr} \equiv \eta_e^+ \dot{\epsilon}, \tag{2.14}$$

where σ_{zz} and σ_{rr} are the corresponding components of the stress tensor $\boldsymbol{\sigma}$, and η_e^+ is the transient extensional viscosity. At the minimum filament radius where the measurements are taken, the local strain rate of the slender filament can be calculated as

$$\dot{\epsilon} = -\frac{2\dot{R}(t)}{R(t)}. \tag{2.15}$$

The term $F_a(t)$ describes an axial force exerted at the end of the filament from adjacent fluid elements, which, by dimensional analysis, can be expressed as $F_a(t) = 2\pi X R \Gamma$. Here, X is a dimensionless geometric correction factor that accounts for the slenderness of the filament shapes (*i.e.*, $X = 1$ corresponds a cylindrical filament). The capillary

pressure contribution ΓK is calculated from the Young-Laplace equation [193], and the mean curvature K can be expressed as

$$K = \frac{1}{R[1+(\partial_z R)^2]^{1/2}} + \frac{\partial_{zz} R}{[1+(\partial_z R)^2]^{3/2}}, \tag{2.16}$$

where $\partial_z R \equiv \partial R/\partial z = 0$ and $\partial_{zz} R \equiv \partial^2 R/\partial z^2 \approx 0$ at the position where the filament radius reaches minimum under the assumption of a slender filament. In Equation (2.14), the first normal stress difference $N_1 \equiv \sigma_{zz} - \sigma_{rr}$ must be derived from the selected constitutive equation. For a Newtonian fluid with constant shear viscosity η, the temporal evolution of $R(t)$ can be expressed as

$$R(t) = R_0 - (2X_{\mathrm{N}} - 1)\frac{\Gamma}{6\eta}t, \tag{2.17}$$

where R_0 is the filament radius at $t = 0$, and the non-trivial geometric correction factor $X_{\mathrm{N}} = 0.7127$ for a Newtonian fluid arises from a similarity solution of the filament shape [207]. Another widely-adopted solution is derived from the Hookean dumbbell model to describe the elasto-capillary thinning of dilute viscoelastic polymer solutions, in which a single polymer chain can be modeled as two masses connected by a massless Hookean spring, and the constitutive equation is derived from an ensemble average of all the dumbbell conformations. Consequently, the temporal evolution of the filament radius can be expressed [208] as

$$R(t) = \left(\frac{GR_0^4}{2\Gamma}\right)^{1/3} \exp\left(-\frac{t}{3\lambda}\right), \tag{2.18}$$

where $G = nkT$ is the elastic modulus that can be alternatively derived from kinetic theories [209], and λ is the relaxation time incorporated in the dumbbell model.

The capillary breakup extensional rheometry has been extensively applied to a wide range of complex material systems for accurate measurements of their extensional rheological properties. A number of examples from previous studies include Newtonian fluids [210], dilute polymer solutions [29, 208, 211, 212], yield-stress fluids and emulsions [203, 205, 206], particulate suspensions [202, 213, 214], magnetorheological fluids [204], as well as more complex systems such as cellulose solutions [215], liquid food additives [216, 217] and consumes products such as nail varnishes [218]. When there are multiple stress contributions in the constitutive model, the corresponding filament thinning profile becomes increasingly complex, and numerical calculations may be necessary to obtain more detailed fluid kinematics. In Chapter 3 and 4, the filament

thinning solutions for more complex constitutive models are calculated, from which a robust constitutive model for the GDNC materials can be progressively attained.

2.3 Summary

This chapter has provided an extensive review of the material systems and rheological techniques applied in this thesis. Section 2.1 presented the structures, properties, production and applications of graphene-derived nanofillers and the GDNC materials, showing their promising potentials in property enhancement for a variety of polymer matrices. However, major challenges that inhibit or delay mass applications of the GDNC systems arise from a lack of understanding in their complex rheology in both shear and extensional flows for the optimization of material processing, in particular, the state of dispersion. The emergent rheological complexity is primarily attributed to the presence of nanofillers and the interactions of different phases over multiple length- and timescales. Previous studies on the rheology of similar nanocomposite systems have captured generic features in both linear and non-linear regimes, including a low-frequency plateau storage modulus, a yield stress and the shear-thinning behavior. These findings have been further combined with microscopic or scattering studies to reveal rich structure-rheology information manifested at different lengthscales, which can be practically used to characterize the state of dispersion for nanofillers in the solution or melt mixing processes through rheological characterizations. In Section 2.2, the rheological techniques used in this thesis were briefly introduced. Notably, fractional constitutive models comprised of "springpots" were demonstrated to produce a broad relaxation time spectrum using a minimal set of parameters, which are suitable to describe complex viscoelastic responses of the GDNC systems that arise from their sophisticated microstructures. In contrary, rheological characterizations of the GDNC systems in extensional flow, despite being in the infancy, are pivotal in understanding the morphological variation under large deformation in a real manufacturing process. Different state-of-the-art techniques to measure the extensional rheology were introduced with a special focus on the capillary breakup extensional rheometry, which can potentially provide a rapid measuring protocol to probe the complex dynamics for generic nanocomposite systems. Nevertheless, in order to obtain accurate constitutive parameters from the measured filament thinning profiles, an accurate calculation of the filament thinning prediction based on an appropriately selected constitutive model is prerequisite.

This page is intentionally left blank.

3 | Extensional Rheology of Weakly Elastic Complex Fluids

3.1 Construction of an improved Capillary Breakup Extensional Rheometer

In this section, the construction of a customized Capillary Breakup Extensional Rheometer is briefly introduced based on the author's master work [64]. This new instrument, with improved performance in the motor actuation and filament measurements as well as enhanced capability of environmental control, is aimed at rapid and accurate characterizations of the extensional rheology for an expanded variety of industrial fluids under various working conditions. Figure 3-1 shows the design and assembly of the customized CaBER instrument. The system is comprised of (i) two linear motors (Model No. LCA8-010, SMAC-MCA Inc., USA) that are aligned vertically in opposite directions; (ii) a charged-coupled device (CCD) laser micrometer (IG-028, Keyence Corp., Japan) with a minimum detectable object size of 100 μm, a resolution of 5 μm, and a maximum sampling frequency of 2000 Hz; (iii) a high-speed imaging system (Camera: Phantom M320s, Vision Research Inc., USA; Lens: Nikon Corp., Japan) with an averaged frame rate of 4000 fps and an observation window sized 500 px × 700 px with a resolution of 17 μm/px (the resolution can be further improved with a higher-magnification lens); (iv) a uniform backlighting system (IR Backlight, Phlox Inc., France) sized 40 mm × 40 mm and an approximate luminous flux of 530 lm; (v) a number of home-manufactured interchangeable threaded aluminum discs with different diameters (2 mm, 4 mm and 6 mm) attached to the heads of linear motors for sample holding; (vi) two resistance heating jackets incorporating resistance temperature detectors (RTD) attached to the aluminum discs driven by pulse width modulation (PWM), which enables a maximum attainable temperature of 250 °C with an accuracy of ±1 °C; (vii) a I/O device (USB-6002, National Instruments, USA) con-

trolled in a LabVIEW-based graphical user interface (National Instruments, USA); (viii) a customized aluminum-based frame to assemble the instrument. Appendix A shows the necessary calibrations for the motors and the laser micrometer in detail.

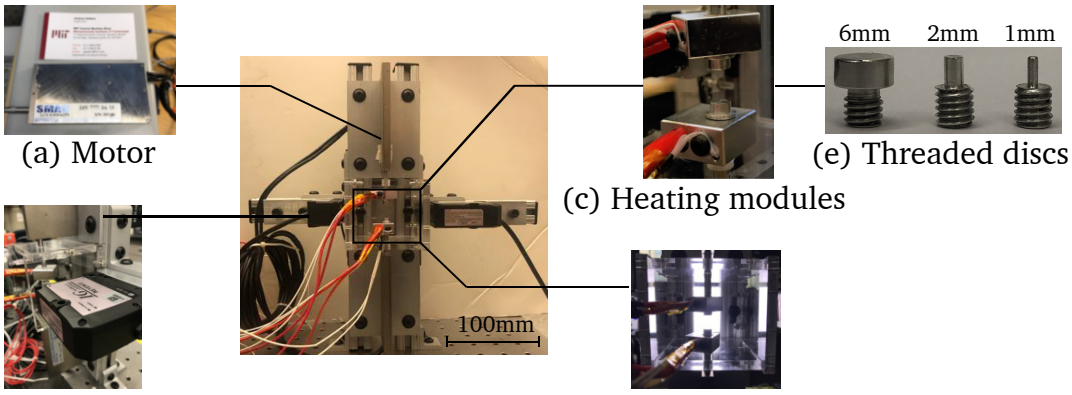

(a) Motor (b) Laser micrometer (c) Heating modules (d) Chamber and backlight (e) Threaded discs

Figure 3-1: Assembly of the customized CaBER instrument with detailed views of the components: (a) Namecard-sized linear-motion motors. (b) Laser micrometer aligned close to the center of the two linear-motion motors. (c) Two heating jackets attached to the head of the linear-motion motors. (d) Acrylic chamber enclosing both heads of the linear-motion motors with the backlight turned on. (e) Home-manufactured interchangeable discs with a range of diameters (2 mm, 4 mm and 6 mm).

3.2 Dilute polymer solutions with viscous solvents

3.2.1 Synthetic automotive lubricants

In this section, the complex extensional rheology of two commercially-available synthetic automotive lubricants are characterized through the aforementioned CaBER instrument. As will be shown in later sections, these results eventually inspire the design and application of a more accurate measuring protocol for the polymer nanocomposite systems that feature increased rheological complexity with multiple stress contributions in the constitutive models.

From a rheological perspective, the everyday automotive lubricants are representative of a family of synthetic nanofilled lubricants that find extensive applications in automotive industry [219]. This type of materials is generally comprised of alkane refined from crude oil and undergoes further modifications by low-concentrated ad-

ditives to introduce enhanced thermal, chemical and tribological performance [220]. For synthetic automotive lubricants, a broad range of additives has been developed over the past few decades, including polymers as viscosity index improvers [221], zinc dithiophosphate (ZDDP) [222–224] and other metal compounds [225], micro- or nanoparticles [226–228], antioxidants [225, 229, 230] and surfactants [231]. The search for more effective additives has been an ongoing topic in both industry and academia [225].

Synthetic automotive lubricants are commonly categorized as multi-grade oils based on the fluid kinematic viscosities at cold and hot temperatures [219]. The additives as viscosity index improvers effectively reduce the viscosity difference at the extremes of temperatures to introduce enhanced durability and functionality. Concomitantly, they add up to the rheological complexity that arises from the dispersed additive phases and the resulting hydrodynamic interactions, which has been extensively studied in similar material systems such as particle suspensions [232, 233], emulsions [234] and polymer solutions [196]. In addition, the fluid properties become increasingly susceptible to the extreme working conditions (*e.g.*, pressure, humidity, temperature, electric or magnetic field) as well as the geometrical complications (*e.g.*, converging pipes and ducts, jet impingement and atomization), in which the shear and extensional deformation coexist [235]. In such a complex flow field, substantial morphological changes to the fluid may lead to material anisotropy, particle jamming and strain-hardening of the polymer chains [35, 136]. Such rheological complexities ultimately drive significant modifications to the lubricant performance [236]. Consequently, it is essential to obtain a comprehensive knowledge of the fluid rheological properties with a rapid characterizing protocol to optimize the lubricant performance and the service lifetime.

For this purpose, two commercially-available synthetic motor oils are selected for the rheological characterizations: Castrol High-Mileage Synthetic Blends (denoted as CSB; Castrol, UK) and Mobil 1 (denoted as M1; ExxonMobil, USA). An SAE grade of 10W-30 [219] is identified for both oils, indicating similar shear viscosity measurements under the same working conditions. This agreement is verified by independent shear measurements on a commercial rotary rheometer (DHR-3, TA Instruments, USA) at 25 °C as shown in Figure 3-2. Table 3.1 lists the necessary shear rheological characterizations as well as the surface tension measurements (DCAT, dataphysics, Germany) of the two motor oils. The Ohnesorge number, $\mathrm{Oh} \equiv \eta/\sqrt{\rho\Gamma R_0}$ and the initial Bond number $\mathrm{Bo}_0 \equiv \rho g R_0^2/\Gamma$ (Equation (2.13)) are calculated for both motor oils and are identified to a range of $\mathrm{Oh} \gtrsim 0.5$ and $\mathrm{Bo}_0 > 1$, which justifies negligible inertial and gravitational effects in the capillarity-driven thinning dynamics.

To investigate the extensional rheology of the two motor oils using the customized

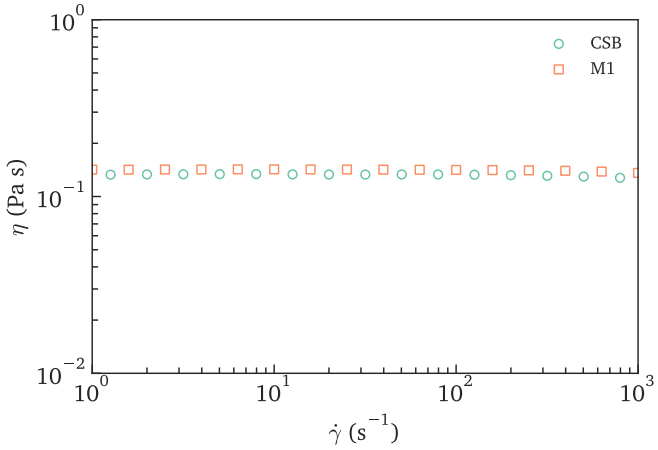

Figure 3-2: Measurements of steady shear viscosity for the two motor oils at 25 °C.

Table 3.1: Shear viscosity, surface tension measurements, and characteristic dimensionless numbers of the two selected motor oils.

Material	Viscosity index	η (Pa s)	Γ (mN/m)	Oh	Bo_0
CSB	138.1	0.132 ± 0.002	23.10 ± 0.02	0.54	3.29
M1	146.0	0.142 ± 0.001	24.80 ± 0.01	0.56	3.07

CaBER instrument, a general configuration of the experimental parameters is applied and listed in Table 3.2. This configuration of parameters will be used for all the CaBER measurements throughout this thesis, unless otherwise specified.

Figure 3-3(a) and (b) show the snapshots of the capillarity-driven thinning profiles for the CSB and M1 motor oil under the experimental parameters as stated in Table 3.2, respectively. In Figure 3-3(c) and (d), the liquid bridge profiles at different times during the filament thinning process before the singularity occurs are extracted from the snapshots, in which the r- and z-axis are nondimensionalized using the disc radius R_0 and the final gap of two discs L_f, respectively. The shaded regions where $|z/L_\mathrm{f}| \gtrsim 0.3$ correspond to the liquid reservoirs formed within a distance of the capillary length $l_\mathrm{cap} \equiv \sqrt{\Gamma/\rho g} \approx 1.52\,\mathrm{mm}$ ($l_\mathrm{cap}/L_\mathrm{f} \approx 0.20$). In these regions, the liquid profiles are primarily governed by the interaction between the gravitational and capillary effects, hence are not accounted for in the data processing.

As shown in Figure 3-3, the liquid profiles at $t \lesssim 90\,\mathrm{ms}$ for both motor oils exhibit

Table 3.2: Experimental parameters of the customized CaBER instrument for the characterizations of the two motor oils.

Parameters	Values
Disc diameter, $2R_0$	6 mm
Temperature	25.0 °C ± 0.5 °C
Actuation time, t_M	30 ms
Initial and final gaps, L_0 and L_f	2.0 mm and 7.7 mm
Hencky strain, ϵ	1.35
Frame rate of high-speed camera	6700 fps
Image resolution	17 μm/px

similar curved shapes that are skewed slightly downwards due to gravity. Such filament shapes qualitatively resemble the classic self-similar solution for a Newtonian fluid [207]. As $t \gtrsim 90$ ms, the liquid profiles for both motor oils diverge in their shapes, while the liquid filament of the CSB oil becomes increasingly cylindrical with a more retarded breakup time compared with the M1 counterpart.

To quantify the kinematics in the capillarity-driven thinning process for both motor oils, the minimum filament radius $R(t)$ is extracted from the snapshots of Figure 3-3. The results for both motor oils can be plotted in Figure 3-4, which displays a consistent trend as in the snapshots from Figure 3-3. When $t \lesssim 90$ ms, the minimum filament radius decays linearly with time. In this regime, the filament thinning dynamics are akin to the behavior predicted by a Newtonian fluid under a visco-capillary balance described by Equation (2.17). This prediction line can be determined based on the material properties from Table 3.1, and is plotted as the dotted curve in Figure 3-4. The experimental data for both motor oils show excellent agreement with this prediction for $t \lesssim 90$ ms. In contrary, when $t \gtrsim 90$ ms, the capillarity-driven thinning dynamics for both motor oils progressively deviate from the Newtonian prediction. This discrepancy becomes significant when the filament radius becomes sufficiently small (and the strain rate becomes large according to Equation (2.15)), and can be better visualized by switching the ordinate to a logarithmic scale as in Figure 3-4(b) and (c). Consequently, a retardation in the filament breakup is captured for both motor oils, in which the breakup time can be determined as $t_C \approx 123$ ms for the CSB oil and $t_C \approx 108$ ms for the M1 oil.

Because of an identical shear viscosity implied by the viscosity index for the two motor oils, their difference in the capillarity-driven thinning dynamics at $t \gtrsim 90$ ms is rea-

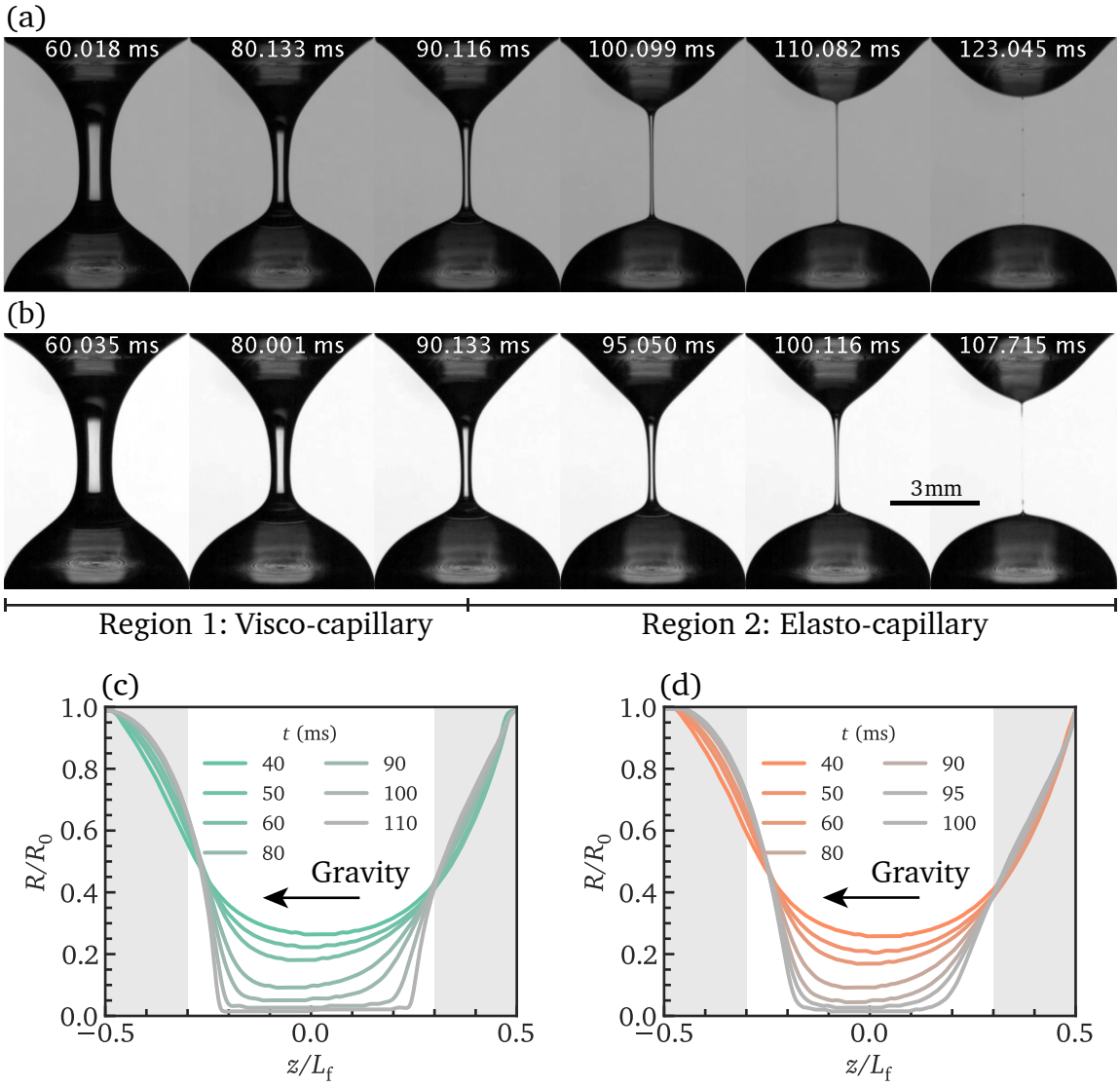

Figure 3-3: (a-b) Snapshots of the liquid filament captured by the high-speed imaging system during the capillarity-driven thinning process for the two motor oils: (a) CSB; (b) M1. (c-d) Extracted filament profiles at varying times for the two motor oils: (c) CSB; (b) M1.

soned to arise from the additives that introduce rheological complexity at high strain rates. Noticeably, the two motor oils behave differently in this region by virtue of the distinct chemical and mechanical features introduced by the additives. As a result, dif-

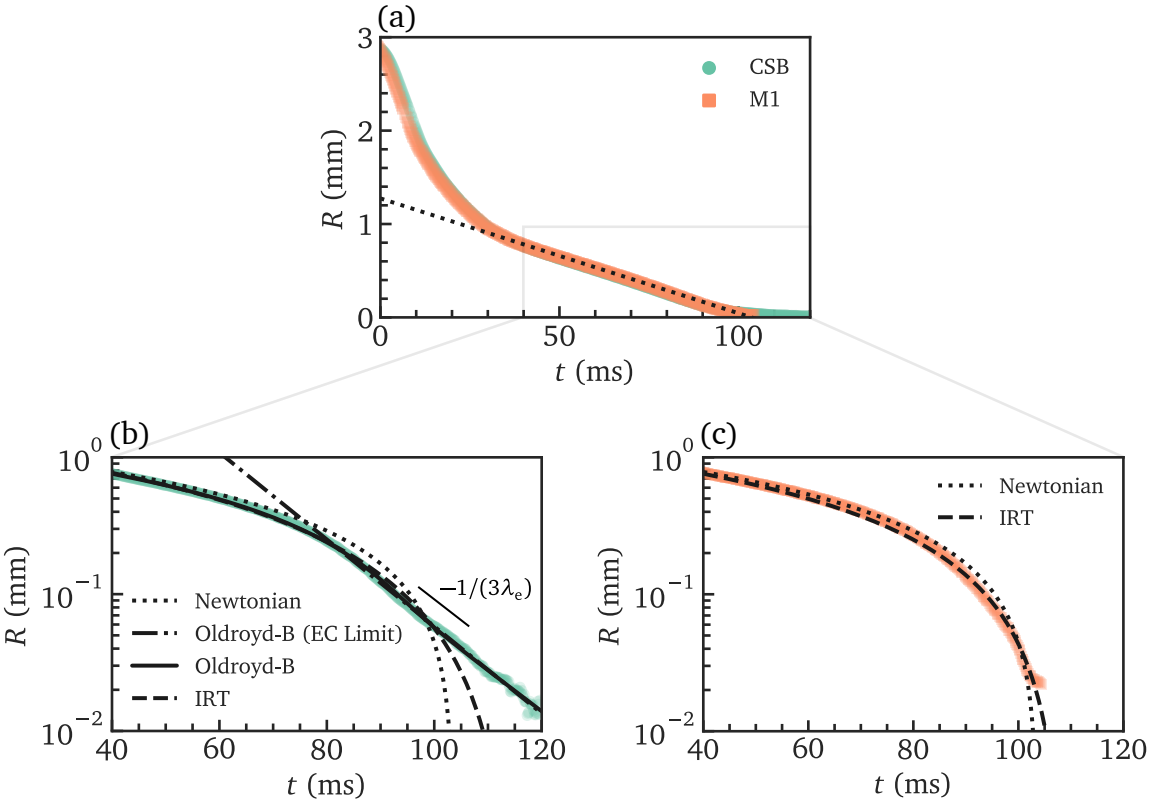

Figure 3-4: Temporal evolution of the minimum filament radius $R(t)$ for both motor oils, overlapped with the fitting lines from the selected constitutive models. (a) The ordinate plotted on a linear scale. (b-c) The ordinate plotted on a logarithmic scale for (b) CSB; (c) M1.

ferent constitutive models must be applied to account for their rheological responses accurately. Revisiting the trend of the filament thinning curves at $t \gtrsim 90\,\text{ms}$ reveals an exponential decay with time for the CSB oil. This exponential trend is reminiscent of the filament thinning dynamics under an elasto-capillary balance as described by Equation (2.18). By fitting experimental data in this segment (dotted dashed line in Figure 3-4(b)), an extensional relaxation time can be extracted as $\lambda_e = 4.56\,\text{ms}$, and the strain rate of the slender filament remains constant at $\dot{\epsilon} = 2/(3\lambda_e) = 146.2\,\text{s}^{-1}$, or in the form of a dimensionless notation using the Weissenberg number as

$$\text{Wi} \equiv \lambda_e \dot{\epsilon} = 2/3. \tag{3.1}$$

As a result, the CSB oil exhibits two distinct trends in the filament thinning dynamics

as the strain rate grows, signaling a transition in the dominant stress balance of the filament thinning dynamics from a visco-capillary balance at low strain rates ($t \lesssim 90\,\text{ms}$) to an elasto-capillary balance at high stain rates ($t \gtrsim 90\,\text{ms}$) that is likely to arise from the stretching of the additive polymer chains [237]. The M1 oil experiences a more progressive deviation from the linear decay but an exponential-decaying trend is never attained. Compared with the filament thinning under an elasto-capillary balance induced by the stretching of polymer chains, the hydrodynamic interactions between the dispersed additives and the continuous base oils play more critical roles in altering the rheological response of the M1 oil. Therefore, the prediction from an elasto-capillary balance (Equation (2.18)) results in an overestimated retardation in the filament thinning, and is thus not suited for the data fitting to extract accurate constitutive parameters.

To describe the rheological responses of the two motor oils in extensional flow more accurately, two constitutive models are proposed to provide more comprehensive predictions of the filament thinning kinematics that reconcile the asymptotic solutions under a visco-capillary balance (Equation (2.17)) at low strain rates ($t \lesssim 90\,\text{ms}$) and the non-Newtonian behavior at high strain rates ($t \gtrsim 90\,\text{ms}$). The applied constitutive models are featured with multiple stress contributions, which result in strain- or rate-dependent rheological properties. The results justify the necessity of an optimal model selection with a well-regularized set of constitutive parameters to retain the fitting fidelity with the experimental data.

Oldroyd-B model

The Oldroyd-B model is a well-studied constitutive model to describe the rheological response of viscoelastic liquids such as Boger fluids and dilute solutions of flexible polymer chains [136, 201, 211, 212]. The constitutive relation is expressed as the addition of two stress contributions - a Newtonian stress and a viscoelastic stress to describe the contributions from the solvent and the polymer chains, respectively. Mathematically, the constitutive equation can be expressed [136] as

$$\boldsymbol{\sigma} = \eta_{\text{S}} \overset{\triangledown}{\boldsymbol{\gamma}} + \boldsymbol{\sigma}_{\text{P}}, \tag{3.2a}$$

$$\overset{\triangledown}{\boldsymbol{\sigma}}_{\text{P}} + \frac{1}{\lambda}\boldsymbol{\sigma}_{\text{P}} = G\overset{\triangledown}{\boldsymbol{\gamma}}, \tag{3.2b}$$

where η_{S} is the solvent viscosity, and $\boldsymbol{\sigma}_{\text{P}}$ is the viscoelastic stress governed by the Upper Convective Maxwell (UCM) model [136]. The constitutive parameters G and λ correspond to the elastic modulus and the relaxation time in the UCM model. The notation

of "$\triangledown$" refers to the upper-convected derivative defined as $\overset{\triangledown}{\boldsymbol{A}} \equiv \mathrm{D}\boldsymbol{A}/\mathrm{D}t - (\boldsymbol{\nabla v})^{\mathrm{T}} \cdot \boldsymbol{A} - \boldsymbol{A} \cdot (\boldsymbol{\nabla v})$ for any tensor $\boldsymbol{A}$ to describe a frame-invariant material derivative [136]. Using this notation, the strain rate tensor defined in Equation (2.11) can be equivalently expressed as $\overset{\triangledown}{\boldsymbol{\gamma}} = \dot{\boldsymbol{\gamma}}$. From kinetic theories, the Oldroyd-B model describes an asymptotic solution in the limit of infinite extensibilities in the polymer chains of the Finite Extensible Non-linear Elastic (FENE) model [209], which has been widely utilized to model a variety of dilute polymer solutions [35].

The filament thinning dynamics predicted by the Oldroyd-B model can be solved numerically by substituting Equation (3.2) into Equation (2.14) with the first normal stress difference $\sigma_{zz} - \sigma_{rr}$. The resulting filament radius shows two asymptotes at low and high strain rates. In the initial stage of the filament thinning, where $\mathrm{Wi} \equiv \lambda\dot{\epsilon} \ll 2/3$, the stress contribution from the Newtonian solvent dominates the filament thinning dynamics, and the temporal evolution of the filament radius resembles Equation (2.17). As Wi approaches 2/3, the magnitude of the viscoelastic contribution increases rapidly and overtakes the Newtonian counterpart. As a result, the solution for the filament radius is reduced to Equation (2.18) under an elasto-capillary balance. The numerical solution is subsequently fitted to the experimental data of the CSB oil, as shown in Figure 3-4(b) in the solid line, which are in good agreement with the evolution of $R(t)$ over a broad range of filament lifetime ($40\,\mathrm{ms} \leq t \leq t_{\mathrm{C}} \approx 120\,\mathrm{ms}$).

Inelastic rate-thickening (IRT) model

It is evident that the filament thinning prediction from the Oldroyd-B model with an asymptote of exponential decay provides a poor description for the experimental data of the M1 oil, and a new constitutive model is worth further exploration. From the kinetic theory, the stretching of a polymer chain simplified by a spring-dumbbell model generates a large stress along the spring axis, contributing to a strong elasticity to the bulk solution. However, under the circumstances of low additive concentrations or increased additive rigidity with small extensibilities, the resulting elasticity arising from the entropy-driven chain retraction is less evident. Instead, the hydrodynamics interactions between the additives and the continuous phase appear to contribute to the filament thinning dynamics in an inelastic manner.

The difference of additive phase between the two selected motor oils can be better demonstrated by their molecular weight distributions measured from gel permeation chromatography (GPC). Here, tetrahydrofuran (THF) is chosen as the eluent at 30 °C, and monodisperse polystyrenes dissolved in THF are used for the calibration. In Figure 3-5, the relative number concentration RC is plotted against the molecular weight

Table 3.3: Number and weight average molecular weights for each mode obtained from log-normal fitting for the two motor oils.

Sample	Peak number	M_n (Da)	M_w (Da)	PDI
CSB	1	163	212	1.30
	2	27 173	63 305	2.33
M1	1	164	207	1.26
	2	321	335	1.04
	3	723	1578	2.18
	4	38 617	59 292	1.54

M (Da). From this figure, the lowest molecular weights ($M < 1 \times 10^3$ Da) correspond to the base oil with the number of carbon ranging from 15 to 40 [238]. In addition, both motor oils show broadly similar molecular distributions at high molecular weights ($M > 1 \times 10^4$ Da), which is consistent with the characteristics of the macromolecular additives. Notably, the M1 oil features additional modes in an intermediate range of molecular weights (1×10^3 Da $\leq M \leq 1 \times 10^4$ Da). The characteristic molecular weight of each component in the solutions can be identified by fitting the relative number concentration with a sum of log-normal distributions, or Wesslau distributions [239] that describes the natural distributions of single-mode molecular weights. The number and weight average molecular weights, M_n and M_w, can be calculated accordingly for each mode as

$$M_n = \frac{\sum \mathrm{RC}_i}{\sum \mathrm{RC}_i / M_i}, \tag{3.3a}$$

$$M_w = \frac{\sum \mathrm{RC}_i M_i}{\sum \mathrm{RC}_i}, \tag{3.3b}$$

where M_i and RC_i are the molecular weight and the normalized relative number concentration of the i-th discrete component. The results of each molecular-weight mode for the two motor oils are summarized in Table 3.3.

From Table 3.3, the M1 oil is featured with two additional modes at $M_n = 321$ Da and $M_n = 723$ Da. As the strain rate increases, these intermediate-molecular weight components appear to be more susceptible to the flow deformation and reaches the finite extensibility more rapidly than the high-molecular-weight counterparts. Beyond this point, the contribution from the additives to the rheological response of the bulk solu-

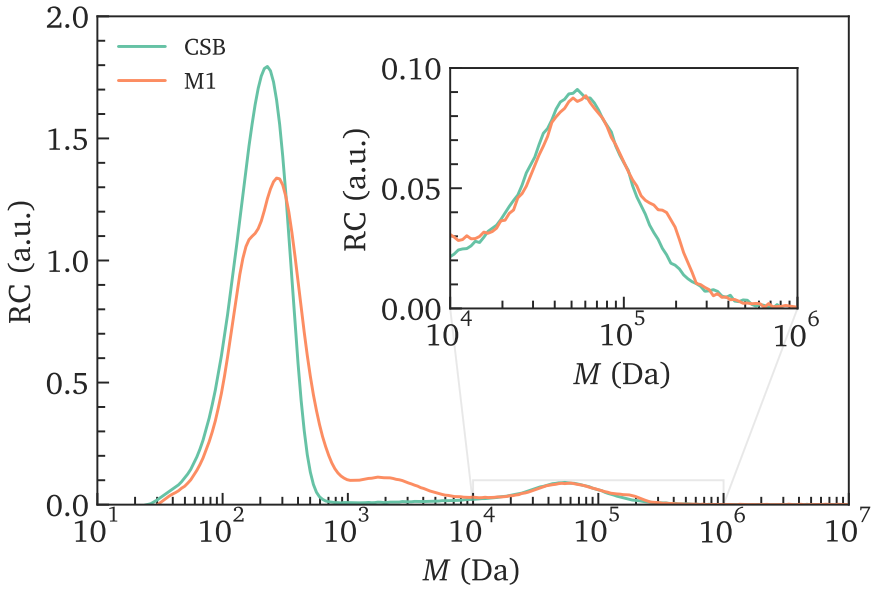

Figure 3-5: Measurements of the molecular weight distribution for the two motor oils from gel permeation chromatography. Inset: The molecular weight distribution in the high-molecular-weight region ($M > 1 \times 10^4$ Da).

tions primarily arises from the hydrodynamic interactions with the continuous phase, and the rheological properties are altered in an inelastic manner that relies increasingly on the strain-rate variation. Notably, the stress contributions from the solvent and the additive phases remain comparable in magnitude over a large strain-rate range. Therefore, an inelastic model is necessary to describe the rheological responses that arise from the hydrodynamic interactions. In the absence of a molecular-level description, the number of constitutive parameters in an inelastic model is likely to decrease compared with the Oldroyd-B model, leading to a more parsimonious and general constitutive framework for this type of the materials.

Here, a simple Inelastic Rate-Thickening (IRT) model is proposed to describe the rheological responses in both shear and extensional flows. Inspired by the previous study of Debbaut and Crochet [240], the constitutive equation of the IRT model is written in the form of a Generalized Newtonian Fluid (GNF) [136, 241] as

$$\boldsymbol{\sigma} = \eta(\mathrm{II}_{\dot{\gamma}}, \mathrm{III}_{\dot{\gamma}})\dot{\boldsymbol{\gamma}}, \tag{3.4}$$

where the rate-dependent viscosity $\eta(\mathrm{II}_{\dot{\gamma}}, \mathrm{III}_{\dot{\gamma}})$ is expressed as a function of the second and third invariants of the strain rate tensor $\dot{\boldsymbol{\gamma}}$ (the first invariant vanishes for incompressible fluids) [136] as

$$\mathrm{II}_{\dot{\gamma}} = \mathrm{tr}(\dot{\boldsymbol{\gamma}} \cdot \dot{\boldsymbol{\gamma}}), \tag{3.5a}$$

$$\mathrm{III}_{\dot{\gamma}} = \mathrm{tr}(\dot{\boldsymbol{\gamma}} \cdot \dot{\boldsymbol{\gamma}} \cdot \dot{\boldsymbol{\gamma}}). \tag{3.5b}$$

The magnitudes of the strain rates in a simple shear flow and a uniaxial extensional flow can be expressed in combination of the two invariants with mathematical equivalence to Equation (2.15) as

$$\dot{\gamma}(\mathrm{II}_{\dot{\gamma}}, \mathrm{III}_{\dot{\gamma}}) = \sqrt{\frac{1}{2}\mathrm{II}_{\dot{\gamma}}}, \tag{3.6a}$$

$$\dot{\epsilon}(\mathrm{II}_{\dot{\gamma}}, \mathrm{III}_{\dot{\gamma}}) = \frac{\mathrm{III}_{\dot{\gamma}}}{\mathrm{II}_{\dot{\gamma}}}. \tag{3.6b}$$

Notably, rate-dependent flow behavior is observed exclusively in an extensional flow for the M1 oil. As a result, the simplest possible form for the viscosity $\eta(\mathrm{II}_{\dot{\gamma}}, \mathrm{III}_{\dot{\gamma}})$ is taken as

$$\eta(\mathrm{II}_{\dot{\gamma}}, \mathrm{III}_{\dot{\gamma}}) = \eta_0 + k_2\dot{\epsilon}, \tag{3.7}$$

where η_0 is the zero-shear viscosity, and k_2 is defined as the rate of extensional thickening. Equation (3.7) describes a linear extension-thickening relation, and the stress contributions from the solvent and the dispersed phase remain comparable in magnitude when the extensional rate $\dot{\epsilon} \sim \eta_0/k_2$. Accordingly, a new an alternative Weissenberg number can be defined using a new characteristic timescale as $\mathrm{Wi} \equiv k_2\dot{\epsilon}/\eta_0 \sim 1$. The expression of Equation (3.7) can be derived from the steady extensional viscosity of an Oldroyd-B fluid in the limit of $\mathrm{Wi} \ll 1$ [136], when the accumulated strain on an entropic spring connecting the dumbbell remains low in magnitude as

$$\eta_\mathrm{e} = 3\eta_\mathrm{S} + \frac{2G\lambda}{1-2\lambda\dot{\epsilon}} + \frac{G\lambda}{1+\lambda\dot{\epsilon}} \xrightarrow{\mathrm{Wi}\ll 1} 3(\eta_\mathrm{S} + G\lambda) + 3G\lambda^2\dot{\epsilon}. \tag{3.8}$$

In this limit, the number of constitutive parameters is reduced from 3 (η_S, G and λ) to 2 (η_0 and k_2).

Finally, the capillarity-driven thinning dynamics described by the IRT model can be calculated numerically by substituting Equation (3.7) into Equation (2.14). This numerical result is fitted into the experimental data of both motor oils, as shown in Figure 3-4(b) and (c) in the dashed lines. For the M1 oil, the experimental data at

Table 3.4: Constitutive parameters from the Newtonian fluid model, the Oldroyd-B model and the IRT model obtained from data fitting for the two motor oils.

Sample	Model	Parameters	Values
CSB	Newtonian	η_0 (Pa s)	0.138
	Oldroyd-B	η_S (Pa s)	0.236
		G (Pa)	9.49
		λ (ms)	4.94
M1	Newtonian	η_0 (Pa s)	0.141
	IRT	η_0 (Pa s)	0.290
		k_2 (mPa s^2)	0.647

$t > 40$ ms agree well with the fitting curves till filament breakup ($t_C \approx 105$ ms). In contrary, substantial deviations are observed for the CSB oil close to the filament breakup ($t > 90$ ms), which justify a stronger elasticity in the fluid that is poorly described by the inelastic model. The obtained constitutive parameters of both motor oils using the Newtonian fluid model, as well as the two comprehensive constitutive models are shown in Table 3.4.

Compared with the filament thinning dynamics predicted by the Oldroyd-B model, in which a strong elasto-capillary balance dominates the filament breakup at sufficiently high strain rates (Wi $= 2/3$), the IRT model predicts a more progressive rate-thickening trend with a milder retardation in the approach to filament breakup. As a result, the strain rate (or the Weissenberg number) described by the IRT model is not bounded by an upper limit throughout the filament thinning process, whereas in the Oldroyd-B model, the Weissenberg number is constrained by Wi $\leq 2/3$ because of the exponentially increasing elastic stress that balances the capillarity-driven thinning of the filament radius. To better visualize the extensional rheological response at different strain rates for the two motor oils, an apparent extensional viscosity is calculated from the transient filament radius $R(t)$ according to

$$\eta_{e,app}(t) \equiv \frac{\Gamma/R(t)}{\dot{\epsilon}(t)} = \frac{\Gamma}{-2\dot{R}(t)}, \tag{3.9}$$

where $\dot{\epsilon}(t)$ is the transient strain rate calculated at the minimum filament radius (necking position) defined in Equation (2.15), and Γ is the surface tension with the values tabulated in Table 3.1. The expression of Equation (3.9) is different from the true

extensional viscosity η_e by a factor of $(2X-1)$ according to

$$\eta_e(t) = [2X(t)-1]\eta_{e,app}(t), \tag{3.10}$$

where $X(t)$ is the geometric correction factor that accounts for the capillary pressure in a non-cylindrical filament. When the filament thinning is dominated by the balance between the capillary pressure and a single stress contribution, the geometric correction factor is broadly constant, as has been shown in Section 2.2 for a Newtonian fluid ($X = X_N = 0.7127$) and the Hookean dumbbell model ($X = 1$). For more complex constitutive models, such as the Oldroyd-B and the IRT models, the value of $X(t)$ evolves temporally with a transition in the stress contribution that balances the driving capillary pressure. To calculate the apparent extensional viscosity according to Equation (3.9), the first-order derivative of $R(t)$ is obtained using a Savitzky-Golay (S-G) filter with a polynomial order n and a filtering length $2L+1$ [242]. Here, an optimal parameter set of the S-G filter is taken from a previous study [243] as $n = 2$ and $L = 14$ to guarantee the smoothness of the filtered curve, while keeping the fidelity of the filter with the original experimental data. The results are shown in Figure 3-6, where both $\eta_{e,app}$ and η measured in steady shear flow are compared, as well as the predictions lines from fitting in the Newtonian fluid model (dotted line), the Oldroyd-B model (solid line) and the IRT model (dashed line). It is evident that the apparent extensional viscosities of both motor oils remain broadly constant at low strain rates, and progressively increase in magnitude as the strain rate goes beyond approximately $100\,s^{-1}$. This critical strain rate is found to be consistent with the transient strain rate at $t \approx 90\,ms$, which is the transition time when the filament thinning profiles for both motor oils deviate from the linear-decaying trend under a visco-capillary balance. The CSB oil exhibits a stronger viscoelastic response beyond this point, and the value of $\eta_{e,app}$ grows unbounded as the strain rate approaches $135\,s^{-1}$ ($Wi \to 2/3$). For the M1 oil, the increase of $\eta_{e,app}$ is more progressive over an unbounded range of the strain rate. Compared with the Oldroyd-B model, fitting with the IRT model leads to a better agreement with the experimental data of this more weakly rate-thickening oil.

Selection of the best-fit model (BFM)

The two selected motor oils, despite their identical viscosity index that leads to similar shear viscosity measurements, exhibit substantially distinct rheological responses in extensional flow due to the variations in their molecular structures or conformation of the additive polymer chains in a strong flow. As a result, different constitutive models are applied for the extraction of a parsimonious set of constitutive parameters with faithful reflection of the kinematics and the physics behind the rheological complex-

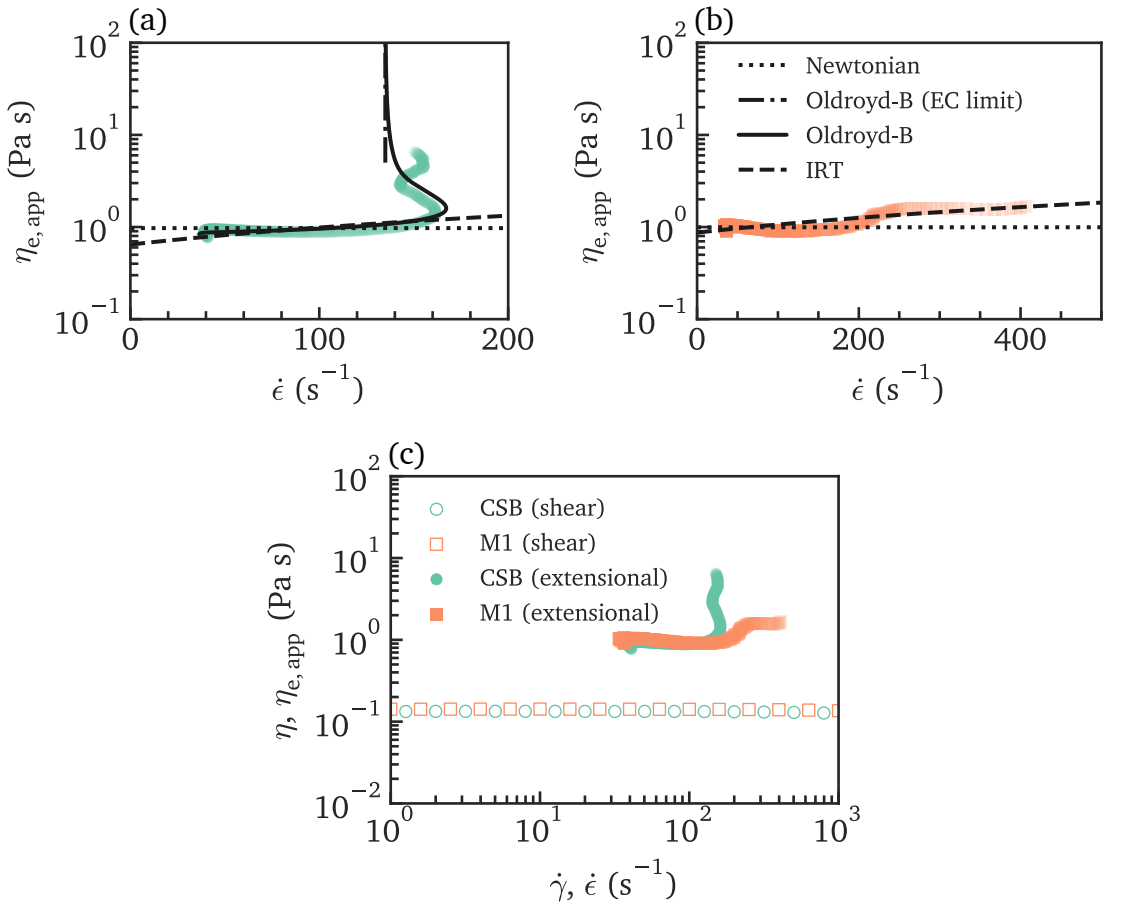

Figure 3-6: Apparent extensional viscosity $\eta_{e,app}$ plotted against strain rate $\dot{\epsilon}$ for the two motor oils with the prediction lines from the Newtonian fluid model (dotted lines), the Oldroyd-B model in the elasto-capillary limit (dashed dotted lines), the Oldroyd-B model (solid lines) and the IRT model (dashed lines): (a) CSB; (b) M1. (c) Shear viscosity η and apparent extensional viscosity $\eta_{e,app}$ plotted against shear and extensional rates, $\dot{\gamma}$ and $\dot{\epsilon}$ for the two motor oils, respectively.

ity. In practice, the selection of the best-fit model (BFM) is an insight-driven process based on a profound knowledge of the capillarity-driven thinning dynamics predicted by a variety of constitutive models. However, in industrial applications, a rapid testing protocol with a determinate algorithm for the selection of the BFM is more desired to assist in high-throughput characterizations of multiple material samples through autonomous data processing. Therefore, a more rigorous and unambiguous criterion

is needed to distinguish and evaluate the goodness of fitting for various constitutive models.

Here, a kinematic-based criterion is proposed specifically to select the BFM between the Oldroyd-B model and the IRT model based on the temporal evolution of the minimum filament radius $R(t)$. A robust statistics-based criterion will be proposed in Section 3.2.2 to provide a more generic guideline of automating the selection of the BFM from a library of suitable constitutive models and to subsequently obtain the constitutive parameters that retain excellent fidelity with the material physics.

By reviewing the kinematics of the minimum filament radius $R(t)$, the difference in the filament thinning kinematics derived from the weakly rate-thickening IRT model and the strongly viscoelastic Oldroyd-B model arises at sufficiently high strain rates, when the non-Newtonian stress contribution progressively increases in magnitude and dominates the subsequent filament thinning dynamics. At a transition time $t_{\text{V-E}} < t_{\text{C}}$, the temporal evolution of $R(t)$ starts to evolve from the trend of a linear decay at low strain rates (which is characterized by the zero-rate viscosity or the solvent viscosity) to a different asymptote at higher strain rates. When the extension-thickening is strong (*e.g.*, Oldroyd-B model or similar bead-spring models), an abrupt change in the filament profiles of $R(t)$ is identified close to $t = t_{\text{V-E}}$. Such change in $R(t)$ has been documented by a number of analytical and numerical studies [32, 244, 245]. Due to the continuity of $R(t)$, the two asymptotic solutions coincide at $t = t_{\text{V-E}}$, leading to

$$R_{\text{N}}(t_{\text{V-E}}) = R_{\text{EC}}(t_{\text{V-E}}), \tag{3.11}$$

where $R_{\text{N}}(t)$ and $R_{\text{EC}}(t)$ are the asymptotic solutions of the filament radius predicted by a Newtonian fluid (Equation (2.17)) and the elasto-capillary thinning (Equation (2.18)), respectively. When the material exhibits a more weakly rate-thickening response, the resulting evolution of the filament radius $R(t)$ is interposed between the two asymptotic solutions when $t > t_{\text{V-E}}$, and the filament breakup is slightly retarded compared with that of a Newtonian fluid with the identical zero-shear viscosity. The most significant feature between the strongly viscoelastic Oldroyd-B model and the weakly rate-thickening IRT model is the profile of transition at $t = t_{\text{V-E}}$, which exhibits more abrupt for the Oldroyd-B model. To quantify the transition in the filament profile, an elasto-capillary number $\text{Ec}_{\text{V-E}}$ is defined at $t = t_{\text{V-E}}$ to describe the relative magnitude of the non-Newtonian stress over the visco-capillary interaction at the transition time as

$$\text{Ec}_{\text{V-E}} \equiv \frac{\lambda\Gamma}{\eta_0 R(t_{\text{V-E}})}. \tag{3.12}$$

By definition, the elasto-capillary number $\mathrm{Ec}_{\text{V-E}}$ is an intrinsic material property that describes characterizes the ratio of the elasto-capillary and visco-capillary timescales, $t_{\text{E}} = \lambda$ and $t_{\text{V}} = \eta_0 R(t_{\text{V-E}})/\Gamma$ evaluated at the transition time $t_{\text{V-E}}$.

Despite the necessity of Equation (3.11) to describe a continuous evolution in the filament thinning dynamics, no information of the sharpness in the transition is provided. This is described by an additional constraint in the form of a critical elasto-capillary number $\mathrm{Ec}^*_{\text{V-E}}$, which can be obtained when the two asymptotic solutions are smoothly connected at $t = t_{\text{V-E}}$, or mathematically described as

$$\dot{R}_{\text{N}}(t_{\text{V-E}}) = \dot{R}_{\text{EC}}(t_{\text{V-E}}). \tag{3.13}$$

Combining Equation (3.11) and Equation (3.13), the critical value of $\mathrm{Ec}^*_{\text{V-E}}$ can be analytically expressed as

$$\mathrm{Ec}^*_{\text{V-E}} \equiv \frac{\lambda\Gamma}{\eta_0 R(t_{\text{V-E}})} = \frac{2}{2X_{\text{N}} - 1} \approx 4.7, \tag{3.14}$$

where the subscript of $R(t_{\text{V-E}})$ is hidden due to equal filament radii from both asymptotic solutions at $t = t_{\text{V-E}}$. The zero-shear viscosity η_0 is a measure obtained from fitting Equation (2.17) into the experimental data at $t < t_{\text{V-E}}$. Equation (3.14) describes a critical condition under which the two asymptotic solutions of $R(t)$ are C^1 continuous at $t = t_{\text{V-E}}$. It can be used as a dimensionless criterion to select the BFM between the Oldroyd-B model and the IRT model. When $\mathrm{Ec}_{\text{V-E}} < \mathrm{Ec}^*_{\text{V-E}}$, the filament radius profile is inflection-free, representing a weakly rate-thickening behavior that can be described by the IRT model. If $\mathrm{Ec}_{\text{V-E}}$ exceeds the critical value of $\mathrm{Ec}^*_{\text{V-E}}$, the filament radius profile exhibits a strong exponential decay beyond the transition time $t_{\text{V-E}}$, and the Oldroyd-B model is justified to be a better-fit model. In the study of the two motor oils, the elasto-capillary numbers for the CSB and M1 oils can be calculated as $\mathrm{Ec}_{\text{V-E}} = 11.4 > \mathrm{Ec}^*_{\text{V-E}}$ and $\mathrm{Ec}_{\text{V-E}} = 3.7 < \mathrm{Ec}^*_{\text{V-E}}$, respectively. As a result, an identical conclusion is reached for the selection of the best-fit models for both motor oils as shown previously in Figure 3-6.

The condition of Equation (3.14) can be retroactively substantiated from a number of previous experimental studies on different viscoelastic fluid systems [32,243,246,247]. The calculated transition elasto-capillary number ($\mathrm{Ec}_{\text{V-E}}$) for each combination and the extensional relaxation time are summarized in Table 3.5, as well as their molecular weights and polymer concentrations. In the two studies with aqueous polyethylene oxide solutions, an evident exponential thinning of the filament radius is identified when $\mathrm{Ec}_{\text{V-E}} \gg \mathrm{Ec}^*_{\text{V-E}}$. The resulting filament thinning dynamics are consistent with

those for the CSB oil under an elasto-capillary balance, as shown in Figure 3-4. For the other two material systems, as $\mathrm{Ec}_{\mathrm{V\text{-}E}}$ decreases and approaches the critical value of $\mathrm{Ec}^{*}_{\mathrm{V\text{-}E}}$, the temporal evolution of the filament departs from the visco-capillary thinning more progressively. The Oldroyd-B model with an exponential decay in the filament radius close to the filament breakup is thus less applicable to provide an accurate description of the filament thinning behavior. Particularly, in the first material system at a concentration of $c = 0.2\,\mathrm{wt\%}$ with a molecular weight of $M_{\mathrm{w}} = 306\,\mathrm{kg/mol}$, the elasto-capillary number $\mathrm{Ec}_{\mathrm{V\text{-}E}} = 3.2$ drops below the critical value. The resulting filament thinning profile in Figure 8 of Ref. 243 thus does not exhibit an evident trend of exponential decay. Consequently, the extracted extensional relaxation time λ_{e} is biased from conceivable overfitting and hence shows substantial deviation from the other three samples with higher concentrations or larger molecular weights. Notably, the inverse trend of $\mathrm{Ec}_{\mathrm{V\text{-}E}}$ with concentrations in Refs. [246] and [32] demonstrates a decoupled relation between an increased polymer concentration and an exponential decay of the filament radius expected from an elasto-capillary balance because of the viscous stress that can grow more rapidly than the elastic counterpart, thus delaying the transition to the elasto-capillary balance to a higher strain rate. Therefore, the criterion based on a dimensionless number of $\mathrm{Ec}^{*}_{\mathrm{V\text{-}E}}$, which directly compares the stress contributions from the viscous and the elastic terms, appears to be a better metric than the dimensional extensional relaxation time to evaluate the application of a viscoelastic model in fitting the experimental data and extracting accurate constitutive parameters.

Table 3.5: List of the selected material systems, extensional relaxation times, and their elasto-capillary numbers $\mathrm{Ec}_{\text{V-E}} \equiv \lambda\Gamma/[\eta_0 R(t_{\text{V-E}})]$, where $t_{\text{V-E}}$ is the experimentally-measured transition time when the temporal evolution of filament radius deviates from the linear visco-capillary thinning. The results in which $\mathrm{Ec}_{\text{V-E}} < \mathrm{Ec}^*_{\text{V-E}}$ are shaded.

Material system	M_w (kg/mol)	c (wt%)	λ_e (ms)	$\mathrm{Ec}_{\text{V-E}}$	Ref.
Polystyrene/Diethyl phthalate[a]	110	0.5	0.197 ± 0.016	19.6	243
	210	0.4	0.092 ± 0.014	9.1	
	306	0.2	≈ 0.030	3.2	
	488	0.1	0.083 ± 0.005	9.3	
Polyethylene oxide/Water[b]	7000	0.5	194 ± 49	2677	246
		0.05	6 ± 3	13 800	
Polyethylene oxide/Water[c]	4000	0.025	10.1 ± 0.4	293.1	247
		0.05	19.4 ± 0.5	563.0	
		0.075	26.5 ± 1.8	571.3	
		0.1	33.4 ± 4.2	560.0	
		0.25	105 ± 9	720.2	
		0.5	182 ± 18	305.2	
Hydroxyethyl cellulose/Water[d]	720	0.17	0.22	42.0	32
		0.25	0.23	24.1	
		0.40	0.24	13.1	
		0.50	0.29	9.4	
		0.75	0.45	4.4	

[a] From Table 2 of Ref. 243. The critical filament radius is estimated from Figure 8 as $R(t_{\text{V-E}}) \approx 30\,\mu\text{m}$.

[b] From Table 1 of Ref. 246. The critical filament radius is estimated from Figure 6 as $R(t_{\text{V-E}}) \approx 25\,\mu\text{m}$.

[c] The zero-shear viscosity is estimated from Figure 1 of Ref. 247 at $10\,\text{s}^{-1}$, and the outer radius of the nozzle as stated in section "Dripping-on-substrate rheology measurements" is applied to approximate the critical filament radius $R(t_{\text{V-E}})$.

[d] Only concentrations lower than $c_e \approx 0.5\,\text{wt\%}$ to 1 wt% are taken for the calculation to avoid rheological complexities arising from the polymer chain entanglements. The critical filament radius $R(t_{\text{V-E}}) \approx 0.15R_0 = 95.3\,\mu\text{m}$ is estimated from Figure 3(b) and (c) of Ref. 32. The surface tension measurement is not available, and a reference value of 40 mN is taken from Nahringbauer [248] for the calculation.

3.2.2 Dynamics governed by multiple stress contributions

A numerical study for the full filament profiles predicted by IRT model

The constitutive models proposed and applied in the previous section provide insights for a more comprehensive understanding of the filament thinning dynamics for a complex fluid, in which their capillarity-driven dynamics are resulted from a balance between the capillary pressure and multiple stress contributions from the constitutive equation. In the Oldroyd-B model, a sharp transition in the filament radius evolution can be identified in the proximity of the transition time $t_{\text{V-E}}$, and the asymptotic solutions of the visco-capillary and the elasto-capillary thinning can be applied separately in distinct time ranges to extract the underlying constitutive parameters. In contrary, the IRT model predicts more progressively increased rate-thickening behavior according to Equation (3.7), in which the contribution from the rate-dependent term $k_2\dot{\epsilon}$ remains comparable in magnitude with the zero-shear viscosity η_0 over a large strain-rate range. Under this circumstance, a full capillarity-driven thinning solution, rather than the asymptotic solutions dominated by a singe stress contribution, needs to be applied for the fitting process, if accurate constitutive parameters are to be obtained.

In a more complex system, such as graphene-derived nanocomposites, the bulk extensional rheology is susceptible to the strong hydrodynamic interactions between the matrix and the nanofiller phases. The elasto-capillary number $\text{Ec}_{\text{V-E}}$ defined in Equation (3.12) remain relatively small in magnitude because of the high polymer matrix viscosity ($\eta \sim 10\,\text{Pa s}$ to $1\times10^3\,\text{Pa s}$ for concentrated polymer matrix or polymer melts at the processing temperatures [249]). As a result, both continuous and dispersed phases actively contribute to the rheological complexity over a large range of strain rates, and fitting with a full-dimensional constitutive equation that incorporates multiple stress contributions is more applicable to a CaBER measurement for such complex-fluid systems.

The feature of multiple stress contributions in the IRT model and other similar constitutive models concomitantly brings increased complexity to the filament thinning dynamics, *i.e.*, a time-varying geometric correction factor $X = X(t)$. As explained in Section 3.2, the factor of X arises from a non-cylindrical filament shape. Expressed in the stress balance relation of Equation (2.14), this factor is essential to determine an accurate value of the apparent extensional viscosity $\eta_{\text{e,app}}$, as well as the filament radius evolution. Despite a handful of previous studies on the extensional rheology of complex material systems that exhibits an interplay of multiple stress contributions in the filament thinning have been studied in the past [206, 211, 244], a non-trivial evolution of the factor X has been persistently neglected in the data analysis and calculations.

Because of a close connection between the liquid filament shape and the geometric correction factor, the evolution of X can be obtained through the numerical analysis of full filament profiles. Here, numerical calculations are performed on the IRT model to elucidate the transition in the stress contributions during a filament thinning process. The momentum equation that governs the filament thinning dynamics is solved numerically in a geometrical configuration as shown in Figure 3-7, which resembles an axisymmetric filament undergoing the self-thinning process upon the separation of the coaxial discs with radius R_0 to a final distance of L in a CaBER measurement. The filament kinematics can be characterized by the filament radius $R(z,t)$ and the axial velocity $v(r,z,t)$, both of which vary in the time and space dimensions. To obtain a more general description of the filament kinematics, the following nondimensionalization schemes are used as shown in Table 3.6.

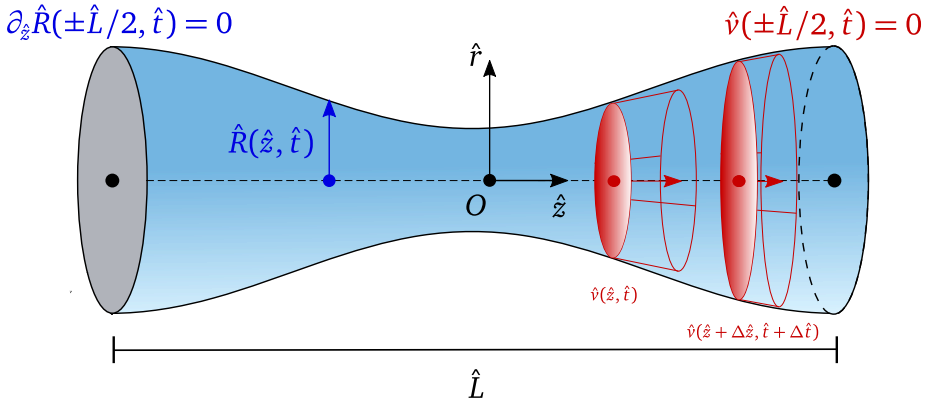

Figure 3-7: Geometrical configuration of the capillarity-driven thinning predicted by the IRT model. All quantities have been nondimensionalized.

In Table 3.6, the visco-capillary timescale t_V is defined in Equation (3.12), where $R = R_0$. The separation of the two discs L is nondimensionalized to describe the geometric aspect ratio of the filament $\hat{L}$, and the axial position between the two discs is set by $-\hat{L}/2 \leq \hat{z} \leq \hat{L}/2$. For a sufficiently slender filament, or when $\hat{L} \gg 1$, Eggers [250] has rigorously proved by perturbation analysis that the leading order of $\hat{r}$ in the expression of the axial velocity field $\hat{v}(\hat{r},\hat{z},\hat{t})$ is higher than that of $\hat{z}$. Consequently, the axial velocity can be treated as uniform in any cross section of the filament, and thus is simplified to be independent on $\hat{r}$. In the numerical analysis, appropriate initial and boundary conditions are specified following the previous study by Papageorgiou [207] for a Newtonian fluid and the instability criterion by Slobozhanin and Perales [251],

Table 3.6: Numerical calculation schemes of the capillarity-driven thinning predicted by the IRT model, including the nondimensionalization scheme and initial/boundary conditions.

Type	Definitions
Position and time	$\hat{r} \equiv \frac{r}{R_0}, \hat{z} \equiv \frac{z}{R_0}, \hat{t} \equiv \frac{t}{t_V} = \frac{t}{\eta_0 R_0/\Gamma}$
Kinematics and geometry	$\hat{R} \equiv \frac{R}{R_0}, \hat{v} \equiv \frac{v}{R_0/t_V}, \hat{L} \equiv \frac{L}{R_0}$
Operators	$\hat{\nabla} \equiv R_0\nabla, \partial_{\hat{t}} \equiv t_V\partial_t, \partial_{\hat{z}} \equiv R_0\partial_z$
Dimensionless parameters	
Intrinsic elasto-capillary number Ec_0	$\mathrm{Ec}_0 \equiv \frac{k_2/\eta_0}{t_V} = \frac{k_2\Gamma}{\eta_0^2 R_0}$
Weissenberg number Wi	$\mathrm{Wi} \equiv t_V\dot{\epsilon}$
Initial conditions	
	$\hat{R}(\hat{z},0) = 0.5 - 0.1\cos\left(\frac{2\pi\hat{z}}{\hat{L}}\right)$
	$\hat{v}(\hat{z},0) = 0$
Boundary conditions	
	$\partial_{\hat{z}}\hat{R}(\pm\hat{L}/2,\hat{t}) = 0$
	$\hat{v}(\pm\hat{L}/2,\hat{t}) = 0$

as summarized in Table 3.6. Under the assumption of a slender filament, the momentum equation can be derived from the Navier-Stokes equation in the radial and axial directions in a cylindrical coordinate system. Together with the continuity equation, a closed-form of the governing equations can be expressed as

$$\partial_{\hat{t}}(\hat{R}^2\hat{v}) + \partial_{\hat{z}}(\hat{R}^2\hat{v}^2) = \partial_{\hat{z}}\left[\hat{R}^2\left(\hat{K} + \mathrm{Tr}\cdot\mathrm{Wi} + \frac{(\partial_{\hat{t}}\hat{R})^2}{2}\right)\right] - \hat{R}^2\cdot\mathrm{Bo}_0, \tag{3.15a}$$

$$\partial_{\hat{t}}(\hat{R}^2) + \partial_{\hat{z}}(\hat{R}^2\hat{v}) = 0, \tag{3.15b}$$

where the dimensionless strain rate for a slender filament can be denoted using the Weissenberg number defined in Equation (3.1) with $\mathrm{Wi} = \partial_{\hat{z}}\hat{v} = -2\partial_{\hat{t}}\hat{R}/\hat{R}$ from the

continuity equation. The time-varying Bond number is defined by Equation (2.13). The dimensionless mean curvature $\hat{K}$ of the liquid profile in the cylindrical coordinate system is expressed according to Equation (2.16) by substituting $R \to \hat{R}$ and $z \to \hat{z}$. The true extensional viscosity is nondimensionalized with the zero-shear viscosity as the Trouton ratio $\mathrm{Tr} \equiv \eta_e(\mathrm{Wi})/\eta_0$, and can be calculated from the constitutive equation as $\mathrm{Tr} = 3(1+\mathrm{Ec}_0 \cdot \mathrm{Wi})$, where $\mathrm{Ec}_0 \equiv k_2\Gamma/(\eta_0^2 R_0)$ is defined as the intrinsic elasto-capillary number using the zero-shear viscosity η_0 and the rate of extensional thickening k_2.

To capture the underlying capillarity-driven thinning dynamics predicted by the constitutive model, assumptions are made with negligible inertial and gravitational effects. As a result, the third and fourth terms on the right-hand side of Equation (3.15a) vanish, and from the boundary conditions, Equation (3.15) is further connected to the stress balance relation of Equation (2.14), and the transient geometric correction factor can be expressed as

$$X(\hat{t}) = \frac{[\mathrm{Tr} \cdot \mathrm{Wi} + \hat{K}_{\mathrm{mid}}(\hat{t})]\hat{R}_{\mathrm{mid}}(\hat{t})}{2}, \tag{3.16}$$

where $\hat{K}_{\mathrm{mid}}(\hat{t}) \equiv \hat{K}(0,\hat{t})$ and $\hat{R}_{\mathrm{mid}}(\hat{t}) \equiv R(0,\hat{t})$ are defined as the dimensionless mean curvature and filament radius at the symmetry plane ($\hat{z} = 0$).

Equation (3.15) is solved numerically following the procedures of Eggers and Dupont [250]. The dimensionless filament radius $\hat{R}(\hat{z},\hat{t})$ and the axial velocity $\hat{v}(\hat{z},\hat{t})$ are discretized both temporally and spatially: At the n-th time step ($n = 0, 1, ..., T$), $\hat{R}^{n,i}$ defines the discrete filament radius on the i-th grid node ($i = 0, 1, ..., N$) at $\hat{z} = \hat{z}^i$, while $v^{n,i+1/2}$ is defined on the edge that connects the $\hat{z}^i$ and $\hat{z}^{i+1}$. Consequently, the discrete derivative term $\partial_{\hat{z}}(\hat{R}^2\partial_{\hat{z}}\hat{v})$ that appears in Equation (3.15) can be expressed as

$$[\partial_{\hat{z}}(\hat{R}^2\partial_{\hat{z}}\hat{v})]^{n,i} = \frac{(\hat{R}^{n,i+1})^2(\partial_{\hat{z}}\hat{v})^{n,i+1} - (\hat{R}^{n,i})^2(\partial_{\hat{z}}\hat{v})^{n,i}}{\hat{z}^{i+1} - \hat{z}^{i-1}}, \tag{3.17}$$

where discrete partial derivative of $\hat{v}$ is calculated from

$$(\partial_{\hat{z}}\hat{v})^{n,i} = \frac{v^{n,i+1/2} - v^{n,i-1/2}}{\hat{z}^{i+1/2} - \hat{z}^{i-1/2}}. \tag{3.18}$$

Finally, a finite-difference form of Equation (3.15) can be obtained from the substitutions of Equation (3.17) and Equation (3.18). The final expression is rearranged by

moving the time derivative term $\partial_{\hat{t}}$ to the left-hand side as

$$\frac{(\hat{R}^2\hat{v})^{n+1,i} - (\hat{R}^2\hat{v})^{n,i}}{\hat{t}^{n+1} - \hat{t}^n} = \mathscr{F}_i(\hat{\boldsymbol{R}}^{n+\theta}, \hat{\boldsymbol{v}}^{n+\theta}), \tag{3.19a}$$

$$\frac{(\hat{R}^2)^{n+1,i} - (\hat{R}^2)^{n,i}}{\hat{t}^{n+1} - \hat{t}^n} = \mathscr{G}_i(\hat{\boldsymbol{R}}^{n+\theta}, \hat{\boldsymbol{v}}^{n+\theta}), \tag{3.19b}$$

where $\hat{\boldsymbol{R}}^{n+\theta}$ and $\hat{\boldsymbol{v}}^{n+\theta}$ represent all the spatially discrete values at time step $n+\theta$. $\mathscr{F}_i$ and $\mathscr{G}_i$ represent the right-hand sides of the discretized forms of Equation (3.15) evaluated at the $(n+\theta)$-th time step, where $0 \leq \theta \leq 1$. The discretized equations become completely explicit or implicit when $\theta = 0$ or 1. Here, a semi-implicit scheme is implemented to produce smoother discrete solutions while keeping the leading-order truncation errors in the time marching process sufficiently small. Specifically, the forms of the discrete filament kinematics at the $(n+\theta)$-th time step can be defined as

$$\hat{\boldsymbol{R}}^{n+\theta} \equiv \hat{\boldsymbol{R}}^n + \theta(\hat{\boldsymbol{R}}^{n+1} - \hat{\boldsymbol{R}}^n), \tag{3.20a}$$

$$\hat{\boldsymbol{v}}^{n+\theta} \equiv \hat{\boldsymbol{v}}^n + \theta(\hat{\boldsymbol{v}}^{n+1} - \hat{\boldsymbol{v}}^n). \tag{3.20b}$$

Here, a value of $\theta = 0.55$ is taken to be consistent with Eggers and Dupont [250]. The number of the grid nodes is set to $N = 128$ and $\Delta\hat{t} = \hat{t}^{n+1} - \hat{t}^n = 0.01$ for $n = 0, 1, ..., N-1$. The magnitude of Ec_0 is confined to $\mathrm{Ec}_0 \leq 1$ to conform to the condition of Equation (3.14). The characteristic aspect ratio is set as $\hat{L} = 10$.

In Figure 3-8(a) and (b), a family of filament profiles at different time are plotted for $\mathrm{Ec}_0 = 0$ (Newtonian fluid) and $\mathrm{Ec}_0 = 0.5$ (weakly rate-thickening). Comparisons of the filament profiles at approximately identical radius show that the profiles for $\mathrm{Ec}_0 = 0.5$ are more slender in shape, which can be attributed to the additional stress contribution in the constitutive equation that scales quadratically in magnitude with the strain rate and overtakes the Newtonian stress in finite time. As the filament approaches the pinchoff singularity, this quadratic stress component progressively dominates the filament thinning dynamics. Figure 3-8(c) and (d) further plot the axial velocity $\hat{v}(\hat{z}, \hat{t})$ for the two values of Ec_0, respectively. Two scaling factors $\mathbb{Z}(\hat{t})$ and $\mathbb{V}(\hat{t})$ are extracted from the coordinate of the maximum axial velocity where the strain rate vanishes ($\partial_{\hat{z}}\hat{v} = 0$). Filament within $-\mathbb{Z}(\hat{t}) \leq \hat{z} \leq \mathbb{Z}(\hat{t})$ are deemed slender. The abscissa and the ordinate are subsequently normalized by the extracted scaling factors $(\hat{z}/\mathbb{Z}, \hat{v}/\mathbb{V})$, such that the position where $\partial_{\hat{z}}\hat{v} = 0$ is reduced to $(\pm 1, \pm 1)$. The resulting profiles of the scaled velocity are plotted in Figure 3-8(e) and (f) in the window of $-1 \leq \hat{z}/\mathbb{Z} \leq 1$ and $-1 \leq \hat{v}/\mathbb{V} \leq 1$. When $\mathrm{Ec}_0 = 0$, the curves at different time overlap with each other, indicating a scale-free velocity profile during the filament thinning process. On

the contrary, the reduced velocity profile for $\mathrm{Ec}_0 = 0.5$ substantially reshapes while approaching the filament breakup, where the dominant stress contribution from extensional thickening gives rise to a distinct velocity profile from the one induced by the rate-independent stress contribution.

The filament radius at the symmetry plane $\hat{R}_{\mathrm{mid}}(\hat{t})$ can be extracted from the numerically calculated filament profiles for a range of intrinsic elasto-capillary numbers $0 \leq \mathrm{Ec}_0 \leq 1$, as shown in Figure 3-9(a). In Figure 3-9(b), the mid-plane radius is plotted against the temporal distance to the pinch-off singularity where $\hat{R}_{\mathrm{mid}}$ vanishes, $\hat{\tau} \equiv \hat{t}_{\mathrm{C}} - \hat{t}$. Here, $\hat{t}_{\mathrm{C}}$ is the dimensionless breakup time and its notation is consistent with the definition on page 73. The value of $\hat{t}_{\mathrm{C}}$ is obtained through extrapolation due to the numerical singularity arising at $\hat{R}_{\mathrm{mid}} = 0$. When $\mathrm{Ec}_0 = 0$ (Newtonian fluid, blue line), the mid-plane radius exhibits a linear decay with time. This numerical result is in good agreement with the prediction of Equation (2.17) with a slope of $-(2X_{\mathrm{N}} - 1)/6 \approx -0.0709$ (dashed line). When $\mathrm{Ec}_0 > 0$, however, the evolution of the mid-plane radius becomes substantially different from the Newtonian-fluid counterpart. An apparent retardation in the filament breakup is identified to increase from approximately 6.6 ($\mathrm{Ec}_0 = 0$) to 12.6 ($\mathrm{Ec}_0 = 1$), and can be attributed to the additional resistance to the capillarity arising from the extensional thickening. In addition, the evolution of the mid-plane filament radius deviates from the linear decay to a quadratic trend regarding to $\hat{\tau}$ close to filament breakup. This filament thinning trend suggests a new self-similar solution dominated by the balance between the capillarity and the stress from extensional thickening ($k_2\dot{\epsilon}^2$).

To substantiate this new asymptotic solution, the temporal evolution of the geometric correction factor X is subsequently calculated according to Equation (3.16). For plot legibility, the contribution to the overall geometric correction factor is decomposed as

$$X(t) = \underbrace{\frac{3\mathrm{Wi} \cdot \hat{R}_{\mathrm{mid}}}{2}}_{X_1(t)} + \underbrace{\frac{3\mathrm{Ec}_0 \cdot \mathrm{Wi}^2 \cdot \hat{R}_{\mathrm{mid}}}{2}}_{X_2(t)} + \underbrace{\frac{\hat{K}_{\mathrm{mid}}\hat{R}_{\mathrm{mid}}}{2}}_{X_{\mathrm{cap}}(t)}, \tag{3.21}$$

where X_1, X_2 and X_{cap} denote the contributions to the geometric correct factor X from the zero-shear viscosity term, the extensional-thickening term and the capillarity term, respectively. The contribution from the capillarity X_{cap} remains constant of 0.5 throughout the filament thinning process according to Equation (2.16). In Figure 3-10, the temporal evolution of $X_1(\hat{t})$ (squares), $X_2(\hat{t})$ (triangles) and $X(\hat{t})$ (diamonds) are plotted for an identical range of the elasto-capillary number $0 \leq \mathrm{Ec}_0 \leq 1$. The increase in the overall geometric correction factor $X(\hat{t})$ from $\hat{t} = 0$ to $\hat{t} \approx 4$ is attributed to

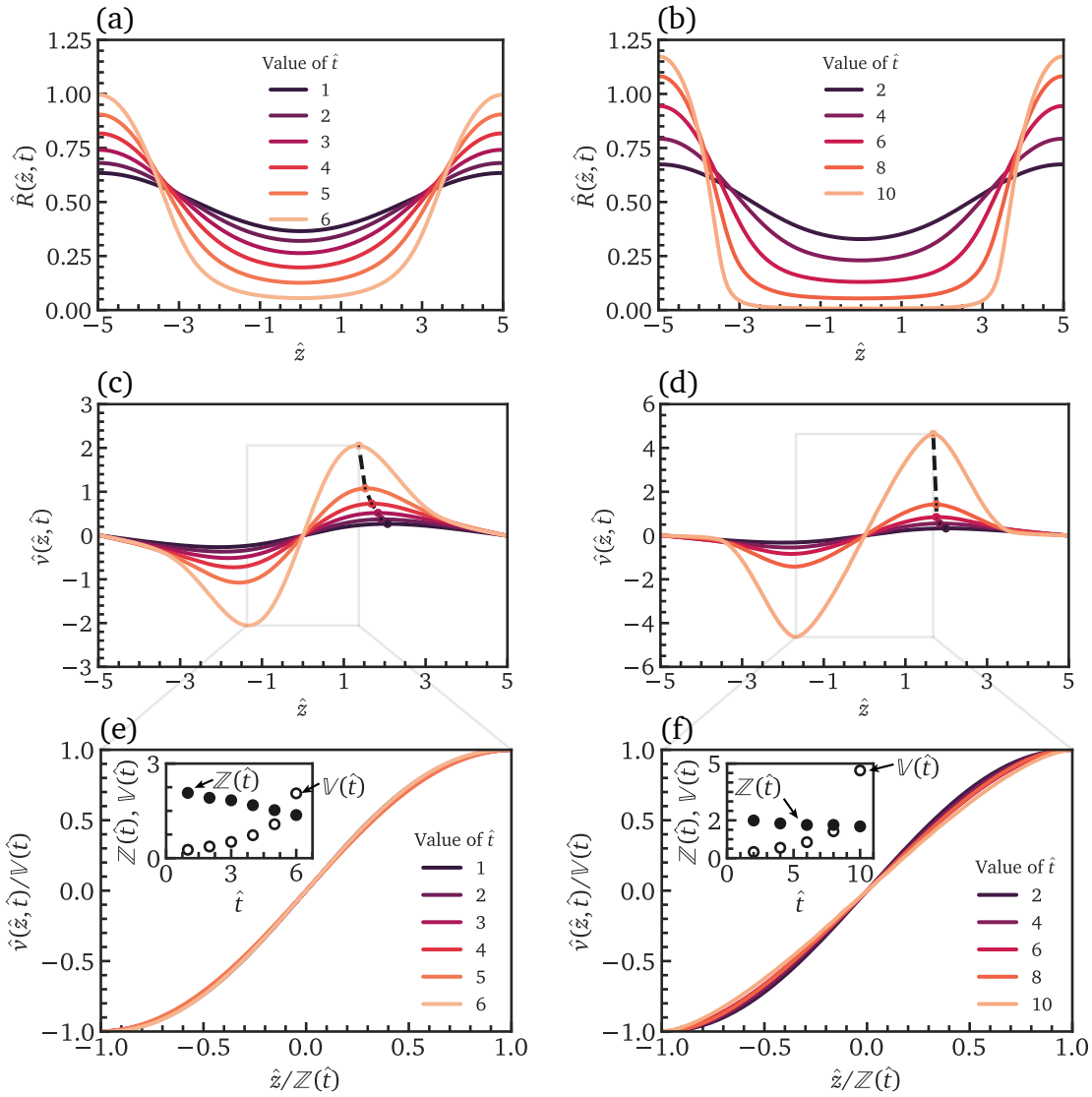

Figure 3-8: Filament kinematics predicted by the IRT model at (a,c,e) $\mathrm{Ec}_0 = 0$ and (b,d,f) $\mathrm{Ec}_0 = 0.5$ at varying time. (a-b) Filament radius. (c-d) Axial velocity with the evolution of the maximum velocity illustrated with dashed lines. (e-f) Collapsed axial velocity with the coordinate of the maximum axial velocity $(\mathbb{Z}(\hat{t}), \mathbb{V}(\hat{t}))$ different time. Inset: evolution of the maximum axial velocity $\mathbb{V}(\hat{t})$ and the axial position of the maximum axial velocity $\mathbb{V}(\hat{t})$.

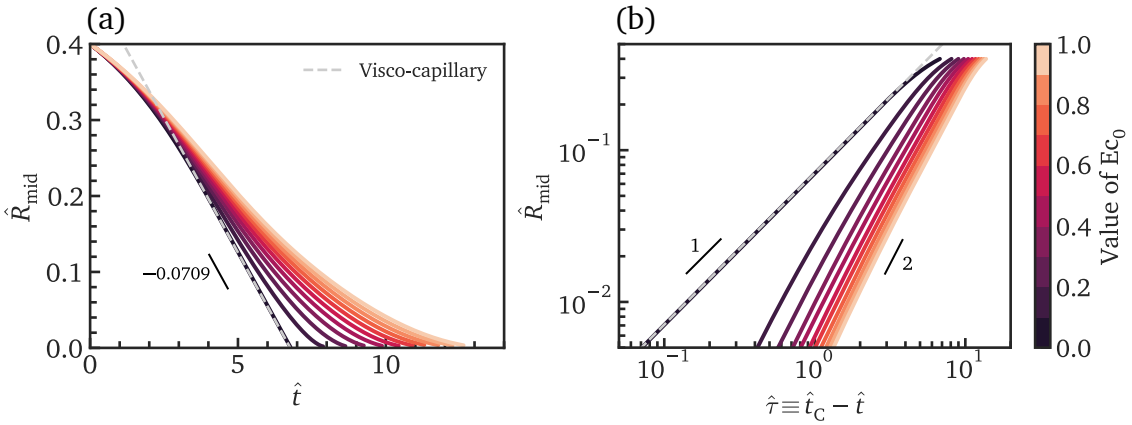

Figure 3-9: Mid-plane filament radius $\hat{R}_{\mathrm{mid}}(\hat{z}, \hat{t})$ for varying intrinsic elasto-capillary numbers $0 \leq \mathrm{Ec}_0 \leq 1$. (a) $\hat{R}_{\mathrm{mid}}$ against the thinning time t; the gray dashed line represents the linear visco-capillary thinning derived from the self-similar solution for a Newtonian fluid. (b) $\hat{R}_{\mathrm{mid}}$ against the time distance to the pinch-off singularity $\tau \equiv \hat{t}_{\mathrm{C}} - \hat{t}$; the dashed gray line represents the linear visco-capillary thinning derived from the self-similar solution for a Newtonian fluid. When $\mathrm{Ec}_0 > 0$, a quadratic thinning of the filament radius is identified close to filament breakup.

the filament acceleration due to the static initial condition, and is thus not accounted for as part of the asymptotic solution [207]. Beyond $\hat{t} \approx 4$, the evolution of the geometric correction factors exhibits two distinct trends distinguished by the value of Ec_0: For $\mathrm{Ec}_0 = 0$ (Newtonian fluid), X_1 remains constant. The overall geometric correction factor $X(\hat{t})$ approaches the asymptote under a visco-capillary balance at $X_{\mathrm{N}} \approx 0.7127$. When $\mathrm{Ec}_0 > 0$, however, the value of $X_1(\hat{t})$ reaches a maximum value at $\hat{t} \approx 4$ and subsequently follows a decaying trend. The magnitude of $\max(X_1)$ also decreases as Ec_0 increases, showing a diminished impact from the rate-independent stress contribution on the overall filament thinning dynamics. On the contrary, the contribution from the extensional-thickening contribution $X_2(\hat{t})$ increases steadily from zero in magnitude, and ultimately overtakes $X_1(\hat{t})$ to dominate the filament thinning process when sufficiently close to filament breakup. Notably, the overall geometric correction factor $X(\hat{t})$ for $\mathrm{Ec}_0 > 0$ converges to a new constant X_{RT} (not plotted) with a smaller magnitude than the result of $X_{\mathrm{N}} \approx 0.7127$ that describes the visco-capillary thinning.

The temporal evolution of the geometric correction factor $X(\hat{t})$ in the IRT model shows an increased complexity in the analysis of the filament thinning dynamics due to the interplay of two distinct stress contributions. By substituting the unknown constant X_{RT}

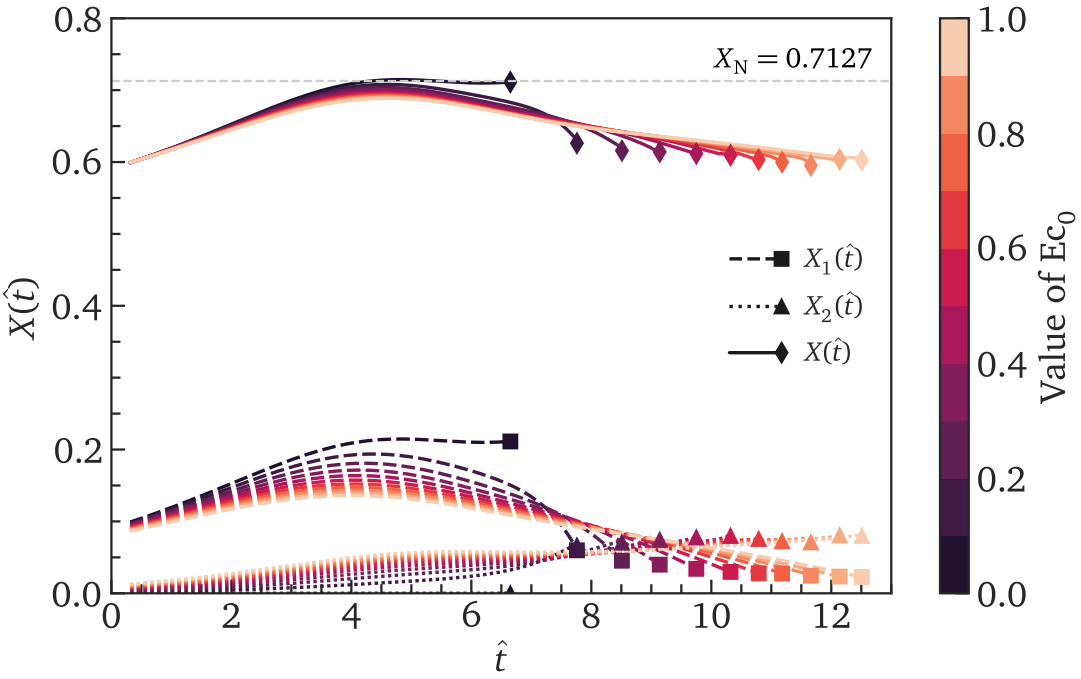

Figure 3-10: Temporal evolution of the geometric correction factor $X(\hat{t})$ and its components from two stress contributions, $X_1(\hat{t})$ and $X_2(\hat{t})$ for the IRT model for a range of intrinsic elasto-capillary numbers $0 \leq \mathrm{Ec}_0 \leq 1$.

into Equation (2.14), one can obtain an asymptotic solution for the mid-plane filament radius governed by the extensional-thickening contribution as

$$\hat{R}_{\mathrm{mid}}(\hat{\tau}; \mathrm{Ec}_0) = \frac{2X_{\mathrm{RT}} - 1}{48\mathrm{Ec}_0}\hat{\tau}^2, \tag{3.22}$$

in which the time distance to the filament breakup $\hat{\tau}$ is used to express in the vicinity of the pinch-off singularity. This quadratic trend is also evident in Figure 3-9. A similar expression has been previous obtained by McKinley [35], albeit X_{RT} was assumed to be unity based on the assumption of a cylindrical filament shape.

Inspired by the analytical solution from Renardy [252] and Papageorgiou [207], the constant of X_N that characterizes the filament shape of a Newtonian fluid can be derived from a self-similar solution. The analytical solution is based on the ansatz of the liquid

profiles as

$$\hat{R}(\hat{z},\hat{\tau}) = \hat{\tau}^{\alpha}\mathscr{R}(\zeta), \tag{3.23a}$$

$$\hat{v}(\hat{z},\hat{\tau}) = \hat{\tau}^{\gamma}\mathscr{V}(\zeta). \tag{3.23b}$$

A self-similar variable $\zeta = \zeta(\hat{z},\hat{\tau})$ that incorporates both the temporal and spatial information is defined as

$$\zeta \equiv \frac{\hat{z}}{\hat{\tau}^{\beta}}. \tag{3.24}$$

The parameters α, β, γ are the self-similar exponents. For a Newtonian fluid under a visco-capillary balance, Renardy [252] has analytically derived $\alpha_{\mathrm{N}} = 1$, $\beta_{\mathrm{N}} = 0.175$ and $\gamma_{\mathrm{N}} = \beta_{\mathrm{N}} - 1 = -0.825$. The forms of the self-similar functions $\mathscr{R}_{\mathrm{N}}$ and $\mathscr{V}_{\mathrm{N}}$ are expressed as functions of the self-similar variable ζ and can be calculated numerically or analytically under the condition of an infinitely long filament shape.

Here, the new self-similar solution governed by the extensional-thickening contribution in the IRT model is premised on a similar procedure. Specifically, in the limit of vanishing zero-shear viscosity contribution as well as the inertial and gravitational effects, the momentum equation (Equation (3.15)) can be rewritten as

$$\partial_{\hat{z}}[\hat{R}^2(\hat{K} + 3\mathrm{Ec}_0 \cdot \mathrm{Wi} \cdot |\mathrm{Wi}|)] = 0, \tag{3.25}$$

where the absolute sign is originated from Equation (3.7), in which the extensional rate $\dot{\epsilon}$ is derived from the second and third invariants of the strain-rate tensor, and remains non-negative regardless of the flow direction. Because of the self-similar nature, a solution in the same form of the ansatz in Equation (3.23)) can be presumed with a different set of self-similar parameters (α_{RT}, γ_{RT}, β_{RT}, ζ_{RT}, $\mathscr{R}_{\mathrm{RT}}$, $\mathscr{V}_{\mathrm{RT}}$). In the following analysis, the subscript "RT" is dropped for writing simplicity. The value of α can be readily obtained by substituting Equation (3.23) with the new self-similar parameters into Equation (3.25) as

$$\partial_{\hat{z}}\left\{\hat{\tau}^{\alpha}\partial_{\zeta}\mathscr{R} + (12\mathrm{Ec}_0)\hat{\tau}^{2\alpha-2}\left[\left(\alpha\mathscr{R} - \beta\zeta\partial_{\zeta}\mathscr{R}\right)\left|\alpha\mathscr{R} - \beta\zeta\partial_{\zeta}\mathscr{R}\right|\right]\right\} = 0, \tag{3.26}$$

which is valid for any $\hat{\tau}$. Therefore, all terms with $\hat{\tau}$ should cancel out, leading to $\alpha = 2$. This value is consistent with the asymptotic solution of Equation (3.22), in which the mid-plane filament radius has a quadratic dependence on $\hat{\tau}$. To calculate other parameters, the equivalence of the axial position z in a Lagrangian frame can be

defined as

$$\phi(\hat{z},\hat{\tau}) \equiv \int_0^{\hat{z}} \hat{R}^2(\xi,\hat{\tau})\mathrm{d}\xi, \tag{3.27}$$

which scales with the filament volume between the axial positions from 0 to $\hat{z}$. Because of the monotonicity of ϕ with $\hat{z}$, there is a determinate inverse function such that $\underline{\hat{z}} = \underline{\hat{z}}(\phi,\hat{\tau})$, where the underline corresponds to a function defined in the Lagrangian frame that satisfies $f(\hat{z},\hat{\tau}) = \underline{f}[\phi(\hat{z},\hat{\tau}),\hat{\tau}]$. By using the chain rules, the aforementioned functions and operators in a Eulerian frame can be transformed to a Lagrangian frame according to

$$\partial_\phi \hat{z} = \underline{\hat{R}}^{-2}(\phi,\hat{\tau}), \tag{3.28a}$$

$$\partial_{\hat{\tau}} \hat{z} = -\underline{\hat{v}}(\phi,\hat{\tau}), \tag{3.28b}$$

$$\partial_\phi = \underline{\hat{R}}^{-2}(\phi,\hat{\tau})\partial_{\hat{z}}. \tag{3.28c}$$

As a result, Equation (3.25) can be transformed to

$$-\frac{1}{2}\frac{\partial_{\phi\phi}\hat{z}}{(\partial_\phi \hat{z})^{3/2}} - 3\mathrm{Ec}_0\partial_\phi\left[\frac{\partial_{\phi\hat{\tau}}\hat{z}\left|\partial_{\phi\hat{\tau}}\hat{z}\right|}{(\partial_\phi\hat{z})^3}\right] = 0, \tag{3.29}$$

where $\partial_{xy}() \equiv \partial^2()/(\partial x \partial y)$. Using the transformation of Equation (3.28) again and substituting $z(\phi,\hat{\tau})$ with $\underline{\hat{R}}(\phi,\hat{\tau})$, the momentum equation in a Lagrangian frame can be expressed as

$$\partial_\phi \underline{\hat{R}} + 12\mathrm{Ec}_0\partial_\phi(\partial_{\hat{\tau}}\underline{\hat{R}}|\partial_{\hat{\tau}}\underline{\hat{R}}|) = 0. \tag{3.30}$$

Similar to $\hat{R}(\hat{z},\hat{\tau})$ in Equation (3.23), $\underline{\hat{R}}(\phi,\hat{\tau})$ in a Lagrangian frame is expected to follow the identical form with a different self-similar variable $\zeta \equiv \phi/\hat{\tau}^{\underline{\beta}}$. The value of $\underline{\beta}$ can be determined from the definition of ϕ in Equation (3.27), as in a leading-order expression, $\phi = \hat{\tau}^{\underline{\beta}}\underline{\zeta} \sim \hat{R}^2\hat{z} = \hat{\tau}^{4+\underline{\beta}}\mathscr{R}^3(\zeta)\zeta$. To retain the self-similar nature of $\underline{\zeta}$, the following ansatz is imposed in a Lagrangian frame as

$$\underline{\zeta} \equiv \frac{\phi}{\hat{\tau}^{\underline{\beta}+4}}, \tag{3.31a}$$

$$\underline{\hat{R}}(\phi,\hat{\tau}) = \hat{\tau}^2\underline{\mathscr{R}}(\underline{\zeta}). \tag{3.31b}$$

By substituting Equation (3.31) into Equation (3.30), and integrating on both sides

regarding to $\underline{\zeta}$, one can obtain

$$\mathscr{C}(\hat{\tau}) = \underline{\mathscr{R}} + 12\mathrm{Ec}_0[2\underline{\mathscr{R}} - (\beta+4)\underline{\zeta}\partial_{\underline{\zeta}}\underline{\mathscr{R}}]^2. \tag{3.32}$$

Here, the absolute sign is eliminated by noticing that $\partial_{\hat{\tau}}\underline{\hat{R}} = \hat{\tau}[2\underline{\mathscr{R}} - (\beta+4)\underline{\zeta}\partial_{\underline{\zeta}}\underline{\mathscr{R}}] > 0$, which can be rigorously proved from $\partial_{\hat{\tau}}\underline{\mathscr{R}} > 0$ at $\underline{\zeta} = 0$ (the mid-plane filament radius decreases monotonically), and that Equation (3.32) is valid for $\underline{\mathscr{R}} > 0$. Because the right-hand side of Equation (3.32) is a function of $\underline{\zeta}$ only, if letting $k(\underline{\zeta}) \equiv (\mathscr{C} - \underline{\mathscr{R}})^{1/2}$, Equation (3.32) can be rearranged to

$$\frac{k}{2\sqrt{12\mathrm{Ec}_0}} = \mathscr{C} - k^2 + (\beta+4)k\underline{\zeta}\partial_{\underline{\zeta}}k. \tag{3.33}$$

By separating k and $\underline{\zeta}$ to either side of the equation, and integrating both sides, one can finally obtain

$$\ln\left|\frac{\underline{\zeta}}{\underline{\zeta}_0}\right| = (\beta+4)\int_{k_0}^{k} \frac{\kappa \mathrm{d}\kappa}{\kappa^2 + \dfrac{\kappa}{2\sqrt{12\mathrm{Ec}_0}} - \mathscr{C}}. \tag{3.34}$$

When $\underline{\zeta}_0 \to 0^+$, κ approaches k_0, and singularities arise on both sides. To retain the equality for any values of k, these singularities must cancel each other. Therefore, k_0 and $\mathscr{C}$ can be calculated as

$$k_0 = \frac{1}{4\sqrt{12\mathrm{Ec}_0}(\beta+3)}, \tag{3.35a}$$

$$\mathscr{C} = \frac{2\beta+7}{192\mathrm{Ec}_0(\beta+3)^2}. \tag{3.35b}$$

From Equation (3.34) and Equation (3.35), one can obtain an explicit form of $\underline{\zeta}$ as a function of k as

$$\underline{\zeta}(k) = \left(\frac{1}{2\sqrt{12\mathrm{Ec}_0}}\frac{\beta+4}{\beta+3}\right)^{-(\beta+3)/2}\left(k + \frac{1}{4\sqrt{12\mathrm{Ec}_0}}\frac{2\beta+7}{\beta+3}\right)^{(2\beta+7)/2}(k-k_0)^{1/2}. \tag{3.36}$$

From the transformation in Equation (3.28) and Equation (3.36), there exists $\underline{f}(\underline{\zeta})$

such that $\partial_{\underline{\zeta}} \underline{f} = k^{-2}$, and the integration of Equation (3.33) leads to

$$2\sqrt{12\mathrm{Ec}_0}\mathscr{C} = \frac{\int_{-\infty}^{\infty} \underline{f}^{-3} \mathrm{d}\underline{\zeta}}{\int_{-\infty}^{\infty} \underline{f}^{-4} \mathrm{d}\underline{\zeta}}. \tag{3.37}$$

Finally, this equation is expressed in term of hypergeometric integrals [253] as

$$\frac{(2\beta+7)(-1-\beta)}{2(\beta+3)(-1/2-\beta)} = \frac{F\left[-(5+2\beta)/2, -1-\beta; -1/2-\beta; -7-2\beta\right]}{F\left[-(5+2\beta)/2, -\beta; 1/2-\beta; -7-2\beta\right]}. \tag{3.38}$$

Using the bisection method, this equation can be numerically solved with six significant figures as

$$\beta = \beta_{\mathrm{RT}} = 0.212515... \tag{3.39}$$

The solution of the mid-plane radius $\hat{R}_{\mathrm{mid}}(\hat{\tau})$ close to the filament breakup for the IRT model can thus be expressed as

$$\hat{R}_{\mathrm{mid}}(\hat{\tau}) = \frac{0.00324253...}{\mathrm{Ec}_0} \hat{\tau}^2. \tag{3.40}$$

Consequently, the overall geometric correction factor X_{RT} can be calculated as

$$X_{\mathrm{RT}} = \frac{7-2\beta_{\mathrm{RT}}}{4(3+\beta_{\mathrm{RT}})} = 0.577821... \tag{3.41}$$

By comparing with Figure 3-10, this result is consistent with the new asymptotic value close to the filament breakup for $\mathrm{Ec}_0 > 0$. This self-similar solution of the capillary thinning dynamics governed by the extensional-thickening contribution in the IRT model can be justified more rigorously by comparing with the numerically calculated filament profiles. The simplest idea is to directly substitute the value of X_{RT} into the asymptotic solution of Equation (3.22) and to compare with the mid-plane filament radius in Figure 3-9. However, this method requires an accurate evaluation of the filament breakup time $\hat{t}_{\mathrm{C}}$, which is hardly accessible due to numerical singularity. In practice, the determination of $\hat{t}_{\mathrm{C}}$ requires extrapolation to the limit of $\hat{R}_{\mathrm{mid}} = 0$ by horizontally shifting the curve of $\hat{R}_{\mathrm{mid}}(\hat{t})$ to coincide a power-law trend. Because the asymptotic solution of Equation (3.22) becomes evident only when sufficiently close to the filament breakup, or when $\hat{\tau}$ approaches zero, the extracted filament breakup time is subject to a large error. Here, instead of using $\hat{R}_{\mathrm{mid}}$ directly for the comparison, another dimensionless variable is adopted that is expressed in a time-implicit form to avoid the conversion from $\hat{t}$ to $\hat{\tau}$. For this purpose, the ratio of filament profile curvatures in the axial and

radial directions, Π is evaluated at the mid-plane ($\hat{z} = 0$), which can be expressed as

$$\Pi \equiv \frac{\kappa_z}{\kappa_r} = \left| \frac{\partial_{\hat{z}\hat{z}}\hat{R}}{\left[1 + (\partial_{\hat{z}}\hat{R})^2\right]^{3/2}} \right| \Bigg/ \left| \frac{1}{\hat{R}\left[1 + (\partial_{\hat{z}}\hat{R})^2\right]^{1/2}} \right|. \tag{3.42}$$

By including the curvatures in both axial and radial directions, this ratio quantity incorporates the full-dimensional information of the filament geometry. Subsequently, the ansatz of Equation (3.23) is substituted into Equation (3.42) to obtain an asymptotic solution governed by the zero-shear viscosity contribution (denoted as "N") and the rate-thickening contribution (denoted as "RT") respectively as

$$\Pi_{\mathrm{N}}(\hat{\tau}) \sim \hat{\tau}^{2-2\beta_{\mathrm{N}}} \sim \hat{R}_{\mathrm{mid}}^{2-2\beta_{\mathrm{N}}}(\hat{\tau}), \tag{3.43a}$$

$$\Pi_{\mathrm{RT}}(\hat{\tau}) \sim \hat{\tau}^{4-2\beta_{\mathrm{RT}}} \sim \hat{R}_{\mathrm{mid}}^{2-\beta_{\mathrm{RT}}}(\hat{\tau}). \tag{3.43b}$$

In Figure 3-11, the numerical calculations of the curvature ratio are plotted for different values of Ec_0. The analytically obtained power-law relations from Equation (3.43) are also plotted as gray lines. As shown in this figure, the numerical calculations follow closely with the asymptotic power-law trends as $\hat{R}_{\mathrm{mid}} \to 0$ for $\mathrm{Ec}_0 = 0$ (black solid line), and when the filament thinning dynamics are solely governed by the rate-thickening contribution (Equation (3.25)) with $\mathrm{Ec}_0 = 1$ (solid blue line). As Ec_0 grows positive, both the zero-shear viscosity and extensional-thickening contribute in comparable magnitude to the capillarity-driven thinning dynamics. The resulting curvature ratio departs from the power law of $(2-2\beta_{\mathrm{N}})$ for a Newtonian fluid towards a new exponent of $2-\beta_{\mathrm{RT}}$. This new curvature ratio asymptote with a smaller exponent corresponds to a more slender liquid filament profile, as has been demonstrated in Figure 3-8. Notably, as shown in Figure 3-11(a), even a weakly rate-thickening response quantified by a small positive value of Ec_0 can substantially alter the resulting capillarity-driven thinning dynamics close to the filament breakup, which is attributed to a faster-growing axial stress that scales quadratically with the time to filament breakup, arising from the extensional-thickening contribution.

In Figure 3-11(b), the mid-plane radius (blue thick line) and the curvature ratio (pink thick line) from numerical calculations are plotted against the time distance to the filament breakup $\hat{\tau}$ when the zero-shear viscosity contribution is set to vanish and the intrinsic elasto-capillary number is set to unity. The value of $\hat{t}_{\mathrm{C}}$ is obtained from the best manual horizontal shift such that both curves coincide power-law trends close to the filament breakup, as predicted from the analytical results shown as the thin solid lines. The numerical results of the filament mid-plane radius and the mean curvature

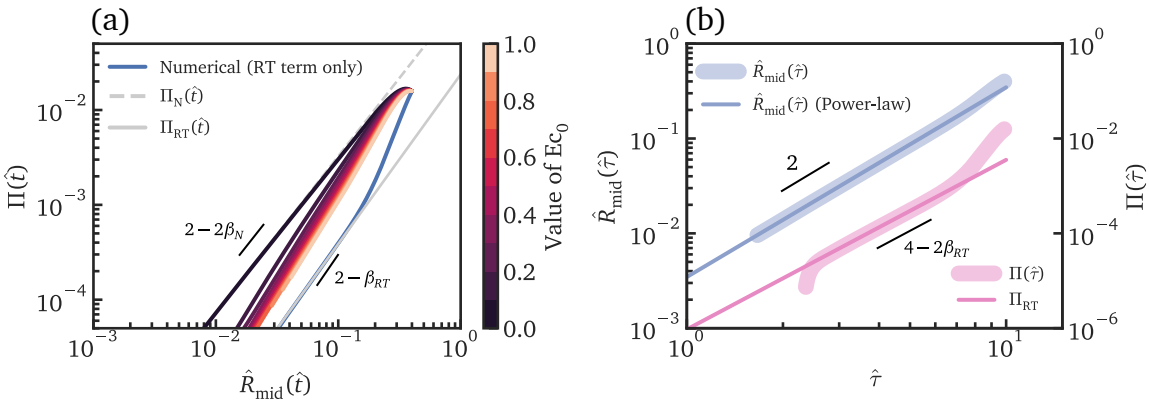

Figure 3-11: (a) Curvature ratio at the filament mid-plane from the numerical calculations at varying intrinsic elasto-capillary numbers Ec_0 as well as the asymptotic solutions of Equation (3.43) with power-law trends (gray lines). (b) The mid-plane radius $\hat{R}_{mid}$ and curvature ratio Π plotted against the time distance to the filament breakup $\hat{\tau}$ for the capillarity-driven thinning dynamics governed solely by the extensional-thickening contribution in the IRT model.

ratio are in excellent agreement with the asymptotic solutions that exhibit a power-law relation with the exponent of 2 and $(4-2\beta_{RT})$, respectively. Notably, the asymptotic solution of the filament mid-plane radius (thin blue line) coincides with the numerical result not only in the power-law trend, but also in the front factor within 7% error. Such an error is likely to arise from the conversion from $\hat{t}$ to $\hat{\tau}$, the numerical calculation close to the filament breakup as well as the infidelity to the assumption of an infinitely long filament in the ansatz of Equation (3.23) in the numerical calculation.

CaBER measurements with a time-varying geometric correction factor

An accurate value of the geometric correction factor X is necessary to recover the true extensional viscosity from the measured filament thinning kinematics using Equation (3.10). For a Newtonian fluid, this value has been obtained with a constant of $X_N \approx 0.7127$. However, in the IRT model (and other models with multiple stress contributions to the capillarity-driven thinning dynamics), the value of X evolves with time, and an explicit form of $X(t)$ is not readily accessible without *a priori* knowledge of the constitutive parameters and a full-dimensional numerical calculation of the filament profiles. Inspired by the numerical calculation from the previous section, an implicit method is proposed here that will finally lead to a measuring and dataprocessing protocol to account for the temporal variation in the geometric correction factor.

The apparent Trouton ratio defined on page 91 using the apparent viscosity (obtained from Equation (3.9)) can be plotted from the numerical calculation for the IRT model at $\mathrm{Ec}_0 = 0,\ 0.1$ and 1 in Figure 3-12 as solid lines. The segments of the curves with $\mathrm{Wi} \lesssim 0.7$ exhibit an artifact rate-thinning region due to to the initial acceleration of the liquid filament in the numerical calculation, and does not reflect the real constitutive relation. The evolution of the apparent Trouton ratio for each Ec_0 is compared with the two asymptotic solutions of $X_{\mathrm{N}} \approx 0.7127$ (thin dashed lines) and $X_{\mathrm{RT}} \approx 0.5778$ (thin solid lines). When $\mathrm{Ec}_0 = 0$, the solution of a Newtonian fluid is recovered, and the apparent Trouton ratio from the numerical calculation $\mathrm{Tr}_{\mathrm{app}} = 3/(2X_{\mathrm{N}}-1) \approx 7.052$ agrees with the asymptotic solution under a visco-capillary balance. When $\mathrm{Ec}_0 > 0$, the apparent Trouton ratio $\mathrm{Tr}_{\mathrm{app}}$ is contributed by both the zero-shear viscosity and rate-thickening contributions, and hence its magnitude remains between the two asymptotic solutions (shaded area). As the Weissenberg number increases, the apparent Trouton ratio seamlessly evolves from the asymptote governed by $X = X_{\mathrm{N}}$ to $X = X_{\mathrm{RT}}$. For $\mathrm{Ec}_0 = 0.1$ at $\mathrm{Wi} = 10$, the magnitude of $\mathrm{Tr}_{\mathrm{app}}$ reaches 23 in the numerical calculation, approximately 54% higher than the asymptotic solution from $X = X_{\mathrm{N}}$ (where $\mathrm{Tr}_{\mathrm{app}} \approx 14.1$) and 283% higher than the asymptotic solution from $X = 1$ (where $\mathrm{Tr}_{\mathrm{app}} = 6$). This specific combination of the intrinsic elasto-capillary number and the Weissenberg number is carefully selected to represent the fluid and flow properties for a number of automotive lubricants under their working conditions [26, 201]. Consequently, the application of a Newtonian-fluid assumption $X = X_{\mathrm{N}}$ or an assumption of cylindrical filament shapes $X = 1$ in processing the CaBER measurements is likely to generate large errors when the true extensional viscosity is to be recovered, even at moderate strain rates for a weakly rate-thickening fluid.

To render a more accurate measurement of the extensional viscosity from filament thinning techniques, an approximation of the transient geometric correction factor can be obtained through a linear interpolation based on the magnitudes of the each stress contributions as

$$\frac{X(\mathrm{Wi}) - X_{\mathrm{N}}}{X_{\mathrm{RT}} - X_{\mathrm{N}}} = \frac{\Delta\sigma_{\mathrm{RT}}}{\Delta\sigma_{\mathrm{N}} + \Delta\sigma_{\mathrm{RT}}} = \frac{\mathrm{Ec}_0 \cdot \mathrm{Wi}}{1 + \mathrm{Ec}_0 \cdot \mathrm{Wi}}, \tag{3.44}$$

where $\Delta\sigma_{\mathrm{N}} = 3\eta_0\dot{\epsilon}$ and $\Delta\sigma_{\mathrm{RT}} = 3k_2\dot{\epsilon}^2$ are the stress contributions from the zero-shear viscosity term and the rate-thickening term, respectively. This expression leads to a new prediction line of the apparent Trouton ratio at each selected value of Ec_0, as plotted in Figure 3-12 in dash-dotted lines. The new prediction lines based on linear interpolation are bounded by the two asymptotic solutions for each Ec_0 and are in good agreement with the corresponding numerical calculations. In practice, the true Trouton ratio (hence the true extensional viscosity) can be readily obtained by incorporating

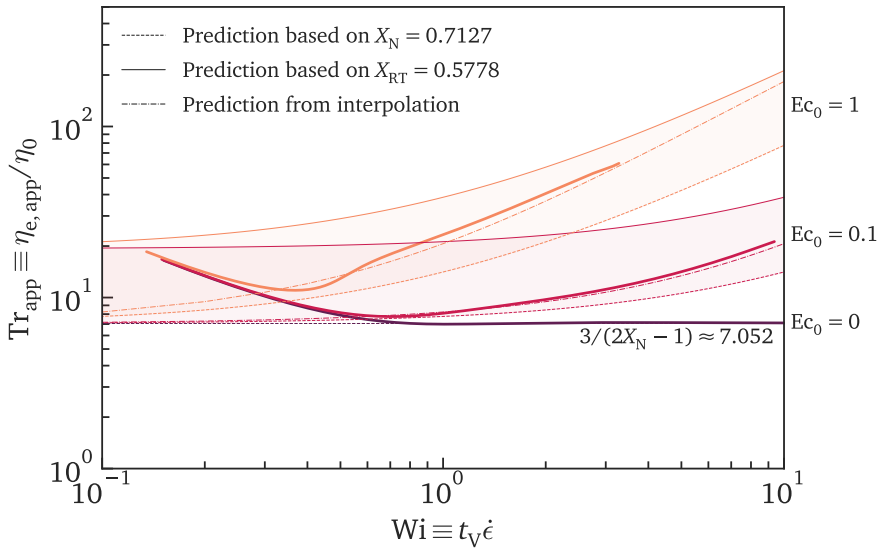

Figure 3-12: Apparent Trouton ratio Tr_{app} against Weissenberg number from the numerically calculated filament thinning dynamics predicted by the IRT model (solid lines) as well as the asymptotic solutions governed by each individual stress contribution (zero-shear: thin dotted lines; extensional-thickening: thin solid lines) at intrinsic elasto-capillary numbers $\mathrm{Ec}_0 = 0,\ 0.1$ and 1. For $\mathrm{Ec}_0 = 0$, the asymptotic solution for a Newtonian fluid is recovered, where $\mathrm{Tr}_{app} = 3/(2X_N - 1) \approx 7.052$ (purple dotted line). In the numerical calculations, the apparent rate-thinning behavior for $\mathrm{Wi} \lesssim 0.7$ is attributed to the filament acceleration at the onset of filament thinning, and is thus excluded from the constitutive relation. Linear interpretations based on the magnitudes of each stress contribution are plotted as thin dashed dotted lines, which show good agreement with the numerical calculations.

Equation (3.44) into Equation (2.14), considering that $X = X(\boldsymbol{\sigma})$. The modified stress balance equation is subsequently fitted to the experimental data to obtained a more accurate measurement of all the constitutive parameters.

A time-varying geometric correction factor for the Oldroyd-B model

A similar interpolation protocol can also be applied to the more widely-used Oldroyd-B model to incorporate a time-varying geometric correction factor for the measurements of constitutive parameters. As justified in the previous section, even if the asymptote solutions for $\dot{\epsilon} \to 0$ (visco-capillary thinning governed by the solvent vis-

cosity) and $\dot{\epsilon} \to 2/(3\lambda)$ (elasto-capillary limit) are available, an increasing number of the materials with larger solvent viscosities, low polymer concentrations or molecular weights exhibit the capillarity-driven thinning behavior with a more progressive transition between the two asymptotic solutions governed by individual stress contributions ($3\eta_S\dot{\epsilon}$ and the polymer stress $N_{1,\mathrm{P}}$) as the filament thinning dynamics evolve. It has been shown previously that an intrinsic elasto-capillary number $\mathrm{Ec}_0 \equiv \lambda\Gamma/(\eta_0 R_0) \lesssim 1$ can be utilized to categorize such behavior. To obtain an accurate solution of the capillarity-driven thinning dynamics predicted by the Oldroyd-B model, a similar numerical protocol is applied with the inertial term being retained in the momentum equation to avoid numerical instability. The numerical calculation schemes including the initial/boundary conditions are summarized in Table 3.7, which resemble Table 3.6 except that the Rayleigh timescale $t_{\mathrm{Ra}} \equiv \sqrt{\rho R_0^3/\Gamma}$ is adopted for the nondimensionalizing purpose.

As a result of the nondimensionalization, three constitutive parameters arise in momentum equation: the dimensionless relaxation time $\hat{\lambda} \equiv \lambda/t_{\mathrm{Ra}}$, the solvent Ohnesorge number $\mathrm{Oh}_\mathrm{S} \equiv \eta_S/\sqrt{\rho\Gamma R_0}$, and the zero-shear viscosity ratio between the elastic stress and the viscosity stress (denoted as "viscosity ratio") $\hat{\eta}_\mathrm{P} \equiv G\lambda/\eta_\mathrm{S}$. In addition, a Weissenberg number can be defined using the Rayleigh timescale as $\mathrm{Wi} \equiv t_{\mathrm{Ra}}\dot{\epsilon}$. One may notice that during the elasto-capillary thinning, the value of $\sigma_{\mathrm{P},zz}$ increases exponentially with time and becomes progressively larger than its rr-counterpart. As a result, the stress balance and continuity equations for the numerical calculation are simplified in the limit of $N_{1,\mathrm{P}} \approx \sigma_{\mathrm{P},zz}$ with the gravitational and inertial effects to vanish, similar to the form of Equation (3.15) as

$$\partial_{\hat{t}}(\hat{R}^2\hat{v}) + \partial_{\hat{z}}(\hat{R}^2\hat{v}^2) = \partial_{\hat{z}}\left[\hat{R}^2\left(\hat{K} + 3\mathrm{Oh}_\mathrm{S}\cdot\mathrm{Wi} + \hat{N}_{1,\mathrm{P}}\right)\right], \tag{3.45a}$$

$$\partial_{\hat{t}}(\hat{R}^2) + \partial_{\hat{z}}(\hat{R}^2\hat{v}) = 0, \tag{3.45b}$$

$$\partial_{\hat{t}}\hat{N}_{1,\mathrm{P}} = \left(2\mathrm{Wi} - \frac{1}{\hat{\lambda}}\right)\hat{N}_{1,\mathrm{P}} + \frac{2\hat{\eta}_\mathrm{P}\cdot\mathrm{Oh}_\mathrm{S}}{\hat{\lambda}}\mathrm{Wi}, \tag{3.45c}$$

where the polymer stress contribution is nondimensionalized as $\hat{N}_{1,\mathrm{P}} \equiv N_{1,\mathrm{P}}/(\Gamma/R_0)$. For the numerical calculation, the filament aspect ratio is set as $\hat{L} = 10$ to be consistent with the numerical study for the IRT model. Identical configurations of the initial conditions, the boundary conditions, and the finite-difference scheme are applied as for the IRT model in the numerical calculation. In addition, previous studies have found numerical singularities close to the boundaries on both sides due to the failure of the slender assumption [237]. This singularity can been reconciled by imposing a solvent

Table 3.7: Numerical calculation schemes of the capillarity-driven thinning predicted by the Oldroyd-B model, including the nondimensionalization scheme and initial/boundary conditions.

Type	Definitions
Position and time	$\hat{r} \equiv \frac{r}{R_0}, \hat{z} \equiv \frac{z}{R_0}, \hat{t} \equiv \frac{t}{t_{\mathrm{Ra}}} = \frac{t}{\sqrt{\rho R_0^3/\Gamma}}$
Kinematics and geometry	$\hat{R} \equiv \frac{R}{R_0}, \hat{v} \equiv \frac{v}{R_0/t_{\mathrm{Ra}}}, \hat{L} \equiv \frac{L}{R_0}$
Operators	$\partial_{\hat{t}} \equiv t_{\mathrm{Ra}}\partial_t, \partial_{\hat{z}} \equiv R_0\partial_z$
Dimensionless constitutive parameters	
Relaxation time $\hat{\lambda}$	$\hat{\lambda} \equiv \frac{\lambda}{t_{\mathrm{Ra}}}$
Solvent Ohnesorge number $\mathrm{Oh_S}$	$\mathrm{Oh_S} \equiv \frac{\eta_S}{\sqrt{\rho\Gamma R_0}}$
Relative polymer viscosity $\hat{\eta}_{\mathrm{P}}$	$\hat{\eta}_{\mathrm{P}} \equiv \frac{G\lambda}{\eta_{\mathrm{S}}}$
Weissenberg number Wi	$\mathrm{Wi} \equiv t\dot{\epsilon}$
Initial conditions	
	$\hat{R}(\hat{z},0) = 0.5 - 0.1\cos\left(\frac{2\pi\hat{z}}{\hat{L}}\right)$
	$\hat{v}(\hat{z},0) = 0$
Boundary conditions	
	$\partial_{\hat{z}}\hat{R}(\pm\hat{L}/2,\hat{t}) = 0$
	$\hat{v}(\pm\hat{L}/2,\hat{t}) = 0$
	$\partial_{\hat{z}}\hat{N}_{1,\mathrm{P}}(\pm\hat{L}/2,\hat{t}) = 0$

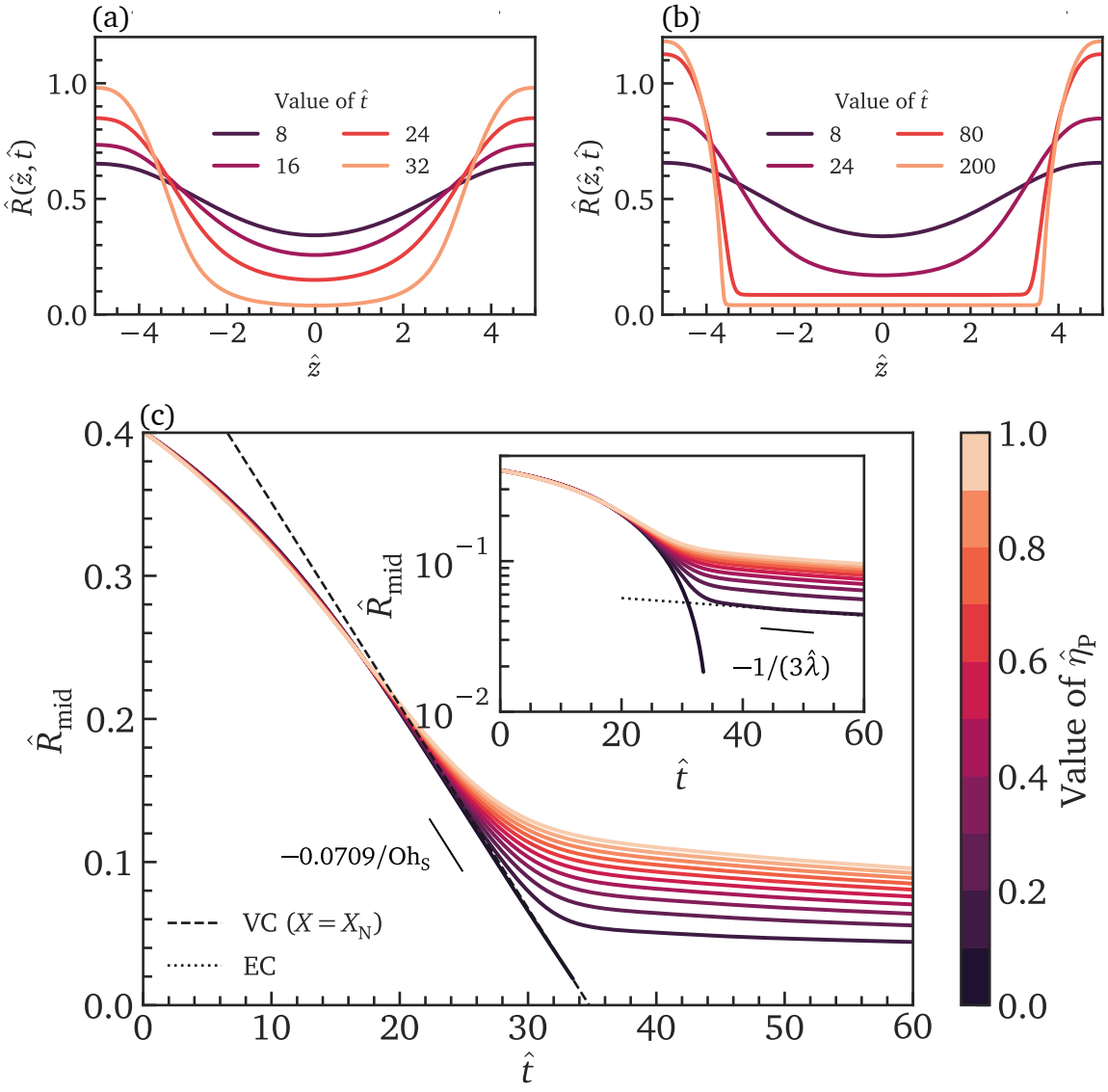

Figure 3-13: (a-b) Numerically calculated filament profiles predicted by the Oldroyd-B model for $\text{Oh}_S = 5$ and $\hat{\lambda} = 50$ at different time: (a) $\hat{\eta}_P = 0$ (Newtonian fluid); (b) $\hat{\eta}_P = 1$. (c) Numerically calculated mid-plane filament radius predicted by the Oldroyd-B model for a range of viscosity ratios $0 \leq \hat{\eta}1$. The dashed line corresponds to the linear decaying asymptotic solution for visco-capillary thinning with a slope of $-0.0709/\text{Oh}_S$. Inset: Identical plot when the ordinate is replotted on a logarithmic scale. The dashed line corresponds to the exponential decaying asymptotic solution for elasto-capillary thinning with a slope of $-1/(3\hat{\lambda})$.

viscosity that increases dramatically near the boundaries to progressively "freeze" the fluid motion. Here a specific form of the solvent viscosity is taken as

$$\tilde{\eta}_S(\hat{z}) = \begin{cases} \eta_S, & |\hat{z}| \le \alpha\hat{L} \\ \eta_S \exp[\beta(|\hat{z}| - \alpha\hat{L})/\hat{L}], & |\hat{z}| > \alpha\hat{L} \end{cases} \tag{3.46}$$

where $\tilde{\eta}_S$ is the assigned solvent viscosity for numerical purposes only. The two dimensionless control parameters α and β are supposed to control the affected range and the rate of increase for the assigned solvent viscosity. In this numerical study, $\alpha = 0.9$ and $\beta = 1$ are taken to optimally accommodate the calculation without impairing the accuracy.

As shown in Figure 3-13(a) and (b), the filament profiles with identical parameters of $Oh_S = 5$ and $\hat{\lambda} = 50$ but different $\hat{\eta}_P = 0$ and $\hat{\eta}_P = 1$ are calculated and plotted at different time $\hat{t} < \hat{t}_C$. The filament profiles for $Ec_0 = 0$ reduce to the predictions from a Newtonian fluid, which have been illustrated in Figure 3-8. As $\hat{\eta}_P$ grows positive, the filament becomes close to a cylindrical shape in the approach to filament breakup due to the exponentially increased axial stress contribution from the polymer. In Figure 3-13(c), the mid-plane filament radius for a range of $0 \le \hat{\eta}_P \le 1$ is extracted. While $\hat{\eta}_P = 0$ exhibits a linear trend that is consistent with the visco-capillary thinning, a clear transition in the filament shape is manifested for $\hat{\eta}_P > 0$. At $\hat{t} \lesssim 30$, the minimum filament radius exhibits a linear trend with the slope of $-0.0709/Oh_S$ (black dashed line), and the filament thinning dynamics are dominated by the visco-capillary thinning governed by the solvent viscosity. Beyond $\hat{t} \approx 30$, the temporal evolution of the filament radius progressively approaches an exponential trend as expected for the elasto-capillary thinning with a slope of $-1/(3\hat{\lambda})$ on a logarithmic scale in the ordinate (dotted line in the inset). This exponential-thinning has been described by the asymptotic solution of Equation (2.18).

Following a similar protocol for the calculation of the axial driving force as in Figure 3-10, the contributions to the geometric correction factor from the two stress terms in the constitutive equation, $X_S(\hat{t})$ (solvent) and $X_P(\hat{t})$ can be calculated, while the contribution from the capillary pressure remains at constant of $X_{cap} = 0.5$. Figure 3-14(a) plots the temporal evolution of X_S, X_P and X for $\hat{\eta}_P = 1$. Notably, the magnitude of $X(\hat{t})$ evolves from $X_N = 0.7127$ (gray dashed line) to an asymptote of $X_{EC} = 1$. This transition appears to be more rapid than the IRT model in Figure 3-10 because of the exponentially increased viscoelastic stress contribution, compared with the quadratically increased rate-thickening contribution in the IRT model. Nonetheless, the scheme using a linear interpolation similar to Equation (3.44) can still be applied to render a

time-implicit expression for a varying geometric correction factor as

$$\frac{X(\mathrm{Wi}) - X_\mathrm{N}}{X_\mathrm{EC} - X_\mathrm{N}} = \frac{N_{1,\mathrm{P}}}{3\eta_\mathrm{S}\dot{\epsilon} + N_{1,\mathrm{P}}}, \tag{3.47}$$

where $X_\mathrm{N} = 0.7127$ and $X_\mathrm{EC} = 1$ are the geometric correction factors solely governed by a visco-capillary balance and an elasto-capillary balance, respectively. As shown in Figure 3-14(b), Equation (3.47) leads to a collapsed curve for a range of $\hat{\eta}_\mathrm{P}$, and the linear interpolation (dashed line) shows broad agreement with the collapsed curve from the numerical calculation.

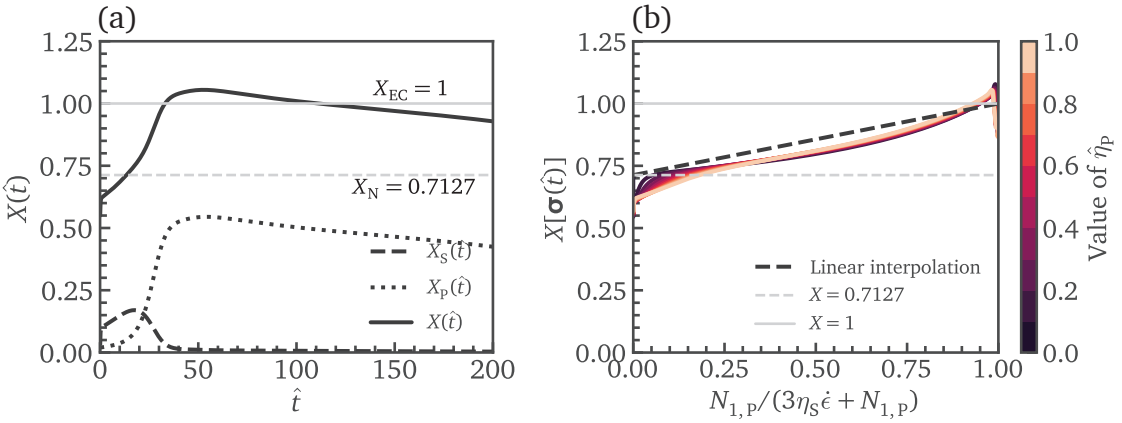

Figure 3-14: (a) Temporal evolution of the geometric correction factor X and its two contributions from the solvent viscosity term X_S and the polymer stress term X_P predicted by the Oldroyd-B model. The dashed and solid lines in gray correspond to the asymptotic solutions of $X_\mathrm{N} = 0.7127$ and $X_\mathrm{EC} = 1$, respectively. (b) Collapsed geometric correction factor assuming the validity of Equation (3.47), which is shown as the black dashed line. A broad agreement between the numerical calculation and the expression of Equation (3.47) is manifested. The two gray lines show identical asymptotic solutions as in (a).

Equation (3.47) is subsequently combined with Equation (2.14) and the constitutive relation of Equation (3.2), leading to a modified ordinary differential equation with a more accurate description of the filament thinning dynamics by virtue of multiple stress contributions. In Figure 3-15, two evolutions of the mid-plane filament radius predicted by the Oldroyd-B model are plotted with $X = 1$ (red solid line) and $X[\sigma(\hat{t})]$ according to Equation (3.47) (black solid line). In both numerical solutions, the consti-

tutive parameters are set as $\mathrm{Oh}_S = 5$, $\hat{\lambda} = 50$ and $\hat{\eta}_P = 1$. Two reference lines predicted by the visco-capillary thinning are plotted for $X = 1$ (red dotted line) and $X = X_N$ (black dotted line) with substantially different slopes. When the value of X differs, the exponential decaying trend predicted by the elasto-capillary thinning is retained with an identical slope of $-1/(3\hat{\lambda})$. However, the prediction line with a temporally-evolving X produces a consistent result with the self-similar solution predicted by the visco-capillary thinning (black dotted line) when the solvent viscosity dominates the filament thinning dynamics. The transition time between the visco-capillary thinning and the elasto-capillary thinning $t_{V\text{-}E}$, as defined previously and marked in black, is thus delayed by approximately 100% compared with that for $X = 1$ (marked in red), showing a substantial change in the filament thinning patterns. The mid-plane filament radius predicted by the IRT model as introduced in Section 3.2 is plotted as well for comparison purposes, as shown in the red dashed line for $X = 1$, and the black dashed line for $X[\sigma(\hat{t})]$ according to Equation (3.44). To keep the constitutive parameters comparable between the two models, the asymptotic solution from Equation (3.8) is applied such that the constitutive parameters in the IRT model are set as

$$\mathrm{Oh} \equiv \frac{\eta_0}{\sqrt{\rho \Gamma R_0}} \text{ (IRT)} \Rightarrow \mathrm{Oh}_S(1 + \hat{\eta}_P) \text{ (Oldroyd-B)} = 5.5, \tag{3.48a}$$

$$\mathrm{Oh} \cdot \mathrm{Ec}_0 \equiv \frac{k_2}{\rho R_0^2} \text{ (IRT)} \Rightarrow \hat{\eta}_P \mathrm{Oh}_S \hat{\lambda} \text{ (Oldroyd-B)} = 25. \tag{3.48b}$$

From Figure 3-15, a better comparison can be made between the Oldroyd-B model and the IRT model with consistent constitutive parameters. From inspecting the filament thinning profiles, the IRT model predicts a more progressive deviation from the visco-capillary thinning trend (dotted lines) due to the slowly increased magnitude of the extensional-thickening contribution, and the transient extensional viscosity at an early stage of the filament thinning is larger for the IRT model. The filament thinning profiles predicted by the IRT model become distinct in shape from the Oldroyd-B model only in the late stage of filament thinning, where the strain rate becomes large in magnitude ($\mathrm{Wi} \sim 2/3$), and the approximation of Equation (3.8) fails. Despite that the constitutive equation of the IRT model can be derived from Equation (3.8) as an asymptotic solution of the Oldroyd-B model, these two models are treated independently in this study. The rate-dependent contributions to the filament thinning dynamics differ substantially in either model, as depicted by their distinct asymptotic geometric correction factors ($X_{RT} = 0.5778$ for the IRT model, and $X_{EC} = 1$ for the Oldroyd-B model). Noticeably, the two asymptotic values of X lie on either side of X_N for a Newtonian fluid. For the IRT model, both the rr- and zz-components of the

stress tensor grow in magnitude in a filament thinning process, and a self-similar solution can be identified to describe the shape of the filament profiles. The value of X is a physical quantification that describes the self-similar nature, which has been explicitly expressed for other analytical solutions of the filament profiles [254,255]. The resulting filament can grow increasingly slender than the Newtonian counterpart, despite that the value of X evolves farther away from $X = 1$ (assumed for a cylindrical filament). In contrary, for the Oldroyd-B model, the zz-component grows overwhelmingly large in magnitude than the rr-component in the elasto-capillary thinning region, and the fluid becomes increasingly anisotropic. Consequently, a self-similar solution fails to describe the whole filament thinning profiles accurately, and the value of X is merely a summation of the stress contribution in the axial direction.

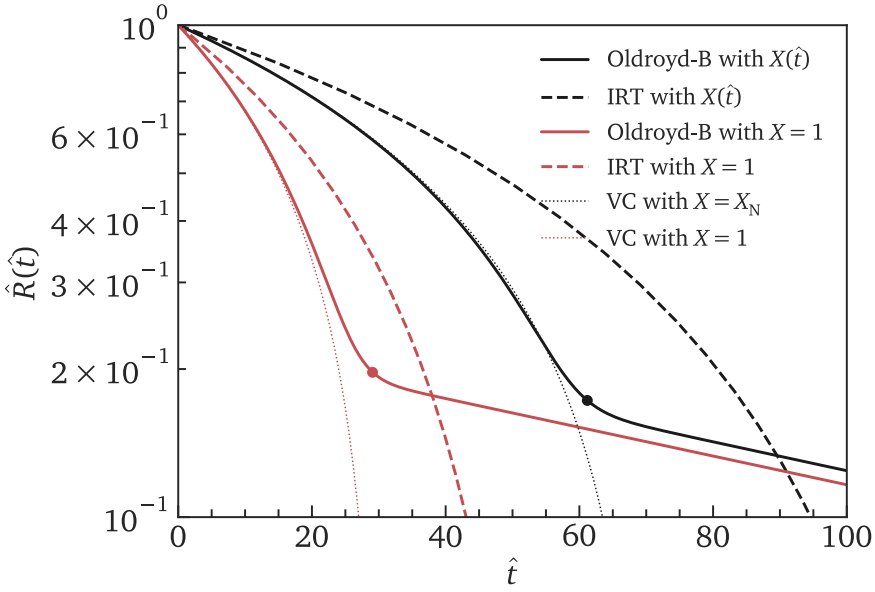

Figure 3-15: Temporal evolution of the mid-plane filament radius predicted by the Oldroyd-B model with $X = X(\hat{t})$ according to Equation (3.47) (black solid line) and $X = 1$ (red solid line) for $\mathrm{Oh_S} = 5$, $\hat{\lambda} = 50$ and $\hat{\eta}_P = 1$; the IRT model with $X = X(\hat{t})$ according to Equation (3.44) (black dashed line) and $X = 1$ (red dashed line) with the constitutive parameters defined in Equation (3.48); visco-capillary thinning with $X = X_N$ (black dotted line) and $X = 1$ (red dotted line). The markers denote the time when $3\eta_S\dot{\epsilon} = N_{1,P}$ for two prediction lines from the Oldroyd-B model (black: $X = X(\hat{t})$; red: $X = 1$).

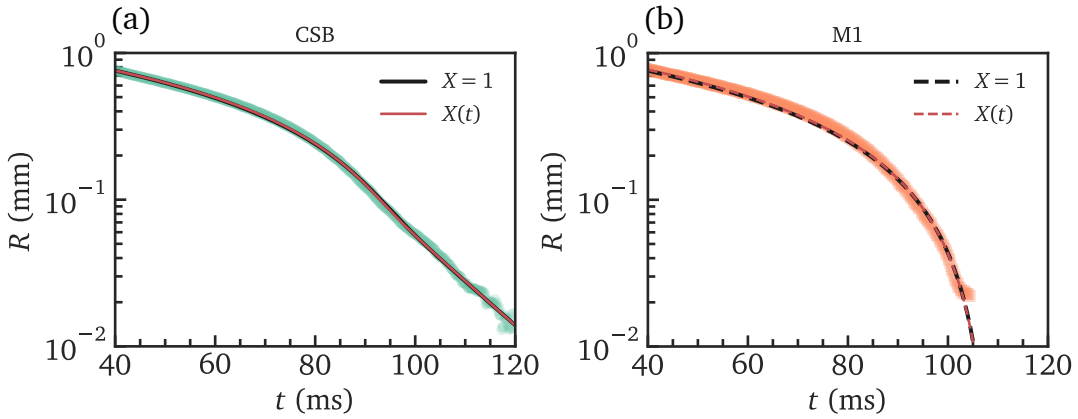

Figure 3-16: Filament thinning profiles for (a) CSB and (b) M1 motor oils fitted with their best-fit models (CSB: Oldroyd-B; M1: IRT) based on cylindrical filament assumptions ($X = 1$, black lines) and temporally-evolving geometric correction factors ($X(t)$, red lines).

Table 3.8: Estimates of the zero-rate viscosities extracted from steady-shear flow measurements and fitting the filament thinning profiles with the best-fit models based on cylindrical filament assumptions ($X = 1$) and temporally-evolving geometric correction factors. Values in parentheses show error percents compared with the measurements in shear flow.

Materials	Best-fit models	Estimates of the zero-rate viscosities (Pa s)		
		η (Steady-shear)	η_0 ($X = 1$)	η_0 ($X(t)$)
CSB	Oldroyd-B	0.132 (-)	0.236 (78.8%)	0.134 (1.5%)
M1	IRT	0.142 (-)	0.290 (104.2%)	0.147 (3.5%)

Finally, to show the significance of a temporally-evolving geometric correction factor in extracting accurate constitutive parameters from the CaBER measurements, results from the two motor oils as shown in Section 3.2.1 are revisited. To be more specific, the CaBER measurements in Figure 3-4 are refitted with the predictions using temporally-evolving geometric correction factors. As shown in Figure 3-16, the filament thinning profiles from CaBER measurements for the CSB and M1 motor oils are fitted with the Oldroyd-B model (solid lines) and the IRT model (dashed lines), respectively, which correspond to the best-fit models for each fluid sample. Predictions by the same constitutive models using temporally-evolving geometric correction factors based on Equation (3.47) and 3.44 are plotted in red, which overlap with the solutions based on cylindrical assumptions using $X = 1$ (black lines), and both fitting lines agree with the experimental data very well. However, the extracted zero-rate viscosities as tabulated in Table 3.8 are distinct in values as the geometric correction factor becomes temporally-evolving. Comparing with independent steady-shear flow measurements, only the predictions based on temporally-evolving geometric correction factors result in accurate measurements of the zero-rate viscosities from both constitutive models, while retaining the rate-dependent contributions in the constitutive equation. From the fitting results in Figure 3-16, it can be concluded that accurate constitutive parameters can only be extracted with correct evaluations of the geometric correction factor, in spite of apparent agreement in the fitted filament thinning profiles.

3.3 Statistics-based protocol for model selection

The increased rheological complexity observed in many material systems, including nanocomposites, motivates the important topic of modeling selection in the capillary breakup extensional rheometry. As prerequisite of the data fitting process, the best-fit constitutive model, featured with sufficiently high fitting accuracy to the experimental data as well as a well-regularized set of fitting parameters, is key to the extraction of valid extensional rheological parameters from the measured filament thinning dynamics. This idea has been briefly discussed in Section 3.2, where the weakly rate-thickening behavior is distinguished from the strongly viscoelastic response through a constraint on the elasto-capillary number. However, this constraint, as is derived from the phenomenological observations of filament thinning dynamics, is not readily extended to other constitutive models. In addition, the statistical ambiguity in this criterion brings unwanted subjectivity to the model selection and the subsequent data fitting. To address this limitation, a statistics-based protocol is proposed in this section that enables a robust selection of the best-fit model (BFM) from a library of constitutive

equations. The proposed protocol, without the introduction of additional parameters, has the potentials to accelerate and automate the data processing that may constitute a high throughput technique for extensional rheological characterizations.

Figure 3-17 shows the overall flowchart of the proposed protocol, which is comprised of four main steps. First, the filament thinning profiles of a fluid sample are measured by the capillary breakup extensional rheometer. During the capillarity-driven thinning process, the temporal evolution of the minimum filament radius $R(t)$ is captured by a high-speed optical transducer (*e.g.*, high-speed camera, or laser micrometer). With an independent measurement of the fluid surface tension, the filament radius evolution $R(t)$ can be fitted into the predictions from a number of candidate constitutive models, and the corresponding model parameters can be extracted. In the fitting process for each constitutive model, a non-trivial geometric correction factor X must be incorporated to obtain accurate constitutive parameters. If multiple stress contributions are identified from the constitutive equation, this geometric correction factor will still be expected to be time-varying, and can be simply expressed as a linear interpolation based on the magnitude of each stress contribution, as exemplified in Equation (3.44) for the IRT model. The asymptotic solutions of X governed by each individual stress contribution can be obtained through full-dimensional analysis of the filament thinning profiles, if necessary. Finally, each candidate model is assigned with a single metric that incorporates both the regression errors and the model regularization, from which the best-fit model (BFM) and the constitutive parameters can be readily selected. In the proposed protocol, the parameter-free Bayesian information criterion (BIC) is applied, which is defined [256] as

$$\mathrm{BIC} \equiv \ln(n)N_\theta - 2\ln(\bar{L}), \tag{3.49}$$

where n is the number of datapoints in an experimental dataset $\{x_i, y_i\}$ $(i = 1, 2, ..., n)$. In the fitting process, there are $N_\theta = N_f + 1$ parameters, where $\theta = \{p_1, p_2, ..., p_{N_f}, \sigma^2\}$. Here, $\{p_j\}$ $(j = 1, 2, ..., N_f)$ are N_f constitutive parameters, and σ^2 is the variance as an additional fitting parameter. The dataset $\{x_i, y_i\}$ is fitted into the constitutive equation $f(x; \{p_1, p_2, ..., p_{N_f}\})$ with N_f parameters. In practice, the system output $Y(x)$ as a random variable is assumed to follow a Gaussian distribution with a mean value of $f(x; \bar{\theta})$ and a variance of $\bar{\sigma}^2$, where the best estimator (with the bar notation) of the model parameters $\bar{\theta} \equiv \{\bar{p}_1, \bar{p}_2, ..., \bar{p}_{N_f}, \bar{\sigma}^2\}$ is calculated by maximizing the likelihood function $L \equiv p(\{y_i\}|\theta)$ such that

$$\bar{\theta} \equiv \arg\max[p(\{y_i\}|\theta)]. \tag{3.50}$$

A common form of the likelihood function $L = p(\{y_i\}|\theta)$ is derived from least square

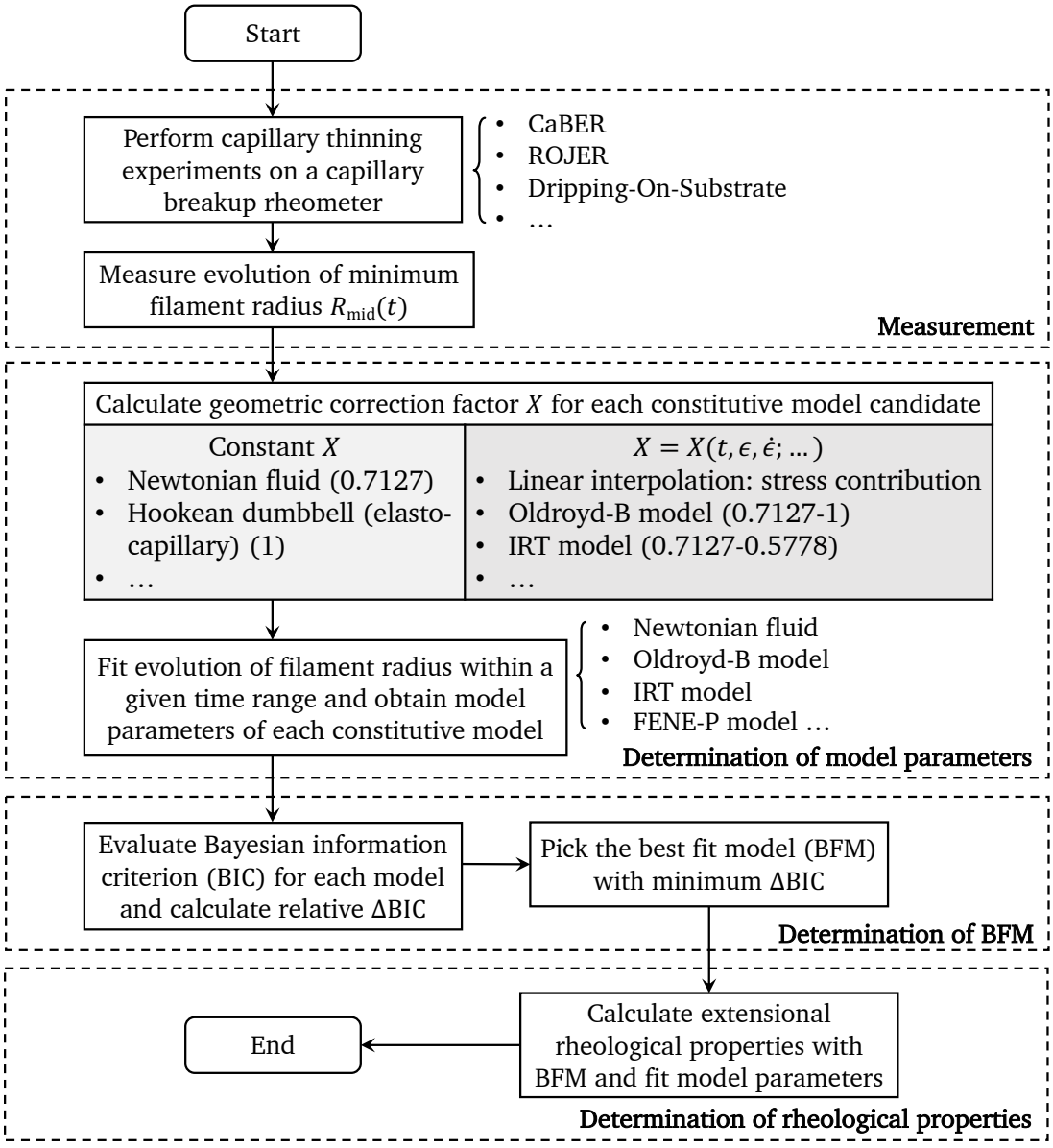

Figure 3-17: Flowchart of the statistics-based protocol to select the best-fit model (BFM) for the data fitting and extraction of the constitutive parameters from the measured filament thinning profiles.

regression (LSR), where a logarithmic form of L is expressed as

$$\ln[L(\{x_i, y_i\}; f; \theta)] = -\frac{n}{2}\ln(2\pi) - \frac{n}{2}\ln(\sigma^2) - \frac{1}{2\sigma^2}\sum_{i=1}^{n}\left[y_i - f(x; \{p_1, p_2, ..., p_{N_f}\})\right]^2. \tag{3.51}$$

The best estimator of model parameters $\bar{\theta}$ and the maximum value of the likelihood function L can be obtained by letting $\nabla \ln L = 0$, and solving the corresponding N_θ equations. Consequently, the best estimator of the variance $\bar{\sigma}^2$ can be expressed as

$$\bar{\sigma}^2 = \frac{1}{n}\sum_{i=1}^{n}\left[y_i - f(x;\{\bar{p}_1,\bar{p}_2,...,\bar{p}_{N_f}\})\right]^2. \tag{3.52}$$

Finally, the magnitude of BIC can be calculated as

$$\mathrm{BIC}(n,N_f,\bar{\sigma}^2) = \ln(n)(N_f+1) + n[\ln(2\pi)+1] + n\ln(\bar{\sigma}^2), \tag{3.53}$$

which provides an appropriate metric in the absence of additional parameters to evaluate the "fitness" of a constitutive model candidate with an optimal balance between the fitting accuracy ($\bar{\sigma}^2$) and the number of constitutive parameters (n and N_f). The best-fit model can be selected as the one with the minimum value of BIC.

This proposed protocol is subsequently validated by applying to the experimental measurements from a number of selected material systems at 25 °C: glycerol, aqueous PEO solution ($M_w \approx 5$ MDa; Sigma-Aldrich, USA) and polyisobutylene (PIB) ($M_w \approx 1$ MDa; Sigma-Aldrich, USA) solutions in hexadecane (C16; Sigma-Aldrich, USA). All samples used for validation are summarized in Table 3.9.

Table 3.9: Selected material systems to validate the proposed statistics-based protocol for the selection of the best-fit constitutive model among the Newtonian fluid (N), the Oldroyd-B model in the elasto-capillary limit [O-B (EC)], the IRT model and the Oldroyd-B (O-B) model. Models with the minimum values of BIC are marked in gray.

Materials	c	BIC				Figure
	(wt%)	N	O-B (EC)	IRT	O-B	
Glycerol	-	−1696.77	−506.73	−1658.15	−1685.81	3-18(a)
PEO/Water	0.20	−1464.43	−5823.78	−3580.58	−5104.50	3-18(b)
PIB/C16	6.47	−8695.37	−5431.68	−18 244.84	−16 578.83	3-18(c)
PIB/C16	4.07	−768.64	−2651.67	−2325.62	−4495.58	3-18(d)

The capillarity-driven dynamics of the four material systems are measured using the customized CaBER system introduced in Section 3.1 with an identical geometrical and stretch configuration as in the measurements for the two motor oils (Table 3.2). As shown in Figure 3-18, the measured filament radius is plotted separately for each

sample in four subplots. Four models are selected to fit the experimental data for $t > t_M = 30\,\text{ms}$ (t_M is specified in the CaBER software): the Newtonian fluid model (Equation (2.17); dotted line), the Oldroyd-B model in the elasto-capillary limit (Equation (2.18); dotted dashed line), the IRT model (Equation (3.7); dashed line) and the Oldroyd-B model (Equation (3.2); solid line). For the latter two models, a time-varying geometric correction factor is applied following Equation (3.44) and Equation (3.47), respectively. In the calculation of BIC in Equation (3.53), a logarithmic form of the filament radius is used for regression (*i.e.*, $y_i = \ln(R_i)$) to generate an unbiased fitting regardless of the magnitude of the filament radius. This transform arises from Equation (3.9), in which the (apparent) extensional viscosity is independent of the filament radius. Accordingly, all subplots of Figure 3-18 are plotted with the radius R on a logarithmic scale to better visualize the fitting errors. The corresponding values of BIC for each sample and constitutive model are calculated and reported in Table 3.9, in which the minimum value of BIC is highlighted in gray.

The four material systems are selected such that each of the four model candidates is justified as the BFM for one material. By comparing the fitting curves from the BFM and the other model candidates in Figure 3-18, the proposed statistics-based criterion provides accurate guidance in selecting the BFM with a sufficiently regularized set of parameters. This is evidently demonstrated for glycerol (which is well-known to behave as a Newtonian fluid) in Figure 3-18(a), where the Newtonian model outperforms the IRT model and the Oldroyd-B model in the value of BIC with the application of a smaller number of parameters, despite that fitting from the latter two models appears to be identically consistent, if not better, with the experimental data. This principle of parsimony is also visualized in Figure 3-18 for an aqueous PEO solution with a relatively large molecular weight, in which the elasto-capillary balance dominates almost the entire lifetime of the filament thinning, and the Oldroyd-B model in the elasto-capillary limit is conceivably the best choice. When multiple stress contributions are involved in the capillarity-driven thinning for PIB/hexadecane solutions, the criterion using BIC enables us to distinguish the two complex models fairly well. As the concentration of PIB decreases from 6.47 wt% (Figure 3-18(c)) to 4.07 wt% (Figure 3-18(d)), the best-fit model (BFM) switches from the IRT model to the Oldroyd-B model by virtue of an enhanced contribution from the elasto-capillary balance. This result is in excellent agreement with the rheology-based criterion of Equation (3.14), where the elasto-capillary numbers $\text{Ec}_{\text{V-E}}$ for the two samples can be calculated as 3.6 (6.47 wt%) and 7.8 (4.07 wt%), respectively, and lie on both sides of the critical value of $\text{Ec}^*_{\text{V-E}} = 4.7$.

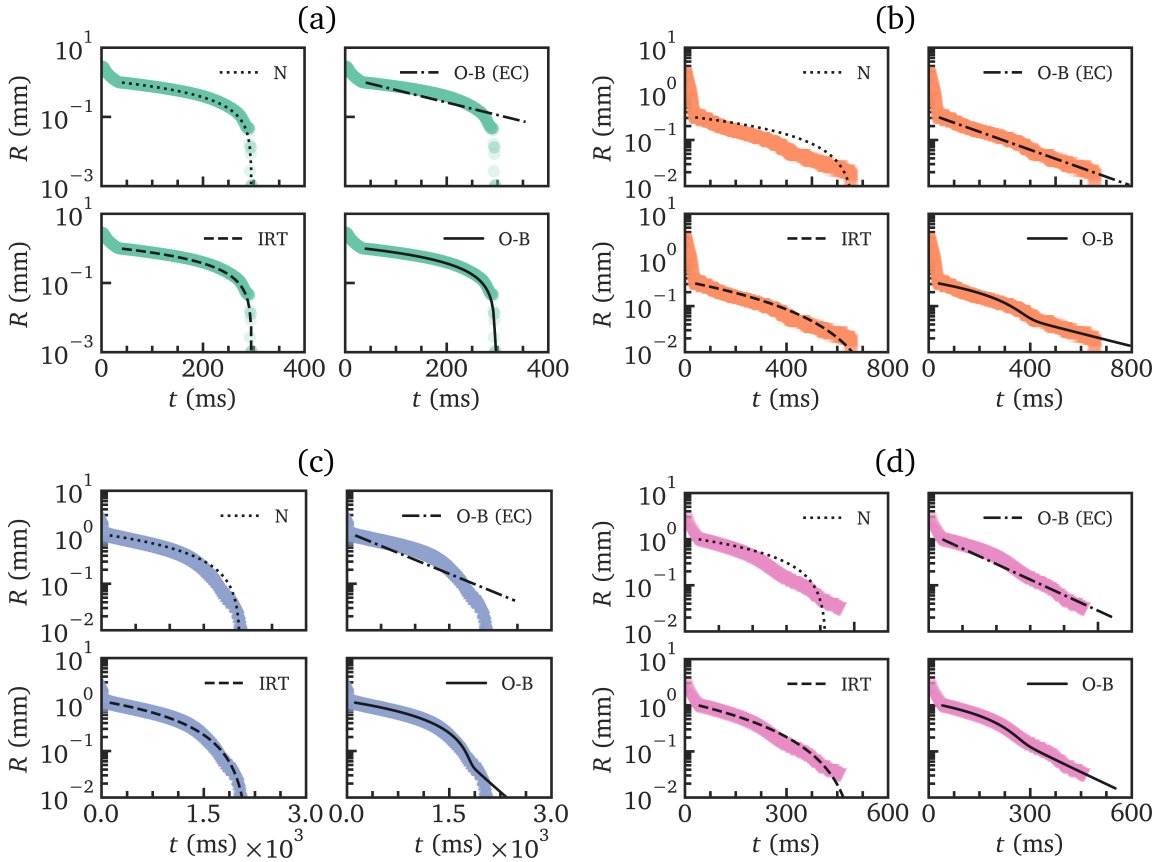

Figure 3-18: Evolution in the measured minimum filament radius for the four material systems: (a) Glycerol; (b) PEO/Water (0.20 wt%); (c) PIB/C16 (6.47 wt%); (d) PIB/C16 (4.07 wt%). In each subplot, the identical experimental data are fitted with four selected constitutive models: the Newtonian fluid model (dotted line), the Oldroyd-B model in the elasto-capillary limit (dotted dashed line), the IRT model (dashed line) and the Oldroyd-B model (solid line).

3.4 Summary

This chapter explored the extensional rheological characterization measured by capillary breakup techniques for a variety of material systems, in which the filament thinning dynamics are governed by multiple stress contributions. Typical material systems include polymer solutions with highly viscous solvents or weakly elastic behavior due to small polymer molecular weights or concentrations. Distinct evolution of the stress contributions gives rise to a multi-stage filament thinning profile, and the asymptotic

solutions based on single stress contributions from previous studies are not sufficient to describe the whole filament thinning dynamics accurately.

To progressively construct a theoretical framework and propose a measuring protocol for such complex filament thinning dynamics, this chapter constitutes a series of experimental and numerical studies on two constitutive frameworks, namely, the IRT model for weakly rate-thickening fluids, and the Oldroyd-B model for strongly viscoelastic fluids. These models provided accurate rheological characterizations for two selected synthetic motor oils with subtle but critical rate-thickening behavior attributed to the low-concentration polymer additives. In light of the "waxing and waning" of comparable stress contributions to the filament thinning dynamics from each term in the constitutive equation, a temporally evolving geometric correction factor $X(t)$ was incorporated in the data processing. The numerical calculations from the two constitutive models justified the use of a linearly interpolated form of the geometric correction factor $X[\boldsymbol{\sigma}(t)]$ as a function of the magnitude of each stress contribution to accurately describe the transition of different asymptotic solutions. Revisiting the CaBER measurements of the two motor oils shows the necessity of applying temporally-evolving geometric correction factors to obtain accurate constitutive parameters. Finally, a practical measuring protocol for the selection of a parsimonious best-fit model was proposed based on the Bayesian information criterion (BIC). This protocol was demonstrated to identify consistent constitutive relations with the previously-proposed rheology-based criterion using a critical elasto-capillary number $\mathrm{Ec}^{*}_{\text{V-E}} = 4.7$ for a selected range of fluid samples, from which accurate constitutive parameters were obtained to exhibit their different degrees of viscoelasticity.

The models and measuring protocols proposed in this chapter provide valuable insights into understanding the complex extensional rheology of fluids with multiple significant stress contributions that are likely to arise from different material phases or length scales. In Chapter 4, a multi-stage filament thinning profile reappears for concentrated polymer solutions, the dynamics of which can be characterized by comprehensive constitutive equations based on tube models. It will be shown later that the extensional rheology of GDNC materials can also be accurately described by these tube models as a result of the dynamics governed by the interactions between the polymer matrix and the nanofillers over a broad spectrum of length and time scales. All of these calculations are based on the protocols proposed in this chapter for accurate data processing and analysis.

This page is intentionally left blank.

4 | Extensional Rheology of Entangled Polymer Systems

4.1 Entangled polymer solutions

4.1.1 Tube models and reptation theory

The constitutive models in the previous chapter provide phenomenological descriptions of a polymer solution dissolved in a viscous Newtonian solvent that exhibits rate-thickening phenomena in extensional flow. Nonetheless, a direct application of such models to the nanocomposite system is hampered with additional challenges. First, common polymer matrices are in the state of melts or entangled solutions with high polymer concentrations. Strong intermolecular interactions between the polymer chains result in more complex microstructural dynamics that lead to distinct relaxation mechanisms over a wide range of time- and lengthscales during the material deformation, processing and manufacturing [196,249]. Consequently, most entangled polymer systems exhibit strongly nonlinear rheological behavior, such as rate-thinning viscosities, stress overshoots following step strains, and onset of transient elastic instabilities [249]. In addition, the graphene-derived nanofillers in the GDNC systems further contribute to the rheological complexity of bulk nanocomposites in a variation of enhanced polymer-filler and filler-filler interactions due to the increased surface area, as well as a flow-induced anisotropy due to the nanofiller reorientation [17, 19, 196]. These additional complexities arising from multiple stress contributions are likely to induce a broader relaxation time spectrum, as well as a non-monotonic extensional viscosity with the strain or strain rate.

The filament thinning dynamics of polymer solutions in the semi-dilute or entangled regimes have been an ongoing topic with a handful of experimental studies [32, 199, 200, 257] that cover a variety of material systems, including aqueous polyethylene

oxide (PEO), polystyrene (PS), hydroxyethyl cellulose (HEC), and wormlike micelle solutions. In these studies, a common pattern in the filament thinning profile is identified when the concentration increases beyond the entangled threshold, which deviates notably from the elasto-capillary thinning behavior [208, 209]. Observations reveal two unique features in the measured extensional rheological behavior in the entangled regime. First, the extensional relaxation time λ_e fitted from an exponential decay of the filament radius is evidently smaller than that independently extracted in shear flow (λ_s), and the ratio of the two relaxation times λ_e/λ_s is found to decrease at higher concentrations. Arnold et al. [200] has suggested the use of a damping function in the K-BKZ form of the constitutive equation to reconcile the different relaxation times in shear and extensional flows. However, additional fitting parameters are introduced in the fitting process, and it remains unclear if these parameters are robust to material and concentration variations due to the absence of a clear physical interpretation. Secondly, the evolution of the mid-plane filament radius in the entangled regime progressively shifts away from an exponential decay expected for a dilute polymer solution [201] towards a power-law relation with the time to filament breakup $\tau = t_C - t$ [32]. This power-law trend concomitantly results in a transient extensional viscosity that decreases with an increased strain rate. Phenomenological inelastic models have been proposed by previous studies to fit the filament thinning profiles in this regime [32, 258]. However, the microstructural origin of this rate-thinning trend has not been considered in depth, and a physical model that incorporates the evolution of polymer conformation inside the material element is lacking, hampering the extraction of accurate constitutive parameters from the measured filament thinning response.

To introduce a comprehensive modeling framework that incorporates the structural information in an entangled polymer system, extensive efforts have been made from previous studies to characterize their rheological complexity [249, 259]. Significant progress has been witnessed since the milestone work of the reptation theory, which provides a coarse-grained canonical framework to understand the dynamical response of interactive polymer chains [260]. In the reptation theory, each polymer chain is fully or partially confined by surrounding polymer chains in a mean-field imaginary tube. The entangled chains interact with each other at their topological crossovers, or entanglements, which form geometrical constraints that inhibit the transverse motion of a single chain and only allow for diffusive motion, or "reptation," along the imaginary tube with a significantly reduced diffusivity [261, 262]. This low diffusivity in the tube results in a conceivable slowdown in the polymer chain relaxation. Based on this concept, Doi and Edwards [263] proposed a full-dimensional constitutive model for monodisperse entangled linear polymers derived from the Lodge rubberlike liquid [136]. In the original Doi-Edwards (DE) model, the tube segments are reoriented

in the flow direction based on the "independent alignment approximation (IAA)." Under this assumption, the bulk stress originates from an affine transformation of the tube segments instead of the tube stretch [197]. The primitive chains between entanglements are simplified as rigid rods. This approximation only applies to an intermediate strain-rate range of $1/\lambda_D \leq \dot{\gamma} \ll 1/\lambda_R$ in the stress relaxation process [196]. Here λ_R is the Rouse time quantifying the duration of retraction for a single polymer chain in the tube, and λ_D is the disengagement time characterizing the time in which a single polymer chain reptates out of its constraining tube. These two timescales are related through a geometrical description of the entanglements [30] as

$$\lambda_D = p(Z)\lambda_R = p(Z)\frac{\xi_0(Nb)^2}{6\pi^2 kT}, \tag{4.1a}$$

$$p(Z) = 3Z\Big(1 - \frac{3.38}{\sqrt{Z}} + \frac{4.17}{Z} - \frac{1.55}{Z^{3/2}}\Big), \tag{4.1b}$$

where the Rouse time λ_R is defined explicitly as a function of the monomeric friction coefficient ξ_0 and the statistical contour length of (Nb) [249]. $Z = M/M_e$ is the number of entanglements per polymer chain [264]. M and M_e are the molecular weights of a single polymer chain and that between entanglements, respectively. The form of the function $p(Z)$, the ratio of λ_D and λ_R is a truncated Taylor expansion of $Z^{-1/2}$ that has been numerically calculated by Likhtman and McLeish [30] to incorporate the effects of contour length fluctuation (CLF) in polymer chains with realistic finite lengths and the number of entanglements.

The DE model successfully captures a number of key rheological features for a variety of entangled polymer systems, such as a molecular-weight independent storage modulus, a non-trivial second-order normal stress difference in steady shear flow and strain-softening behavior at long time in a step-strain experiment at large strains [264, 265]. However, this model is well-known to produce an underestimated scaling of the zero-shear viscosity with the molecular weight, $\eta_0 \propto M^3$, compared with $\eta_0 \propto M^{3.4}$ from experiments [249]. In addition, excessive levels of rate-thinning are predicted in both steady shear and extensional flows that lead to flow instabilities [197, 264]. Subsequent studies have attributed these deficiencies to the absence of two critical non-reptative contributions to this chain dynamics in the DE model: (i) a finite rate of chain retraction at short timescales or at high strain rates (*i.e.*, when $t < \lambda_R$ or $\lambda_R\dot{\gamma} > 1$), and (ii) convective constraint release over intermediate to long timescales of a relaxation process (*i.e.*, $t > \lambda_D$ or $1/\lambda_D < \dot{\gamma} < 1/\lambda_R$) [266]. These deficiencies have been addressed by a number of more sophisticated constitutive models based on the underlying micro-mechanical framework derived from the reptation theory, includ-

ing the Doi-Edwards-Marrucci-Grizzuti model [266], the GLaMM model [267] and the Rolie-Poly model [268].

To bridge the theoretical gap in describing the filament thinning dynamics of entangled polymer solutions, two representative microstructural-based constitutive models are selected, both of which are derived from reptation theory but differ slightly in the non-reptative mechanisms that are included. Their capillarity-driven thinning dynamics are numerically calculated based on the assumption of a cylindrical filament ($\partial_z R = 0$ and $\partial_{zz} R = 0$) to simplify the calculation. In the remainder of this section, the resulting evolution of the mid-plane filament radius predicted by both models is shown to exhibit a shared complex three-stage sequence governed by the tube reorientation, the polymer chain stretching and ultimately the finite extensibility of single polymer chains, respectively. The asymptotic solutions for filament thinning evolution at each stage are calculated analytically, from which a non-trivial expression for the ratio of apparent shear and extensional relaxation times is obtained. The application of the selected tube models is subsequently justified by comparing with the experimental data from a variety of polymer systems reported in previous studies, and a general agreement is observed in both shear and extensional rheological responses without introducing any additional fitting parameters. Finally, a dimensional analysis of the filament thinning profiles for aqueous polyethylene oxide (PEO) solutions with varying concentrations is presented below, at and above the entangled concentration threshold. The close similarity of the predicted filament thinning profiles to the previously published experimental data provides additional physical insights into the capillarity-driven thinning for an expanded variety of complex nanocomposite systems.

Doi-Edwards-Marrucci-Grizzuti (DEMG) model

Marrucci and Grizzuti [266] modified the DE model by introducing an additional relaxation process characterized by the Rouse time λ_R to describe the chain stretch of flexible polymers, in conjunction with the tube reorientation and chain reptation characterized by the disengagement time λ_D. This new relaxation process only becomes evident at high strain rates when $\lambda_R \dot{\gamma} \sim O(1)$ [269], and quantifies the stretching of polymer chains along its primitive path length within an orientated tube segment. Pearson et al. [270] proposed a closed differential form of the constitutive equation for the DEMG

Table 4.1: Nondimensionalization scheme for the numerical analysis of capillarity-driven thinning dynamics for the selected tube models.

Type	Definitions
Kinematics and time	$\hat{R} \equiv \dfrac{R}{R_0} = \dfrac{R}{R(0)}$, $\hat{t} \equiv \dfrac{t}{\lambda_{\mathrm{R}}}$
Operators	$\partial_{\hat{t}} \equiv \lambda_{\mathrm{R}} \partial_t$, $\partial_{\hat{z}} \equiv R_0 \partial_z$
Dimensionless constitutive parameters	
Weissenberg number	$\mathrm{Wi} \equiv \lambda_{\mathrm{R}} \dot{\epsilon}$, $\mathrm{Wi}_{\mathrm{D}} \equiv \lambda_{\mathrm{D}} \dot{\epsilon}$
Intrinsic elasto-capillary number	$\mathrm{Ec}_0 \equiv \dfrac{G_{\mathrm{N}} R_0}{\Gamma}$

model as

$$\overset{\triangledown}{\boldsymbol{S}} = -2(\boldsymbol{\nabla v}^{\mathrm{T}} : \boldsymbol{S})\boldsymbol{S} - \frac{1}{\lambda_{\mathrm{D}} \Lambda^2}(\boldsymbol{S} - \frac{1}{3}\boldsymbol{I}), \tag{4.2a}$$

$$\dot{\Lambda} = (\boldsymbol{\nabla v}^{\mathrm{T}} : \boldsymbol{S})\Lambda - \frac{f(\Lambda)}{\lambda_{\mathrm{R}}}(\Lambda - 1), \tag{4.2b}$$

$$\boldsymbol{\sigma} = 3G_{\mathrm{N}} f(\Lambda)\Lambda^2 \boldsymbol{S}. \tag{4.2c}$$

In Equation (4.2), $\boldsymbol{S}$ is the averaged tube orientation tensor, which is the ensemble average of the end-to-end vector for each tube segment. The scalar Λ describes the ensemble strain imposed on the polymer chain segments within the tubes. The notation of "$\triangledown$" is the upper-convected derivative as defined on page 77, and $\boldsymbol{\nabla v}$ is the velocity gradient tensor.

The finite extensibility factor for a single polymer chain $f(\lambda)$ is given by the inverse Langevin function, which can be written in a single explicit form using Cohen's Padé approximation [271] as

$$f(\Lambda) = \frac{1 - 1/\Lambda_{\mathrm{m}}^2}{3 - 1/\Lambda_{\mathrm{m}}^2} \cdot \frac{3 - \Lambda^2/\Lambda_{\mathrm{m}}^2}{1 - \Lambda^2/\Lambda_{\mathrm{m}}^2}, \tag{4.3}$$

where Λ_{m} describes the maximum polymer extensibility which scales with square root of the molecular weight, $M^{1/2}$. From Equation (4.2)(a), evolution of the averaged tube orientation tensor $\boldsymbol{S}$ is a result of the interplay between the imposed convective flow

and the decay in the tube segment orientation characterized by the disengagement time λ_D. By definition, the averaged tube orientation tensor is constrained by $\mathrm{tr}\,\boldsymbol{S} \equiv 1$ and $\boldsymbol{S} : \boldsymbol{S} \leq 1$. When $\boldsymbol{S} = \boldsymbol{I}/3$, the tube segments are randomly oriented [266].

For mathematical simplicity, a nondimensionalizing scheme can be applied as shown in Table 4.1 using the initial filament radius R_0 and Rouse time λ_R. An intrinsic elasto-capillary number specific to the tube models is defined as $\mathrm{Ec}_0 \equiv G_N R_0/\Gamma$. Noticeably, an identical notation has been defined in the previous sections for the IRT model and the Oldroyd-B model, which slightly differs in the definition. Nonetheless, both expressions retain a similar physical interpretation in which the elasto-capillary timescale is nondimensionalized by the specified characteristic timescale. Notably, in tube models the zero-shear viscosity $\eta_0 = G_N \lambda_D$. The expression for Ec_0 can be rewritten as $\mathrm{Ec}_0 \sim (\eta_0 R_0/\Gamma)/\lambda_D$, where the numerator denotes the elasto-capillary timescale[1] as a function of the plateau modulus G_N.

The stress balance equation can be expressed in dimensionless form as

$$\frac{1}{\hat{R}} = 3\mathrm{Ec}_0 f(\Lambda)\Lambda^2 \Delta S, \tag{4.4}$$

where $\Delta S \equiv S_{zz} - S_{zz}$ is the magnitude of the tube alignment calculated from the difference between the zz- and rr-components of the tube reorientation tensor, and Ec_0 is the intrinsic elasto-capillary number defined in the foregoing Table 4.1. Because of the axisymmetric filament shape and the irrotational nature in the extensional flow, the rr- and $\theta\theta$-components of the reorientation tensor are identical in magnitude. Therefore, the trace of the reorientation tensor satisfies $\mathrm{tr}\,\boldsymbol{S} = S_{zz} + 2S_{rr} \equiv 1$, and the governing equation for the temporal evolution of ΔS can be rewritten in a simpler form as

$$\partial_{\hat{t}} \Delta S = \mathrm{Wi}(\Delta S + 1) - 2\mathrm{Wi}\Delta S^2 - \frac{1}{p(Z)\Lambda^2}\Delta S. \tag{4.5}$$

where the ratio of disengagement and Rouse timescales in Equation (4.5), $p(Z) = \lambda_D/\lambda_R$, can be expressed as a function of the number of entanglements per polymer chain Z according to Equation (4.1).

[1] Admittedly, this elasto-capillary timescale is expressed in the form of a visco-capillary timescale as defined in the vicinity of Equation (3.12). Such inconsistency, however, does not compromise the validity of the elasto-capillary claim because the scaling relation between the shear viscosity and $G_N\lambda_D$ only applies to small Weissenberg numbers (Wi_D) and can be treated as an asymptotic solution only. The definition of Ec_0 in Table 4.1 is also widely accepted in the rheological study of polymer solutions [178, 237, 272], hence is retained by convention.

Rolie-Poly (RP) model

In addition to the finite rates of polymer chain stretching and retraction within the tube incorporated in the DEMG model, convective constraint release (CCR) has been recognized more recently as another critical non-reptative mechanism that substantially alters the non-linear rheology of entangled polymer systems in both steady and transient flows [249, 267, 273, 274]. This effect is manifested at an intermediate strain rate $\dot{\epsilon} > 1/\lambda_D$, when polymer chains disengage from the physically entangled network at a rate faster than the reptation due to the surrounding polymer molecules being convected away from the chain of interest in a strong flow field. To obtain a more comprehensive understanding of how CCR affects the capillarity-driven thinning dynamics, the more sophisticated Rolie-Poly (RP) model [268] is adopted and the resulting temporal evolution of the filament thinning profiles is compared with that obtained from the DEMG model. A specific form of the constitutive equation similar to Equation (4.2) is taken that separates the averaged tube reorientation and the polymer chain stretch [249] as

$$\overset{\triangledown}{\boldsymbol{S}} = -2(\boldsymbol{\nabla v}^{\mathrm{T}} : \boldsymbol{S})\boldsymbol{S} - \frac{1}{\Lambda^2}\left[\left(\frac{1}{\lambda_D} + 2\beta f(\Lambda)\frac{1-1/\Lambda}{\lambda_R}\Lambda^{\delta}\right)\left(\boldsymbol{S} - \frac{1}{3}\boldsymbol{I}\right)\right], \tag{4.6a}$$

$$\dot{\Lambda} = (\boldsymbol{\nabla v}^{\mathrm{T}} : \boldsymbol{S})\Lambda - \frac{f(\Lambda)}{\lambda_R}(\Lambda - 1) - \left(\frac{1}{\lambda_D} + 2\beta f(\Lambda)\frac{1-1/\Lambda}{\lambda_R}\Lambda^{\delta}\right)\frac{\Lambda^2 - 1}{2\Lambda}, \tag{4.6b}$$

$$\boldsymbol{\sigma} = 3G_N f(\Lambda)\Lambda^2 \boldsymbol{S}, \tag{4.6c}$$

where the notations for $\boldsymbol{S}$, λ and $\boldsymbol{\nabla v}$ are identical to those defined in Equation (4.2), and the Padé approximation for the inverse Langevin function $f = f(\Lambda)$ is evaluated according to Equation (4.3). The dimensionless coefficients of β and δ are two model parameters that quantify the magnitude of the CCR effect and the contribution of the polymer chain stretch to the CCR effect, respectively. Previous studies have suggested that $\beta = 1$ and $\delta = -0.5$ produce the best-fitting results to the full kinetic model over a wide range of shear rates [268, 273], and these values are inherited in the following calculation and asymptotic analysis.

Following the numerical procedure for the DEMG model, the differential equation for the temporal evolution of the magnitude of the averaged tube orientation $\Delta S \equiv S_{zz} - S_{rr}$ can be rewritten in a similar form as in Equation (4.5) with the addition of the CCR-related term as

$$\partial_{\hat{t}}\Delta S = \mathrm{Wi}(\Delta S + 1) - 2\mathrm{Wi}\Delta S^2 - \frac{1}{\Lambda^2}\left[\frac{1}{p(Z)} + 2\beta f(\Lambda)(1 - 1/\Lambda)\Lambda^{\delta}\right]\Delta S, \tag{4.7}$$

Table 4.2: Initial conditions based on the value of Ec_0 for the numerical calculation of the capillarity-driven thinning dynamics predicted by the selected tube models.

Condition for Ec_0	Boundary conditions
$\mathrm{Ec}_0 \geq \frac{1}{3}$	$S_{rr}(0) = \frac{1}{3}\left(1 - \frac{1}{3\mathrm{Ec}_0}\right)$, $S_{zz}(0) = \frac{1}{3}\left(1 + \frac{2}{3\mathrm{Ec}_0}\right)$, $\Lambda(0) = 1$
$\mathrm{Ec}_0 < \frac{1}{3}$	$S_{rr}(0) = 0$, $S_{zz}(0) = 1$, $f[\Lambda(0)]\Lambda(0)^2 = \frac{1}{3\mathrm{Ec}_0}$ (numerically solved)

where the time-varying Weissenberg number $\mathrm{Wi} \equiv \lambda_R \dot{\epsilon}$ has been defined previously, and the stress balance equation given by Equation (4.4) remains applicable.

4.1.2 Evolution of filament thinning profiles

Numerical calculations of the capillarity-driven thinning dynamics for the two selected tube models are performed for a range of representative material parameters. An initial condition of the reorientation tensor and the chain stretch is shown in Table 4.2 for both constitutive models separated by a critical value at $1/3$. This critical value of Ec_0 is selected when the tube segments approach a uniform orientation but the polymer chains remain unstretched ($\Lambda = 1$) according to Equation (4.4), and a more rigorous analysis and substantiation of this critical value will be shown shortly.

The filament radius $\hat{R}$, the magnitude of the tube reorientation $\Delta S = S_{zz} - S_{rr}$ and the chain stretch Λ predicted by both models (dashed line for DEMG model, and solid line for RP model) are plotted in Figure 4-1. Four intrinsic elasto-capillary numbers are selected that range from 0.1 to 2 to represent the initial conditions of Table 4.2, and the number of entanglements is fixed at $Z = 10$. The filament radius predicted by the two tube models shows similar trends, except that the RP model predicts a noticeably faster filament thinning (corresponding to a lower viscosity) due to the additional CCR effect. Figure 4-1 sets an especial focus on the early-thinning stage, and the polymer chain extensibility is presumed to only affect the filament thinning behavior close to the filament breakup. As a result, a generic condition is set for all curves as $\Lambda_m \to \infty$. By inspecting the temporal evolution of the filament thinning profiles at $\mathrm{Ec}_0 = 2$ (lines in amber), two distinct filament thinning regimes can be identified. At early times, the filament radius decays slowly (Figure 4-1(b)), and the magnitude of the tube reorientation ΔS increases progressively to unity ($0 \leq \hat{t} \lesssim 80$ in Figure 4-1(c)) in the ap-

proach to a uniform tube alignment towards the extensional direction (zz); the polymer molecules, however, remain broadly unstretched (Figure 4-1(d)). Once the magnitude of tube reorientation saturates to unity, the filament radius starts to decay in an exponential manner (Figure 4-1(a)). The filament dynamics in this exponential-thinning stage can be attributed to the dominance of polymer chain stretch that resembles the elasto-capillarity thinning in Equation (2.18). When $\mathrm{Ec}_0 = 1/10 < 1/3$ (lines in violet), the normal stress arising from the tube reorientation does not ever suffice to balance the driving capillary pressure at $t = 0$. As a result, a non-trivial initial polymer stretch $\Lambda(0) > 1$ is necessary to produce additional normal stress to counteract the driving capillary pressure, which can be numerically solved as specified in Table 4.2. Consequently, for $\mathrm{Ec}_0 \leq 1/3$, only the second exponential-thinning regime is manifested.

When plotted on a linear scale as shown in Figure 4-1(b), the temporal evolution of the filament radius exhibits a linear trend at $\hat{R} \gtrsim 0.4$ when Ec_0 is sufficiently large (in this case, $\mathrm{Ec}_0 \gtrsim 1$). Noticeably, the filament kinematics in this early-thinning regime are similar to those predicted by a Newtonian fluid [210]. In practice, a measure of the shear viscosity at low strain rates can be obtained from this linear decaying region assuming that the filament remains a cylindrical shape. This apparent shear viscosity η_{app} can be analytically calculated by imposing $\Lambda = 1$ in the constitutive equations (Equation (4.2) and Equation (4.6)) as

$$\eta_{\mathrm{app}} = \left(1 + \frac{1}{6\mathrm{Ec}_0} - \frac{2}{9\mathrm{Ec}_0^2}\right) G_{\mathrm{N}} \lambda_{\mathrm{D}}. \tag{4.8}$$

Equation (4.8) is further plotted against Ec_0 in Figure 4-2. In this figure, a threshold of $\mathrm{Ec}_0^* \equiv 8/(3 + \sqrt{297}) \approx 0.395$ can be identified when a positive apparent viscosity is expected. This condition is substantially consistent with the piecewise initial conditions as specified in Table 4.2, in which the filament thinning dynamics are solely dominated by the tube reorientation in the early thinning stage for a sufficiently large value of Ec_0. As Ec_0 increases, the apparent shear viscosity η_{app} approaches the zero-shear viscosity of $\eta_0 = G_{\mathrm{N}} \lambda_{\mathrm{D}}$ as expected for the selected tube models.

The exponential-thinning regime observed from the filament thinning profiles predicted by the selected tube models at an intermediate time, as shown in Figure 4-1(a) (*e.g.*, when $\mathrm{Ec}_0 = 1$ for $\hat{t} \gtrsim 35$), is reminiscent of the elasto-capillary thinning profile as stated in Equation (2.18). Nevertheless, it remains unclear if the relaxation process is identical to that expected for a dilute polymer system. To obtain an accurate measure of the extensional rheological properties from the capillarity-driven thinning dynam-

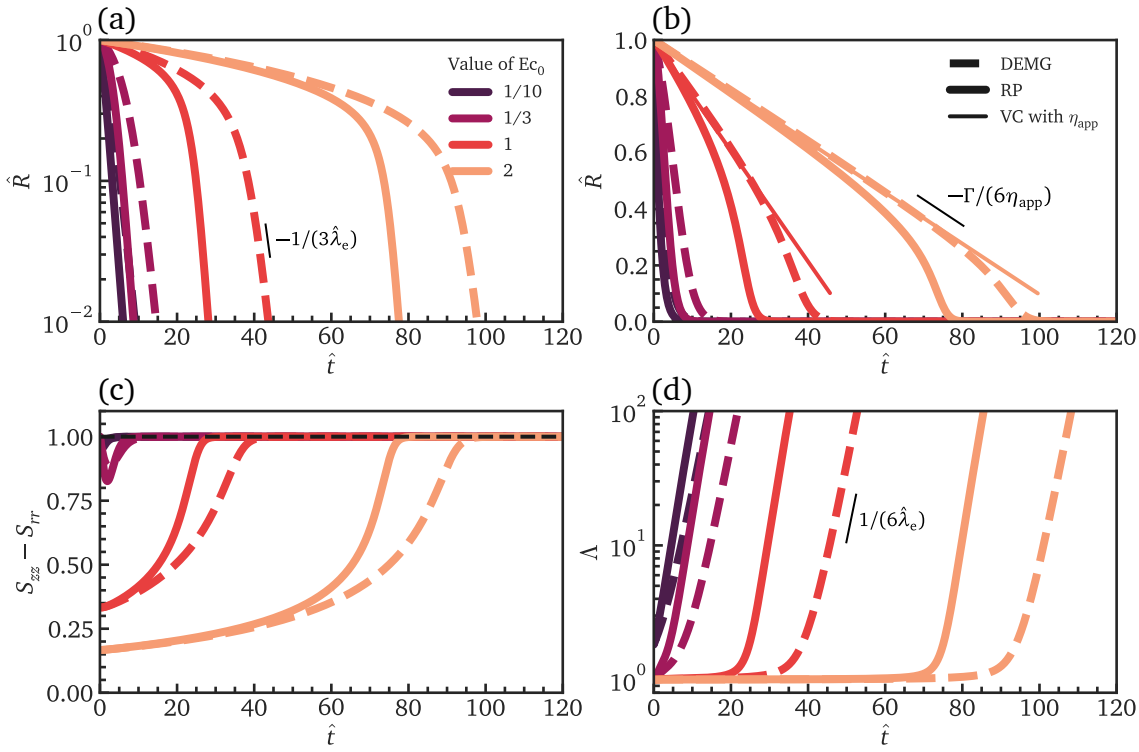

Figure 4-1: Temporal evolution of the capillarity-driven thinning dynamics predicted by the two selected models (dashed lines for DEMG model and solid lines for Rolie-Poly model) with varying intrinsic elasto-capillary numbers $\mathrm{Ec}_0 = 1/10$, $1/3$, 1 and 2 at a fixed number of entanglements per polymer chain, $Z = 10$ ($\lambda_\mathrm{D}/\lambda_\mathrm{R} = 8.97$). An infinite extensibility of the polymer chain ($\Lambda \to \infty$) is assumed to simplify the calculation. When $\mathrm{Ec}_0 > 1/3$, the filament thinning profiles are two-staged within the scope of the figures. (a) Dimensionless filament radius $\hat{R}$ plotted on a logarithmic scale. The slope of $-1/(3\hat{\lambda}_\mathrm{e})$ is identified close to the filament breakup. (b) Dimensionless filament radius $\hat{R}$ plotted on a linear scale. The thin solid lines correspond to the visco-capillary thinning using an apparent shear viscosity defined in Equation (4.8) for $\mathrm{Ec}_0 = 1$ and $\mathrm{Ec}_0 = 2$. (c) Magnitude of the tube reorientation ΔS. The black dashed line corresponds to $\Delta S = 1$, where a uniform tube orientation towards the extensional direction is induced. (d) Chain stretch Λ. An exponentially-increasing region is identified with a slope of $1/(6\hat{\lambda}_\mathrm{e})$ that corresponds to the region when the filament radius decays in an exponential trend.

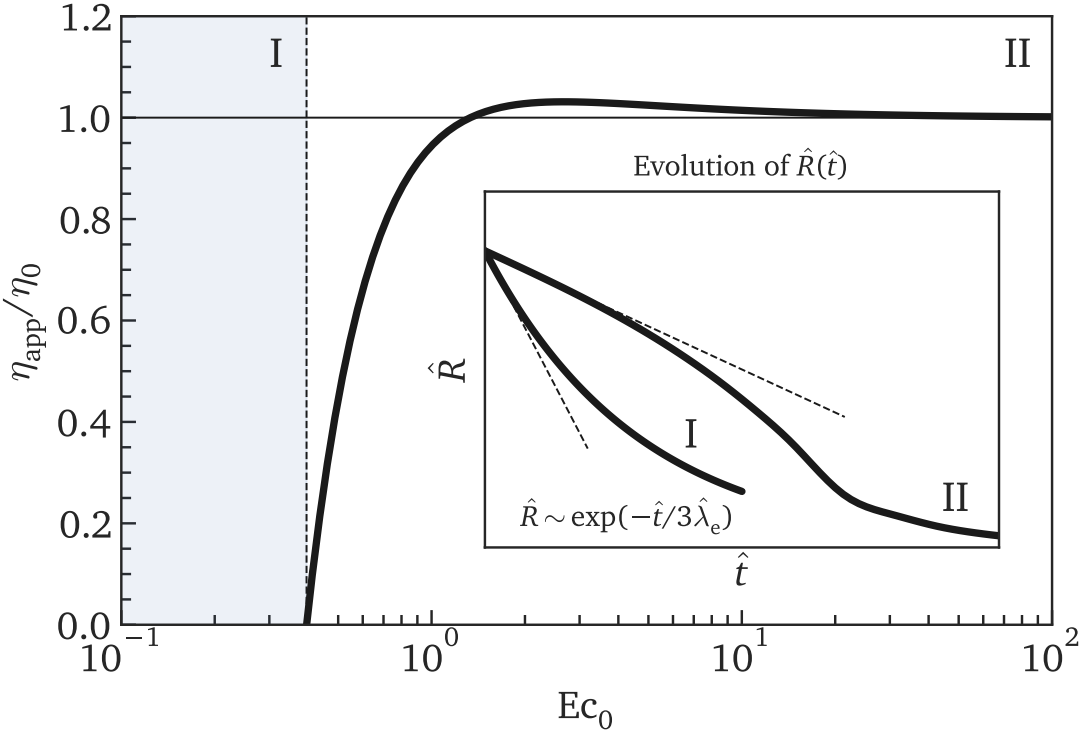

Figure 4-2: Apparent shear viscosity $\eta_{app}(\mathrm{Ec}_0)$ obtained from the filament radius with an apparent linear decay trend in the early thinning regime. A valid viscosity is obtained when $\mathrm{Ec}_0 \gtrsim \mathrm{Ec}_0^* = 0.395$ (thin dashed vertical line) in region II. As Ec_0 grows sufficiently large, the apparent shear viscosity approaches the zero-shear viscosity $\eta_0 = G\lambda_D$ predicted by both tube models (thin solid horizontal line). Insets: Schematic of the filament radius evolution with time for $\mathrm{Ec}_0 < \mathrm{Ec}_0^*$ (I) and $\mathrm{Ec}_0 \geq \mathrm{Ec}_0^*$ (II). The dashed lines are approximate reference lines where $\hat{R}$ decreases linearly with time.

ics, filament thinning profiles with varying finite extensibilities Λ_m are calculated with a fixed elasto-capillary number $Ec_0 = 1$ and the number of entanglements per polymer chain set as $Z = 10$. As shown in Figure 4-3, a consistent exponential-thinning trend can be observed at intermediate time for the both models with slightly different slopes. From previous discussions, this exponential-thinning trend in the filament radius results from an exponentially increasing polymer chain stretch Λ induced by the strong extensional flow. As Λ approaches the specified finite maximum chain stretch Λ_m, the filament radius essentially deviates from the exponential-thinning trend and approaches filament singularity.

While the filament thinning dynamics derived from the tube models for entangled polymer systems are essentially distinct from those predicted by the Oldroyd-B model for dilute polymer solutions, it is possible to extract an extensional relaxation time from the exponential-thinning regime. To mitigate the ambiguity in the interpretation of the measurements from the application of different models, an *apparent* extensional relaxation time denoted as λ_e (which is nondimensionalized by the Rouse time λ_R, and then denoted as $\hat{\lambda}_e$) can be defined with its value obtained from fitting the slope in the exponential-thinning region, where $\hat{R}(\hat{t}) \sim \exp[-\hat{t}/(3\hat{\lambda}_e)]$.

Analytical solutions of the apparent extensional relaxation time can be obtained for both models by substituting the constitutive equations into Equation (4.4) in the limit of $Ec_0 \to 0$ and $\Lambda_m \to \infty$ as

$$\text{DEMG: } \hat{\lambda}_e = \frac{1}{2}, \tag{4.9a}$$

$$\text{Rolie-Poly: } \hat{\lambda}_e = \frac{1}{2 + 1/p(Z)}, \tag{4.9b}$$

where $p(Z) = \lambda_D/\lambda_R$ is the ratio of the two timescales from the constitutive model, as defined in Equation (4.1). This formula is plotted in Figure 4-4, for a range of $2 \leq Z \leq 100$ that is specified according to the validity of the numerical calculation of Equation (4.1) [30]. The apparent extensional relaxation times λ_e derived from both models scale primarily with the Rouse time λ_R. Compared with the DEMG model, the expression for the Rolie-Poly model has an additional weak dependence on the disengagement time λ_D (through $p(Z)$), which is attributed to the CCR effect and becomes comparable in magnitude with the Rouse-time contribution when Z is relatively small so that $p \ll 3$. Notably, as $Z \to \infty$, the value of λ_e in both models approaches an identical limit of $\lambda_R/2$.

Finally, the filament thinning profiles close to the filament singularity are calculated nu-

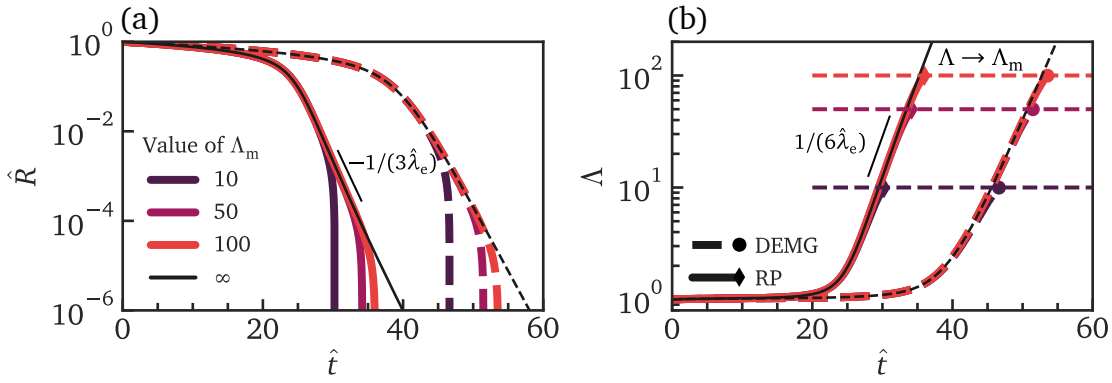

Figure 4-3: Capillarity-driven thinning dynamics described by the two selected tube models (dashed lines: DEMG model; solid lines: Rolie-Poly model) with varying finite extensibility factors $\Lambda_m = 10$, 50 and 100 and $\Lambda_m \to \infty$ (black solid/dashed lines) with a fixed intrinsic elasto-capillary number $\mathrm{Ec}_0 = 1$ and a fixed number of entanglements per polymer chain $Z = 10$. (a) The filament radius $\hat{R} \equiv R/R_0$ plotted on a logarithmic scale at intermediate times. A consistent exponential thinning trend is manifested for both models. An exponential-thinning region is identified at intermediate time with an identical slope for each model, from which an apparent extensional relaxation time λ_e can be obtained. The filament radius subsequently deviates to zero due to the presence of a finite time singularity if Λ_m is finite. (b) The polymer chain stretch Λ plotted on a logarithmic scale. An exponentially-increasing trend is manifested at intermediate time with a slope of $1/(6\hat{\lambda}_e)$. Close to the filament breakup, the value of Λ approaches the specified maximum stretch of Λ_m (horizontal dashed lines).

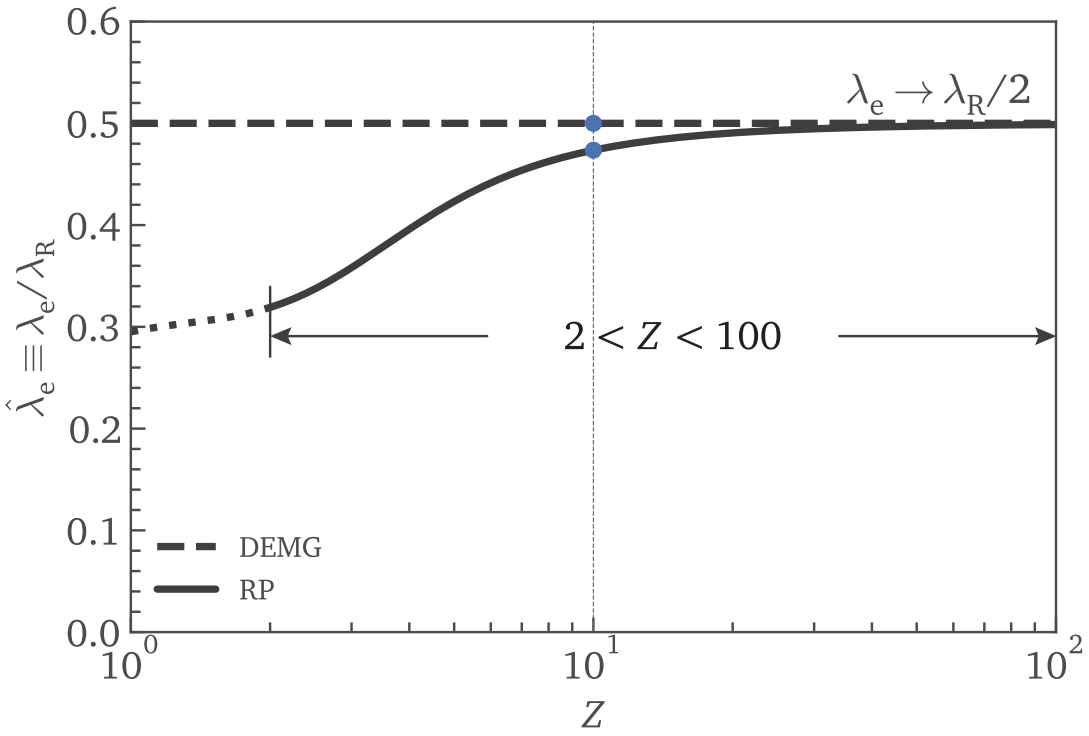

Figure 4-4: Apparent extensional relaxation time nondimensionalized by the Rouse time $\hat{\lambda}_e \equiv \lambda_e/\lambda_R$ extracted from the exponential-thinning trend for the filament radius against the number of entanglements per polymer chain Z. For the DEMG model (dashed line), a constant of $1/2$ is identified. For the Rolie-Poly model (solid line), a monotonic trend is observed, which coincides with the asymptotic value from the DEMG model at $Z \to \infty$. The range of $2 < Z < 100$ denote the applicability of Equation (4.1) from Likhtman and McLeish [30]. The blue marker shows the result at $Z = 10$ used in Figure 4-1, Figure 4-3 and Figure 4-5.

merically, where the polymer chain stretch Λ approaches the finite extensibility limit Λ_m and the temporal evolution of the filament radius deviates from the exponential-thinning trend. For plot legibility and better analysis close to the filament singularity, the time axis is transformed to the time to filament breakup $\hat{\tau} = \hat{t}_C - \hat{t}$ according to the previous definition on page 73, nondimensionalized by the Rouse time. The value of $\hat{t}_C$ can be numerically obtained from the extrapolation of the filament radius to $\hat{R} = 0$. As shown in Figure 4-5, the temporal evolution of $\hat{R}(\hat{t})$ with the same parameter varia-

tion as in Figure 4-3 is plotted for the two selected models. As the filament approaches singularity ($\hat{\tau} \to 0^+$), the filament radius starts to decay linearly, and the resulting kinematics from the two models with the same finite extensibility Λ_m become increasingly close to each other.

The linear decay of the filament radius close to the filament breakup has also been observed for the FENE-P model [244]. This asymptotic linear trend is comparable with the visco-capillary thinning for a Newtonian fluid [210]. Accordingly, a finite terminal extensional viscosity $\eta_{e,\infty}$ can be extracted from the slope of thinning in this linearly-thinning regime by rewriting Equation (4.4) in the form of a Taylor expansion with respect to $1/\Lambda$. Consequently, an analytical expression for the terminal extensional viscosity can be obtained as

$$\eta_{e,\infty} = \frac{3G_N\Lambda_m^2}{1-1/\Lambda_m}. \tag{4.10}$$

The asymptotic solution for the filament radius using $\eta_{e,\infty}$ with varying finite extensibilities Λ_m are plotted in Figure 4-5 as thin dashed lines. These values are consistent with the numerical calculations of the filament thinning dynamics in the approach to filament breakup.

4.1.3 Ratio of apparent extensional and shear relaxation times

In practice, the shear relaxation time λ_s can be routinely obtained from the small amplitude oscillatory shear (SAOS) as $1/\omega_c$, where ω_c is the critical angular frequency at which the storage and loss moduli coincide. For dilute polymer solutions described by the FENE-P model, there is a single relaxation time to characterize the polymer chain retraction regardless of the flow types. However, a number of previous studies on the filament thinning dynamics of different entangled polymer solutions have revealed distinct measures of the relaxation times in shear and extensional flows [32,199,200,257]. The dumbbell model with a flow-independent relaxation mode does not readily reconcile the difference in the relaxation times for polymer chains in an entangled state.

In this section, a theoretical framework is established using the tube models to interpret the difference in shear and extensional relaxation times observed in the entangled polymer solutions. It has been shown in Figure 4-3 that the temporal evolution of the filament radius predicted by the selected tube models resulted features an exponential-thinning trend at intermediate time. In this stage, an *apparent* extensional relaxation time is obtained and broadly scales with the Rouse time λ_R. This, however, is in contrast with the shear relaxation time, which can be analytically calculated by imposing an oscillatory shear to the DEMG and the Rolie-Poly constitutive equations. When the

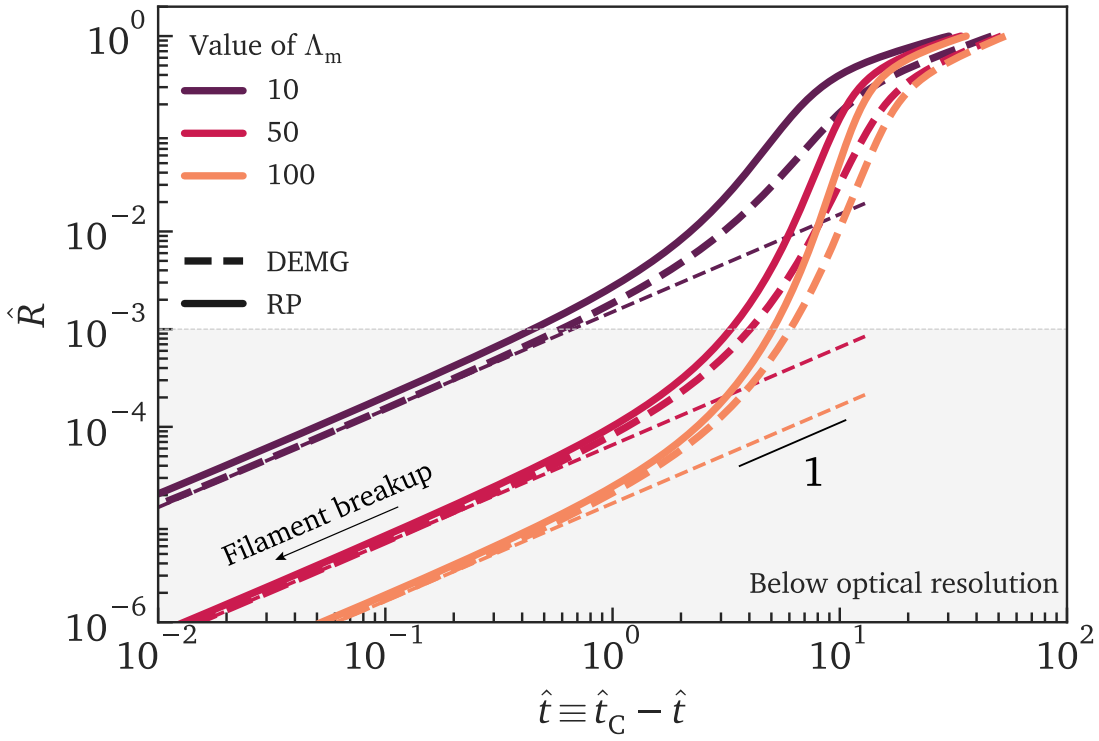

Figure 4-5: Temporal evolution of the filament radius with varying finite extensibility factors $\Lambda_m = 10,\ 50$ and 100 at a fixed elasto-capillary number $Ec_0 = 1$ and with the number of entanglements per polymer chain $Z = 10$. The filament radius is plotted against $\tau = t_C - t$ (nondimensionalized by λ_R as $\hat{\tau}$), where t_C is the time when the filament breaks up. A linear decaying trend of the filament radius is identified in the proximity of filament breakup, which is comparable with the filament thinning response for a Newtonian fluid. A terminal extensional viscosity $\eta_{e,\infty}$ can be obtained analytically from the filament thinning solutions, from which the asymptotic solutions are plotted as thin dashed lines and are consistent with the numerical calculations from the two models when the filament is close to breakup. The gray area specifies an optical limit in practical measurements below $\hat{R} < 1 \times 10^{-3}$.

imposed oscillatory strain is infinitesimal, the dynamic moduli from both tube models are reduced to the case of Hookean dumbbell model with a relaxation time of $\lambda = \lambda_D$ and the modulus of $G = 3G_N$. This result is not surprising, as the tubes under small shear strains can effectively shield non-reptative mechanisms that occur within. As a result, the relaxation process in shear flow primarily results from the tube deformation and reorientation, which can be characterized by the disengagement time λ_D. Table 4.3 summarizes the apparent shear and extensional relaxation times of the Hookean dumbbell model and the two selected tube models.

Table 4.3: Dynamic moduli G' and G'', the crossover angular frequency ω_c at $G' = G''$, and *apparent* shear and extensional relaxation times λ_s and λ_e for the Hookean dumbbell model, the DEMG model, and the Rolie-Poly model. The apparent extensional relaxation time in the limit of $Z \to \infty$ is also tabulated.

Model	$G'(\omega)$	$G''(\omega)$	ω_c	λ_s	λ_e	λ_e $(Z \to \infty)$
Hookean	$\frac{G\omega^2\lambda^2}{1+(\omega\lambda)^2}$	$\frac{G\omega\lambda}{1+(\omega\lambda)^2}$	$\frac{1}{\lambda}$	λ	λ	λ
DEMG	$\frac{G\omega^2\lambda_D^2}{1+(\omega\lambda_D)^2}$	$\frac{G\omega\lambda_D}{1+(\omega\lambda_D)^2}$	$\frac{1}{\lambda_D}$	λ_D	$\frac{\lambda_R}{2}$	$\frac{\lambda_R}{2}$
Rolie-Poly	$\frac{G\omega^2\lambda_D^2}{1+(\omega\lambda_D)^2}$	$\frac{G\omega\lambda_D}{1+(\omega\lambda_D)^2}$	$\frac{1}{\lambda_D}$	λ_D	$\frac{\lambda_R}{2+1/p(Z)}$	$\frac{\lambda_R}{2}$

Without introducing additional fitting parameters, an expression for the ratio of the two relaxation times can be readily obtained using the constitutive parameters of the tube models. For entangled polymer solutions, the molecular weight between entanglements M_e grows larger than that for the polymer melts due to a sparser spacing of the polymer chains. To incorporate the polymer concentration into the expression of the relaxation time ratio, an effective molecular weight between entanglements in the entangled solutions can be calculated [275, 276] as

$$M_e(c) = M_{e,0}c^{-1/(3\nu-1)}, \tag{4.11}$$

where c is the mass fraction of the polymers in solutions, and $M_{ent,0}$ is the molecular weight between entanglements in the corresponding polymer melts (where $c = 1$). The excluded volume parameter is $\nu = 0.5$ for θ-solvents, and $\nu = 0.6$ for good solvents.

From Equation (4.1), the number of entanglements per chain in the entangled polymer solutions Z_{sol} can be expressed as a function of the polymer mass fraction c as

$$Z_{\mathrm{sol}}(c) = \frac{M}{M_{\mathrm{e},0}} c^{1/(3\nu-1)} \equiv Z_0 c^{1/(3\nu-1)}, \tag{4.12}$$

where the number of entanglements for polymer melts is denoted as $Z_0 \equiv Z(1) = M/M_{\mathrm{e},0}$. From Equation (4.12), the relaxation time ratio $\lambda_{\mathrm{e}}/\lambda_{\mathrm{s}}$ can be finally evaluated as a function of the number of entanglements per chain in polymer solutions $Z_{\mathrm{sol}}(c)$ as

$$\frac{\lambda_{\mathrm{e}}}{\lambda_{\mathrm{s}}} = \frac{\hat{\lambda}_{\mathrm{e}}[Z_{\mathrm{sol}}(c)]}{p[Z_{\mathrm{sol}}(c)]} = \begin{cases} \dfrac{1}{6Z_{\mathrm{sol}}(1 - \dfrac{3.38}{\sqrt{Z_{\mathrm{sol}}}} + \dfrac{4.17}{Z_{\mathrm{sol}}} - \dfrac{1.55}{Z_{\mathrm{sol}}^{3/2}})}, & \text{(DEMG)} \\ \dfrac{1}{6Z_{\mathrm{sol}}(1 - \dfrac{3.38}{\sqrt{Z_{\mathrm{sol}}}} + \dfrac{4.17}{Z_{\mathrm{sol}}} - \dfrac{1.55}{Z_{\mathrm{sol}}^{3/2}}) + 1}, & \text{(Rolie}-\text{Poly)} \end{cases} \tag{4.13}$$

where the dimensionless apparent extensional relaxation time $\hat{\lambda}_{\mathrm{e}}$ is referred in Table 4.3 and the ratio of the disengagement time and the Rouse time $p(Z)$ is expressed in Equation (4.1). Equation (4.13) thus provides a theoretical prediction of the relaxation time ratio without additional fitting parameters.

To systematically substantiate the analytical prediction of Equation (4.13), we compare the prediction with a number of experimental data points from previous studies [200, 257, 277] on two different polymer solutions at varying molecular weights and concentrations. To ensure the validity for the application of the tube models, only concentrations in the entangled regime ($c > c_{\mathrm{e}}$) are inspected. The material properties and the experimental measurements of the selected materials systems are listed in Table 4.4. The molecular weight between entanglements M_{e} is evaluated at 20 °C, and the number of entanglements per chain for the polymer melts Z_0 is calculated based on the assumption of monodisperse polymer chains.

As shown in Figure 4-6, the experimental data from Table 4.4 are compared with the analytical prediction of Equation (4.13) from the two selected tube models (dashed line: DEMG model; solid line: RP model). The predicted lines from both models show an overall descending trend of the relaxation time ratio against the number of entanglements per chain in the entangled polymer solutions. Both prediction lines are applicable within the range of $2 < Z_{\mathrm{sol}}(c) < 100$ due to the validity of Equation (4.1) [30]. As $Z_{\mathrm{sol}}(c)$ increases, the two predictions coincide and the relaxation time ratio approaches

Table 4.4: Polymer properties, concentrations and experimentally measured ratios of the apparent shear and extensional relaxation times λ_e/λ_s for a selected range of material systems from previous studies.

Materials	M_e (Da)	M (Da)	c (wt%)	c/c_e	λ_e/λ_s
PEO/Water [200]	2200 [278]	1×10^6	2.5	1.3	0.168 ± 0.042
			3.0	1.5	0.197 ± 0.049
		2×10^6	1.5	1	0.125 ± 0.031
			2.0	1.3	0.104 ± 0.026
PEO/Water [257]	2200	1×10^6	2.0	1	0.34
			2.5	1.3	0.24
			3.0	1.5	0.24
			3.5	1.8	0.15
		2×10^6	1.5	1	0.12
			2.0	1.3	0.10
		4×10^6	1.0	1.5	0.10
			1.5	2.3	0.05
			2.0	3.0	0.02
PS/DEP [257]	16 600 [279]	3×10^6	3.0	1.2	0.71
			4.0	1.6	0.50
			5.0	2	0.24
PS/DEP [277]	16 600	13.2×10^6	1.41	1.8	0.36
			1.77	2.2	0.31

an asymptotic scaling relation of $\lambda_e/\lambda_s \sim Z_{sol}^{-1}$. From Figure 4-6, the experimental data of varying polymer systems, molecular weights and concentrations are broadly collapsed onto a single master curve, which agrees well with the predictions from both tube models. This general agreement between the experimental data and the analytical prediction lines without additional fitting parameters provides a physical insight into the origin of the non-trivial difference in the shear and extensional relaxation times observed in experiments: The tube networks constitute the larger-scale topology of the entangled polymer systems and effectively shield the contribution of chain stretching from single polymer chains to the bulk shear rheology under small deformation. However, the integrity of these tube structures becomes increasingly susceptible to a strong

extensional flow as the tubes are forced to align towards a uniform direction. This is justified by the magnitude of reorientation ΔS approaching unity before the onset of the elasto-capillary thinning, as shown in Figure 4-3. As a result, the free energy of polymer chains decreases, and the material relaxation becomes less inhibited by the tube structures.

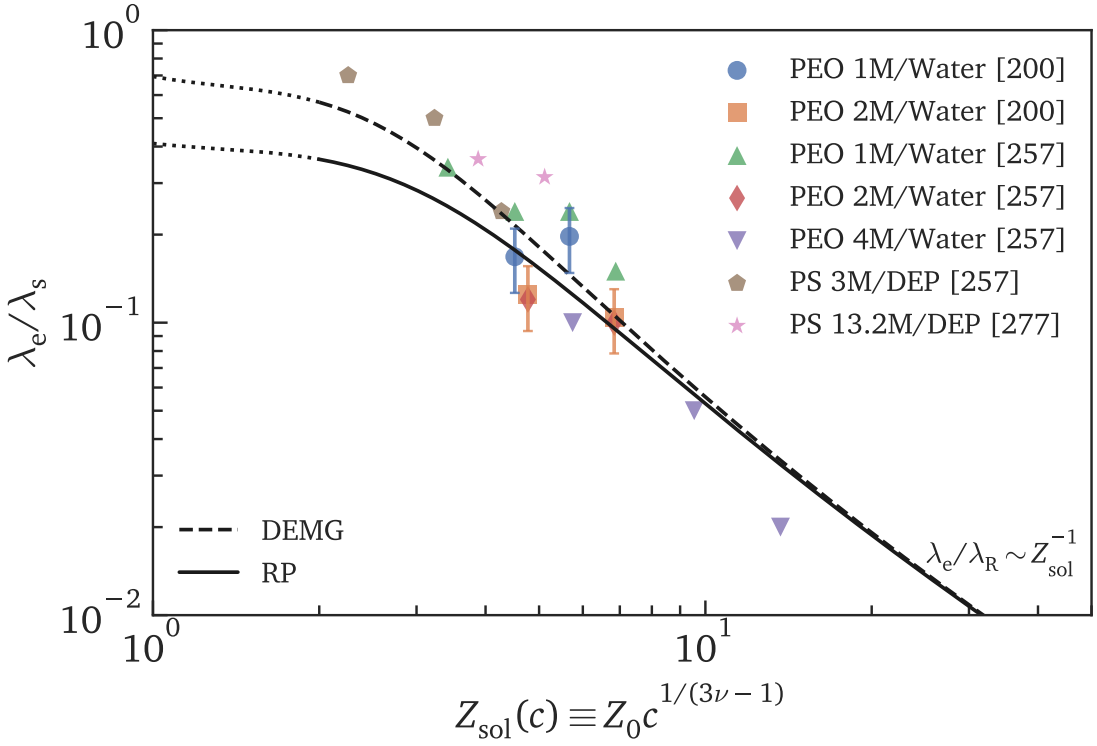

Figure 4-6: The ratio of apparent extensional and shear relaxation times λ_e/λ_s against the number of entanglements per chain in entangled polymer solutions $Z_{sol}(c) = Z_0 c^{1/(3\nu-1)}$. The dashed and solid lines correspond to the prediction lines from the DEMG and the Rolie-Poly models, respectively, within a range of $2 < Z_{sol}(c) < 100$ due to the validity of Equation (4.1) [30]. The experimental data from a variety of material systems with different molecular weights and concentrations are broadly collapsed onto a monotonically descending master curve, and show excellent agreement with the predictions from both tube models free of additional fitting parameters.

4.1.4 Extensional-thinning for highly entangled polymer systems

Another critical feature extracted from the measured capillarity-driven thinning dynamics of the entangled polymer solutions is the rate-thinning extensional viscosity [32]. This extensional-thinning feature becomes prominent when the polymer solutions become increasingly viscoelastic and entangled (practically by increasing the concentration or the molecular weight). This trend can also be captured by the selected tube models. As shown in Figure 4-7, the transient extensional viscosity is extracted from the temporal evolution of the filament radius with the same parameter variation as in Figure 4-3. The Trouton ratio has been defined previously as the transient extensional viscosity scaled by the zero-shear viscosity η_0. For both tube models studied in this work, the zero-shear viscosity can be analytically calculated as $\eta_0 = G_N \lambda_D$. To be consistent with the zero-shear viscosity, the strain rates are nondimensionalized by the disengagement time λ_D as a new Weissenberg number Wi_D. When $\mathrm{Wi}_D \to 0$, the apparent Trouton ratio approaches a constant of $\mathrm{Tr}_{app} = 3$, similar to a Newtonian fluid.

The transient Trouton ratio extracted from the filament thinning dynamics predicted by the two tube models exhibit complex rate-dependent rheological behavior. When $1 \ll \mathrm{Wi}_D \ll p(Z)$, the extension at an intermediate strain rate is resisted by the Brownian motion of the chains in the tube and the flow-induced orientation of the tube. As a result, these tubes are forced to align towards the direction of extension, which induces a faster relaxation during the reptation process and hence a rate-thinning trend in the extensional viscosity. In contrary, in a fast extensional flow where $\mathrm{Wi}_D \gg p(Z)$ or correspondingly $\mathrm{Wi} \gg 1$, the finite rate of the polymer chain retraction dominates the polymer conformation. Consequently, the tube reorientation does not effectively contribute to the extensional rheology of the systems. The entropic spring resistance arising from the polymer chain stretch dominates the overall viscoelastic response from the material, thus increasing the extensional viscosity. As the strain rate continues to increase, the extensional viscosity approaches a terminal value expressed in Equation (4.10) as the polymer chain approaches its maximum finite extensibility Λ_m.

In a filament thinning experiment, the strain rate $\dot{\epsilon}_{mid}(t)$ varies throughout the experiment. The transient extensional viscosity extracted from these capillarity-thinning dynamics can be further compared with those obtained from *steady* extension. As shown in Figure 4-7, the steady extensional viscosities from the two tube models (DEMG model: black dashed line; RP model: black solid line) broadly overlap with the observation that would be made during the transient process (thick colored lines) at low or intermediate strain rates. A major discrepancy between the steady and tran-

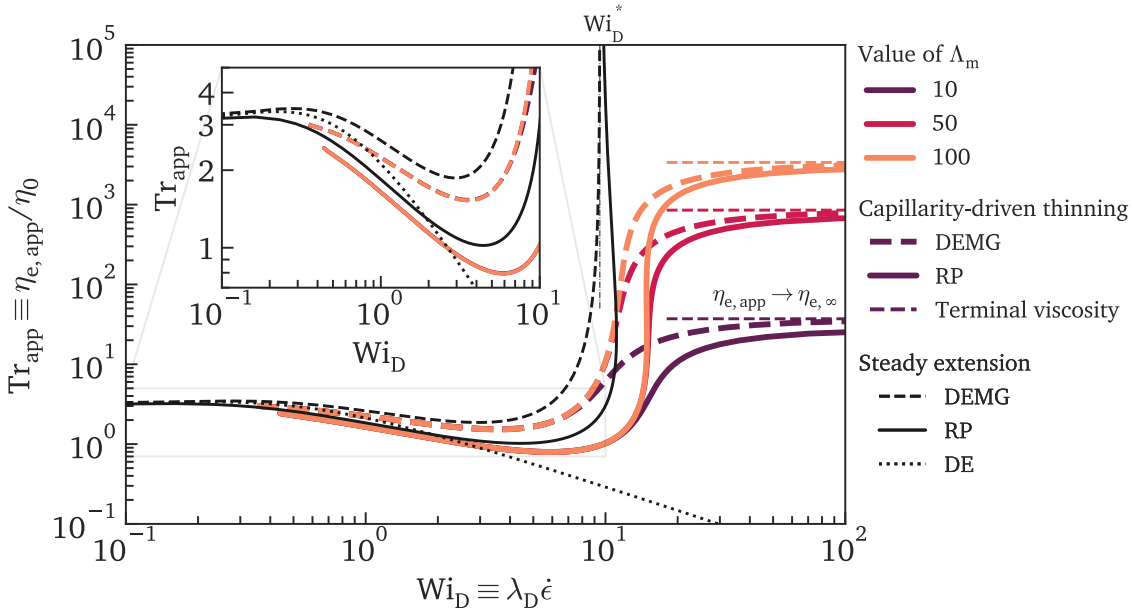

Figure 4-7: The transient apparent Trouton ratio $\mathrm{Tr}_\mathrm{app} \equiv \eta_{\mathrm{e,app}}/\eta_0 = \eta_{\mathrm{e,app}}/(G_\mathrm{N}\lambda_\mathrm{D})$ (from page 91) against the Weissenberg number based on the disengagement time $\mathrm{Wi}_\mathrm{D} \equiv \lambda_\mathrm{D}\dot{\epsilon}$ extracted from the filament thinning dynamics of the DEMG model (thick dashed lines) and the Rolie-Poly model (thick solid lines) with varying finite extensibilities $\Lambda_\mathrm{m} = 10,\ 50$ and 100 at a fixed intrinsic elasto-capillary number $\mathrm{Ec}_0 = 1$ and fixed number of entanglements $Z = 10$. As Wi_D increases, the transient extensional viscosity undergoes the trend of rate-thinning, rapid thickening and plateauing at $\eta_{\mathrm{e},\infty}$ in sequence. Three reference lines are drawn from the *steady* extension predicted by the Rolie-Poly model (thin black solid line), the DEMG model (thin black dashed line) and the original Doi-Edwards model (thin black dotted line) with an infinite extensibility of the polymer chain stretch (if applicable). The prediction lines from the steady extension of the two tube models that incorporate the polymer chain stretch closely follow the trends of those extracted from filament thinning until approaching the finite extensibilities, and diverge at $\mathrm{Wi} = \mathrm{Wi}_\mathrm{D}^*$. In contrary, the predicted response from the DE model (dotted line) without additional chain stretch terms predict a persistent rate-thinning trend for $\mathrm{Wi}_\mathrm{D} \gg 1$. Inset: Same figure in a zoom-in view for $1 \times 10^{-1} \leq \mathrm{Wi}_\mathrm{D} \leq 1 \times 10^{1}$.

sient responses is the critical Weissenberg number Wi_D^* at which the extensional viscosity diverges. In steady homogeneous extension, this critical value is $\mathrm{Wi}_\mathrm{D}^* = p(Z)$ (DEMG) and $\mathrm{Wi}_\mathrm{D}^* = (p(Z) + 1/2)$ (RP); whereas in the transient response, a new critical Weissenberg number can be analytically calculated as $\mathrm{Wi}_\mathrm{D}^* = 4p(Z)/3$ (DEMG) and $\mathrm{Wi}_\mathrm{D}^* = (4p(Z)+2)/3$ (RP). The difference between steady extension and transient capillarity-driven flows arises from the non-vanishing rate of chain stretch $\dot{\Lambda}$ as a result of the temporal evolution of $\Lambda(t)$ in the filament thinning. Notably, the flow response predicted by the RP model exhibits a metastable region for $\mathrm{Wi}_\mathrm{D} > \mathrm{Wi}_\mathrm{D}^*$ with a large magnitude of Wi_D^* compared with the DEMG model, which is likely to arise from the additional CCR effect that accelerates tube disengagement while concomitantly inducing chain stretch. In practice, if rate-thinning behavior is prominent in the capillarity-driven thinning dynamics for a tested fluid, the elasto-capillary number is reasonably large. As a result, the exponential-thinning regime of the filament radius derived from the polymer chain stretch is unlikely to be observed within a measurable range. To parsimoniously describe the rate-thinning kinematics, the original Doi-Edwards (DE) model with no description of the polymer chain stretch is applied for reference. A differential form of the constitutive equation can be obtained from Equation (4.2) by setting $\Lambda = 1$ [249].

Figure 4-8 shows the dimensionless shear (blue) and extensional (black) viscosities predicted by the RP model (solid line), the DEMG model(dashed line) and the DE model (dotted line) for $\mathrm{Ec}_0 = 1$, $Z = 10$ and $\Lambda_\mathrm{m} \to \infty$ (if applicable). A wide range of Weissenberg numbers $0.1 < \mathrm{Wi}_\mathrm{D} < 10$ is inspected here for the observation of a comprehensive rate-dependent behavior. All three models predict persistent shear-thinning behavior, as a result of the progressive tube alignment at large shear rates. The extensional viscosity, on the contrary, shows very distinct trends between the DE model and the other two (more sophisticated) models that incorporate polymer chain stretch. The asymptotic solutions of the shear and extensional viscosities as $\mathrm{Wi}_\mathrm{D} \to \infty$ predicted by the DE model are representative of the rate-dependent material response expected purely from tube reorientation. They are analytically calculated and approximated as a function of Wi_D as

$$\frac{\eta}{G_\mathrm{N}\lambda_\mathrm{D}} \approx \frac{3}{12^{1/3}\mathrm{Wi}_\mathrm{D}^{4/3}} \cdot \frac{1}{1-4/(12^{2/3}\mathrm{Wi}_\mathrm{D}^{2/3})} \sim \mathrm{Wi}_\mathrm{D}^{-4/3}, \tag{4.14a}$$

$$\mathrm{Tr}_\mathrm{app} \approx \frac{9}{3\mathrm{Wi}_\mathrm{D}+1} \sim \mathrm{Wi}_\mathrm{D}^{-1}. \tag{4.14b}$$

Therefore, the shear and extensional viscosities asymptotically approach a scaling law of $\mathrm{Wi}_\mathrm{D}^{-4/3}$ and $\mathrm{Wi}_\mathrm{D}^{-1}$, respectively, in the limit of $\mathrm{Wi}_\mathrm{D} \gg 1$. The larger-than-unity power

in the shear-flow scaling is well-known to produce flow instability [249]. Nevertheless, the extensional-thinning trend predicted by the DE model shows a pronounced strain-rate dependence and suggests a plateau in the extensional stress difference $\Delta\delta$ (as from $\mathrm{Tr}_{\mathrm{app}} \cdot \mathrm{Wi}_{\mathrm{D}}$) when Wi_{D} grows sufficiently large. This predicted plateau provides an underestimated extensional stress magnitude due to the absence of non-reptative mechanisms in the DE model, and has been disproved in a number of experimental studies [249]. However, the DE model still provides valuable insights in understanding the extensional rheology behavior for highly viscous polymer melts, in which the tube deformation plays a predominant role.

Analysis for a real material system: Polyethylene oxide

To demonstrate the capillarity-driven thinning dynamics of a real material system, a well-studied polymer solution of polyethylene oxide (PEO) at a molecular weight of 1 MDa is selected for numerical calculations over a wide range of the concentrations in both the dilute and the entangled regimes. Table 4.5 lists the polymer properties and configurations obtained from previous experimental studies or derived from the theories of polymer physics as noted at the end of the table. The modulus in the FENE-P model for the dilute polymer solutions can be calculated from the kinetic theories [244] as $G = nkT = ckT/\left\langle R_0^2 \right\rangle^{3/2}$. The plateau modulus of the entangled polymer solutions can be calculated from the Graessley-Fetters definition [249] as

$$G_{\mathrm{N}}(c) = \frac{4\rho_{\mathrm{sol}} cRT}{5M_{\mathrm{e}}(c)}, \tag{4.15}$$

where ρ_{sol} is the solution density, and the molecular weight between entanglements for solutions $M_{\mathrm{e}}(c)$ is expressed in Equation (4.11). The constitutive equation for semi-dilute polymer solutions is taken from Prabhakar et al. [31] by adding a concentration- and strain-dependent correction factor to the relaxation time in the FENE-P model as

$$\lambda(c/c^*, \Lambda) = \nu(c/c^*, \Lambda)\lambda_{\mathrm{Z}}, \tag{4.16}$$

where c^* is the overlap concentration, and λ_{Z} is the Zimm time that describes the relaxation time in the limit of infinite dilution. The polymer chain stretch Λ can be expressed [31, 209, 244, 282] as

$$\Lambda = \frac{\sqrt{\mathrm{tr}\,\langle \boldsymbol{QQ} \rangle}}{\left\langle R_0^2 \right\rangle^{1/2}}, \tag{4.17}$$

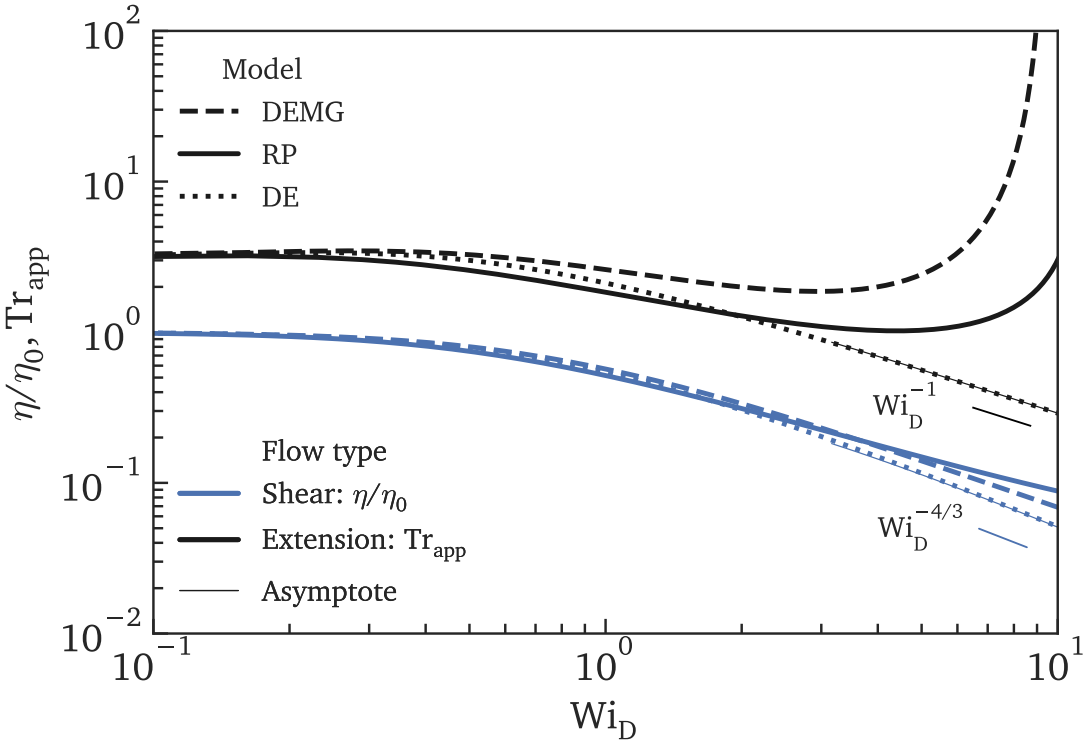

Figure 4-8: Evolution in the dimensionless shear and apparent extensional viscosities, $\eta(\dot{\gamma})/\eta_0$ (where $\eta_0 = G_{\mathrm{N}}\lambda_{\mathrm{D}}$, blue lines) and $\mathrm{Tr}_{\mathrm{app}}$ (black lines) against the Weissenberg number based on the disengagement time Wi_{D} for the Rolie-Poly model (solid lines), the DEMG model (dashed lines) and the Doi-Edwards model (dotted lines) at $\mathrm{Ec}_0 = 1$, $Z = 10$ and $\Lambda_{\mathrm{m}} \to \infty$ (if applicable). The shear viscosities among the three tube models shows a persistent shear-thinning trend until close to $\mathrm{Wi}_{\mathrm{D}} = 10$. In extensional flow, a broadly consistent extensional-thinning trend is observed at low Wi_{D} for all the selected models. Beyond $\mathrm{Wi}_{\mathrm{D}} \approx 3$, the two more sophisticated tube models which incorporate the additional polymer chain stretch predict a rapidly increasing extensional viscosity, while the DE model continues to predict a steadily decreasing trend. The asymptotic solutions of both the shear and extensional viscosities for the DE model at a large value of Wi_{D} are plotted as thin lines, which exhibit a power-law scaling of $\eta/\eta_0 \sim \mathrm{Wi}_{\mathrm{D}}^{-4/3}$ and $\mathrm{Tr}_{\mathrm{app}} \sim \mathrm{Wi}_{\mathrm{D}}^{-1}$, respectively.

where $\boldsymbol{Q}$ is the end-to-end vector of a *single* polymer molecule and the angle brackets correspond to the ensemble average of all dumbbells.

Table 4.5: List of properties and configurations for the numerical calculations of filament thinning dynamics for aqueous PEO solutions at varying concentrations.

Properties	Values
Molecular weight M (g/mol)	1×10^6
Monomer size M_0 (g/mol)	44
Degree of polymerization N	22 727[a]
Molecular weight between entanglements in melts M_e (g/mol) [278]	2200
Characteristic ratio C_∞ [262]	5.6
Monomer length l (nm) [280]	0.35
Kuhn step N_K	4058[b]
Kuhn length b_K (nm)	2[c]
End-to-end distance $\left\langle R_0^2 \right\rangle^{1/2}$ (nm)	125[d]
Statistical length b (nm)	0.83[e]
Temperature for solutions T (°C)	25
Surface tension Γ (mN/m) [281]	62.2
Initial filament radius R_0 (mm)	1
Zimm time λ_Z (ms) [212]	0.51
Friction coefficient of monomer ζ_0	1.4×10^{-11}
Rouse time λ_R (ms)	20.2[f]
Overlap concentration c^* (wt%) [212]	0.161
Entanglement concentration c_e (wt%) [257]	1.7

[a] $N = M/M_0$.
[b] $N_K = N/C_\infty$ and $N_K = \Lambda_m^2$ in dilute polymer solutions [262].
[c] $b_K = C_\infty l$ [262].
[d] $\left\langle R_0^2 \right\rangle^{1/2} = \sqrt{N_K} b_K$ [262].
[e] $b = b_K \sqrt{N}$ [249].
[f] $\lambda_R = \zeta_0 N^2 b^2/(6\pi^2 kT)$ [249].

To illustrate the filament thinning profiles, six concentrations are selected in the dilute and semi-dilute regimes ($c = 0.0016$ wt%, 0.081 wt% and 0.24 wt%; predicted by the FENE-P model with a corrected relaxation time; marked in blue) as well as the entangled regime ($c = 2.0$ wt%, 2.5 wt% and 3.0 wt%; predicted by the RP model; marked in yellow and red). Based on the properties listed in Table 4.5, all the concentration-specific parameters can be calculated for the numerical calculation, as shown in Table 4.6. It is noted that both the (plateau) moduli and the number of entanglements

Table 4.6: List of the selected concentrations and concentration-specific properties of aqueous PEO solutions for the numerical calculation of filament thinning dynamics. The colored lines next to the concentrations are consistent with those in Figure 4-9.

Concentrations (wt%)	c/c^*	c/c_e	G or G_N (Pa)	Z_{sol}	Λ_m^2
0.0016 (▬)	9.9×10^{-3}	9.4×10^{-4}	0.02	N/A	4058
0.081 (▬)	0.50	0.048	1.06	N/A	4058
0.24 (▬)	1.49	0.14	3.17	N/A	4058
2.0 (▬)	12.42	1.17	135.59	1.5	1187
2.5 (▬)	15.53	1.47	224.02	2.3	898
3.0 (▬)	18.63	1.76	337.63	3.4	715

increase with the concentration, while the maximum polymer chain stretch decreases as the polymers are increasingly entangled, thus shortening the length of a single tube segment.

In Figure 4-9, the time axis is dimensional to help illustrate the magnitude of change in the breakup time. As the concentration increases from below c^* to above c_e, the filament breakup time is progressively retarded by approximately two orders of magnitude. In Figure 4-9(b) and (c), the two exponential-thinning asymptotes characterized by the Zimm time (black dashed lines, in which $\lambda_e = \lambda_Z$) and the Rouse time (gray dashed line, in which $\lambda_e \approx \lambda_R/2$ from Table 4.3) are plotted separately. These two asymptotes set two lower bounds for the filament radius evolution in dilute/semi-dilute and entangled regimes, and can be practically used to identify the most appropriate constitutive model for the extraction of accurate extensional rheological properties. The kinematics of the filament radius evolve from a broadly exponential-thinning trend under an elasto-capillary balance to a smoother thinning trend at concentrations above c_e. In this stage, the filament thinning rate is significantly slowed down as the highly entangled tube structures increasingly impede the disengagement of the polymer chains in an extensional flow.

In practice, the measurement of the filament radius is also limited by the resolution of the image capturing devices. A measurable range that covers three orders of magnitude down to $\hat{R} = 1 \times 10^{-3}$ is realistic. As a result, the slow-thinning trend at the onset of the filament thinning tend to last longer and is more evident in the experimental data. To quantify the duration of the "slow-thinning" behavior in entangled solutions, a specific time stamp $t_{V\text{-}E}$ is obtained when the transient strain rate reaches the critical value under an elasto-capillary balance at $\mathrm{Wi} = 2/(3\hat{\lambda}_e)$ (marked in circles in Figure 4-9(c)

and (d)). The notation of $t_{\text{V-E}}$ is inherited from Section 3.2 in the study of motor oils, from which a similar description of the transition is retained. Beyond this time stamp, the filament radius decays in an approximately exponential trend until the polymer chain stretch approaches the maximum stretch, as illustrated in Figure 4-3. As shown in Figure 4-9(d), where the filament radius for each polymer solution in the entangled regime is plotted on a linear scale, the transition to the exponential-thinning trend occurs considerably close to the filament pinch-off. As a result, the majority of the filament thinning profile agrees well with the prediction from the DE model, of which the initial shear viscosity is identical to the apparent zero-shear viscosity calculated in Equation (4.8).

From the numerical calculations in the entangled regime, three timescales can be defined and suffice for approximate description of the filament thinning profiles: (1) the transition time $t_{\text{V-E}}$ when the exponential-thinning trend is manifested at $\text{Wi} = 2/(3\hat{\lambda}_{\text{e}})$; (2) the filament breakup time t_{C} obtained by extrapolating the filament radius to $R = 0$; (3) the filament breakup time $t_{\text{C,V}}$ predicted by extrapolating the linear-decay trend generated from the visco-capillary thinning with the apparent zero-shear viscosity in Equation (4.8). As shown in Figure 4-10, all three timescales are plotted against a refined mesh for $1 \leq c/c_{\text{e}} \leq 2.4$, with the three selected concentrations in Table 4.6 marked out separately. From this figure, the filament breakup time t_{C} (black line) increases in a broadly exponential trend for $c > c_{\text{e}}$. At $c/c_{\text{e}} \approx 1.7$, the filament breakup time t_{C} is approximately identical to $t_{\text{C,V}}$, where the rate-thinning effect induced by the tube reorientation are approximately in equal magnitude with the rate-thickening effect from the polymer chain stretch. Beyond this point, the elasto-capillary transition time $t_{\text{V-E}}$ and the visco-capillary breakup time $t_{\text{C,V}}$ defined previously steadily approach t_C, while $t_{\text{C,V}} > t_{\text{C}} > t_{\text{V-E}}$. The evolution of the three timescales illustrates a delayed transition to the exponential-thinning regime as the concentration increases, in conjunction with an extended filament thinning process governed by the tube reorientation. At sufficiently large concentrations, the tube reorientation that induces a rate-thinning behavior becomes increasingly crucial in determining the final breakup time than the polymer chain stretch where the extensional viscosity increases with the strain rate. Correct asymptotic solutions can be selected accordingly to render a more accurate description of the complex capillarity-driven thinning dynamics of entangled polymer solutions as well as to obtain the key rheological parameters.

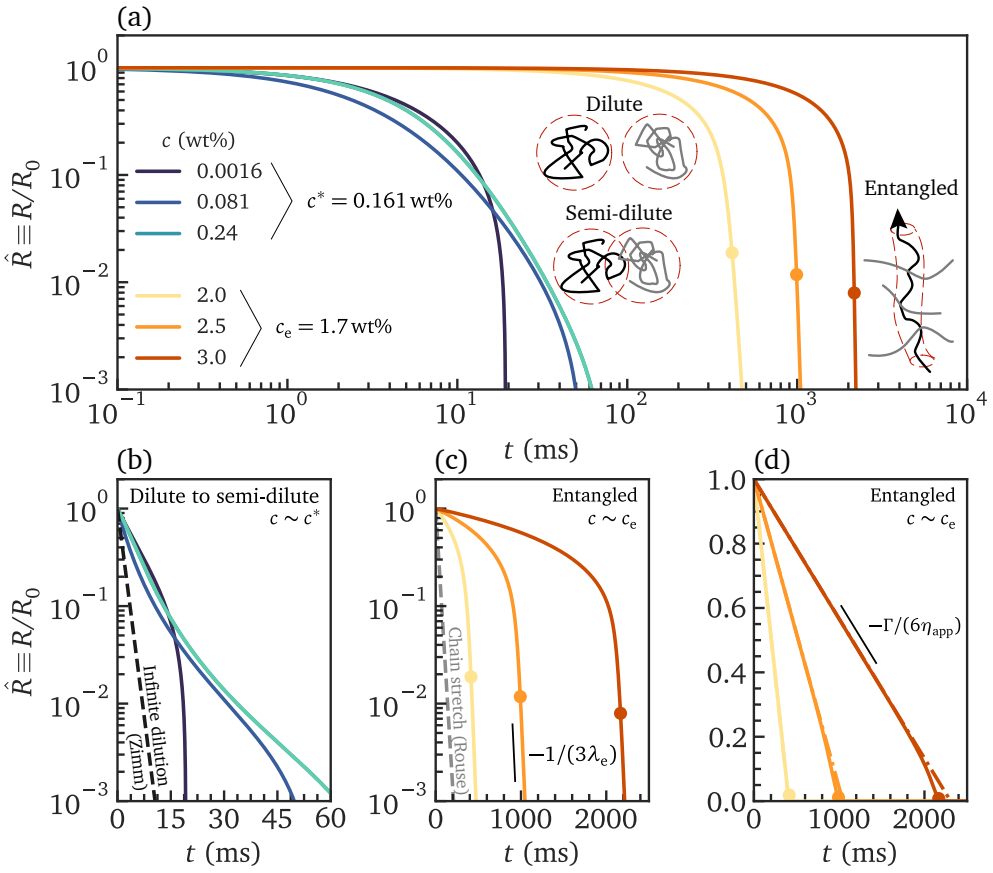

Figure 4-9: (a) Numerically calculated filament radius (nondimensionalized by the initial radius) for aqueous polyethylene oxide (PEO) solutions over the dilute and entangled concentrations, with both axes plotted on logarithmic scales. (b) Filament radius in the dilute and semi-dilute regimes described by a corrected FENE-P model [31], with the ordinate plotted on a logarithmic scale. The asymptotic exponential-thinning trend using the Zimm time ($\lambda_e = \lambda_Z$) is plotted as a black dashed line to show the filament thinning in the limit of infinite dilution. (c) Filament radius in the entangled regime described by the Rolie-Poly model, with the ordinate plotted on a logarithmic scale. The asymptote using $\lambda_e = \lambda_R/2$ is plotted as a gray dashed line to show the filament thinning in the limit of a uniform tube orientation. (d) Same plot as (c) with the filament radius plotted on a linear scale. The dashed dotted lines show the predictions from the visco-capillary thinning with the apparent zero-shear viscosity from Equation (4.8). The markers in (a), (c) and (d) for the entangled solutions denote the transition of the filament thinning to an exponential-thinning trend under an elasto-capillary balance.

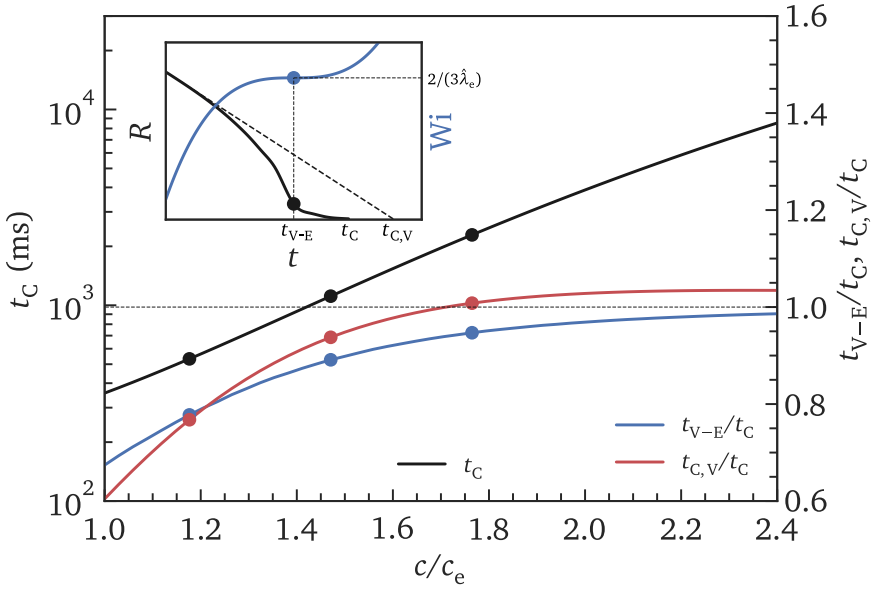

Figure 4-10: The filament breakup time t_C (black line) obtained from extrapolating the prediction line from the RP model to $R = 0$ against c/c_e for $1 \leq c_e \leq 2.4$. The other two timescales $t_{V\text{-}E}$ (blue) and $t_{C,V}$ (red) are plotted as ratios compared to t_C on the right axis, where unity is plotted as a thin dashed line for reference. The three selected concentrations in the entangled regime illustrated in Figure 4-9 are marked in circles on each curve. Inset: Schematic of the temporal evolution in the filament radius and Weissenberg number to illustrate the three timescales.

4.2 A case study: Cellulosic solutions

4.2.1 Concentrated cellulose/ionic liquid solutions

In this section, the aforementioned filament thinning dynamics predicted by the tube models are applied to a prototypical material system of concentrated cellulose/ionic liquid solutions to derive an accurate description of their rheological behavior in both shear and extensional flows. This material system has recently attracted great attention by the rapidly expanding fashion industry as an effort of transition to a circular economy [283]. While cellulose, due to its abundance in nature and superior biodegradability [284], has become one of the most promising alternatives to support an effective and non-toxic workflow in the manufacturing hierarchy, its thermal and chemical stability ascribed to the glucose structures also induce notorious processability and incompatibility with most solvents without destructing the glycosidic bonds, hence the overall polymer structures [285–288]. In many aspects, a recyclable universal solvent that can readily dissolve cellulose chains under mild conditions without compromising the original degree of polymerization (DoP) is desired [289]. Recently studies have suggested the use of ionic liquids for such applications. Ionic liquids (IL) are salts that melt under 100 °C, commonly comprised of large ions that inhibit the formation of crystalline structures. As a result, the amorphous molecular structures with high free energy can induce salt-like properties such as extremely low volatilities [290], while remaining in liquid state over a wide range of temperatures [291]. The free-moving ions can effectively disrupt the hydrogen-bond networks that abundantly contribute to the strong intramolecular attractions in cellulose structures, thus assisting the dissolution process and further tuning the cellulose properties (through altering the conformations) [292]. In practice, acetate, phosphate or chloride based ILs are commonly selected due to their high Kamlet-Taft parameters that enable strong interactions with the hydrogen-bonds [293], and imidazolium derivatives [294, 295] are adopted as the cations. Studies have interconnected the solvent qualities of ILs for cellulose with external conditions such as mixing protocols, temperature and viscosity, which in turn affects the dynamics of the resulting solutions (commonly referred as "dopes") [296, 297]. The dopes can be readily applied for the regeneration of cotton cellulose fibers through fiber-spinning processes, during which the cellulose/ionic liquid solutions undergo notably large shear and extensional deformations to induce the microstructural conformation, and are subsequently coagulated by the diffusion of antisolvent [298–301]. In practice, a high concentration of cellulose (into the entangled regime) is preferred for economic reasons. However, as the dopes become increasingly complex, it remains a challenge to obtain an optimal set of spinning parameters for the

Table 4.7: Concentrations, temperatures and DoPs of the cellulose/IL solutions for the rheological study.

Cellulose	DoP	c (wt%)	Z_{sol}	Temperature (°C)	Figure
CF	2710	2	2	25	4-11
FP	1340		≈ 1		
FP	1340	1	< 1	25	4-12
		2	≈ 1		
		3	2		
		4	4		
FP	1340	2	≈ 1	25	4-13
				40	
				60	
				80	

desired performance of spun fibers, due to an inadequate understanding of the dynamics and structural evolution during the spinning process at variations of the cellulose DoP, concentration and temperature. This limitation is addressed here by applying the previously proposed constitutive framework from Section 4.1, from which meaningful constitutive parameters can be obtained and further used as guidance to optimize of the cellulose spinlines.

Here, two cellulose fibers are selected for the study of the extensional rheology at varying concentrations, temperatures and DoPs: cotton fiber (CF, DoP=2710) and filter paper (FP, DoP=1340). The IL solvent is 1-ethyl-3-methylimidazolium, $[C_2C_1Im][OAc]$ (purity of 90%; Sigma-Aldrich, USA). All chemicals are used without further purification. The cellulose solutions were prepared by slowly adding the weighted solute into the selected IL at a temperature of 80 °C and stirring for 12 h to 36 h until no observation of the undissolved solute. The fully dissolved solution systems are removed from the hot plate and stored at room temperature. A range of different concentrations and temperatures are selected, with the highest temperature at 80 °C to be consistent with the working temperature at the spinneret in a typical spinning process [302]. The selected concentrations, temperatures and DoPs of the tested cellulose/IL solutions are listed in Table 4.7.

The extensional rheology is characterized through the customized CaBER introduced in Section 3.1 with a high-speed imaging system to capture the filament thinning pro-

files. The results are shown in the subfigures (a) of Figures 4-11 to 4-13 with varying DoP, concentrations and temperatures, respectively. From the snapshots, the minimum filament radius broadly exhibits linear decays, which are consistent with the filament thinning profiles governed by a visco-capillary balance. Close to the filament breakup, the filament profiles become increasingly complex and deviates from the linear trend due to the additional contributions from the large cellulose chain deformations. This transient rheological response can be better demonstrated in the subfigures (b) of Figures 4-11 to 4-13, where the apparent extensional viscosity $\eta_{\mathrm{e,app}}$ is calculated according to Equation (3.9). To induce consistent zero-rate viscosity (inelastic limit) with the measurement from shear rheology, the constant geometric correction factor is set as $X = X_{\mathrm{N}} = 0.7127$ predicted for a Newtonian fluid. Here, the surface tension is treated as a fitting parameter, which solely shifts the extensional flow curve in the ordinate without altering the overall trend, and a value of $\Gamma \approx 65 \times 10^{-3}\,\mathrm{mN/m}$ is obtained, which is generally consistent with the previous measurements [215]. To demonstrate the strain dependence of the spun fiber properties specifically relevant to a fiber spinning process, the apparent extensional viscosity $\eta_{\mathrm{e,app}}$ is plotted against the accumulated Hencky strain, which is defined as $\epsilon(t) = \epsilon_0 + \int_0^t \dot{\epsilon}(\xi)\mathrm{d}\xi = \epsilon_0 + 2\ln[R_0/R(t)]$. Here, ϵ_0 represents a residue axial strain in the filament prior to the onset of capillarity-driven thinning, which arises from the pre-induced polymer chain conformation that cannot be randomized in a timely manner due to the large Strokes drag. By comparing subfigures (b) and subfigures (c), which plot steady shear flow curves from independent measurements, the value of $\eta_{\mathrm{e,app}}$ is found to remain approximately at $3\eta_0/(2X_{\mathrm{N}} - 1) \approx 7.05\eta_0$ at small Hencky strains ($\epsilon \lesssim 5$), where η_0 is the zero-shear viscosity. At a small DoP (*i.e.*, FP with DoP=1340) or concentration (*e.g.*, $c \leq 2\,\mathrm{wt\%}$), where the polymer chains are less entangled, the apparent extensional viscosity increases steadily beyond $\epsilon \approx 5$. In contrary, as the degree of entanglements increases, the apparent extensional viscosity notably exhibits strain-softening behavior.

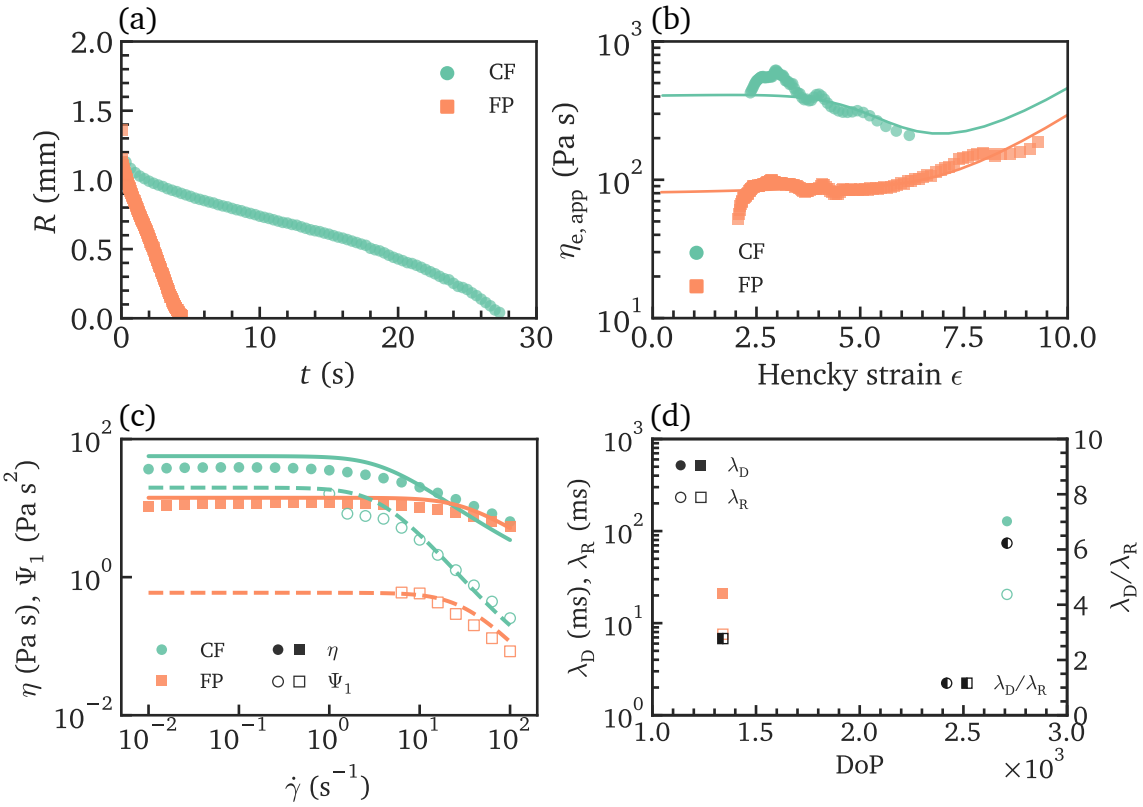

Figure 4-11: Steady shear and transient extensional rheological characterizations for cellulose/ionic liquid solutions at varying cellulose DoPs, cotton fibers (CF) with DoP=2710 and filter papers (FP) with DoP=1340, at $c = 2$ wt% and 80 °C. (a) Temporal evolution of minimum filament radius $R(t)$ from CaBER measurements. (b) Apparent extensional viscosity $\eta_{e,app}$ against Hencky strain ϵ extracted from CaBER measurements. Solid lines: fitted lines from Rolie-Poly model. (c) Steady-state shear viscosities η and first normal stress coefficients Ψ_1. Data of the first normal stress coefficient are truncated below certain shear rates due to approaching the limit of the normal force sensor. Solid and dashed lines: fitted lines of η and Ψ_1 from Rolie-Poly model, respectively. (d) Disengagement time λ_D (filled markers), Rouse time λ_R (hollow markers) and ratio of the two timescales λ_D/λ_R (half-filled markers) against the varying parameter.

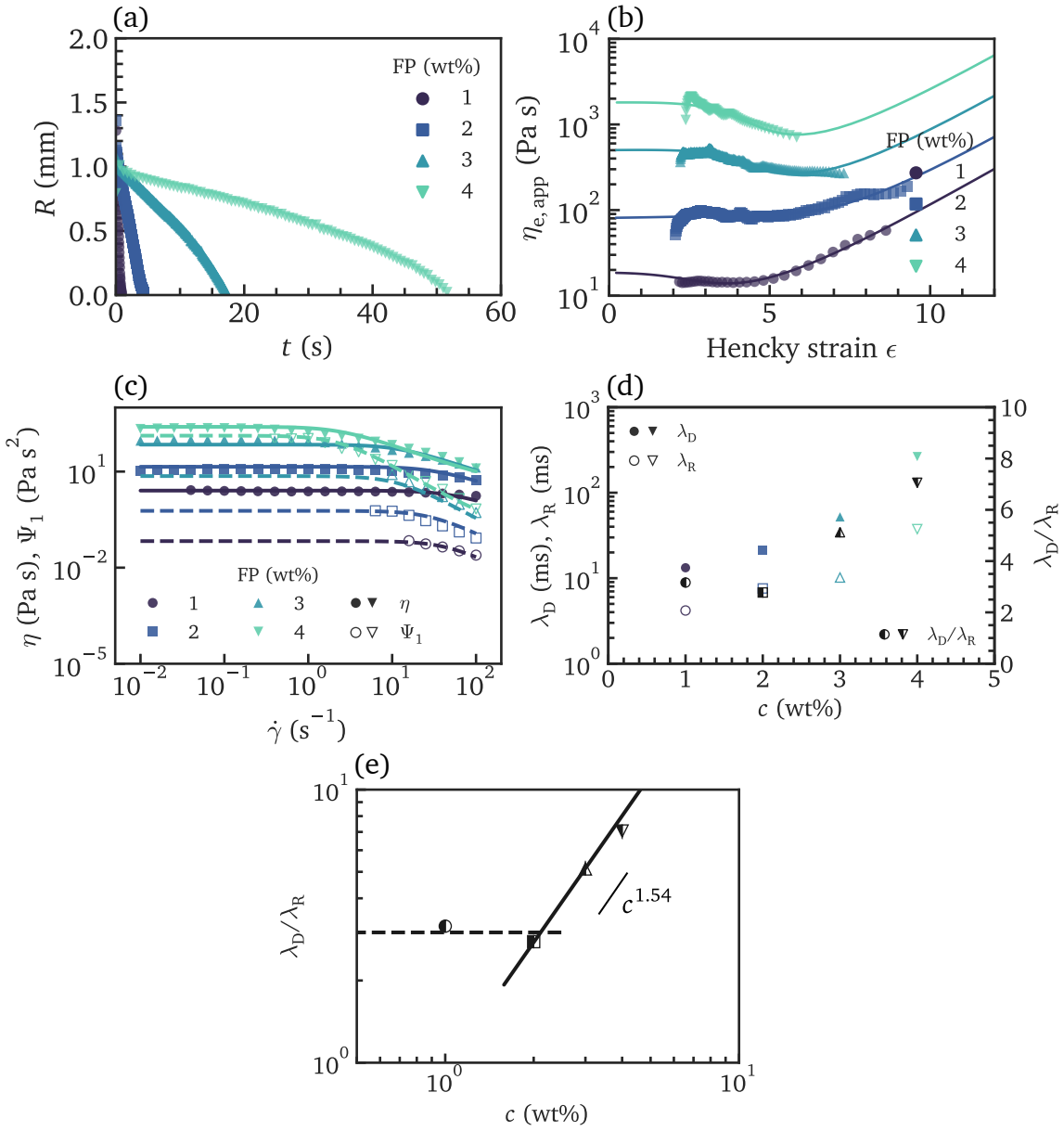

Figure 4-12: Steady shear and transient extensional rheological characterizations for cellulose/ionic liquid solutions at varying cellulose concentrations c = 1 wt%, 2 wt%, 3 wt% and 4 wt% for filter papers at 25 °C. (e) λ_D/λ_R against c on logarithmic scales. A power law trend of with an exponent of 1.54 can be obtained from numerical fitting. Other subfigure formats are identical with Figure 4-11.

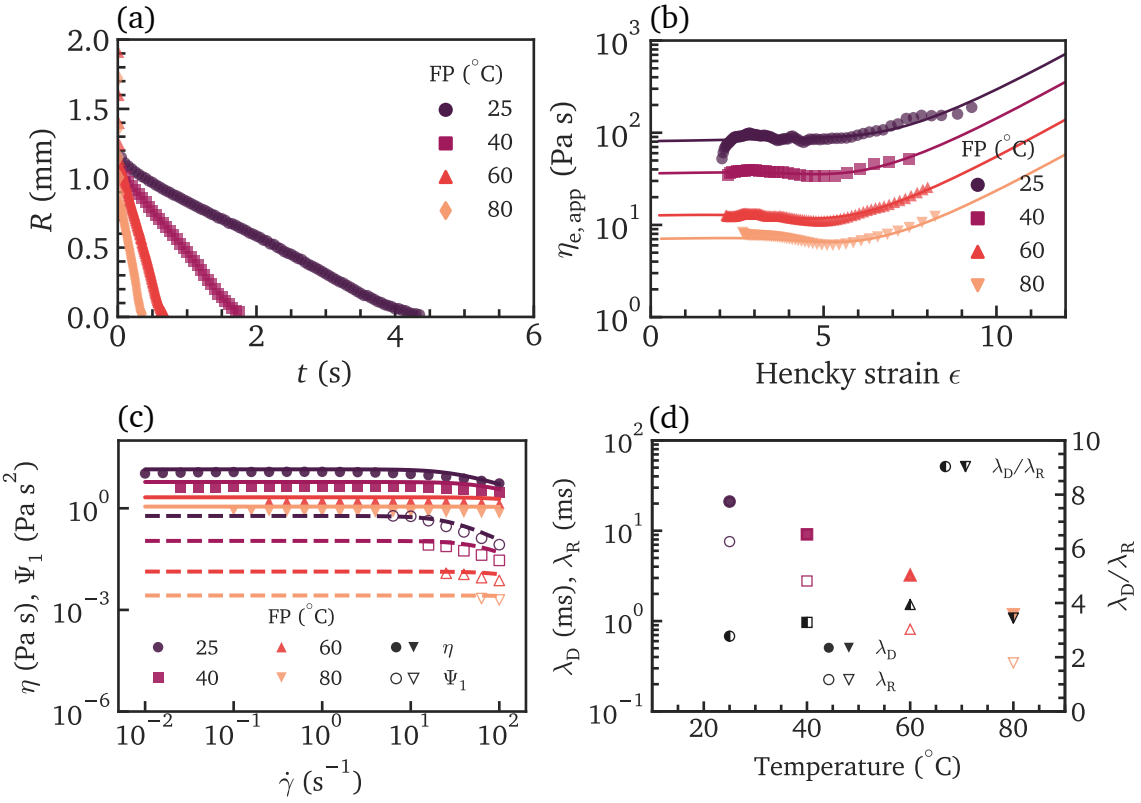

Figure 4-13: Steady shear and transient extensional rheological characterizations for cellulose/ionic liquid solutions at varying temperatures 25 °C, 40 °C, 60 °C and 80 °C for FP at $c = 2$ wt% for filter papers. Subfigure formats are identical with Figure 4-11.

The evolution in $\eta_{e,app}$ is instantly reminiscent of the predictions from the tube models for entangled polymer solutions as illustrated in Section 4.1[2]. Notably, the extensional flow imposes an alignment to the entangled cellulose segments, and the overall resistance to the capillary pressure decreases progressively, resulting in a faster capillarity-driving thinning process close to the filament breakup.

The constitutive parameters can be obtained by fitting the theoretical predictions from the tube models to the extracted flow curve from the CaBER measurements. However,

[2]In Section 4.1, the extensional viscosity as illustrated in Figure 4-7 is plotted against the strain rate (or in the dimensionless form of Wi_D). Nevertheless, both the strain rate and Hencky strain increase monotonically with time by definition, thus the evolution in the apparent extensional viscosity exhibit similar trends.

due to a limited imaging resolution, the CaBER measurements only capture partial features of the theoretical prediction. As a result, a direct extraction that solely relies on the measurements in extensional flow can lead to large overfitting errors. To improve the fitting accuracy, independent steady-shear measurements are performed on the tested samples (DHR-3, TA Instruments, USA) at identical conditions to obtain both shear viscosities (filled markers) and first normal stress coefficients (hollow markers), as shown in the subfigures (c) of Figures 4-11 to 4-13. Subsequently, a comprehensive fitting protocol is implemented to incorporate the measurements from both flows by the addition of their error functions, thus leading to a full-dimensional description of the rheological behavior regardless of the flow type. In addition, the finite extensibility term in the tube models is neglected by setting $\Lambda_m \to \infty$ due to the inaccessible measurements at high Hencky strains, thus reducing the fitting parameters to the plateau modulus G_N, the disengagement time λ_D, the Rouse time λ_R and the surface tension Γ. Finally, the fitting lines from the Rolie-Poly model are plotted in both subfigures (b) and (c) of Figures 4-11 to 4-13 as solid and dashed lines, and they are in excellent agreement with the experimental data at the selected ranges of DoP, concentration and temperature.

The two extracted timescales λ_D and λ_R are explicitly plotted against the varying parameters in the subfigures (d) of Figures 4-11 to 4-13. As shown in these figures, both the extracted disengagement time λ_D (filled markers) and Rouse time λ_R (hollow markers) increase in magnitude with DoP (Figure 4-11(d)) or concentration (Figure 4-12(d)), and their ratio λ_D/λ_R (half-filled markers) also exhibits similar trends. Such increasing trends can be justified from an increased number of entanglements per chains according to Equation (4.1). Notably, Figure 4-12(e) plots λ_D/λ_R against c on logarithmic scales, and a piecewise trend can be identified. When $c \lesssim 2\,\text{wt\%}$, the time ratio remains approximately constant at 3. From Equation (4.1), this corresponds to a nearly unentangled state. However, beyond $c \approx 2\,\text{wt\%}$, the time ratio is shows a power-law trend, which can be numerically fitted to obtain an exponent of 1.54. This value agrees well with Equation (4.12) and Equation (4.1) when an approximation of $\nu = 0.55$ is specified under a good-solvent condition. In contrary, the magnitude of $p(Z)$ remains broadly constant at varying temperatures (Figure 4-13(d)) because the state of entanglements remains nearly unmodified.

The characterizations of the extensional rheological properties of the cellulose/ionic liquid solutions unravel the details in the complex dynamics of the materials during large extensional deformation occurring in a spinning process. In particular, the strain-softening behavior is exclusively captured from the tube models. Such rate-dependence may induce subtle flow instability, which can be critical to determine the

dope "spinnability". The extraction of the two timescales further justify a faster relaxation process dominated by the Rouse time in extensional flow at high Hencky strains, compared with a longer disengagement time in shear flow. A more profound understanding of the extensional rheology has provided abundant information in designing the optimal spinning parameters for the concentrated cellulose/IL solutions.

4.2.2 Hydroxyethyl cellulose solutions

Hydroxyethyl cellulose (HEC) is another type of derivative from natural cellulose, which finds extensive applications in cosmetic and oil industries to improve dissolution and flow assurance [26]. The extensional rheology is of central interest in the processing of these materials and previous studies have applied capillarity-driven breakup techniques to characterize the extensional rheology of these materials over a wide range of strain rates that are closely related to real applications [26,32,245,303,304].

In particular, a recent study by Dinic et al. [32] using the dripping-on-substrate (DOS) rheometry has identified general power-law trends for the filament radius, namely, $R \sim (t_C - t)^n$ at high HEC concentrations beyond the entangled concentrations c_e. Close to filament breakup, distinct filament thinning behavior arises, in which the filament radius undergoes a short period of exponential thinning trend, followed by a linear thinning trend till pinch-off singularity. This trend implies the existence of an elasto-capillary thinning regime at high strain rates, as well as a finite terminal extensional viscosity. To describe the measured filament thinning profiles, Dinic et al. fitted the particular kinematic region close to the filament breakup using the four-parameter phenomenological expression proposed by Anna and McKinley [258] which can be written as

$$\frac{R(t)}{R_0} = A \cdot \exp(-Bt) - Ct + D. \tag{4.18}$$

This empirical expression is found to give good agreement with experiments for $R/R_0 \lesssim 0.2$. In light of the dynamics characterized for entangled polymer solutions proposed in this chapter, the original data (provided by Dinic et al.) are re-fitted with the Rolie-Poly model. As shown in Figure 4-14, the filament thinning profiles measured from a series of aqueous HEC solutions with molecular weights of 0.72 MDa (circles) and 1.3 MDa (squares) at varying HEC concentrations show distinct filament thinning trends. The entangled concentrations c_e for the two molecular weights are measured as 0.5 wt% and 0.2 wt%, respectively. When the HEC concentration is smaller than c_e, the samples generally exhibit extension-thickening behavior with a concave evolution in the filament radius with time. However, the filament thinning profiles become increasingly

complex as the concentration exceeds c_e, where rate-thinning trends can be observed at early thinning regimes ($0.1 \lesssim R(t)/R_0 \lesssim 0.8$), but subtle rate-thickening regimes can be captured close to filament breakup, where a slight inflection in the filament thinning profile can be noticed (below $R(t)/R_0 \lesssim 0.1$). This complex trend is partially evident in the measurements of the highest concentrations of either molecular weight. The filament thinning trends described in Figure 4-14 are very consistent with

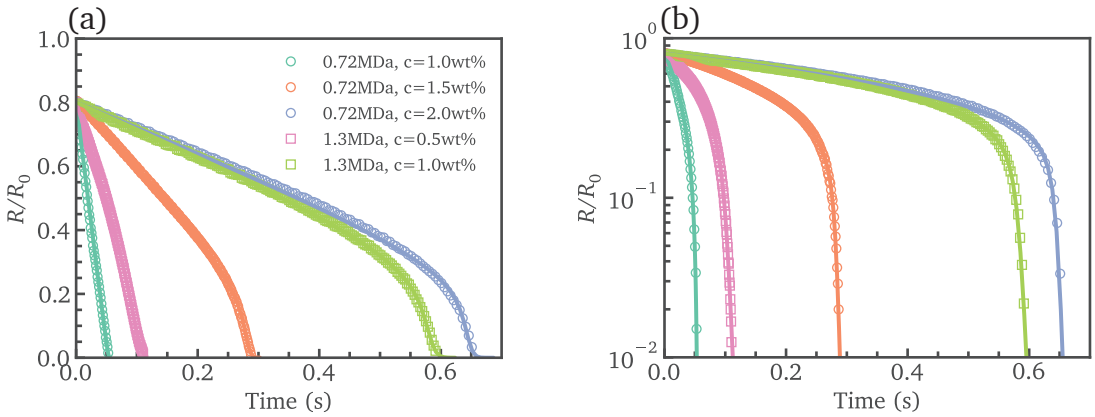

Figure 4-14: Filament thinning profiles for aqueous HEC solutions with molecular weights of 0.72 MDa (circles) and 1.3 MDa (squares) at varying HEC concentrations, with the ordinate plotted on (a) linear scales, and (b) logarithmic scales. Solid lines are fitted lines from the Rolie-Poly model. Experimental data provided by courtesy of Dinic et al. [32].

the predictions from the tube models at varying values of elasto-capillary numbers, as illustrated in previous sections. As a consequence, the Rolie-Poly model can quantitatively capture the filament thinning profiles at varying HEC molecular weights and concentrations within a single unified constitutive framework. Here, Equation (4.7) is numerically calculated, and a best-fit set of parameters (G_N, λ_D and λ_R; an infinite extensibility limit $\Lambda_m \to \infty$ is specified due to a limited range of experimental data) is obtained through least square regression. The results, shown as solid lines in Figure 4-14 are in excellent agreement with the experimental data down to a filament radius of as small as $R/R_0 \approx 0.01$. Considering a typical capillarity-driven experiment, where $R_0 \approx 1$ mm to 3 mm, this accuracy corresponds to a minimum filament radius of approximately 10 µm, which is close to the instrument optical limitation. In Figure 4-15, we plot the timescale ratio λ_D/λ_R for each molecular weight against $c[\eta]$ extracted from data fitting, where $[\eta]$ is the intrinsic viscosity, measured as 5.98 dL/g (for $M = 0.72$ MDa) and 5.98 dL/g (for $M = 1.3$ MDa). From Equation (4.1), the number

of entanglements per chain in solutions Z_{sol} can also be numerically calculated, and the results are plotted on the right ordinate as black markers. As the value of Z increases far above unity, the polymer solutions of both molecular weights become increasingly entangled, and the scaling law of $Z_{sol} \sim c^{1/(3\nu-1)}$ from Equation (4.12) is recovered, as shown in the figure with $\nu = 0.55$ [32] as a black dashed line. The deviation from this power-law trend at the lowest concentration of $M = 0.72\,\text{MDa}$ can be attributed to its marginally entangled state, with $Z_{sol} \approx 1$. The agreement between the measured

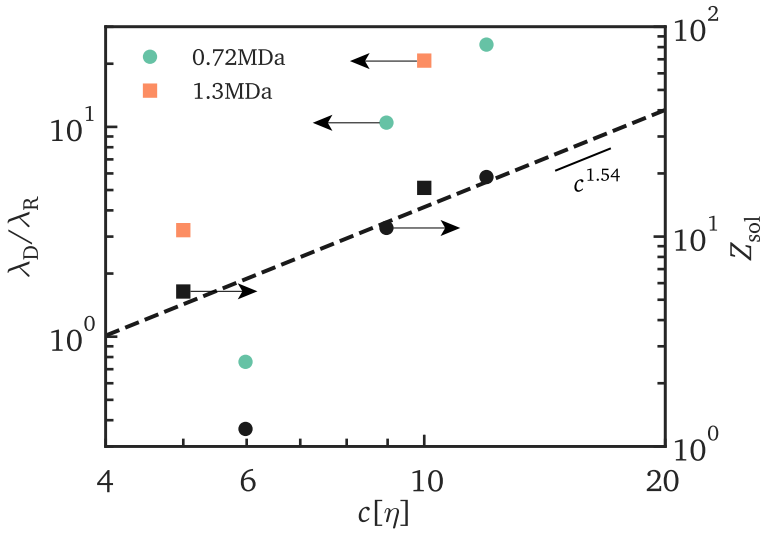

Figure 4-15: Ratio of disengagement time and Rouse time, λ_D/λ_R against $c[\eta]$, where the intrinsic viscosities $[\eta]$ are measured by Dinic et al. as 5.98 dL/g (for $M = 0.72\,\text{MDa}$) and 5.98 dL/g (for $M = 1.3\,\text{MDa}$). The number of entanglements per chain in solutions Z_{sol} is extracted from Equation (4.1), and the results from both molecular weights approach the expected power-law trend of $c^{1/(3\nu-1)}$ shown as a black dashed line, where $\nu = 0.55$ is taken.

filament thinning profiles and the predictions from the Rolie-Poly model demonstrates a more physical picture elucidated by the tube models applied in this chapter on the conformation of polymer chains in entangled polymer solutions under extensional deformation, from which new insights can be provided in the filament thinning dynamics that have been previously fitted with phenomenological expressions such as power-law trends or Anna-McKinley equations.

4.3 Summary

This chapter extended the analysis of capillarity-driven thinning dynamics to the entangled polymer regime, which shows increasingly complex rheological behavior that is governed by multiple timescales. To derive a robust model that incorporates the dynamics of entangled polymer chains, reptation theory was applied and the filament thinning dynamics based on two tube models (the DEMG model and the Rolie-Poly (RP) model) were calculated numerically. While both models incorporate the idea of "tube segments" to describe the interactions of polymer chains as well as the contour length fluctuation in a mean-field framework, the two models differ slightly in constitutive form due to the addition of convective constraint release (CCR) in the RP model. Both models reveal complex filament thinning profiles governed by distinct stress contributions in different thinning stages. At early times, the filament thinning profile is similar to the prediction from a simple visco-capillary balance with a progressive rate-thinning trend due to tube reorientation. An apparent viscosity η_{app} can be determined from numerical fitting that scales with $G_N\lambda_D$, where G_N is the plateau modulus and λ_D is the disengagement time. As the tubes become uniformly aligned in the extensional direction, the filament thinning profile is subsequently governed by the stretching of the chain segments in the aligned tubes, which exhibits an exponential decay that is consistent with the prediction from the Hookean dumbbell model. Notably, an *apparent* extensional relaxation time λ_e can be extracted from fitting this exponential thinning in $R_{mid}(t)$, and its value approaches half the Rouse time ($\lambda_R/2$) as the number of entanglements per chain Z increases. Finally, the tube extension approaches the finite extensibility, and the filament thinning profile approaches a linear decay with time as well as a terminal extensional viscosity of $\eta_{e,\infty} = 2G_N\lambda_R\Lambda_m^2/(1-1/\Lambda_m)$.

Despite the general applicability of the FENE-P model for describing the shear and extensional behavior of dilute polymer solutions, it fails to capture the non-trivial ratio of relaxation times extracted from shear and extensional flows, λ_e/λ_s, when the polymer solutions become sufficiently concentrated. By virtue of the distinct timescales that govern the tube reorientation and the chain stretch processes in the two selected models, an analytical expression for such ratio can be readily derived as a function of the concentration c and the molecular weight between entanglements in the melts $M_{e,0}$ (see Equation (4.13) and Figure 4-6). This expression shows excellent agreement with a number of previous studies focusing on different entangled polymer solutions, and provides a physical origin of the distinct relaxation times arising from different flow kinematics without introducing additional fitting parameters.

Finally, the extensional rheology predicted by the tube models was applied to a case

study of cellulose/ionic liquid solutions, which have recently gained especial attention in the clothing industry for the design of a circular economy through fiber spinning and regeneration. In practice, a high concentration of these solutions in the entangled regime is preferred for economic reasons, which contribute to the rheological complexity of the spinning dopes. It is thus critical to obtain a comprehensive understanding of the rheology of the spinning dopes to optimize the regeneration process and to reach desired mechanical properties for the spun fibers. Both shear and extensional rheological studies were carried out at various degrees of polymerization (DoP), concentrations and temperatures through a commercial shear rheometer and a customized Capillary Breakup Extensional Rheometer. The resulting shear viscosity, first normal stress coefficient and the apparent extensional viscosity can be well described by the Rolie-Poly model with a universal set of constitutive parameters. The measured ratio of the disengagement time and the Rouse time showed consistent trends with the number of entanglements per chain, providing a convenient relationship between the structural information of cellulose conformation in the entangled regime and the resulting rheological behavior.

We also apply our theory to data reported in a previous study which measured filament thinning profiles of a series of aqueous hydroxyethyl cellulose (HEC) solutions. The Rolie-Poly model was applied to the data fitting, and the results showed excellent agreement with the experimental measurements at a range of HEC concentrations and molecular weights.

To conclude this chapter, the filament thinning dynamics for a number of frequently used constitutive models are summarized in Table 4.8 with the addition of the works from this thesis. For readers' information, this table is aimed at providing convenient lookup information to quantify the extensional rheology of an unknown sample measured through the capillary breakup techniques.

Table 4.8: List of common constitutive models and the predicted form of the temporal evolution in the minimum filament radius for extensional rheological characterizations using the capillary breakup technique. Table adapted from Refs. 29 and 35.

Constitutive model	$R(t) =$ (full or asymptotic)	Ref.
Bingham plastic	$\frac{\Gamma}{\sqrt{3}\tau_y}\left\{1-\exp\left[\frac{\tau_y(t-t_C)}{2\sqrt{3}\eta_0}\right]\right\}$	35

(*Continued*)

Table 4.8 (*continued*)

Constitutive model	$R(t) =$ (full or asymptotic)	Ref.
Power-law fluid	$\frac{R_0\Phi(n)\Gamma}{K}(t_C - t)^n$	35, 305
Newtonian fluid	$\frac{0.0709\Gamma}{\eta_0}(t_C - t)$	207, 210, 306
Inelastic rate-thickening (IRT)[a]	$\dot{\epsilon} \ll \eta_0/k_2$: $\frac{\Gamma}{6\eta_0}(t_C - t)$ $\dot{\epsilon} \gg \eta_0/k_2$: $\frac{\Gamma}{48k_2}(t_C - t)^2$	This thesis, 29
Upper-convected Maxwell (UCM)[b]	$\left(\frac{GR_0^4}{2\Gamma}\right)^{1/3} \exp\left(-\frac{t}{3\lambda}\right)$	208, 237
FENE-P[c]	$\dot{\epsilon} \ll 2/(3\lambda)$: $\frac{\Gamma}{6\eta_S}(t_C - t)$ $\dot{\epsilon} \sim 2/(3\lambda)$: $\sim \exp\left(-\frac{t}{3\lambda}\right)$ $\dot{\epsilon} \gg 2/(3\lambda)$: $\frac{\Gamma}{2\eta_{e,\infty}}(t_C - t)$	244
Tube models[d]	$\dot{\epsilon} \ll 4/(3\lambda_R)$: $\frac{\Gamma}{6G_N\lambda_D}(t_C - t)$ $\dot{\epsilon} \sim 4/(3\lambda_R)$: $\sim \exp\left(-\frac{2t}{3\lambda_R}\right)$ $\dot{\epsilon} \gg 4/(3\lambda_R)$: $\frac{\Gamma}{2\eta_{e,\infty}}(t_C - t)$	This thesis

[a] Assume $X = 1$ for the two asymptotic solutions. The incorporation of a temporally evolving X is detailed in Section 3.2.2.

[b] Assume $X = 1.5$. A mathematical derivation of this value can be found in Clasen et al. [237].

[c] Assume $X = 1$ in the limit of $\dot{\epsilon} \ll 2/(3\lambda)$ and $\dot{\epsilon} \gg 2/(3\lambda)$. When $\dot{\epsilon} \sim 2/(3\lambda)$, a scaling relation is presented rather than an asymptotic solution with a determinate prefactor, as the solution of X under the elasto-capillary thinning is still an ongoing debate. In practice, the slope, instead of the prefactor is commonly extracted to obtain an extensional relaxation time. The terminal extensional viscosity $\eta_{e,\infty} = 2G\lambda\Lambda_m^2$.

[d] Using DEMG model. Terminal extensional viscosity $\eta_{e,\infty} = 3G_N\lambda_R\Lambda_m^2/(1 - 1/\Lambda_m)$ (Equation (4.10)).

5 Characterization of Graphene-Derived Nanocomposites and Optimization of Dispersion

5.1 Material preparation and structural characterization

In this chapter, a prototypical GDNC system is selected for a comprehensive rheological characterization based on the measuring protocols proposed in previous chapters. The extracted rheological information can be further connected to a structural characterization obtained from scattering methods to justify the correlation between the material responses and the microstructure. Here, the aqueous graphene-oxide (GO)/polyvinyl alcohol (PVA) system is selected due to the hydrophilic nature of GO molecules as well as their excellent compatibility with the PVA chains to minimize nanofiller agglomeration. The affinity of GO with PVA molecules arises from the formation of strong hydrogen bonds between a number of the carboxyl groups from GO molecules and the hydroxyl groups from PVA molecules, as illustrated in Figure 5-1. As a result, the GO/PVA nanocomposites are widely used as an easily synthesized system for a variety of applications [307–312].

In this study, the weight concentration of PVA is fixed at 9.1 wt% to produce solutions with moderate viscosities to facilitate the measurements. A range of GO concentrations is selected from 0 wt% to 0.4 wt% to investigate the rheological modifications at different GO loadings. Such concentration selections are consistent with the range of loadings for the industrial applications of graphene-derived nanofillers due to economic reasons, in which the state of dispersion becomes critical in the property enhancement [313, 314].

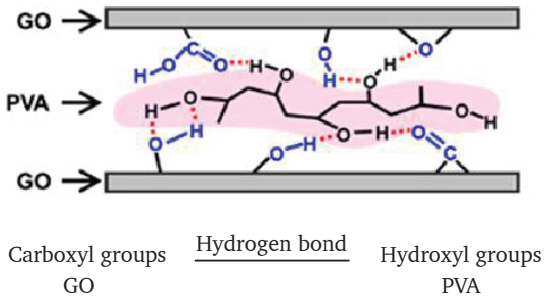

Figure 5-1: Intercalation of nanofillers in GO/PVA nanocomposites, showing the formation of hydrogen bonds between the carboxyl groups on GO molecules and the hydroxyl groups on PVA chains. Reproduced from Ref. [33].

The GO/PVA nanocomposites are synthesized by first mixing 0.4 wt% aqueous GO masterbatch (Graphenea, Spain) with deionized water (VWR International, USA) to obtain the dispersion with desired GO concentrations. The size distribution for the GO nanofillers is characterized using scanning microscope microscope (Zeiss Merlin High-resolution SEM; Zeiss, Germany), and the results are shown in Figure 5-2. A log-normal distribution can be readily fitted and an averaged nanofiller diameter can be obtained as $2a = 3389.3$ nm. The aqueous GO dispersion is subsequently sonicated for 1 hr to obtain a well-exfoliated system. Finally, the aqueous GO dispersion is heated to 90 °C in a water bath with the application of stirring at 400 rpm. PVA powders (M_w: 89 000 Da to 98 000 Da; Sigma-Aldrich, USA) are weighted and gently added to the GO dispersion with a funnel. The mixture is kept stirred for another 2 hrs in the water bath at 90 °C until the solution becomes homogeneous. The solutions are removed from the water bath and cooled to 60 °C, before moving onto a roller mixer for another 2 hrs. All the samples are stored at a temperature of 4 °C.

5.2 Shear rheology

The shear rheology of the PVA/GO nanocomposites is investigated on a commercial shear rheometer (ARES-G2; TA Instruments, USA) with a 40 mm, 2° cone-and-plate geometry at 25 °C. To prevent dehydration during long shearing measurements, the sample between the cone and plate geometry is sealed with nonpolar *n*-decane (Sigma-Aldrich, USA) with negligible impact on the rheological measurements due to its much smaller viscosity (approximately 0.89 mPa s).

The steady flow curves are shown in Figure 5-3 for a shear-rate range of 0.01 s^{-1}

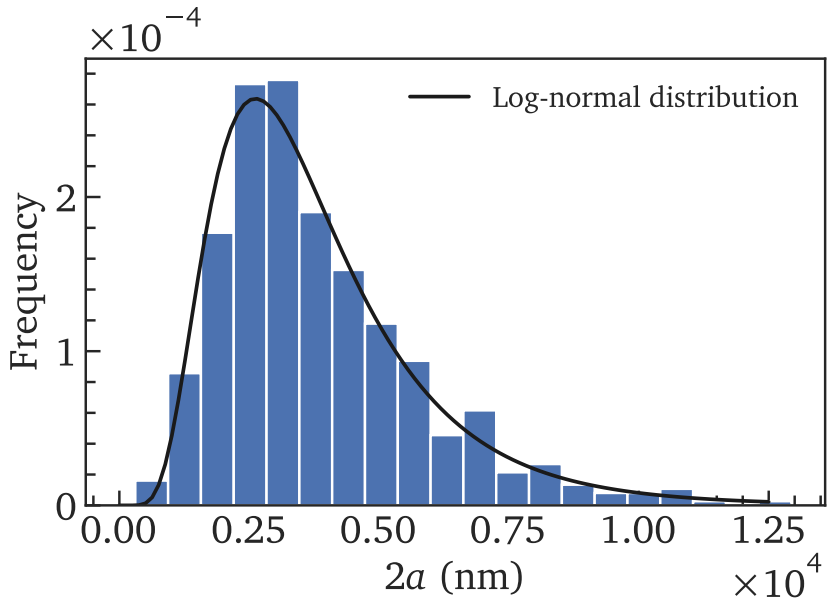

Figure 5-2: Size distribution of the GO nanofillers extracted from SEM imaging. An averaged nanofiller diameter can be obtained from fitting a log-normal distribution (black solid line) as $2a = 3389.3\,\text{nm}$.

to $100\,\text{s}^{-1}$. A clear manifestation of shear-thinning behavior is captured when GO nanofillers are added, and the overall shear viscosity increase with the GO concentration. From Figure 5-3, the shear stress at low shear rates approach constant as a result of the elasticity arising from the formed nanofiller network. This trend in the shear stress can be broadly described by the three-parameter Herschel-Bulkley (H-B) model [135], which can be expressed as

$$\sigma(\dot{\gamma}) = \sigma_\text{y} + k\dot{\gamma}^n. \tag{5.1}$$

Here, $\sigma_\text{y} = \lim_{\dot{\gamma}\to 0}\sigma(\dot{\gamma})$ is the yield stress. The power-law trend of the shear stress at high shear rates can be described by k and n. As shown in Figure 5-3(b), the H-B model (dashed lines) broadly agrees with the experimental data at varying GO concentrations. Notably, at low GO concentrations ($c \lesssim 0.2\,\text{wt\%}$), a non-monotonic trend in the shear viscosity arises at low shear rates, which cannot be accurately captured by the H-B model. This trend has been reported by previous studies on aqueous GO dispersions [106, 107], in which the stress increase at low shear rates can be attributed to the

Brownian diffusion of nanofillers that drives structural reconstruction. As the shear rate increases, the diffusion-driven mechanism is disturbed by a strong convective flow, which weakens the structural integrity of the spanning nanofiller network, leading to a rheological response that is primarily dominated by the hydrodynamic interaction between the nanofillers and the continuous phase. To better describe the trend in the flow curve, a thixotropic term can be readily added to the H-B model, in which the yield stress can be expressed as a function of a structural variable θ [315] as

$$\sigma_{\mathrm{y}} = \theta \sigma_{\mathrm{y,0}}, \tag{5.2}$$

where $\sigma_{\mathrm{y,0}}$ is the yield stress with full microstructural integrity. The structure parameter is a dimensionless internal state variable to characterize the microstructure, and its value is constrained within a range of $0 \leq \theta \leq 1$, where $\theta = 0$ implies full breakdown of the microstructure, and $\theta = 1$ implies a fully recovered structure. The temporal evolution of the structural variable is resulted from shear-induced breakdown and simultaneous buildup. Here, a canonical governing equation can be adopted [316] as

$$\dot{\theta} = -\theta|\dot{\gamma}| + \frac{1-\theta}{\lambda_{\mathrm{th}}}, \tag{5.3}$$

where λ_{th} characterizes a timescale in which the microstructure rejuvenates. Consequently, under a steady-state condition by imposing $\dot{\theta} = 0$, Equation (5.2) can be substituted into the original H-B model (Equation (5.1)), leading to new expression for the steady-state shear viscosity incorporating the microstructural evolution as

$$\sigma(\dot{\gamma}) = \frac{\sigma_{\mathrm{y,0}}}{1 + \lambda_{\mathrm{th}}\dot{\gamma}} + b\dot{\gamma}^{n}. \tag{5.4}$$

The term $\lambda_{\mathrm{th}}\dot{\gamma}$ serves as a measure for the flow-induced microstructural variation. As Figure 5-3 shows, the new fitting results, as plotted as solid lines, capture the trend of shear stress at low shear rates accurately. Figure 5-4 further plots the constitutive parameters extracted from both models (H-B model: filled markers; thixotropic H-B model: hollow markers). General trends in the yield stress (σ_{y} and $\sigma_{\mathrm{y,0}}$) and the power-law exponent n can be identified as the GO concentration varies. In brief, the addition of nanofillers increases the yield stress, while the power-law exponent of n decreases as the concentration increases, resulting in more apparent shear-thinning behavior. As shown in Figure 5-4, the extracted rejuvenation timescale λ_{th} remains broadly constant at approximately 10 s to 15 s at intermediate GO concentrations ($c \leq 2$ wt%). The rapid decrease of λ_{th} at higher GO concentration can be attributed to the non-monotonic trend in shear stress being shifted to a lower shear rate, which is out

of the measuring scope.

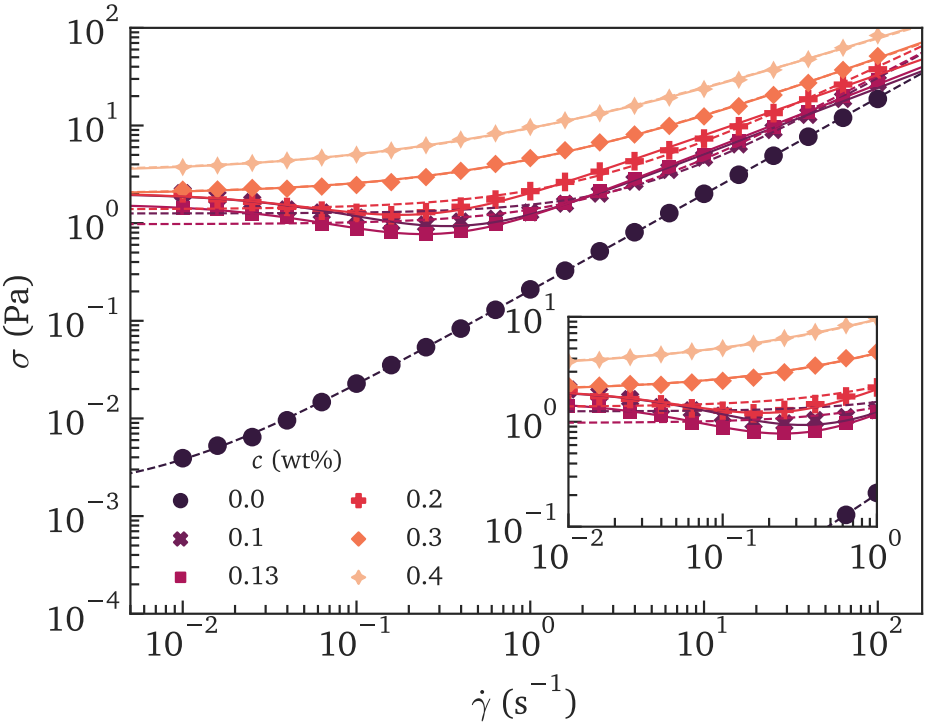

Figure 5-3: Steady shear stress σ of GO/PVA systems against shear rates $\dot{\gamma}$ at varying GO concentrations at 25 °C. The dashed lines are fitted from the Herschel-Bulkley model (Equation (5.1)), and the solid lines are fitted from the thixotropic Herschel-Bulkley model (Equation (5.4)). Inset: Zoom-in view in the shear-rate range of $1 \times 10^{-2}\,s^{-1}$ to $1\,s^{-1}$ and the stress range of 1×10^{-1} Pa to 1×10^{1} Pa.

Because the structural rejuvenation process is primarily driven by the Brownian diffusivity, the Peclet number, Pe can be used as an alternative metric to evaluate the flow strength [107] as

$$\mathrm{Pe} \equiv \frac{a^2\dot{\gamma}}{D}, \tag{5.5}$$

where a is the major-axis lengthscale of spheroidal nanofillers as defined in Figure 2-3, and D is the diffusivity of nanofillers. Due to a high aspect ratio, the nanofiller

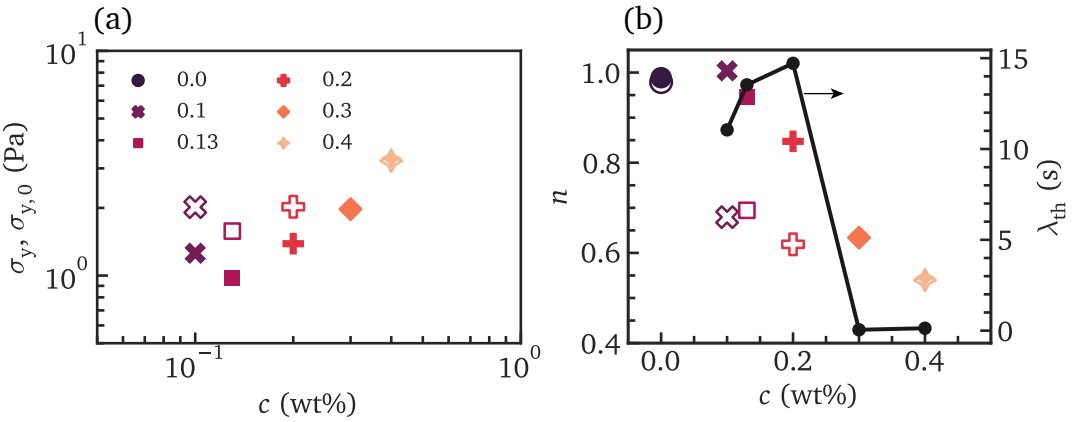

Figure 5-4: Parameters obtained from the H-B model (filled markers) and the thixotropic H-B model (hollow markers): (a) Yield stress σ_y; (d) Power-law exponent n. Solid line: Rejuvenation timescale λ_{th}. Legend indicates the GO concentration, shared by both subfigures.

mobility is mainly attributed to rotation, and the diffusivity for oblate spheroids can be thus approximated [114] as

$$D \approx \frac{3kT}{4\eta_S a}, \tag{5.6}$$

where η_S is the viscosity of the continuous phase. Due to the similarity of $\lambda_{th}\dot{\gamma}$ and the Peclet number in their physical interpretations, the rejuvenating timescale λ_{th} can be expressed in a form of the nanofiller geometry as

$$\lambda_{th} \sim \frac{4\eta_S a^3}{3kT}. \tag{5.7}$$

In the studied GO/PVA system, the averaged nanofiller is approximately $a = 1.7\,\mu m$ from Figure 5-2, and the viscosity of continuous phase is $\eta \approx 0.1\,Pa\,s$, leading to an estimated rejuvenating timescale $\lambda_{th} \approx 158\,s$. This estimate is consistent with the extracted λ_{th} from the steady flow curve, as shown in Figure 5-4(b).

The linear viscoelasticity is characterized through small amplitude oscillatory shear (SAOS). A small strain of $\gamma_0 = 2\%$ is selected to probe the frequency response in the linear regime. As shown in Figure 5-5, the dynamic moduli (storage moduli G': filled markers; loss moduli G'': hollow markers) are plotted separately for each concentration with shared ranges of both the abscissa and ordinate.

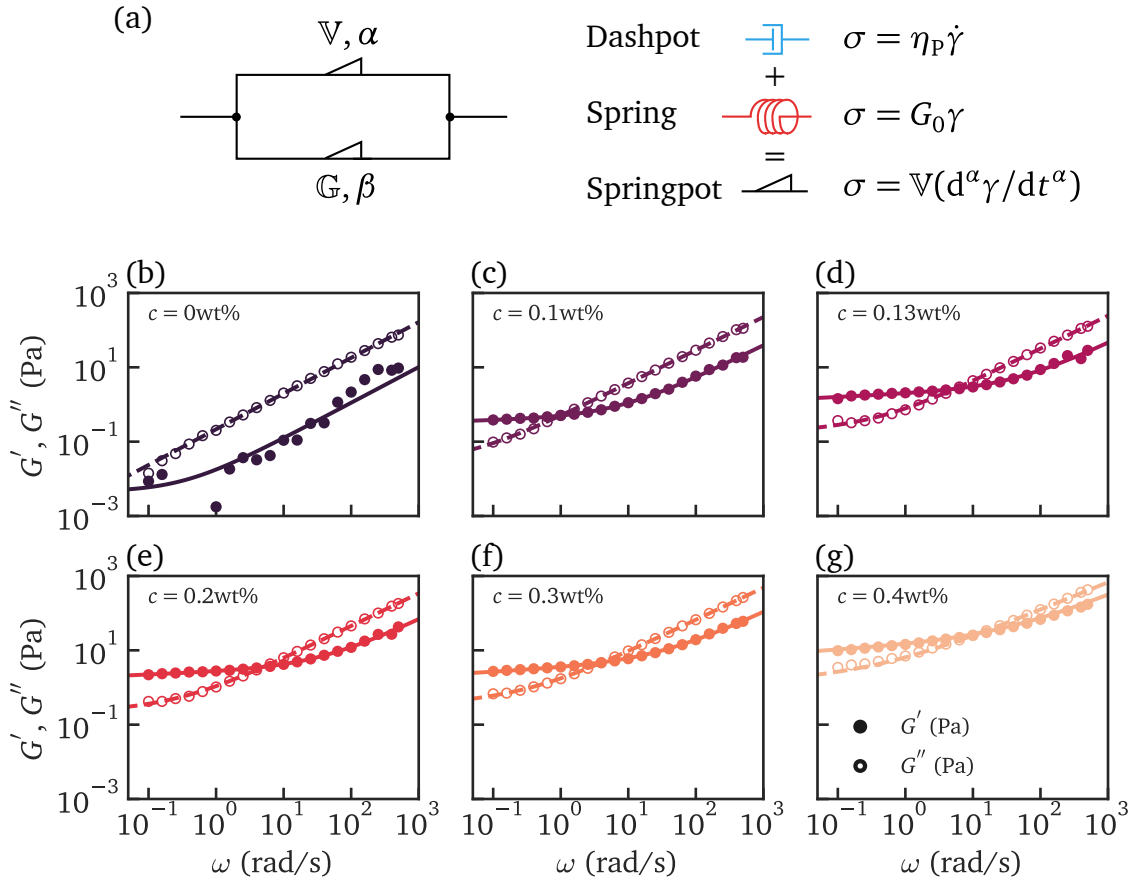

Figure 5-5: (a) Schematic of the fractional Kelvin-Voigt (FKV) model with two *spring-pot* components connected in parallel. (b-g) Frequency responses of dynamic moduli with $\gamma_0 = 2\%$ at varying concentrations (subfigures): (b) 0 wt%; (c) 0.1 wt%; (d) 0.13 wt%; (e) 0.2 wt%; (f) 0.3 wt%; (g) 0.4 wt%. Solid and dashed lines: Fitting lines from the FKV model in Equation (5.9).

To describe the frequency response of the GO/PVA nanocomposites at varying concentrations arising from both the nanofiller structures and the interactions between the nanofiller and the polymer matrix, a constitutive model with a broad relaxation time spectrum is desired. Notably, the storage moduli at low frequencies approach plateau as the GO concentration increases, indicating a gel-sol transition [317]. Nevertheless, a true plateau storage modulus is unlikely to reach due to Brownian diffusion, which induces infinite structural variations. This trend can be further visualized using the van Gurp-Palmen plot as shown in Figure 5-6, in which the phase angle δ s plotted against

the magnitude of complex modulus $|G^*| = \sqrt{G'^2 + G''^2}$. As the GO concentration increases, the curve is shifted towards a lower phase angle with a larger magnitude of complex modulus. The dashed lines show the storage moduli at $\omega = 0.1\,\text{rad/s}$, which can be used to represent the asymptotes of $|G^*|$ at low angular frequencies. The decaying phase angle in this frequency region demonstrates elasticity-dominated material response.

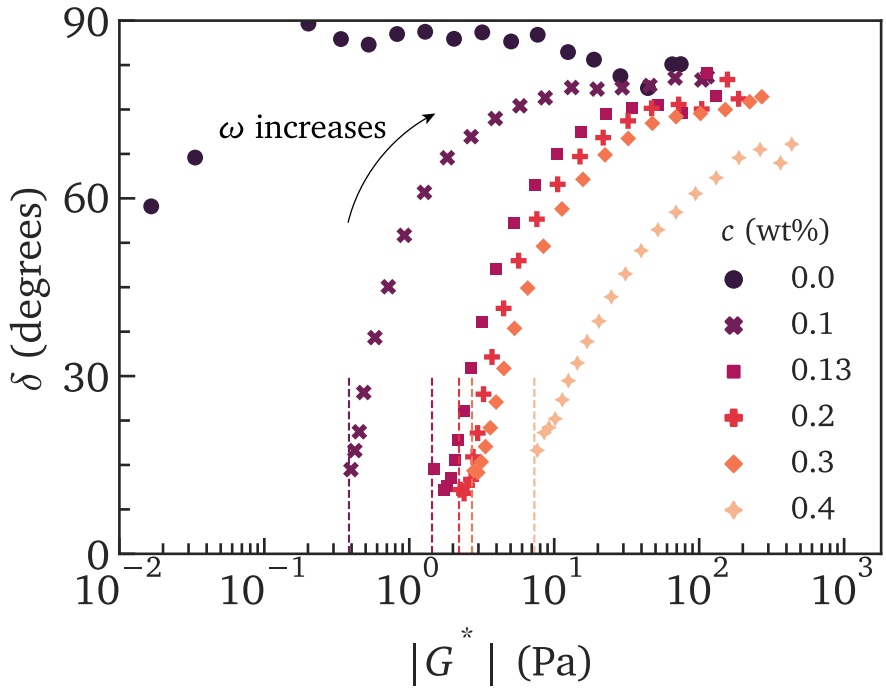

Figure 5-6: van Gurp-Palmen plot with the phase angle $\tan(\delta)$ against the magnitude of complex modulus $|G^*|$ at varying GO concentrations. Dashed lines mark G'_0 for each GO concentration.

To describe the frequency response of the dynamic moduli accurately, the fractional Kelvin-Voigt (FKV) model is applied, in which two fractional *springpots* are connected in parallel [177, 318], as shown in the schematic of Figure 5-5(a). The constitutive equation can be expressed as

$$\sigma = \mathbb{V}\frac{\mathrm{d}^\alpha \gamma}{\mathrm{d}t^\alpha} + \mathbb{G}\frac{\mathrm{d}^\beta \gamma}{\mathrm{d}t^\beta}, \tag{5.8}$$

where $\mathbb{V}$ (in the unit of $\mathrm{Pa\,s}^{\alpha}$) and $\mathbb{G}$ (in the unit of $\mathrm{Pa\,s}^{\beta}$) are the quasiproperties of the two springpots with fractional exponents α and β, respectively. The fractional derivative $\mathrm{d}^{\alpha}/\mathrm{d}t^{\alpha}$ has been introduced and defined in Equation (2.9). The storage and loss moduli predicted by the FKV model can be extracted by taking the Fourier transform of Equation (5.8) as

$$G'(\omega) = \mathbb{V}\omega^{\alpha}\cos\left(\frac{\alpha\pi}{2}\right) + \mathbb{G}\omega^{\beta}\cos\left(\frac{\beta\pi}{2}\right), \tag{5.9a}$$

$$G''(\omega) = \mathbb{V}\omega^{\alpha}\sin\left(\frac{\alpha\pi}{2}\right) + \mathbb{G}\omega^{\beta}\sin\left(\frac{\beta\pi}{2}\right). \tag{5.9b}$$

To distinguish the two symmetric springpots, a constraint on the fractional exponents is imposed as $\alpha \geq \beta$. When $\alpha = 1$ and $\beta = 0$, the FKV model is reduced to the conventional Kelvin-Voigt model. As shown in Figure 5-5, the FKV model is fitted to the experimental data as solid (G') and dashed (G'') lines. Both fitting lines are in excellent agreement with the measurements of dynamic moduli at all the tested concentrations. The extracted fractional exponents are further plotted against the GO concentrations for $c > 0$, as shown in Figure 5-7. From this figure, a general trend in the two fractional exponents can be identified as the GO concentration increases, where β increases from 0 and α decreases from unity. Two power-law relations can be obtained from numerical fitting as $\alpha \sim c^{-0.053}$ (solid line) and $\beta \sim c^{0.077}$ (dashed line). The departure of both exponents of α and β from integer limits implies more complex viscoelastic responses governed by a broader retardation time spectrum $H(\lambda)$ (as introduced in Section 2.2) attributed from the microstructures at different lengthscales. For the FKV model, the retardation time spectrum can be analytically expressed [319] as

$$H(\lambda) = \frac{\mathbb{V}}{\pi}\lambda^{-\alpha}\sin(\pi\alpha) + \frac{\mathbb{G}}{\pi}\lambda^{-\beta}\sin(\pi\beta). \tag{5.10}$$

From Equation (5.10), two power-law asymptotes are identified as $H(\lambda) \sim \lambda^{-\alpha}$ when $\lambda \ll \lambda_{\mathrm{C}}$ and $H(\lambda) \sim \lambda^{-\beta}$ when $\lambda \gg \lambda_{\mathrm{C}}$. Here, a characteristic retardation time λ_{C} is calculated from dimensional analysis as

$$\lambda_{\mathrm{C}} = \left[\frac{\mathbb{V}\sin(\pi\alpha)}{\mathbb{G}\sin(\pi\beta)}\right]^{1/(\alpha-\beta)}. \tag{5.11}$$

This prediction from the FKV model is subsequently compared with the experimental measurements. To extract the retardation modes from $G'(\omega)$ and $G''(\omega)$, the *ReSpect* computing package [320] is applied. Here, a discrete mode is adopted to capture a discernible trend of the time spectrum without overfitting. For each GO concentration,

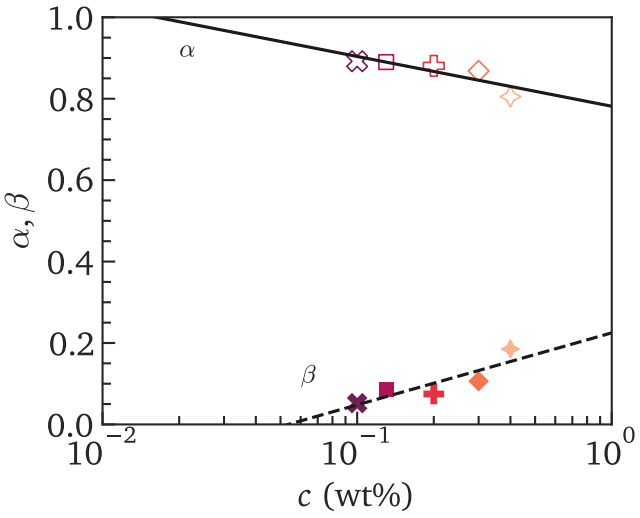

Figure 5-7: Fractional exponents $0 \leq \beta \leq \alpha \leq 1$ extracted from fitting the FKV model at varying GO concentrations. Solid and dashed lines show the trendlines for α and β against GO concentrations from power-law fitting with exponents of -0.053 and 0.077, respectively.

a parsimonious number of 3 to 4 retardation modes are selected using the ρ-η method [320]. As shown in Figure 5-8, the extracted retardation modes from experimental measurements (filled markers) exhibit consistent trends with the prediction from a continuous time spectrum $H(\lambda)$. In the limit of short retardation time $\lambda < 0.1\,\mathrm{s}$, the retardation modes at varying GO concentrations are similar, justifying contributions from the polymer matrix or hydrodynamic effects. In contrary, the continuous spectra or discrete modes at the tail of long retardation time are elevated significantly as the GO concentration increases, which are consistent with the increasing storage moduli at low angular frequencies.

To describe the non-linear rheological response, the FKV model can be subsumed into the more comprehensive K-BKZ constitutive framework [136, 177]. Here, the constitutive equation can be expressed in a general integral form as

$$\boldsymbol{\sigma}(t) = \int_{-\infty}^{t} \frac{\partial G(t-\xi)}{\partial \xi}\left[2\frac{\partial W}{\partial I_1}\boldsymbol{C}^{-1} - 2\frac{\partial W}{\partial I_2}\boldsymbol{C}\right]\mathrm{d}\xi, \tag{5.12}$$

where $G(t)$ is the relaxation modulus measured from linear viscoelasticity. A poten-

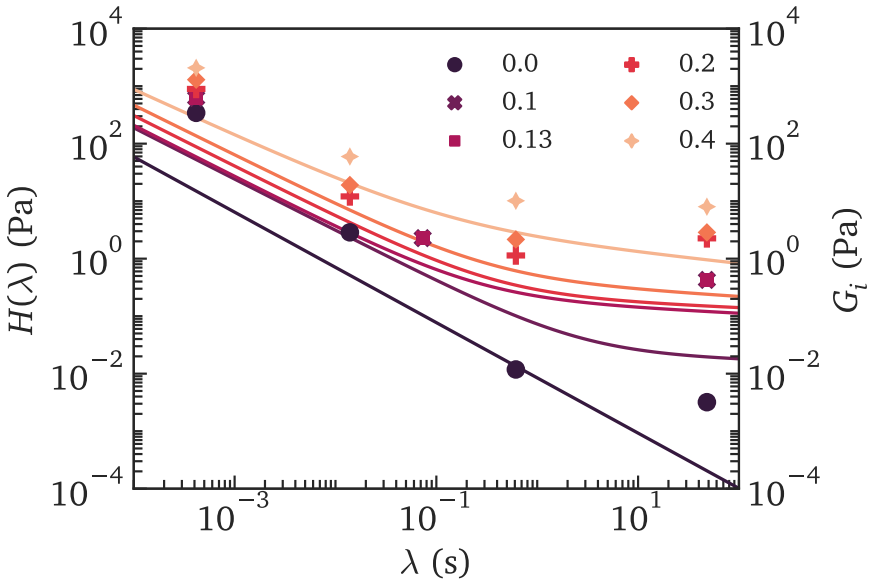

Figure 5-8: Retardation time spectra predicted by the FKV model at varying GO concentrations according to Equation (5.10) (solid lines) and discrete retardation modes extracted from the measured dynamic moduli in Figure 5-5 with the *ReSpect* computing package (filler markers).

tial function W can be expressed in a frame-invariant form using the first and second invariants, I_1 and I_2 of the Finger strain tensor $\boldsymbol{C}^{-1} \equiv (\boldsymbol{F}^{-1})^{\mathrm{T}}\boldsymbol{F}$, which are defined as

$$I_1 \equiv \mathrm{tr}\,\boldsymbol{C}^{-1}, \tag{5.13a}$$

$$I_2 \equiv \mathrm{tr}\,\boldsymbol{C}. \tag{5.13b}$$

At small deformation gradients, $I_1 = I_2 \to 3$ [136]. In shear deformation, $I_1 = I_2 = \gamma^2 + 3$. As a result, the potential function can be expressed in a more compact form as $W = W(I_1)$ [321]. Alternatively, if letting $h(\gamma) \equiv W(I_1)$, the resulting constitutive equation can be expressed specifically as

$$\sigma(t) = \int_{-\infty}^{t} \frac{\partial G(t-\xi)}{\partial \xi} h[\gamma(t,\xi)]\gamma(t,\xi)\mathrm{d}\xi, \tag{5.14}$$

where $\gamma(t,\xi) \equiv \gamma(t) - \gamma(\xi)$ denotes the shear history, and $h(\gamma)$ is defined as the damping function [136, 322], which incorporates strain-dependent response of a material.

From this equation, it is evident that the linear viscoelastic behavior is separated from the non-linear response described by the damping function. Here, the relaxation modulus is derived from the FKV model by taking Laplace transform of Equation (5.8) as

$$G(t) = \frac{\mathbb{V}}{\Gamma(1-\alpha)} t^{-\alpha} + \frac{\mathbb{G}}{\Gamma(1-\beta)} t^{-\beta}, \tag{5.15}$$

where $\mathbb{V}$, $\mathbb{G}$, α and β correspond to the quasiproperties and fractional exponents extracted from the linear viscoelastic measurements. Notably, by letting $\gamma(t) = \gamma_0 \mathscr{H}(t)$, where $\mathscr{H}(t)$ is the Heaviside step function, the resulting stress response from Equation (5.14) is given by

$$\sigma(\gamma_0, t) = \gamma_0 h(\gamma_0) G(t) = \gamma_0 G(\gamma_0, t). \tag{5.16}$$

Consequently, the damping function can be practically determined through stress relaxation experiments at different step strains γ_0. From Equation (5.16), relaxation moduli at different step strains predicted by the K-BKZ constitutive framework are distinguishable only by their prefactors.

To demonstrate the validity of this constitutive framework, a specific GO concentration $c = 0.4\,\text{wt\%}$ is selected for non-linear rheological characterizations. A range of step stains $\gamma_0 = 0.01$ to 10 is selected and imposed with a relaxation duration of 600 s for each strain. As shown in Figure 5-9, the relaxation moduli at different step strains exhibit broadly similar decaying trends on logarithmic scales. The prediction of a relaxation modulus in the linear regime, as described by Equation (5.15) is plotted as the black dashed line, which shows excellent agreement with the stress relaxation curves at small step strains at $\gamma_0 \lesssim 0.1$. Beyond $\gamma_0 \approx 0.3$, the stress relaxation curves $G(\gamma_0, t)$ are shifted downward due to the damping term. To estimate the damping function, two time points are selected at $t_1 = 0.1\,\text{s}$ and $t_2 = 80\,\text{s}$ to represent the material responses in short and long times, respectively. The corresponding values of $G(\gamma_0, t_i)/G(t_i)$ are plotted against different step strains in Figure 5-10 as filled and hollow markers. At both time points, the value of $G(\gamma_0, t_i)/G(t_i)$ remains broadly at unity for $\gamma_0 \lesssim 0.1$ and exhibits power-law trends in the non-linear regime. Such trends can be described by a specific form of the damping function proposed by Soskey and Winter [323], in which a generalized sigmoidal function is specified as

$$h(\gamma_0) = \frac{1}{1 + (\gamma_0/\gamma_C)^b}, \tag{5.17}$$

where γ_C is a critical strain, and b is an exponent to describe the strain-softening be-

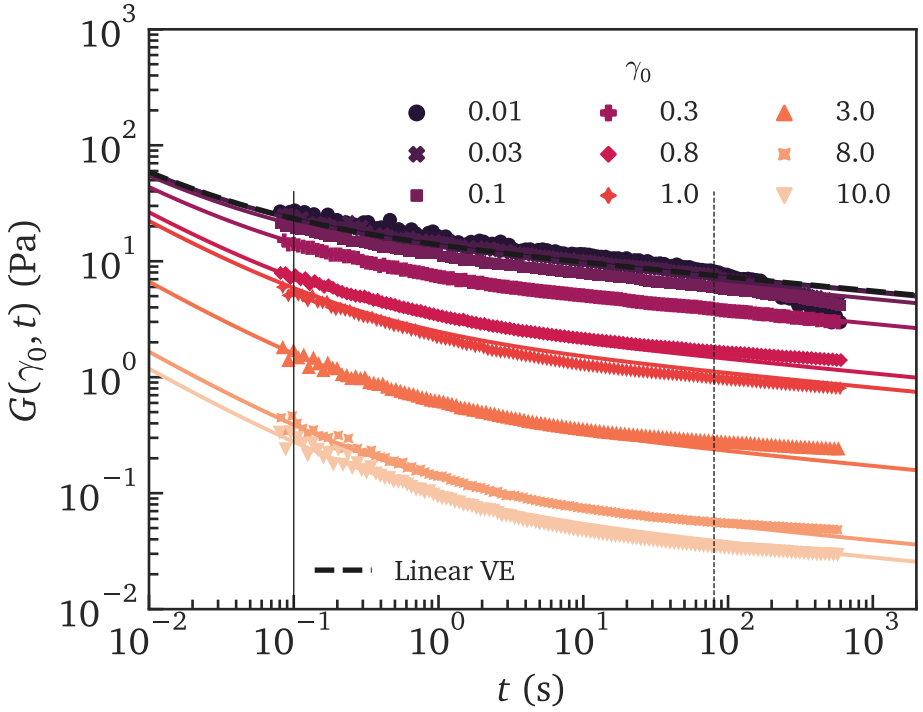

Figure 5-9: Relaxation moduli against step time at varying step strains $\gamma_0 = 0.01$ to 10. Black dashed line (thick): Linear viscoelastic response predicted by Equation (5.15). Solid lines: Fitting lines to a modified K-BKZ constitutive framework with two damping functions on each springpot at varying step strains. A universal set of shape parameters can be obtained as $b_\alpha = 1.55$, $\gamma_{C,\alpha} = 1.04$, $b_\beta = 1.53$ and $\gamma_{C,\beta} = 0.32$. Black solid and dashed lines (thin) show the trends of relaxation moduli at $t_1 = 0.1\,\mathrm{s}$ and $t_2 = 80\,\mathrm{s}$, which are plotted in Figure 5-10 explicitly to demonstrate distinct damping terms at short- and long-time ranges.

havior in the non-linear regime. From numerical fitting, the shape parameters can be obtained as $b = 1.38$ and $\gamma_C = 0.45$ at $t_1 = 0.1\,\mathrm{s}$, and $b = 1.54$ and $\gamma_C = 0.33$ at $t_2 = 80\,\mathrm{s}$. Evidently, the non-linear material responses in a stress relaxation process substantially differ at short and long times. As a result, the constitutive framework with a universal damping function, as expressed in Equation (5.12) cannot describe the non-linear behavior accurately over a broad time spectrum.

To characterize such a complex non-linear response, it is noticed that for a nanofilled system, a percolated network formed by nanofillers at high filler concentrations can induce a new strain-energy relation that is substantially different from that for the

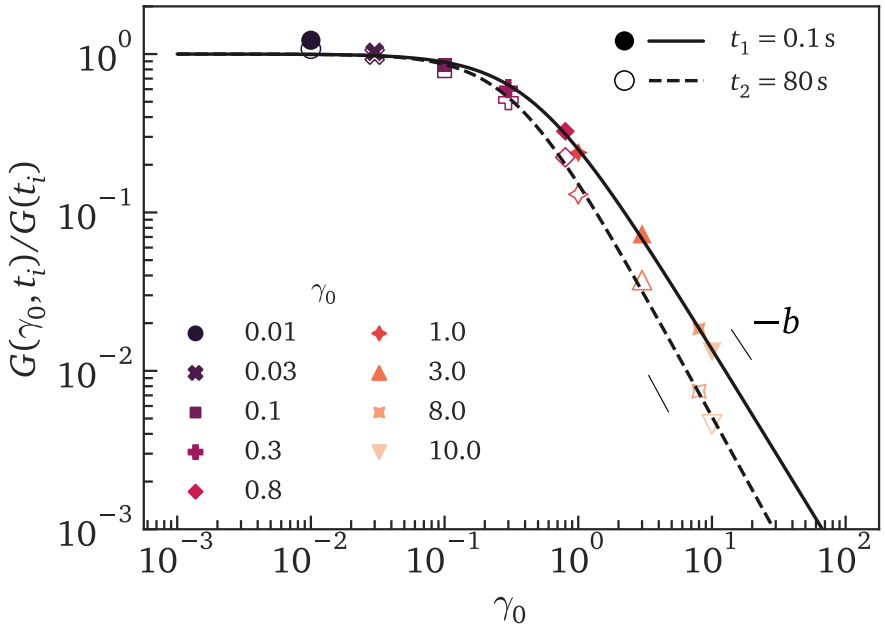

Figure 5-10: Damping functions evaluated at short- (0.1 s) and long-time (80 s) responses. Both data are fitted into Equation (5.17), and distinct shape factors are obtained, showing inconsistent results with the prediction from a universal damping function.

polymer matrix. The linear viscoelastic responses at short and long times are primarily dominated by the springpots with quasiproperties of $\mathbb{V}, \alpha$ and $\mathbb{G}, \beta$, respectively (since $\alpha > \beta$). Therefore, two distinct damping functions of the Soskey-Winter form (Equation (5.17)) can be assigned to each springpot. From a physical perspective, these two damping functions are related to the strain energy that arises from different material structures, which subsequently dominate the short- and long-time non-linear responses with separable constitutive relations. In the limit of $\gamma_0 \ll \gamma_C$, both damping functions reduce to unity, and the fractional Kelvin-Voigt structure is retained. According to this assumption, the overall relaxation modulus can thus be expressed as

$$G(\gamma_0, t) = \frac{\mathbb{V}}{\Gamma(1-\alpha)} t^{-\alpha} h(\gamma_0; b_\alpha, \gamma_{C,\alpha}) + \frac{\mathbb{G}}{\Gamma(1-\beta)} t^{-\beta} h(\gamma_0; b_\beta, \gamma_{C,\beta}). \tag{5.18}$$

To obtain accurate measurements of the two damping functions, numerical fitting of Equation (5.18) is performed to the experimental data at varying step strains, and

the four shape parameters are obtained as $b_\alpha = 1.55$, $\gamma_{C,\alpha} = 1.04$, $b_\beta = 1.53$ and $\gamma_{C,\beta} = 0.32$. The predictions from Equation (5.18) are subsequently plotted in Figure 5-9 in colored solid lines, which show excellent agreement with the measurements at both short- and long-time ranges. Admittedly, measurements at close to $t = 600\,\mathrm{s}$ show slight deviation from the predictions, which may arise from inaccessible data of the dynamic moduli below $\omega = 0.1\,\mathrm{rad/s}$ (as in Figure 5-5).

With the linear viscoelastic response characterized by the FKV model, the modified K-BKZ constitutive framework with two damping functions provides a full-dimensional description of the material response in the non-linear regime. To validate this constitutive framework, the stress response of a transient start-up shear flow is inspected, in which the shear history can be described as $\gamma(t) = \mathscr{H}(t)\dot{\gamma}_0 t$. From Equation (5.12) and 5.18, this transient response can be analytically expressed as

$$\sigma^+(\dot{\gamma}_0, t) = \sigma^+(\dot{\gamma}_0, t; \mathbb{V}, \alpha, b_\alpha, \gamma_{C,\alpha}) + \sigma^+(\dot{\gamma}_0, t; \mathbb{G}, \beta, b_\beta, \gamma_{C,\beta}), \tag{5.19}$$

i.e., a summation of the contributions from the two springpots. The transient stress response from either springpot has an identical form, which can be expressed as

$$\begin{aligned}\sigma^+(\dot{\gamma}_0, t; \mathbb{V}, \alpha, b_\alpha, \gamma_{C,\alpha}) = &\frac{\mathbb{V} h(\dot{\gamma}_0 t; b_\alpha, \gamma_{C,\alpha})\dot{\gamma}_0}{\Gamma(1-\alpha)} t^{1-\alpha} \\ &+ \frac{\alpha \mathbb{V} \dot{\gamma}_0 t^{1-\alpha}}{\Gamma(2-\alpha)} F\left[1, \frac{1-\alpha}{b_\alpha}; \frac{1-\alpha}{b_\alpha} + 1; -\left(\frac{\dot{\gamma}_0 t}{\gamma_{C,\alpha}}\right)^{b_\alpha}\right],\end{aligned} \tag{5.20}$$

where F denotes the hypergeometric function as introduced in Chapter 3. As shown in Figure 5-11(a), a series of start-up flow measurements are performed at varying step shear rates $\dot{\gamma}_0 = 0.01\,\mathrm{s}^{-1}$ to $100\,\mathrm{s}^{-1}$ on logarithmic scales. Notably, the K-BKZ constitutive framework (solid lines) accurately captures the transient stress responses at short times for all shear rates. At longer times, predictions of the stress response at high shear rates ($\dot{\gamma} > 1\,\mathrm{s}^{-1}$) are consistent with the measurement. As the shear rates decrease, the predicted stress progressively deviates from the measured values. Such discrepancy is discussed shortly. Nevertheless, the short-time responses remain in excellent agreement with the predictions.

The trend in the terminal stress response can be better visualized by comparing with the steady-shear viscosity. As shown in Figure 5-11(b), the steady-shear flow curve from Figure 5-3 is revisited (hollow markers). In addition, the complex viscosity from linear viscoelasticity $\eta^*(\omega) \equiv |G^*(\omega)|/\omega$ (solid markers) is plotted at $\omega = \dot{\gamma}$, where the notation of $|G^*| = \sqrt{G'^2 + G''^2}$ represents the magnitude of complex modulus and

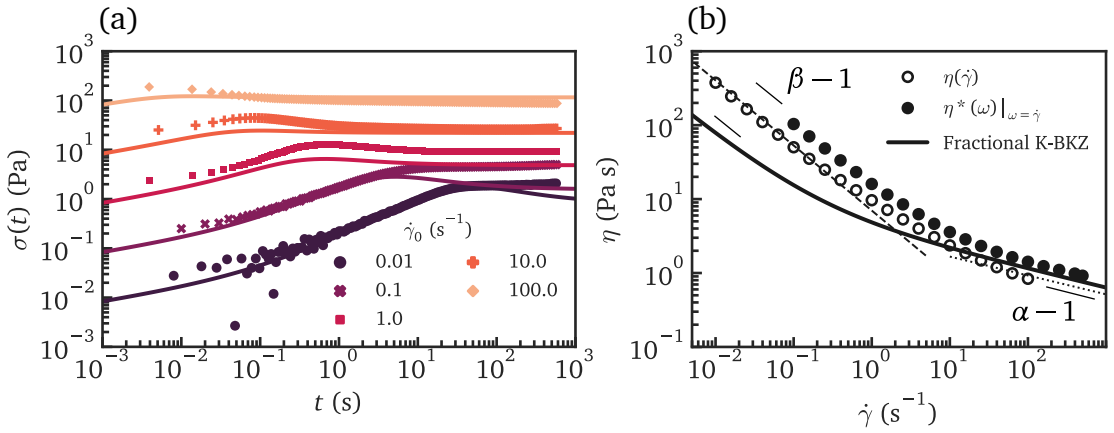

Figure 5-11: (a) Transient stress response in a start-up flow with varying step shear rates at a fixed GO concentration of 0.4 wt%. Solid lines: predictions from the fractional K-BKZ framework. (b) Steady shear flow curve at a fixed GO concentration of 0.4 wt% revisited from Figure 5-3(a). The prediction line from the K-BKZ model describes the general trend of shear-thinning.

has been used in Figure 5-6. The measurements from both flows agree closely over a wide range of shear rates, attesting to the Cox-Merz rule [136]. In contrary, the Rutger-Delaware rule [324], which is commonly used for a yield-stress fluid, fails drastically with $\gamma_0 = 2\%$. The applicability of the Cox-Merz rule suggests a well-defined linear regime, in which the strain remains recoverable. Compared with dense particulate suspensions and other viscoplastic materials that exhibit intrinsically non-linear behavior [177], nanocomposites with intercalated polymer chains introduce additional polymer-nanofiller interactions, which increases the averaged nanofiller distance and diminishes the strong repulsion between nanofillers. As a result, the critical strain beyond which the system becomes non-linear increases significantly and is primarily determined by the extensibility of the polymer matrices, and the bulk rheology of nanocomposites is substantially different from dense nanofiller suspensions, especially under large deformation and shear rates. In Figure 5-11(b), two power-law asymptotes arise at low and high shear rates. From the linear viscoelastic responses, the power-law exponents of these two asymptotes can be analytically determined as $\beta - 1$ and $\alpha - 1$, respectively. These two power-law predictions are further plotted as thin dashed and dotted lines, and they agree with the trends of both steady-shear and complex viscosities in the limits of low and high shear rates (angular frequency), respectively. Finally, these viscosity measurements are compared with the prediction from the modified K-

BKZ model. From Equation (5.19), a terminal viscosity can be readily expressed by letting $t \to \infty$, and an explicit expression can be obtained using Euler's transformation [253] as

$$\begin{aligned}\eta(\dot{\gamma}) = \lim_{t\to\infty} \frac{\sigma^+(t)}{\dot{\gamma}_0} = \frac{\alpha\mathbb{V}}{\Gamma(2-\alpha)}\left(\frac{\dot{\gamma}_0}{\gamma_{C,\alpha}}\right)^{\alpha-1} F\left(\frac{1-\alpha}{b_\alpha}, \frac{1-\alpha}{b_\alpha}; \frac{1-\alpha}{b_\alpha}+1; 1\right) \\ + \frac{\beta\mathbb{G}}{\Gamma(2-\beta)}\left(\frac{\dot{\gamma}_0}{\gamma_{C,\beta}}\right)^{\beta-1} F\left(\frac{1-\beta}{b_\beta}, \frac{1-\beta}{b_\beta}; \frac{1-\beta}{b_\beta}+1; 1\right).\end{aligned} \tag{5.21}$$

As plotted in Figure 5-11(b), this prediction shows good agreement with the trends of both steady-shear and complex viscosities. In particular, Equation (5.21) predicts two power-law asymptotes with identical exponents as in linear viscoelasticity. Such consistency demonstrates the validity of a K-BKZ constitutive framework to describe both the linear and non-linear rheological responses of a nanofilled system. Admittedly, predictions of the terminal viscosity at low shear rates $\dot{\gamma}_0 < 1\,\mathrm{s}^{-1}$ slightly deviate from the measurements. This deviation is likely to arise from a systematic offset in the measured damping function due to thixotropy. From Equation (5.21), the asymptotic solution of the steady-shear viscosity at low shear rates is primarily determined by both the low-frequency response of the dynamic moduli (through β and $\mathbb{G}$) and the damping function associated with the low-frequency springpot (through b_β and $\gamma_{C,\beta}$). As $\beta \ll 1$, the value of $(1-\beta)/b_\beta$ is not far from unity, hence $F[(1-\beta)/b_\beta, (1-\beta)/b_\beta; (1-\beta)/b_\beta + 1; 1]$ increases rapidly (as $F(1,1,1;1) \to \infty$) with decreasing b_β. Since b_β is close to unity, if its value is overestimated, the low-shear-rate component in Equation (5.21) can decrease dramatically, giving rise to an offset in the steady-shear viscosity between the predictions from the K-BKZ model and the experimental measurements. From the steady-shear measurements, it is evident that the studied nanofilled system exhibits non-trivial thixotropic behavior. This additional complexity in rheology is not manifested in the linear regime. However, in a stress relaxation process, where the sample is subject to large step strains, the internal structures undergo rapid destruction with large transient shear rates, resulting in systematic underestimations of the relaxation modulus, and hence a large value of b_β. Nevertheless, the K-BKZ constitutive framework still provides a simple description of the material responses with accurate scaling laws over wide range of shear rates.

5.3 Extensional rheology

The extensional rheology of the GO/PVA nanocomposites is characterized through the customized CaBER device introduced in Chapter 3 with an identical set of experimental parameters as in Table 3.2. Here, the concentration of PVA remains at 9.1 wt%, but a slightly different range of GO concentration is selected to investigate the extensional rheology resulted from varied polymer-nanofiller interactions. Figure 5-12 shows the snapshots of filament evolution for each selected GO concentration, filament thinning profiles at different transient times. The captured snapshots show a significant increase in the filament breakup time t_C from approximately 140 ms to 1100 ms as the GO concentration increases from 0 wt% to 0.4 wt%. At relatively high GO concentrations (*e.g.*, 0.4 wt%), the filament profile exhibits an apparent necking shape, in contrast with the more slender filament shapes at lower GO concentrations. In addition, the fluid reservoir close to the end discs at $c = 0.4$ wt% is conically shaped, distinct from the approximately truncated-spherical shapes at lower GO concentrations as a result of the interaction between gravity and capillary effect. These differences show substantial variations of the capillarity-driven thinning dynamics as the GO concentration increases. The temporal evolution of the minimum filament radius $R(t)$ can be readily extracted from the snapshots. As plotted in Figure 5-13(a), the minimum filament radius at varying GO concentrations exhibits distinct kinematics. When the GO concentration is approximately below 0.08 wt%, the filament profiles evolve from self-similar shapes and become increasingly cylindrical close to the filament breakup. This is reminiscent of the filament thinning dynamics predicted by the viscoelastic models that have been extensively studied in previous chapters. Due to low GO loadings, such behavior can be primarily attributed to the stretching of PVA polymer chains as well as the hydrodynamic interactions arising from low-concentrated nanofillers. This presumption is further justified by the linear decay of minimum filament radius at $t \lesssim 200$ ms, in which the filament thinning profiles are primarily governed by the visco-capillary thinning. Due to a weakly elastic response arising from low-molecular-weight PVA chains, the elasto-capillary thinning appears to arise only sufficiently close to the filament breakup. In contrary, the filament thinning profiles at larger GO concentrations ($c \geq 0.08$ wt%) evidently deviate from the linear-decaying trends at intermediate time ($t \approx 0.6t_C$), leading to a faster filament thinning rate. Notably, the filament thinning appears to slow down very close to filament breakup, as subtly shown for $c = 0.4$ wt% at $t > 1\times10^3$ ms. Such piecewise filament thinning trend reveals a much more complex rheological response in the GO/PVA nanocomposites as the extensional rate is varied.

Prior to fitting the measured filament thinning profile to specific constitutive models,

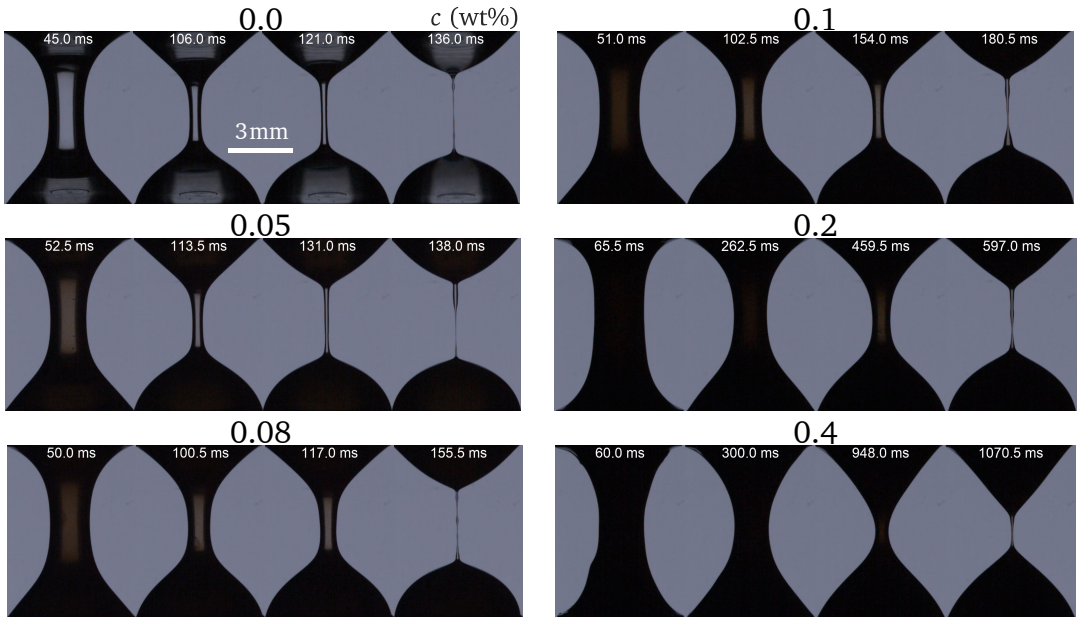

Figure 5-12: Snapshots of the filament thinning profiles for GO/PVA nanocomposites at varying GO concentrations from 0 wt% to 0.4 wt% measured on the customized CaBER device. Time of each snapshot is marked.

a direct comparison between the shear and extensional rheology can be performed through the apparent extensional viscosity $\eta_{e,app}(\dot{\epsilon})$ (Equation (3.9)) extracted from the filament thinning dynamics and an inelastic prediction of the apparent extensional viscosity from shear rheology as $\eta_{e,N}(\dot{\gamma}) = 3\eta(\dot{\gamma})/(2X_N - 1)$, where $\eta = \eta(\dot{\gamma})$ is the steady shear viscosity, and $X_N = 0.7127$ is the geometric correction factor for Newtonian fluids. As shown in Figure 5-13(b), the apparent extensional viscosities from both shear and extensional flows are plotted against the strain rates[1]. The shear and extensional curves are broadly consistent over a wide range of the strain rates, demonstrating inelastic responses at small to intermediate strain rates ($\dot{\epsilon} \lesssim 10\,s^{-1}$). At larger strain rates, the apparent extensional viscosity $\eta_{e,app}$ becomes larger than the inelastic prediction due to additional elastic responses. Notably, this departure leads to global

[1]Admittedly, a direct comparison between the shear and extensional flow curves without modifications to the magnitude of strain rates is flawed due to frame transformation [136]. From Equation (3.6), the shear and extensional rates can be rewritten in the forms of $II_{\dot{\gamma}}$ and $III_{\dot{\gamma}}$. As a result, the apparent extensional viscosities extracted from shear (inelastic) and extensional rheology exhibit slightly different material responses. Nevertheless, slopes of the flow curves remain unchanged when plotted on logarithmic scales, and can be used to signal different material responses in shear and extensional flows.

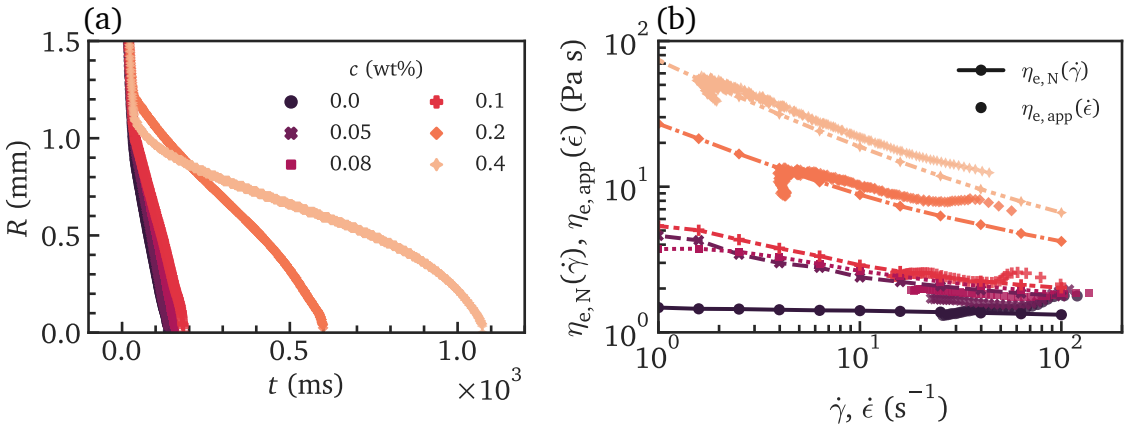

Figure 5-13: (a) Filament radius measured from the customized CaBER system at 600 fps at varying GO concentrations. (b) Apparent extensional viscosity $\eta_{e,app}(\dot{\epsilon})$ and inelastic predictions from the shear viscosity $\eta_{e,N} = \eta(\dot{\gamma})/[(2X_N - 1)/3]$, where $X_N = 0.7127$ is the geometric correction factor for Newtonian fluids. Both subfigures share an identical legend for markers, as shown in (a).

rate-thickening behavior at lower GO concentrations (as exemplified for the pure PVA solution at $\dot{\gamma} \approx 60\,s^{-1}$). At higher GO concentrations, the apparent extensional viscosity keeps decreasing at high strain rates, but the value progressively deviates from the inelastic prediction, as a result of two competitive interactions with opposite effects on the extensional rheology.

Because of distinct filament thinning behavior exhibited at low and high GO loadings, two constitutive models are applied to fit the filament thinning profiles and to extract meaningful model parameters. For $c < 0.08$ wt%, in which extensional-thinning behavior is absent, the Oldroyd-B model (Equation (3.2)) is used. Here, a temporally-evolving form of the geometric correction factor X is incorporated into the fitting process according to Equation (3.47) to produce a more accurate filament thinning prediction. As shown in Figure 5-14, predictions from the Oldroyd-B model (gray solid lines) are in excellent agreement with the experimental data for both GO concentrations over the whole filament thinning process. The extracted model parameters are tabulated in Table 5.1, in which the zero-shear viscosities are consistent with the steady-shear measurements from Figure 5-3. Using Equation (3.12), the elasto-capillary numbers for these two samples are calculated as $Ec_{V\text{-}E} = 2.6$ and 2, and their weakly elastic responses can be readily justified according to the criterion proposed Section 3.1.

As shown in Figure 5-15, at larger GO concentrations, the extensional-thinning trend

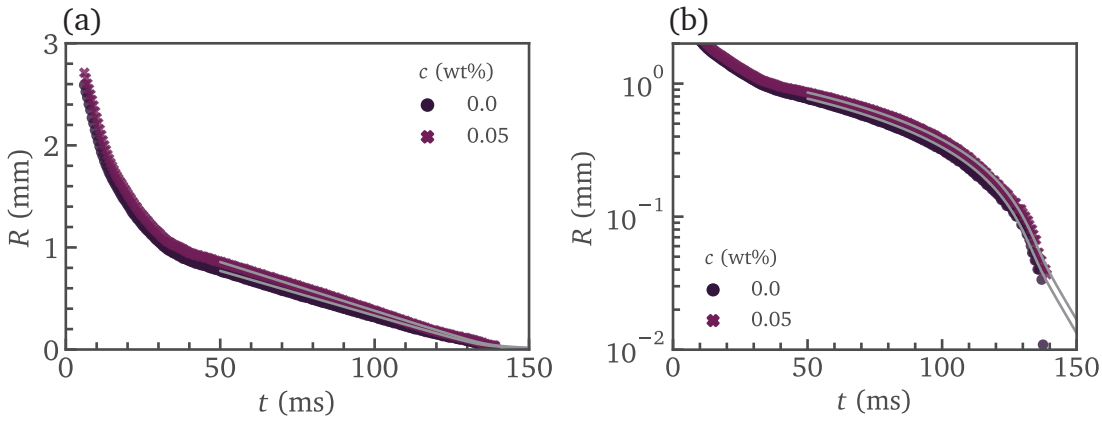

Figure 5-14: Filament thinning profiles at low GO concentrations $c = 0\,\text{wt\%}$ and $0.05\,\text{wt\%}$. Gray solid lines: Fitting lines with the Oldroyd-B model with a temporally-evolving geometric correction factor X for data at $t \geq t_\text{M} \approx 50\,\text{ms}$. (a) R on a linear scale; (b) R on a logarithmic scale.

in apparent extensional viscosity is reminiscent of the filament thinning behavior predicted by tube models as introduced in Chapter 4. Specifically, the extensional-thinning region where the apparent extensional viscosity broadly coincides with the inelastic prediction from shear rheology corresponds to the filament thinning dynamics governed by tube reorientation. In light of such similarity in kinematics, a tube model is explored to describe the filament thinning dynamics of nanocomposite systems at high nanofiller concentrations. Here, the Rolie-Poly model with an infinite chain extensibility $\Lambda_\text{m} \to \infty$ is selected for data fitting. The filament thinning behavior dominated by polymer chain stretch at large strain rates cannot be captured directly due to limited optical resolution, but their impact on the extensional rheology can be readily substantiated from Figure 5-13(b), in which the rate-thinning behavior is characterized by a power-law trend with the exponent larger than -1, in contrary to the prediction of -1 from the Doi-Edwards model without chain stretch (see Figure 4-8). To simplify the fitting process, a constant geometric correction factor of $X = X_\text{N} = 0.7127$ for a Newtonian fluid is assumed because of a pronounced filament thinning kinematic described by viscous-capillary thinning. The time range for fitting is selected from which an evident linear decay is observed (80 ms for $c = 0.08\,\text{wt\%}$ and $0.1\,\text{wt\%}$; 120 ms for $c = 0.2\,\text{wt\%}$ and 200 ms for $c = 0.4\,\text{wt\%}$). As shown in Figure 5-15(a) and (b), the black solid lines show the best fitting lines from the Rolie-Poly model for GO concentrations $c \geq 0.08\,\text{wt\%}$, which is in excellent agreement with the experimental data down to $R = 20\,\mu\text{m}$. The constitutive parameters extracted from numerical fitting are

summarized in Table 5-15.

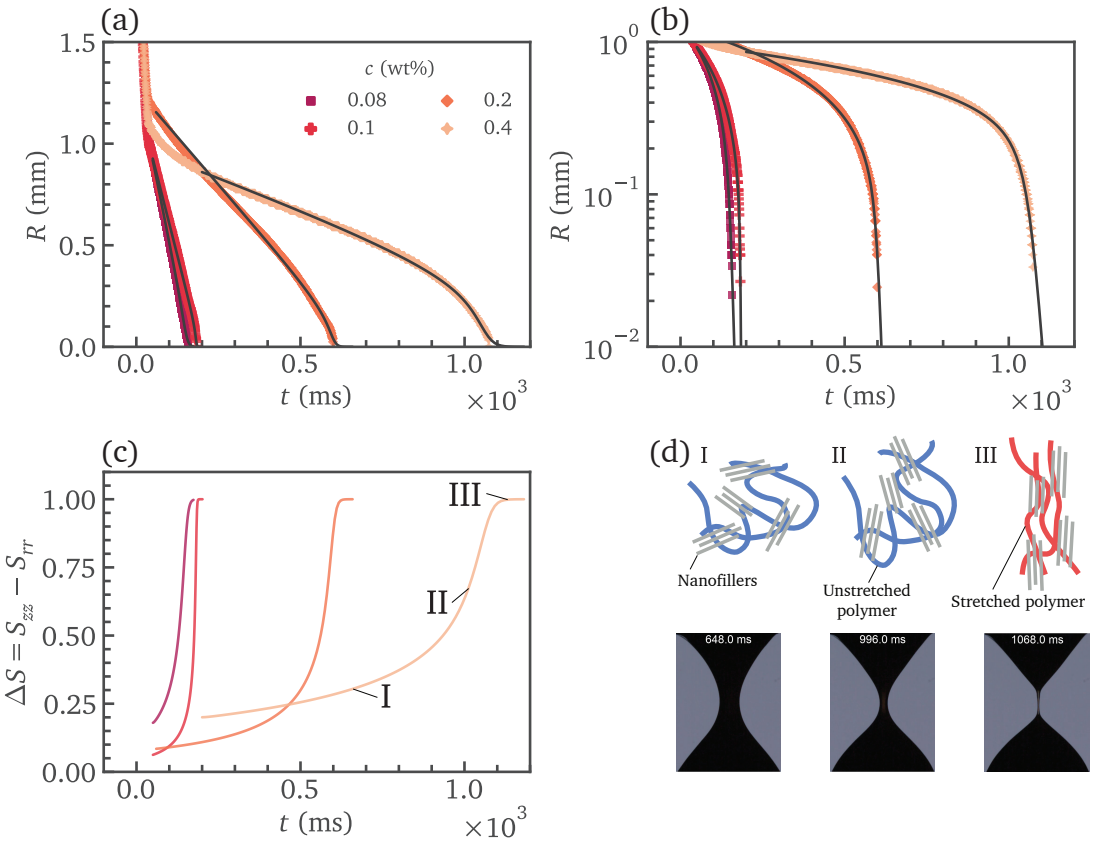

Figure 5-15: (a-b) Filament thinning profiles for GO concentrations $c \geq 0.8$ wt% with (a) R plotted on a linear scale, and (b) R plotted on a logarithmic scale. Black solid lines: Fitting lines from the Rolie-Poly model with the geometric correction factor set to $X_N = 0.7127$. The time range for data fitting is selected at the onset of a notably linear-decaying trend in the filament radius (see text). (c) Magnitude of the tube orientation $\Delta S = S_{zz} - S_{rr}$ at varying GO concentrations. (d) Schematic of the nanocomposite microstructure at different stages of filament thinning (as marked in (c)) with corresponding snapshots of the filament profiles.

A close agreement between measured filament thinning profiles and predictions from the Rolie-Poly model reveals pivotal rheological and conformational similarities between entangled polymer solutions and nanofilled systems. At high GO concentrations, nanofillers form disordered networks at crossovers characterized by larger lengthscales.

Do to their high rigidity, these nanofillers significantly inhibit the mobility of intercalated polymer chains in a similar mechanism as in the tubes formed by entangled polymer chains. Reorientation and deformation of these nanofillers induce complex conformational variations during flow extension and become dominant factors of the resulting material response at intermediate strain rates. As nanofillers approach a well-aligned state, the extensional viscosity decreases. As the strain rate increases, the aligned nanofillers further disengage, exposing the intercalated polymer chains under the strong extensional flow. Beyond this point, the stretch of polymer chains start to dominate the filament thinning behavior, deviating the material response from the inelastic prediction.

The distinct filament thinning profiles predicted by tube models provides new insights into the structural evolution of a nanofilled system in extensional flow. Using the obtained constitutive parameters, a transient evolution of the magnitude of orientation $\Delta S = S_{zz} - S_{rr}$ as in Equation (4.7) can be readily obtained to describe the conformation of nanofillers, as plotted in Figure 5-15(c). It is worth noting that Figure 5-15(a) and (c) share an identical time axis, and a direct comparison can be made between the filament thinning kinematics and the nanofiller orientation. Similarly, the evolution of tube reorientation ΔS is three-folded. As demonstrated for $c = 0.4\,\text{wt\%}$, when $t \lesssim 650\,\text{ms}$ (represented by stage I), the magnitude of ΔS remains low ($\lesssim 0.3$), and the filament radius decays linearly with time. As the filament thinning progresses ($900\,\text{ms} \lesssim t \lesssim 1100\,\text{ms}$, represented by stage II, the magnitude of ΔS rapidly increases and approaches unity. In this stage, the minimum filament radius decays from $R \approx 0.4\,\text{mm}$ to $R \approx 0.05\,\text{mm}$ with increasing thinning rates, implying rate-thinning behavior for the transient extensional viscosity. When the magnitude of ΔS approaches sufficiently close to unity after $t \gtrsim 1100\,\text{ms}$ (represented by stage III), the evolution of the filament thinning profile is subtly inflected from the previous convex trend ($\ddot{R} < 0$) to an exponential decay ($\ddot{R} > 0$), which can be clearly captured in Figure 5-13(b) close to filament breakup ($t > 1 \times 10^3\,\text{ms}$), and the extensional viscosity subsequently deviates from the inelastic rate-thinning trend. The microstructural variations in these three stages of filament thinning can be illustrated in Figure 5-13(d). In stage I, the nanofillers and intercalated polymer chains undergo affine deformation, and the filament profiles are shaped similarly as the predictions from a Newtonian fluid. As the nanofillers rapidly reorient towards the flow direction in stage II, the mobility of polymer chains starts to increase, but polymer chains remain broadly unstretched. As a result, a faster filament thinning trend in this stage can be primarily attributed to a decreased hydrodynamic interaction arising from aligned nanofillers. In the final stage, nanofillers are fully aligned towards the direction of extension. Further disengagement of these nanofillers is retarded by the chain stretch of intercalated polymers. As

Table 5.1: Key constitutive parameters extracted from CaBER measurements at varying GO concentrations.

Model	c (wt%)	G, or G_N (Pa)	λ, or λ_D/λ_R (ms)	η_S or $\eta_0 = G_N\lambda_D$ (Pa s)
Oldroyd-B	0	0.017	4.30	0.23
(G, λ, η_S)	0.05	0.015	4.32	0.21
	0.08	141.3	10.0/5.3	1.41
Rolie-Poly	0.1	403.2	4.5/1.0	1.81
(G_N, λ_D, λ_R)	0.2	238.7	25.5/5.8	6.08
	0.4	135.5	141.2/12.8	19.13

a result, the filament thinning dynamics in this stage are primarily dominated by an elasto-capillary balance similarly as in a dumbbell model. This structural similarity is broadly consistent with the characterizations of shear rheology in Section 5.2, where the steady-shear viscosity and the complex viscosity from linear viscoelasticity collapse through the Cox-Merz rule. In general, entangled polymer systems can be well described by the Cox-Merz rule due to their broad relaxation time spectra, as has been substantiated by numerous studies in the past [273, 325, 326]. Consequently, it can be concluded that a polymer nanocomposite system exhibits similar rheological behavior as an entangled polymer system in both shear and extensional flows. From such rheological similarity, critical structural information of the nanofillers in a polymer matrix under strong flows can be inferred, which may lead to new designs of the flow profiles for beneficial modifications of the nanofiller morphology, as will be introduced in Section 5.4.

5.4 Rheology-assisted nanocomposite compounding

5.4.1 Exponential shear flow

The results from Sections 5.2 and 5.3 reveal a substantial connection between a strong flow and the morphological variation of nanofillers. While a profound understanding of the complex rheological behavior under large deformation is being actively pursued, strong flow that generates a large local stress may potentially assist in an effective breakdown of large-nanofiller aggregates for a nanocomposite system. As introduced in Section 2.2, dispersion methods using strong flows have been historically implemented in the conventional methods of polymer melt blending and solution mix-

ing [121]. However, steady shear flows have shown limitations in the optimization of nanocomposite dispersion when the viscosity ratio of continuous and dispersed phases is sufficiently contrasted [22]. A number of recent studies have justified the application of extensional flow to beneficially modify nanofiller dispersions [169–172]. However, prototyping instruments that enable strong extensional flow exist as either standalone devices or attachments, and additional costs are incurred for maintenance. As a result, innovative flow designs are desired to provide accessible strong flows on existing commercial compounders for industrial applications with minimal costs of maintenance.

In this section, a conceptual dispersion method using a periodical exponential shear (PES) flow is conceived to induce a rheologically equivalent extensional flow from shear deformation. Proof-of-concept experiments are performed to justify similar material responses from a PES flow as in an extensional flow, and guidance to an optimal flow profile to a nanofilled system is provided.

For a material system described by continuum mechanics under an arbitrary flow, the first principal elongation ratio λ_1 provides a frame-invariant description of the deformation for an infinitesimally small material element in a Lagrangian frame. The temporal evolution of λ_1 can be effectively used as a metric to evaluate the flow strength regardless of flow types. From finite strain theories [136], the principal elongation ratios can be obtained by solving the eigenvalues of the Cauchy-Green deformation tensor $\boldsymbol{C} \equiv \boldsymbol{F}^{\mathrm{T}}\boldsymbol{F}$, where $\boldsymbol{F}$ is the deformation gradient tensor. In a shear deformation with time-varying shear strain $\gamma(t)$, the Cauchy-Green deformation tensor can be expressed as

$$\boldsymbol{C}_{\mathrm{s}} = \begin{bmatrix} 1 & \gamma(t) & 0 \\ \gamma(t) & 1+\gamma(t)^2 & 0 \\ 0 & 0 & 1 \end{bmatrix}, \tag{5.22}$$

where the subscripts "s" corresponds to shear flow, and the corresponding first principal elongation ratio λ_1 can be calculated as

$$\lambda_{1,s} = \frac{\gamma + \sqrt{\gamma^2+4}}{2}. \tag{5.23}$$

In a steady simple shear flow, where $\gamma(t)$ increases linearly with time, the principal elongation ratio $\lambda_{1,s}(t)$ asymptotically approaches $\gamma(t)$, and becomes a linear function with time. In contrast, for a planar extensional flow with a constant extensional rate $\dot{\epsilon}$, the first principal elongation ratio can be expressed [136] as

$$\lambda_{1,e} = \exp(\dot{\epsilon}t) = \exp(\epsilon), \tag{5.24}$$

where the subscript "e" corresponds to extensional flow. From this equation, the magnitude of $\lambda_{1,e}$ increases exponentially with time, demonstrating a faster-varying, and substantially stronger flow than the simple shear counterpart. Notably, in shear and planar extensional flows, the first and second invariants of the Finger tensor $\boldsymbol{C}^{-1}$ can be calculated respectively [136] as

$$\text{Shear flow: } I_{1,\text{s}} = I_{2,\text{s}} = 3 + \gamma^2, \tag{5.25a}$$

$$\text{Plannar extensional flow: } I_{1,\text{e}} = I_{2,\text{e}} = \exp(2\epsilon) + \exp(-2\epsilon) + 1, \tag{5.25b}$$

and the third invariant I_3 for both flows remains unity. Evidently, the first and second invariants are equal in the two flow types despite their distinct natures in deformation, indicating similar kinematics shared by both flows. If one lets $I_{1,\text{s}} = I_{1,\text{e}}$, the two flows become substantially identical regarding deformation in the principal directions. Consequently, a transient shear flow with a well-designed flow profile can exhibit kinematic equivalence to a planar extensional flow.

If a flow profile in shear flow is described by a time-varying strain as

$$\gamma(t) = 2\sinh(\dot{\epsilon}_{\text{s}} t), \tag{5.26}$$

where $\dot{\epsilon}_{\text{s}}$ is an effective rate of *elongational* deformation, it can be readily shown that

$$I_{1,\text{s}} = 3 + \gamma^2 = \exp(2\dot{\epsilon}_{\text{s}} t) + \exp(-2\dot{\epsilon}_{\text{s}} t) + 1 = I_{1,\text{e}}, \tag{5.27}$$

where the last equality arises when $\dot{\epsilon} = \dot{\epsilon}_{\text{s}}$. As a result, the proposed transient shear profile in Equation (5.26), defined as an *exponential shear flow*, is kinematically equivalent to a planar extensional flow with an identical extensional rate. The concept of exponential shear flow is not new. First proposed by Sivanshinsky et al. [327], it was used to demonstrate the rate- and history-dependent rheological behavior of polymer solutions in a strong transient flow. By calculating and analyzing the resulting principal elongation ratio, Doshi and Dealy [328] predicted an identical strain-hardening effect arising from an exponential shear flow as seen in an extensional flow for polymer solutions. This rheological equivalence has been subsequently verified by a number of numerical and experimental studies on polymer solutions and polymer melts [34,329]. When applied to a nanofilled system, an exponential shear flow is expected to impose identical deformation to a local material element as in a planar extensional flow. As illustrated in Figure 5-16, a nanofiller aggregate under an exponential shear flow is subject to both rotation and deformation. The deformation in the principal direction can induce beneficial morphological variations to a nanofiller cluster, if a sufficiently

large stress is provided in the principal direction.

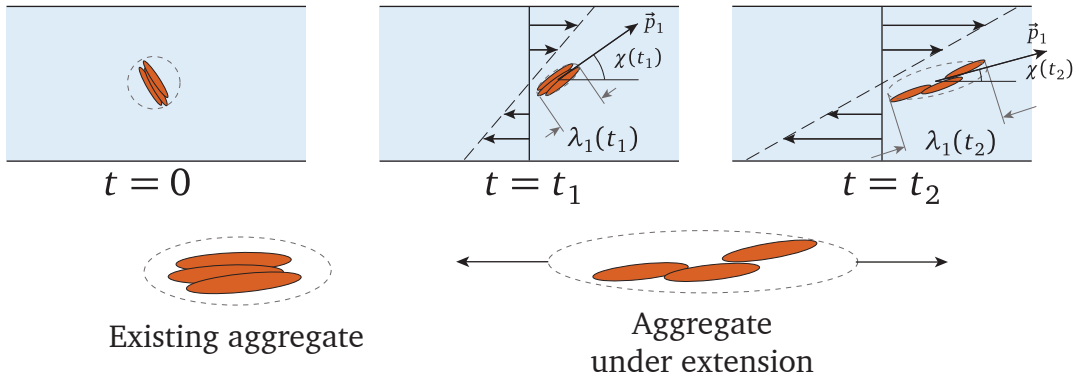

Figure 5-16: Schematic of exponential shear flow on a nanofiller aggregate with a principal direction $\vec{p}_1$ and an extinction angle χ. As the Lagrangian element that contains the aggregate element (ellipse with dashed-line edges) is distorted, morphological variation may arise, if the stress in the principal direction is sufficiently large. Replotted based on Ref. 34.

To describe the material response under an exponential shear flow, an appropriate material function is necessary [34, 328–332]. Because of a non-trivial vorticity arising from shear deformation, the conventional definition of a material function from steady shear flow is less applicable here. Instead, a *local* material response in its principal direction needs to be captured, which is more relevant to the microstructural variation than bulk properties. For this purpose, a rotation-invariant material function can be obtained from the stress components projected on the principal elongation direction, $\vec{p}_1$. As shown in Figure 5-16, the temporally evolving principal direction describes the rotation of an infinitesimally small Lagrangian element that starts at a spherical shape. Due to shear deformation, the spherical element progressively becomes elliptical, during which a preferred direction $\vec{p}$ arises along its major axis. The direction of $\vec{p}$ is described by an extinction angle χ, which can be readily derived from the polar decomposition of the deformation tensor $\boldsymbol{C}$ [34, 136, 333] as

$$\chi = \tan^{-1}\left(\frac{1}{\lambda_{1,s}}\right) = \tan^{-1}\left(\frac{2}{\gamma + \sqrt{\gamma^2 + 4}}\right). \tag{5.28}$$

Consequently, the viscosity function for an exponential shear flow can be defined in a

similar form of Equation (3.9) but in the principal directions [34] as

$$\eta_{\mathrm{es}} \equiv \frac{\sigma_{11}^{\mathrm{P}} - \sigma_{22}^{\mathrm{P}}}{\dot{\epsilon}_{\mathrm{s}}} = \frac{N_1 \cos(2\chi) + 2\sigma_{12}\sin(2\chi)}{\dot{\epsilon}_{\mathrm{s}}}, \tag{5.29}$$

where the superscript P indicates components in the principal directions, and $\dot{\epsilon}_{\mathrm{s}}$ is the effective *elongational* rate defined in Equation (5.26). The normal stress difference $N_1 = \sigma_{11} - \sigma_{22}$ and the shear stress σ_{12} are both defined in the original reference frame. From Equation (5.29), for a Newtonian fluid $\eta_{\mathrm{es}} = 4\eta$, where η is the shear viscosity. This result is well consistent with the prediction from a planar extensional flow, in which the Trouton ratio is a constant of 4. Notably, Equation (5.29) reduces to the form proposed by Doshi and Dealy [328], $\eta_{\mathrm{es}} = \sqrt{N_1^2 + 4\sigma_{12}^2}/\dot{\epsilon}_{\mathrm{s}}$, only if the principal directions of strain and stress tensors coincide, or mathematically when $\tan(2\chi) = 2\sigma_{12}/N_1$. The expression of Equation (5.29) has shown consistent numerical and experimental results with the material functions obtained from simple shear flows [34].

Despite the rheological affinity of an exponential shear flow with a planar extension, the former cannot be practically applied to a real compounding process to improve the nanofiller dispersion due to its transient nature. By noticing that the dispersion is induced through a large local stress regardless of the reference frame, a periodical exponential flow (PES) can be proposed with alternating exponential shear flows, thus allowing for a steady compounding process to modify the nanofiller morphology. Mathematically, such a flow profile can be designed as

$$\gamma(t) = \begin{cases} 2\sinh(\dot{\epsilon}_{\mathrm{s}} t), & kT_0 < t \le kT_0 + \dfrac{T_0}{2} \\ 2\sinh\left(\dfrac{\dot{\epsilon}_{\mathrm{s}} T_0}{2}\right) - 2\sinh\left[\dot{\epsilon}_{\mathrm{s}} t - \dot{\epsilon}_{\mathrm{s}}\left(kT_0 + \dfrac{T_0}{2}\right)\right], & kT_0 + \dfrac{T_0}{2} < t \le (k+1)T_0 \end{cases} \tag{5.30}$$

where $k = 0, 1, 2, \ldots$ and T_0 is the period of PES flow. This flow profile corresponds to alternating elongational motion in the principal directions that are perpendicular to each other in the first and second-half time periods with identical elongational rates.

Given that the net energy input to a periodical flow arises from dissipation, a material function characterizing an averaged viscosity can be readily defined based on Equation (5.29) in the elongational direction as

$$\bar{\eta}_{\mathrm{es}} = \frac{\int_{kT_0}^{kT_0+T_0/2} (\sigma_{11}^{\mathrm{P}} - \sigma_{22}^{\mathrm{P}}) \dot{\epsilon}_{\mathrm{s}} \mathrm{d}t}{\int_{kT_0}^{kT_0+T_0/2} \dot{\epsilon}_{\mathrm{s}} \mathrm{d}t} = \frac{1}{T_0/2} \int_{kT_0}^{kT_0+T_0/2} \eta_{\mathrm{es}} \mathrm{d}t. \tag{5.31}$$

Notably, this equation is defined on the first half-period of one periodical cycle due to flow symmetry from both half periods in a steady PES flow. For a Newtonian fluid with viscosity η, Equation (5.31) again reduces to $\bar{\eta}_{es} = 4\eta$ (Tr = 4), as expected for a planar extensional flow. For a more complex viscoelastic fluid, the value of $\bar{\eta}_{es}$ incorporates additional elastic responses in the principal direction, as shown by a non-trivial normal stress difference N_1. By designing the PES flow profile with properly selected values of $\dot{\epsilon}_s$ and T_0, flow behavior that is commonly observed in an extensional flow can be induced by a transient shear flow in the principal elongation directions.

5.4.2 Experimental verification

To validate the rheological similarity between a PES flow and a planar extensional flow, measurements are taken on a well-studied viscoelastic polymer solution. Here, a polyisobutylene (PIB)/hexadecane (C16) solution is selected at a polymer concentration of 8.26 wt% ($M_{e,0} = 8818$ Da [278], and $Z_{sol} \approx 5$). Similar material systems with different polymer concentrations have been used in Section 3.3 to justify the proposed protocol to determine the best-fit model for CaBER measurements. In those results, strong viscoelastic responses with strain-hardening effects have been identified at varying PIB concentrations in extensional flow.

The selected material system is first tested in shear flow on a commercial rheometer (ARES-G2, TA Instruments, USA). As Figure 5-17(a) shows, strong shear-thinning behavior is exhibited beyond $\dot{\gamma} \gtrsim 1\,s^{-1}$. The overall viscosity trend can be well described by the Carreau-Yasuda model [136] with vanishing plateau viscosity ($\eta_\infty = 0$) as

$$\eta(\gamma) = \eta_0[1 + (\lambda\dot{\gamma})^a]^{(n-1)/a}. \tag{5.32}$$

From numerical fitting, a set of constitutive parameters can be obtained as $\lambda = 0.20$ s, $\eta_0 = 15.46$ Pa s, $a = 0.92$ and $n = 0.38$. In Figure 5-17(b), the dynamic moduli from linear viscoelasticity are measured over different angular frequencies, and a relaxation time can be obtained from the crossover of the two moduli as $\lambda \approx 0.2$ s. This result is consistent with the value of λ obtained from steady shear flow.

The material response of the selected material system in a PES flow is inspected at varying values of $\dot{\epsilon}_s T_0 = 1,\ 2.5,\ 5,\ 7.5$ and 10. For each value of $\dot{\epsilon}_s T_0$, the elongational rate $\dot{\epsilon}_s$ is selected from $0.1\,s^{-1}$ to $100\,s^{-1}$ (some values of $\dot{\epsilon}_s$ are, however, not attainable due to instrument capability). For each set of flow parameters, 50 cycles of periodical exponential shear are performed to reach a steady periodical response. In a PES flow, the value of $\dot{\epsilon}_s$, as introduced previously, characterizes the strength of

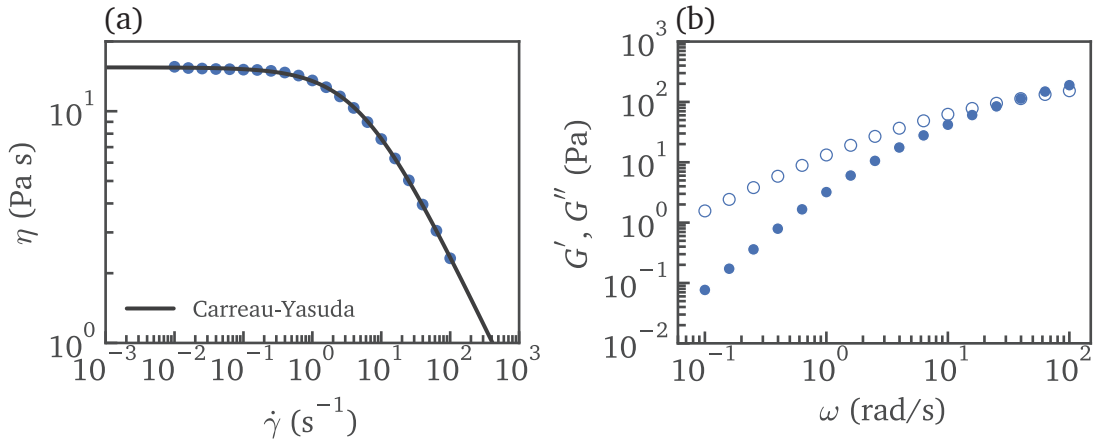

Figure 5-17: (a) Steady shear-flow curve of 8.26 wt% PIB/C16 solution (markers) fitted with Carreau-Yasuda model (black solid line). A set of model parameters can be obtained as $\eta_0 = 15.46\,\text{Pa s}$, $\lambda = 0.20\,\text{s}$, $a = 0.92$ and $n = 0.38$. (b) Storage (filled) and loss (hollow) moduli of the 8.26 wt% PIB/C16 solution measured at an oscillatory strain of $\gamma_0 = 1\%$. The shear relaxation time can be obtained from the crossover of the two moduli as $\lambda \approx 0.20\,\text{s}$, which is consistent with the value obtained from fitting the Carreau-Yasuda model in (a).

an effective extensional flow. Because of the periodical nature, the value of $\dot{\epsilon}_s T_0$ determines the oscillatory strain, which provides additional control over the flow profile over one cycle. From Equation (5.30), if the value of $\dot{\epsilon}_s T_0$ is fixed, the strain input at varying elongational rates can be collapsed by normalizing the abscissa and ordinate with T_0 and $\gamma_0 = 2\sinh(\dot{\epsilon}_s T_0/2)$, respectively. As a result, different values of $\dot{\epsilon}_s T_0$ can be treated as distinct strain inputs to the system. The PES flow is thus suitable to probe both strain-dependent and rate-dependent material responses via the control of $\dot{\epsilon}_s T_0$ and $\dot{\epsilon}_s$, respectively.

In Figure 5-18, key transient responses in a PES flow are demonstrated at a specific flow profile with $\dot{\epsilon}_s = 1\,\text{s}^{-1}$ and $\dot{\epsilon}_s T_0 = 10$ to show distinct rheological behavior from a shear flow. As shown in Figure 5-18(a), temporal evolutions of the shear stress σ_{12} (blue dashed line), normal stress difference N_1 (red dashed-dotted line), principal normal stress difference $\sigma^{\text{P}}_{11} - \sigma^{\text{P}}_{22}$ (black solid line), as well as the extinction angle χ are plotted in the first half period of the 50th cycle. It is evident that as the strain increases, both σ_{12} and N_1 increase in magnitude. Meanwhile, as the extinction angle χ vanishes, the magnitude of $\sigma^{\text{P}}_{11} - \sigma^{\text{P}}_{22}$ becomes progressively dominated by the normal

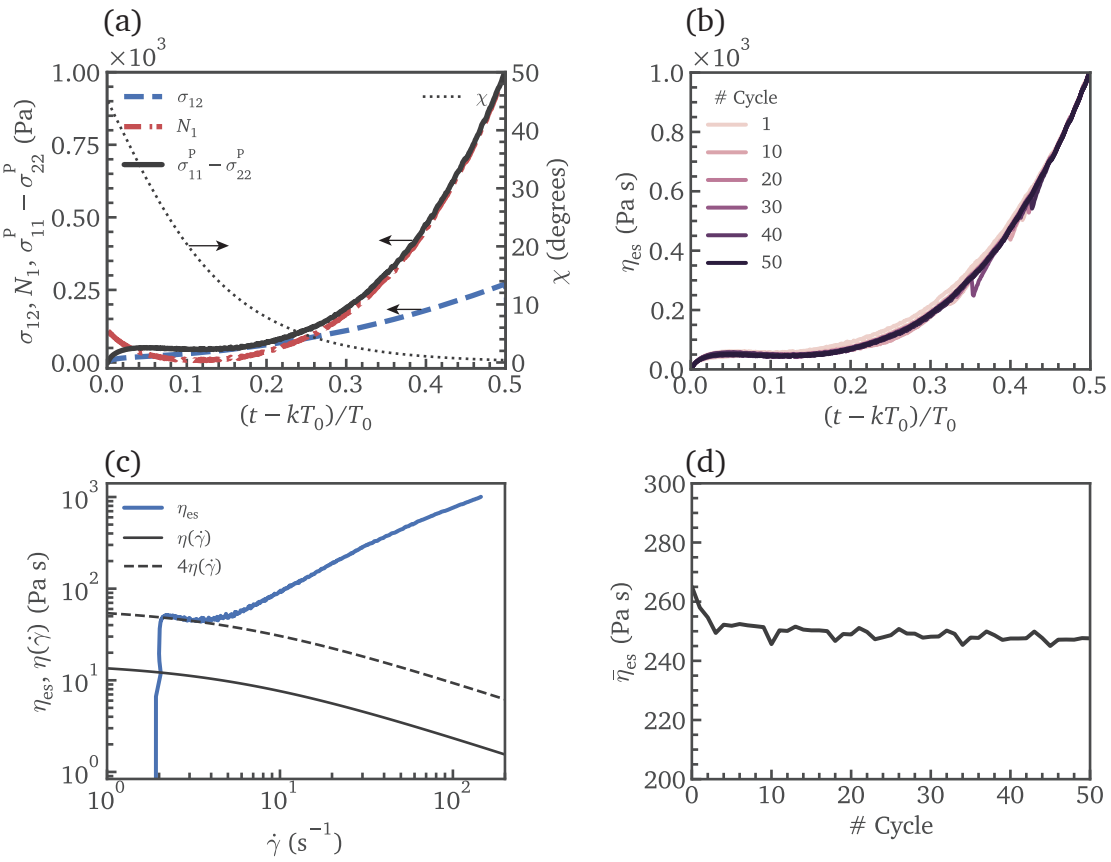

Figure 5-18: Material responses under a PES flow at $\dot{\epsilon}_s = 1\,\mathrm{s}^{-1}$ and $\dot{\epsilon}_s T_0 = 10$. Data in the first half-periods ($kT_0 < t \leq kT_0 + T_0/2$) are shown. (a) Evolutions of shear stress σ_{12}, normal stress difference N_1 and principal normal stress difference $\sigma^{\mathrm{P}}_{11} - \sigma^{\mathrm{P}}_{22}$ (ordinate on the left), as well as extinction angle χ (ordinate on the right) against normalized time $0 < (t - kT_0)/T_0) \leq 0.5$. Data at the 50th cycle are shown. (b) Evolution of the transient viscosity in principal direction η_{es} overlapped by the measurements of all 50 cycles. (c) Transient viscosity in principal direction η_{es} against shear rate ($\dot{\gamma}$). Black solid and dashed lines show predictions from the steady shear viscosity as $\eta(\dot{\gamma})$ and $4\eta(\dot{\gamma})$. Data at the 50th cycle are shown. (d) Evolution of averaged viscosity in principal direction $\bar{\eta}_{\mathrm{es}}$ (Equation (5.31)) over PES cycles.

stress contribution. Because of a large normal stress at high shear rates, the transient viscosity in the principal direction, η_{es} increases rapidly, as shown in Figure 5-18(b). To better compare the material response in a PES flow with that in a steady-shear flow,

Figure 5-18(c) replots the viscosity function against transient shear rates. Here, a prediction from the steady-state flow, $\eta(\dot{\gamma})$ can be readily obtained from Equation (5.32) (black sold line). Another reference line is plotted as $4\eta(\dot{\gamma})$ (black dashed line) to show an inelastic contribution to the overall viscosity in an exponential flow (as $\mathrm{Tr} = 4$ for a planar extensional flow). It is found that at low shear rates, the inelastic prediction overlaps with the trend of η_{es}. This is consistent with Figure 5-18(a) when the extinction angle is well above 0° and the principal normal stress difference is primarily contributed from the shear stress. As the transient shear rate increases, viscosity in the principal direction increases rapidly and deviates from the inelastic prediction. The trend of η_{es} from Figure 5-18(c) is similar to the flow behavior of a polymer solution in an extensional flow, where the stretch of polymer chains induces a strong elastic response and subsequently exhibits rate-thickening behavior.

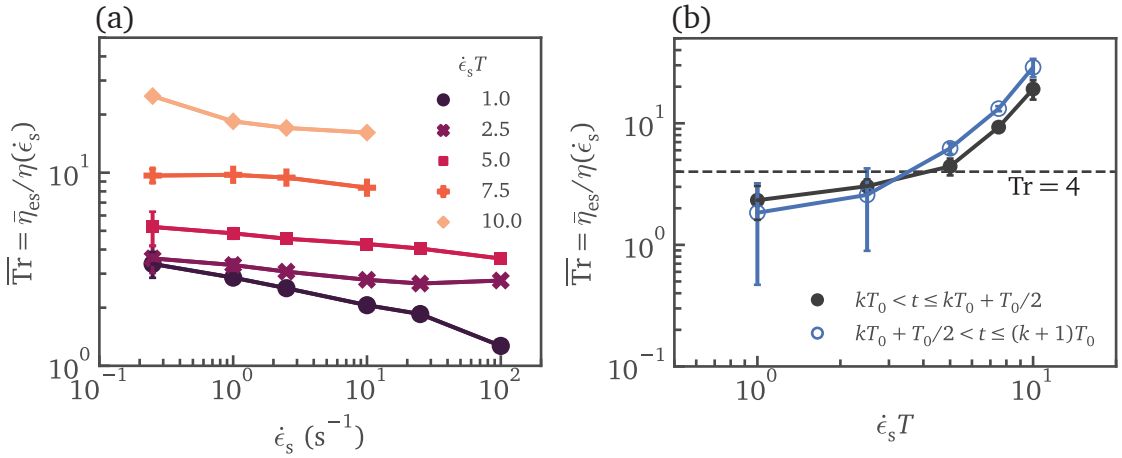

Figure 5-19: (a) Averaged Trouton ratio $\overline{\mathrm{Tr}}$ (from data after 5th cycle) against elongational rate $\dot{\epsilon}_s$ at varying $\dot{\epsilon}_s T_0$. (b) Averaged Trouton ratio $\overline{\mathrm{Tr}}$ over all elongational rates in (a) at fixed values of $\dot{\epsilon}_s T_0$. Data from the material responses in both the first (filled black markers) and second (filled blue markers) halves of one period are obtained. The reference of $\mathrm{Tr} = 4$ is drawn in black dashed line, above which strain-hardening behavior can be justified.

Finally, an averaged Trouton ratio under a PES flow can be calculated as

$$\overline{\mathrm{Tr}} \equiv \frac{1}{|\{n_i\}|} \sum_{\{n_i\}} \frac{\bar{\eta}_{es}}{\eta(\dot{\epsilon}_s)}, \tag{5.33}$$

where $\eta(\dot{\epsilon}_s)$ is the steady-shear viscosity evaluated at $\dot{\epsilon}_s$ using Equation (5.32), and

$\{n_i\}$ is a subset of cycles from which an averaged value is calculated. As justified in Figure 5-18(b) and (d) (as well as the results for other combinations of $\dot{\epsilon}_s$ and T_0, which are not shown here), a steady periodical state is obtained after approximately 5 cycles. As a result, data starting from the 6th cycle are used for the calculation. As shown in Figure 5-19(a), the averaged Trouton ratio is plotted against elongational rates at varying accumulated strains (scales with $\dot{\epsilon}_s T_0$). Here, data at $\dot{\epsilon}_s > 10\,\mathrm{s}^{-1}$ for $\dot{\epsilon}_s T_0 > 5$ are not accessible due to instrument limitations. From Figure 5-19(a), a general trend of the averaged Trouton ratio can be identified, in which $\overline{\mathrm{Tr}}$ increases as the accumulated strain increases and shows strain-hardening behavior. At a fixed accumulated strain (constant $\dot{\epsilon}_s T_0$), however, the averaged Trouton ratio remains broadly constant at varying elongational rates. Admittedly, at $\dot{\epsilon}_s T_0 = 1$, the averaged Trouton ratio shows a decreasing trend as the elonagational ratio increases. It is worth noting that at $\dot{\epsilon}_s = 100\,\mathrm{s}^{-1}$, the half period is $T_0/2 = 0.005\,\mathrm{s}$, which is smaller than the minimum rise time the instrument can apply (0.01 s). As shown in Figure 5-20, the strain evolution has deviated from the designed flow profile (blue dashed line) at high elongational rates $\dot{\epsilon}_s$, leading to an underestimated transient viscosity in the principal direction. Consequently, this apparent rate-thinning behavior, which is more evident at lower accumulated strains, can be attributed to an insufficient time of motor acceleration at higher elongational rates.

From Figure 5-19(a), values of the averaged Trouton ratio, though slightly varying with the elongation rate $\dot{\epsilon}_s$, remain broadly constant at fixed accumulated strains. As a result, a higher-level averaged Trouton ratio can be evaluated on the top of all elongation rates at fixed values of $\dot{\epsilon}_s T_0$, and is plotted against $\dot{\epsilon}_s T_0$ in an attempt to show strain-dependent behavior. As Figure 5-19(b) shows, the averaged Trouton ratio exhibits a strain-hardening trend that goes beyond $\mathrm{Tr} = 4$ which represents an inelastic response. Notably, calculations from the second half-period $kT_0 + T_0/2 < t \leq (k+1)T_0$ are obtained as well and compared with those from the first half-period. Both results are reasonably consistent, showing symmetrical rheological responses independent of the flow direction.

In the previous sections, a structural similarity has been established and justified between an entangled polymer solution and a nanofilled system in both shear and extensional flows. Consequently, a nanofilled system is expected to behave similarly in a PES flow that exhibits strain- and rate-dependent behavior, which can be beneficial to the dispersion of nanofillers under certain flow conditions. Here, preliminary results are shown in Figure 5-21 for a "less-dispersed" GO/PVA nanofilled system. The synthesis is identical to the procedures in Section 5.1, except that nanofillers are fetched from the batch suspension without sonication. The PVA concentrations is fixed at 9.1 wt%

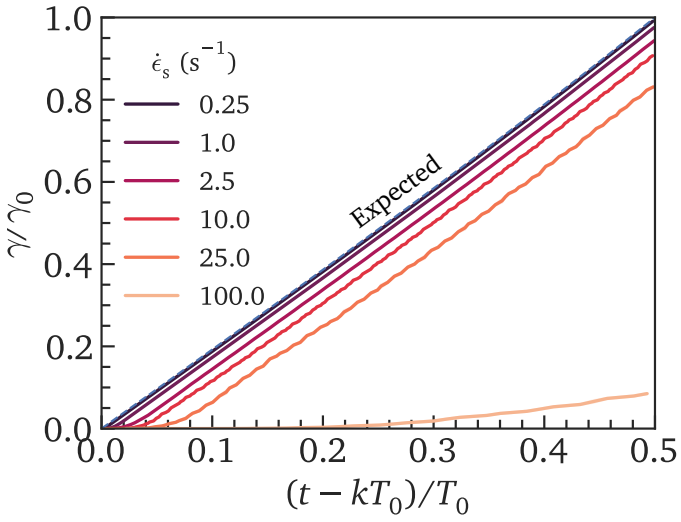

Figure 5-20: Normalized transient evolution of strain response in a half period by oscillatory strain $\gamma_0 = 2\sinh(\dot{\epsilon}_s T_0/2)$ and time period T_0 at varying elongational rates $\dot{\epsilon}_s$ and a fixed value of $\dot{\epsilon}_s T_0 = 1$. Blue dashed line corresponds to an expected response according to Equation (5.30).

with the GO concentration selected at 0.4 wt%. A specific set of PES parameters are selected at $\dot{\epsilon}_s = 5\,s^{-1}$ and $\dot{\epsilon}_s T_0 = 6$, and 1500 cycles are applied to the sample. From Figure 5-21(a), a steady increase of the averaged viscosity in the elongational direction, $\bar{\eta}_{es}$ can be identified as the material undergoes periodical shear deformation, showing structural variation under PES flows. To quantify the state of dispersion before and after applying the PES protocols, storage moduli at $\omega = 1$ rad/s are evaluated in both regimes, and the results are shown in Figure 5-21(b). From this figure, a dramatic variation in the terminal storage modulus is captured with the value increasing from 3.8 Pa to 8.9 Pa before and after applying the PES flow. Compared with Figure 5-5. The terminal storage modulus after applying the PES flow is close to a benchmark value of approximately 10 Pa measured on the same nanocomposite system with sonicated GO nanofillers, showing substantial improvement in the state of dispersion. Notably, the storage modulus after applying the PES flow exhibits a long rise time of approximately 300 s. This timescale is consistent with the rejuvenation timescale as measured at high GO concentrations in Figure 5-3. Such transient response justifies that the PES flow enables effective breakdown of large nanofiller aggregates, and the terminal storage modulus is a result of the buildup of a more percolated nanofiller network.

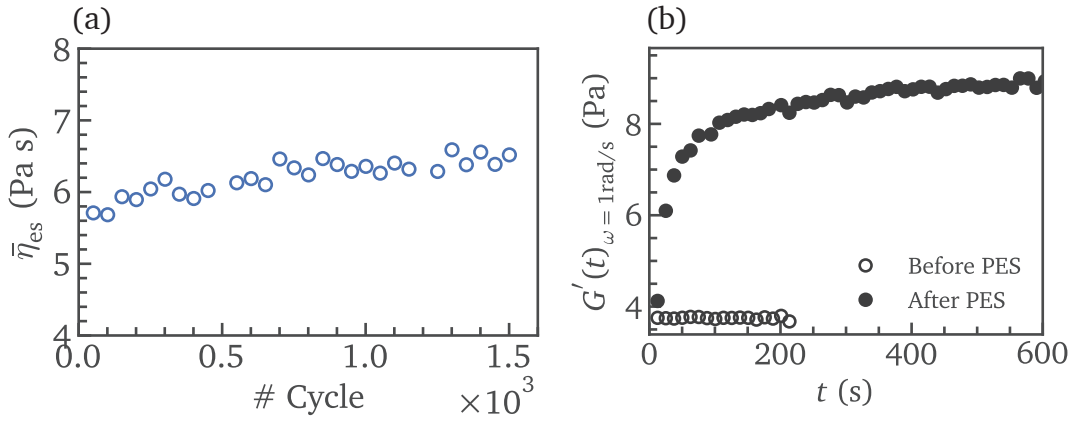

Figure 5-21: PES results on a "less-dispersed" GO/PVA system at a GO concentration of 0.4 wt% with $\dot{\epsilon}_s = 5\,s^{-1}$ and $\dot{\epsilon}_s T_0 = 6$ for 1500 cycles. (a) Evolution of averaged viscosity in the elongational direction $\bar{\eta}_{es}$ over cycles. (b) Temporal evolution of the storage modulus G' evaluated at $\omega = 1\,\text{rad/s}$ before and after the application of PES flows.

To optimize the state of dispersion through the application of PES flows, a sufficiently large principal stress in the vicinity of nanofiller aggregates is necessary to overcome the filler cohesion. As a result, design of an optimal PES flow for nanofiller dispersion is material-specific, and *a priori* characterizations of the nanofiller affinity, as well as other forms of interaction are necessary. In light of the analytical and experimental results as shown previously, a general principle is proposed here to assist in a systematic design of an optimal PES flow. Based on the original work of Grace on drop deformation and burst in immiscible fluids [22], the effectiveness of an external stress in modifying the morphology of a dispersed phase can be quantified by a dimensionless capillary number (Ca) as

$$\text{Ca} \equiv \frac{k\Delta\sigma^{\text{P}} L_{\text{d}}}{\Gamma_{\text{d}}}, \tag{5.34}$$

where $\Delta\sigma^{\text{P}}$ is the principal stress difference as defined in Equation (5.29), and L_{d} is a characteristic lengthscale of the dispersed phase. Γ_{d} is the surface energy of the dispersed phase with an identical unit of surface tension. A dimensionless prefactor k is added to characterize distinct mobilities of the continuous and dispersed phases, and its value generally varies in a range of 1 to 1.2 [334]. Here, a trivial value of unity is assumed for simplicity. In a nanofilled system, there exists a critical capillary number Ca^*, beyond which an external stress is expected to break down nanofiller aggregates. The value of Ca^* in a planar extensional flow has been characterized both numerically

and experimentally, which broadly remains between 0.1 to 1 for both Newtonian fluids and viscoelastic fluids [22,335]. Similar critical values can be presumed for a nanofilled system due to comparable material responses, though a more accurate quantification is yet to be attained from additional experimental measurements. For a typical nanofilled system with $L_d \sim 10\,\mu m$ to $100\,\mu m$ and $\Gamma_d \sim 10\,mJ/m^2$ [62,336], a critical stress can be calculated as 100 Pa to 1000 Pa. This range of stress is consistent with the output from a commercial twin-screw extruder [169]. From Equation (5.34), only a critical stress is required to induce aggregate breakdown. As a result, a PES flow is advantageous over steady-shear flow to initiate identical nanofiller dispersion at lower shear rates due to thickened viscosity in the principal direction. An effective PES flow can be readily designed by combining Equation (5.34) with independent characterizations of the non-linear rheological responses, as presented in Section 5.2 and 5.3.

5.5 Summary

This chapter presented a comprehensive rheological study for a prototypical graphene-derived nanocomposite system, *i.e.*, graphene oxide (GO)/polyvinyl alcohol (PVA) at varying GO concentrations to enhance the understanding of material responses under large shear and extensional deformation.

In shear flow, materials at sufficiently high GO concentrations exhibited yield stresses and power-law trends of shear-thinning at high shear rates, which can be captured by the Herschel-Bulkley (H-B) model. At low shear rates, however, rejuvenation of the nanofillers gives rise to a non-monotonic trend in shear stress, which can be corrected by a modified H-B model that incorporates material thixotropy. The linear viscoelastic response at varying GO concentrations can be accurately described by the fractional Kelvin-Voigt (FKV) model, from which a broad retardation time spectrum was obtained and justified. The FKV model was subsequently subsumed into a slightly modified K-BKZ constitutive framework with individual damping functions assigned to each springpot to comprehensively describe the material responses in both linear and non-linear regimes over the broad time spectrum. As demonstrated by a selected GO concentration at 0.4 wt%, predictions from the obtained constitutive framework are broadly consistent with a number of transient start-up flow and steady-shear measurements. In addition, the Cox-Merz rule was verified from experimental measurements, implying rheological similarity between the selected nanocomposite system and a polymer solution.

The extensional rheology was probed through the customized CaBER device introduced

in previous chapters. Different filament thinning dynamics arose at varying GO concentrations. Measurements at low GO concentrations ($c \leq 0.05$ wt%) showed weakly elastic responses primarily arising from the stretching of PVA chains, and a relaxation time (2 ms to 4 ms) was obtained from fitting into the Oldroyd-B model. In contrary, as nanofillers start to interact at high GO concentrations, the rheological response and nanocomposite microstructure show similarity with those of entangled polymer solutions. The Rolie-Poly model was subsequently applied for data fitting and showed excellent agreement with the measured filament thinning profiles. From the extracted constitutive parameters, the microstructural variation was illustrated in a three-staged process that incorporates nanofiller orientation and polymer chain stretch.

The conformational variation in an extensional flow inspired a new flow design to improve the nanofiller dispersion through a periodical exponential shear (PES) flow. The material function to describe local material response can be defined in the principal elongational direction. The proposed flow profile was inspected on a polyisobutylene/hexadecane solution (8.26 wt%). In contrast with a rate-thinning trend in steady-shear flow, measurements in a PES flow at varying elongational rates and oscillatory strains showed evident strain-hardening behavior, which is consistent with the material response expected in extensional flow. The PES protocol was subsequently tested on a "less-dispersed" nanofilled system synthesized from unsonicated nanofillers, and the results showed effective breakdown of large aggregates, resulting in a more percolated nanofiller network, as justified from the measurement of storage moduli. Finally, a general principle for the design of an optimal PES flow was proposed by comparing the local principal stress with cohesion between nanofillers. Due to a thickened viscosity in a PES flow, a lower shear rate is required to induce an identical principal stress, thus assisting in more accessible optimization of nanofiller dispersion using existing compounding devices.

This page is intentionally left blank.

6 | Conclusions and Future Works

6.1 Summary of results

The conviction of carbon footprint reduction from automotive vehicles has become pivotal in controlling the worldwide greenhouse gas emission. It concomitantly brings challenges and new opportunities to the automotive industry with an increasing demand of enhanced energy efficiency through optimization of innovative product designs as well as adoption of advanced materials and manufacturing processes. As introduced in **Chapter 1**, the emergence and subsequent development of nanofilled systems provide new insights in cost-effective alternatives to the existing material hierarchy for automotive vehicle manufacturing. A mass deployment of these materials to the manufacturing of commercial vehicles, however, has been mostly inhibited so far by a limited understanding of complex material dynamics and the resulting morphological variations of nanofillers during manufacturing processes under large deformation, which are critical in obtaining and retaining the desired property enhancement.

In light of the structure-rheology complexity arising in anisotropic nanofilled systems, **Chapter 2** provides an extensive literature review of recent progress on the rheology of graphene-derived nanocomposites (GDNC) as well as the preliminary knowledge for this thesis. Current challenges in the characterization and processing of these complex systems are introduced, with an especial focus on understanding the complex dynamics in extensional flow, as well as obtaining an optimal state of nanofiller dispersion.

In **Section 2.1**, the structure of graphene nanofillers is briefly introduced, featuring a two-dimensional layered structure with a large aspect ratio and a high specific surface area. The superior mechanical, thermal and electric properties of graphene nanofillers demonstrate their great potentials in enhancing polymeric materials with a minimal nanofiller loading. Graphene-derived nanofillers in polymer matrices can differ in structures and conformations in polymer matrices due to different precursors, syn-

thesizing methods and compounding processes. In practice, nanofillers are selected on the basis of their compatibility with the polymer matrix, which is critical in obtaining an optimal state of nanofiller dispersion to produce high surface areas, hence maximizing the overall property enhancement. The state of dispersion can be characterized through a number of microscopic and scattering techniques, as well as from the rheological characterizations. The optimization of nanofiller dispersion in industry is mostly obtained by solution or melt blending performed on commercial compounding devices. However, the optimal degree of dispersion from a compounding process, in which mixtures of polymer matrices and nanofillers primarily undergo steady shear motion, is limited by a maximum viscosity ratio. Recent studies have presented new designs of compounding instruments or as attachments that induces a strong extensional flow to assist in more vigorous breakdowns of the nanofiller agglomerates, but the kinematic design is limited by the channel geometry and is generally decoupled from *a priori* knowledge of the nanocomposite rheology. These limitations motivate a new design based on exponential shear flow to induce a flexible and more robust rheology-inspired optimization of the nanofillers, which is further elaborated in Chapter 5. **Section 2.2** briefly introduces a number of rheological characterizing techniques commonly applied to probe complex material dynamics. Compared with shear rheology, material response in a strong extensional flow provides a more accurate description for the microstructural evolution of nanofilled systems under large deformation and is more closely connected to a real manufacturing process. However, a paucity of measuring procedures in extensional flow prompts the design and application of rapid characterizing protocols as well as robust constitutive frameworks to capture the rheological complexity of nanofillered systems arising from phase interactions and conformational variations.

In **Chapter 3**, the limitation of characterizing protocols is addressed in two aspects. **Section 3.1** recapitulates the construction of a customized Capillary Breakup Extensional Rheometer (CaBER) with key design parameters and measuring capabilities based on the author's master work. A progressive development and perfection of constitutive frameworks allow for capturing complex filament thinning dynamics governed by multiple stress contributions to the tensile stress in a fluid. In **Section 3.2**, an Inelastic Rate-Thickening (IRT) model parameterized by a zero-rate viscosity and a rate of extensional-thickening is proposed to characterize rate-dependent behavior of two selected synthetic motor oils in extensional flow. When a viscoelastic response becomes stronger, the Oldroyd-B model is applied and leads to evident elasto-capillary thinning behavior with an exponentially decaying filament radius at a constant Weissenberg number of $\mathrm{Wi} = 2/3$. The selection of an appropriate model is determined by a critical intrinsic elasto-capillary number $\mathrm{Ec}^{*}_{\text{V-E}} = 4.7$, which is obtained by imposing a non-

inflective transition from visco-capillary to elasto-capillary thinning in the evolution of filament radius. Due to multiple contributions to the tensile stress in the constitutive equations, new challenges arise when applying the IRT model and the Oldroyd-B model to obtain accurate constitutive parameters from a temporally-evolving geometric correction factor X. Analytical and numerical procedures are carried out to compute full-dimensional filament profiles for both models, from which the evolution in the geometric correction factor is identified. For the IRT model, the results show two asymptotic solutions of $X_{\mathrm{N}} = 0.7127$ and $X_{\mathrm{RT}} = 0.5778$ when the filament thinning dynamics are solely governed by the zero-rate and the rate-thickening contributions, while for the Oldroyd-B model, the two asymptotic solutions become $X_{\mathrm{N}} = 0.7127$ and $X_{\mathrm{EC}} = 1$ arising from the solvent and polymer contributions, respectively. A time-implicit expression of $X(\boldsymbol{\sigma})$ can be obtained through linear interpolation of the magnitude of each stress contribution and is subsequently validated through numerical calculations to collapse the results at varying constitute parameters and geometrical configurations. A corrected solution for the filament thinning profile incorporating this expression of $X(\boldsymbol{\sigma})$ is obtained and shown to agree with the asymptotic solutions of Newtonian fluids at low strain rates. A revisit to the CaBER measurements of the motor oils using protocols that incorporate temporally-evolving geometric correction factors show significant improvement in the accuracy of extracted constitutive parameters. In **Section 3.3**, a statistics-based strategy is proposed to select the best-fit model (BFM) with well-regularized constitutive parameters on the basis of the parameter-free Bayesian information criterion (BIC). This strategy is substantiated by applying to the measured filament thinning profiles of four fluid samples ranging from a Newtonian fluid to a strongly viscoelastic polymer solution, from which the BFM is selected from a number of constitutive models with varying viscoelastic responses. In particular, selection between the IRT model and the Oldroyd-B model is in good agreement with the rheology-based criterion with the critical intrinsic elasto-capillary number $\mathrm{Ec}^{*}_{\mathrm{V\text{-}E}}$.

The filament thinning profiles predicted from the IRT model and the Oldroyd-B model reveal substantially different filament thinning dynamics when multiple stress contributions arise in the momentum equation. However, these two models failed to capture a number of key observations from entangled polymer solutions, including extensional-thinning behavior and distinct relaxation time measures in shear and extensional flows. In **Section 4.1**, the reptation theory is applied in the form of tube models to construct a robust description of the conformational variation of interactive polymer chains beyond entanglement concentrations. To explore the dynamics arising from both reptation and other non-reptative mechanisms, two prototypical tube models are selected, namely, the Doi-Edwards-Marrucci-Grizzuti (DEMG) model and the Rolie-Poly model, both of which are featured with reptation and polymer chain stretch with the addition

of constraint convective release (CCR) effect to the latter model. For both models, the numerically calculated filament thinning dynamics reveal a broadly consistent multi-staged filament thinning profile, varied at different intrinsic elasto-capillary numbers $\mathrm{Ec}_0 = G_\mathrm{N} R_0/\Gamma$: When $\mathrm{Ec}_0 > 1/3$, the filament thinning process undergoes a three-stage process dominated by tube reorientation, polymer chain stretch and finite extensibility of tube segments, respectively. During the process of tube reorientation towards a state of uniform alignment, the polymer chains remain broadly unstretched. The resulting filament thinning is consistent with the kinematics under a visco-capillary balance, with apparent rate-thinning behavior. A transient viscosity can be extracted from the trend of filament thinning and is found to broadly scale with the zero-shear viscosity $\eta_0 = G_\mathrm{N}\lambda_\mathrm{D}$ (Equation (4.8)), where G_N is the plateau modulus and λ_D is the disengagement time. As the tube segments approach full alignment, the polymer chain stretch of tube segments increases the total tensile stress and subsequently induces an evident retardation in filament thinning, leading to elasto-capillary thinning behavior with an apparent extensional relaxation time close to $\lambda_\mathrm{R}/2$ (Equation (4.9)), where λ_R is the Rouse time. In the final stage of filament thinning, the chain stretch of tube segments approaches a specified finite chain extensibility, and the transient extensional viscosity is limited at a plateau value of $\eta_{0,\infty} = 3G_\mathrm{N}\Lambda_\mathrm{m}^2/(1-1/\Lambda_\mathrm{m})$ (Equation (4.10)). In contrary, when $\mathrm{Ec}_0 \leq 1/3$, the initial tensile stress arising from fully aligned tube segments does not suffice to balance the capillary pressure, and additional stress contribution from the polymer chain stretch is necessary. Consequently, the filament thinning profile becomes two-staged, skipping the tube reorientation process. The filament thinning dynamics characterized from shear rheology and filament thinning dynamics in extensional flow predicted for tube models give rise to an analytical, parameter-free expression of the ratio between apparent extensional and shear relaxation times as a function of the polymer concentration c and the number of entanglements per chain Z. The ratio of the two relaxation time measures at varying polymer chain conformations can be collapsed onto a master curve, which shows excellent agreement with the experimental results from a number of polymer systems.

In **Section 4.2.1**, this robust constitutive framework is applied to a concentrated cellulose/ionic liquid system, which is beginning to find applications in fabric recycling and regeneration. Two sources of cellulose (cotton fiber and filter paper) with different degrees of polymerization dissolved in $[\mathrm{C_2C_1Im}][\mathrm{OAc}]$ are studied at varying temperature (25 °C to 80 °C) and concentrations (1 wt% to 4 wt%). Measurements from a commercial shear rheometer and the customized CaBER device reveal general shear-thinning behavior but more complex non-monotonic extensional-rate dependence for both cellulose sources. These measurements can be readily interpreted by the full-dimensional Rolie-Poly model with a universal set of constitutive parameters fitted from steady shear

viscosity, first normal stress coefficient and transient extensional viscosity (Figure 4-11, Figure 4-12 and Figure 4-13). The extracted constitutive parameters, in particular the ratio between the disengagement time and the Rouse time, exhibits consistent trends with the cellulose concentration, from which the state of entanglement can be reliably inferred. In **Section 4.2.2**, the measured filament profiles for a series of hydroxyethyl cellulose (HEC) solutions from a previous study [32] are refitted with the Rolie-Poly model. The fitted filament profiles show excellent agreement with the experimental measurements at varying HEC molecular weights and concentrations down to the instrument optical limit ($R/R_0 \approx 0.01$). The extracted number of entanglements per chain (Z_{sol}) for samples in the entangled regime exhibits a collapsed power-law trend with HEC concentration, and the exponent is well consistent with our prediction with a value of $1/(3\nu - 1)$ (Equation (4.12)).

In **Chapter 5**, a graphene-oxide (GO)/polyvinyl alcohol (PVA) system nanocomposite is selected as a prototypical material to investigate the shear and extensional rheology of a nanofilled system. In **Section 5.2**, shear rheology for a selected range of GO concentrations is characterized through a number of rheological techniques. From the measurements of low-frequency storage moduli, the formation of a percolated nanofiller network at high GO concentrations can be justified. A broad retardation time spectrum is captured from the frequency responses of dynamic moduli, which can be ascribed to complex rheological contributions arising from polymer and nanofiller phases. To characterize such a broad time spectrum, the fractional Kelvin-Voigt (FKV) model is applied, and numerical fitting shows excellent agreement with the measurements. A non-linear material response is subsequently established using the fractional K-BKZ constitutive framework, which is exemplified by the GO/PVA nanocomposite system with a selected GO concentration of 0.4 wt%. To describe the stress-relaxation responses over a wide time range, individual damping functions of the Soskey-Winter form are assigned to each springpot in the FKV model. Predictions from the non-linear constitutive framework broadly agree with the material responses from a series of start-up flows at varying step shear rates in both short- and long-time ranges, and a steady-shear flow curve predicted by the K-BKZ model exhibits consistent power-law asymptotes at low and high shear rates with the measurements. In contrary to the Rutgers-Delaware rule, which commonly applies to dense particulate suspensions, the Cox-Merz rule is validated from the measurements of both linear and steady-shear responses. This observation implies intrinsic rheological similarity of a nanocomposite system with polymer systems due to increased flexibility in the conformation of continuous phases.

Finally, extensional rheology of the GO/PVA nanocomposite at varying concentrations

is characterized in **Section 5.3** by the customized CaBER device. Distinct filament thinning profiles arise as the GO concentration is varied. At low concentrations ($c \leq 0.05$ wt%), the filament thinning profiles exhibit weakly viscoelastic behavior by virtue of the extension of PVA chains. Such behavior is justified by the small extensional relaxation times ($\lambda < 5$ ms) from fitting to the Oldroyd-B model. As the GO concentration increases, the transient material responses exhibit evident rate-thinning behavior before elasto-capillary thinning is captured. This trend resembles the filament thinning dynamics predicted from tube models that characterize entangled polymer systems. From the results in Section 4.1, a similar structural description can be established for nanocomposites, in which rigid nanofillers significantly inhibit the mobility of intercalated polymer chains by the formation of structure-spanning percolated networks, and conformation of polymer chains dominate the flow dynamics only at high extensional rates. Inspired by such structural similarity, the Rolie-Poly model is applied and accurately fits the measured filament thinning profiles, from which the temporal evolution of nanofiller orientation as well as the disengagement time can be extracted. Following predictions from the Rolie-Poly model, a three-stage filament thinning process can be identified: At low strain rates, nanofillers initiate to rotate towards the flow direction due to convective flow, and the flow dynamics are governed by a visco-capillary balance. As the strain rate increases, nanofillers progressively reorient until approaching full alignment, during which the mobility of nanofillers increases, resulting in decreased extensional viscosity. Finally, the stretch of intercalated polymer chains dominates the flow dynamics, and elasto-capillary thinning behavior is reproduced.

In **Section 5.4**, the morphological variation of nanofillers in extensional flow motivates an innovative method to modify and optimize the dispersion state of nanofillers using a periodical exponential shear (PES) flow. A material function can be defined based on the stress components in principal elongational directions as a function of the elongational rate $\dot{\epsilon}_s$ and the oscillatory strain $\dot{\epsilon}_s T_0$. To demonstrate similar material responses from a PES flow and a planar extensional flow, proof-of-concept experiments are performed on an entangled polyisobutylene/hexadecane solution (8.26 wt%), from which a thickened viscosity is captured at large oscillatory strains $\dot{\epsilon}_s T_0 \gtrsim 4$. Preliminary results from applying the PES protocol to a "less-dispersed" nanocomposite system show promising results, in which the storage modulus dramatically increases due to an improved state of nanofiller dispersion and a more percolated nanofiller network. A general principle is proposed to design an optimal PES flow for nanofiller dispersion based on a critical stress. As the viscosity in principal elongational directions rapidly increases at larger oscillatory strains, the maximum shear rate required to induce an identical magnitude of principal stress decreases significantly, making it more accessible to perform optimal nanofiller dispersion on existing compounding devices.

6.2 Future works

In this thesis, a number of key limitations in characterizing the complex rheology of nanofilled systems were addressed through the applications of a variety of instrument constructions and modeling techniques. Looking into the future, continuing efforts will be primarily focused on bridging the gap to scaled-up industrial applications based on the outputs of this thesis to motivate data-driven material characterization and techniques. They are briefly summarized as follows.

6.2.1 Automated data processing of CaBER measurements

In Chapter 3, a more comprehensive protocol to interpret the measurements from capillarity-thinning dynamics was proposed to extract an accurate and well-regularized set of constitutive parameters. To better target more general audience in both academia and industry, a computation library will be developed on an open-source platform with well-documented tutorials and user guides. In this library, multiple features in data processing are incorporated, including

- Efficient extraction of filament thinning profiles from image sequences captured by high-speed imaging systems;
- Data fitting to a preloaded constitutive model, or a user-defined governing equation;
- Accurate calculations of fluid properties from the extracted constitutive parameters;
- Automated selection of the best-fit model based on parameter-free statistical criteria;
- Multi-processing capabilities to enable high-throughput characterizations for a large number of samples.

In light of costly computation in the data-fitting process, machine-learning based protocols will be explored to construct a preselection process to trim the search range of best-fit models prior to the inspection of individual constitutive models. In this preselection process, the measured filament thinning profiles are abstracted as a reduced dataset through feature extraction, which is subsequently loaded to a pattern recognition process to determine the likelihood of each constitutive model candidate. With easily accessible training sets obtained from numerical calculations, these data-driven techniques can provide accurate constitutive inferences for a variety of materials, which

are finding practical interest in industry with an increasing demand for rapid rheological characterizations.

6.2.2 Modeling of extensional deformation of entangled polymer solutions in real manufacturing processes

In Chapter 4, a robust constitutive framework accurately described the complex rheological behavior of entangled polymer solutions in both shear and extensional flows over a wider range of time- and lengthscales. Due to ubiquitous observation of strong extensional flow in real manufacturing processes (*e.g.*, fiber-spinning, melt blowing and 3D printing process), a direct application of this constitutive framework is envisioned to characterize and optimize manufacturing parameters.

In a wet-spinning process of cellulose/ionic liquid dopes, in particular, the addition of a dry-jet process with an air gap between the spinneret and the coagulation bath has shown significant enhancements of mechanical properties in the spun fibers [302]. While the mechanism of such property enhancement is less well understood, the flow dynamics of entangled polymer solutions in an extensional flow presented in this thesis provide a new angle of perspective from flow-induced reorientation of cellulose chains. As cellulose chains become progressively anisotropic, their coagulation dynamics are substantially modified due to variations in the solvent (ionic liquid) and anti-solvent (water) diffusivities, thus altering the resulting properties. To seek a robust relation between the rheological properties of spinning dopes and the performance of spun fibers, rheo-optic techniques will be applied to quantify the conformation of cellulose chains during the coagulation process through online birefringence measurements, from which a stress-optic relation will be established under different draw ratios and residence times. This online measuring protocol is aimed at monitoring structural variations and performance of cellulose fibers in a wet-spinning process without *post factum* dynamical analysis. It will provide additional dimensions to evaluate and optimize the fiber performance in generic spinning configurations.

6.2.3 Rheo-spectroscopic characterizations of periodical exponential flows

In Chapter 5, a new flow profile was designed using periodical exponential shear flows to induce a strong principal stress to assist in nanofiller dispersion. However, current designs of the periodical exponential flow profiles are primarily empirical, and a connection is still absent between measured material responses in bulk fluid properties

and morphological variations of nanofillers. Consequently, applications of *in situ* rheo-spectroscopic techniques, such as rheo-nuclear magnetic resonance (rheo-NMR) [337] and rheo-small angle neutron scattering (rheo-SANS) [338] are necessary to examine the spatial flow heterogeneities as well as the state of nanofiller conformations while a transient flow profile is imposed. From these results, the dispersion mechanism through a periodical exponential shear flow can be better understood. More generally, the construction of a robust structure-rheology relationship extended into the non-linear regime through these *in situ* measurements will provide more insights into the flow-induced response of a nanofilled system that may appear in the form of a strong anisotropy due to nanofiller reorientation or a modified percolated network structure due to agglomerate variations. These findings will greatly benefit the optimization of various manufacturing processes through the development of new strategies to retain structural integrity during material processing, from which desired material properties can be faithfully attained.

This page is intentionally left blank.

A | Calibration of the improved CaBER device

A.1 Motor actuation

As shown in Figure A-1, the linear motors used to actuate the step-stain motion for CaBER measurements are calibrated with three different stroke lengths of 2 mm, 5 mm and 8 mm. The temporal evolution of the linear motion is recorded by a high-speed camera at a frame rate of 5900fps. With manually fine-tuned PID parameters, the linear actuator shows a repeatable maximum velocity $v_{\max} \approx 0.2\,\mathrm{m/s}$ with well controlled linearity and minimal position overshoot (8.7%, 4.9% and 2.7%). Under this condition, an overall stroke of 10 mm (5 mm stroke from each motor) leads to an approximate actuation time of $t_{\mathrm{M}} = 25\,\mathrm{mm}$, which is 50% less than a commercial CaBER system [201].

A.2 Laser micrometer and high-speed camera

The laser micrometer is calibrated with a series of surface-finished aluminum rods and standard optical glass fibers with diameters measured by a caliper (precision: 5 µm). For each reference object, five consecutive measurements of the voltage outputs are taken, and the mean values are used for the fitting. As shown in Figure A-2, the measured diameter and analog output voltage from the laser micrometer are plotted. In order to show the data on a logarithmic scale, all the measured voltages are offset by the ground voltage of $V_{\min} = -5\,\mathrm{V}$, which is provided by the sensor manufacturer. Data in Figure A-2(a) are fitted with a linear ($R^2 = 0.990$, green dashed line) and third-order ($R^2 = 0.998$, orange solid line) polynomial. A second-order fit is not utilized here because of its monotonicity in the second-order derivative, which brings superflu-

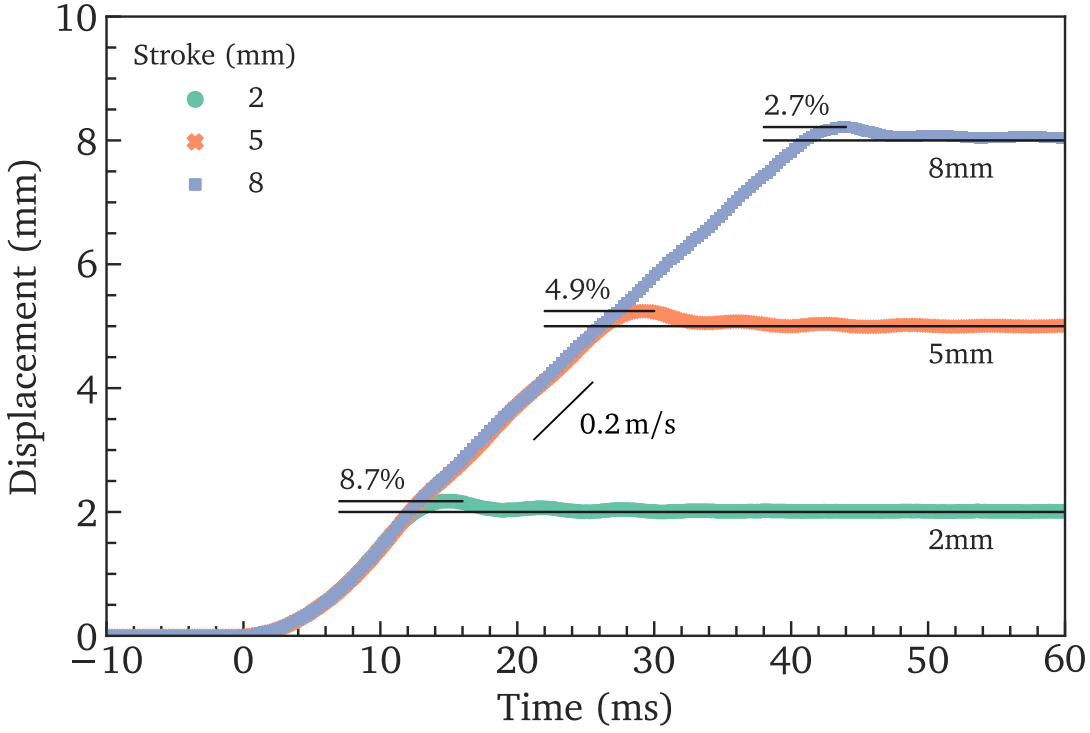

Figure A-1: Stroke tests for the linear actuator. The corresponding PID parameters are manually fine-tuned in the control software. Three stroke distances, 2 mm, 5 mm and 8 mm are imposed, and a max stroke velocity of $v_{max} \approx 0.2$ m/s is configured. The stroke trajectories are captured with a high-speed camera using a frame rate of 5900 fps, from which the temporal evolution of the end discs is extracted. The measured displacements show good linearity with time in the rising region, and the final settling times of the three strokes are approximately 17 mm/s, 32 mm/s and 46 mm/s, with overshoots of 8.7%, 4.9% and 2.7%, respectively.

ous constraints to the data fitting. In general, the data show good linearity above the manufacturer-claimed minimum object size of 100 μm (shaded area).

In Figure A-2(b), thickness of the laser beam is measured by slowly feeding the top and bottom circular discs with finished surfaces (diameter: 6 mm) across the beam. A transition region is incurred as the discs move, and the beam thickness is indicated by the width of the rising region, which reads as approximately 0.1 mm and is consistent in the measurements from both discs. This value is further used to compensate the gap

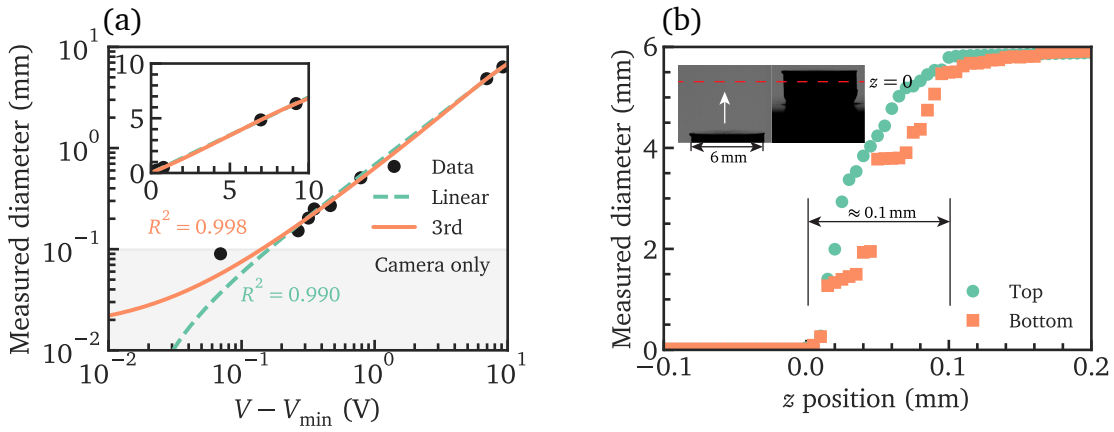

Figure A-2: (a) Calibration of the laser micrometer using a series of aluminum rods and optical fibers with independently measured diameters. The difference between measured voltage (V) and the ground voltage ($V_{min} = -5$ V) is taken. Dashed and solid lines show the first- and third-order polynomial fitting to the data. A manufacturer-claimed minimum object size of 100 µm in diameter is indicated by the shaded area, below which data can only be accessed through a high-speed imaging system. (b) Measurement of the laser beam thickness by slowly feeding the top and bottom circular discs through the beam. An approximate value of 0.1 mm is obtained from the width of the transition region.

during the zeroing process.

For more technical details on the customized CaBER device, readers are referred to the author's previous publications [29, 64].

This page is intentionally left blank.

Bibliography

[1] X. Wei, D. Li, W. Jiang, Z. Gu, X. Wang, Z. Zhang, and Z. Sun. 3D printable graphene composite. *Scientific Reports*, 5:1–7, 2015.

[2] T. C. Shyu, P. F. Damasceno, P. M. Dodd, A. Lamoureux, L. Xu, M. Shlian, M. Shtein, S. C. Glotzer, and N. A. Kotov. A kirigami approach to engineering elasticity in nanocomposites through patterned defects. *Nature Materials*, 14(8):785–789, 2015.

[3] J. S. Lee, K.-Y. Shin, O. J. Cheong, J. H. Kim, and J. Jang. Highly sensitive and multifunctional tactile sensor using free-standing ZnO/PVDF thin film with graphene electrodes for pressure and temperature monitoring. *Scientific Reports*, 5(1):7887, July 2015.

[4] O. Frank, G. Tsoukleri, I. Riaz, K. Papagelis, J. Parthenios, A. C. Ferrari, A. K. Geim, K. S. Novoselov, and C. Galiotis. Development of a universal stress sensor for graphene and carbon fibres. *Nature Communications*, 2(1):255, September 2011.

[5] P. K. Boruah, B. Sharma, N. Hussain, and M. R. Das. Magnetically recoverable Fe_3O_4/graphene nanocomposite towards efficient removal of triazine pesticides from aqueous solution: Investigation of the adsorption phenomenon and specific ion effect. *Chemosphere*, 168:1058–1067, February 2017.

[6] H. Liao, H. Zhang, G. Qin, Z. Li, L. Li, and H. Hong. A macro-porous graphene oxide-based membrane as a separator with enhanced thermal stability for high-safety lithium-ion batteries. *RSC Advances*, 7(36):22112–22120, 2017.

[7] M.-F. Li, Y.-G. Liu, G.-M. Zeng, N. Liu, and S.-B. Liu. Graphene and graphene-based nanocomposites used for antibiotics removal in water treatment: A review. *Chemosphere*, 226:360–380, July 2019.

[8] S. Goenka, V. Sant, and S. Sant. Graphene-based nanomaterials for drug delivery and tissue engineering. *Journal of Controlled Release*, 173:75–88, January 2014.

[9] A. Lerf, H. He, M. Forster, and J. Klinowski. Structure of graphite oxide revisited. *The Journal of Physical Chemistry B*, 102(23):4477–4482, June 1998.

[10] M. J. McAllister, J.-L. Li, D. H. Adamson, H. C. Schniepp, A. A. Abdala, J. Liu, M. Herrera-Alonso, D. L. Milius, R. Car, R. K. Prud'homme, and I. A. Aksay. Single sheet functionalized graphene by oxidation and thermal expansion of graphite. *Chemistry of Materials*, 19(18):4396–4404, September 2007.

[11] L. Stobinski, B. Lesiak, A. Malolepszy, M. Mazurkiewicz, B. Mierzwa, J. Zemek, P. Jiricek, and I. Bieloshapka. Graphene oxide and reduced graphene oxide studied by the XRD, TEM and electron spectroscopy methods. *Journal of Electron Spectroscopy and Related Phenomena*, 195, August 2014.

[12] C.-C. Teng, C.-C. M. Ma, C.-H. Lu, S.-Y. Yang, S.-H. Lee, M.-C. Hsiao, M.-Y. Yen, K.-C. Chiou, and T.-M. Lee. Thermal conductivity and structure of non-covalent functionalized graphene/epoxy composites. *Carbon*, 49(15):5107–5116, December 2011.

[13] J. Y. Jang, M. S. Kim, H. M. Jeong, and C. M. Shin. Graphite oxide/poly (methyl methacrylate) nanocomposites prepared by a novel method utilizing macroazoinitiator. *Composites Science and Technology*, 69(2):186–191, 2009.

[14] H. C. Schniepp, K. N. Kudin, J.-L. Li, R. K. Prud'homme, R. Car, D. A. Saville, and I. A. Aksay. Bending properties of single functionalized graphene sheets probed by atomic force microscopy. *ACS Nano*, 2(12):2577–2584, December 2008.

[15] H. Kim and C. W. Macosko. Morphology and properties of polyester/exfoliated graphite nanocomposites. *Macromolecules*, 41(9):3317–3327, May 2008.

[16] D. Wu, L. Wu, and M. Zhang. Rheology of multi-walled carbon nanotube/poly(butylene terephthalate) composites. *Journal of Polymer Science Part B: Polymer Physics*, 45(16):2239–2251, 2007.

[17] J. Vermant, S. Ceccia, M. K. Dolgovskij, P. L. Maffettone, and C. W. Macosko. Quantifying dispersion of layered nanocomposites via melt rheology. *Journal of Rheology*, 51(3):429–450, 2007.

[18] C. Vallés, R. J. Young, D. J. Lomax, and I. A. Kinloch. The rheological behaviour of concentrated dispersions of graphene oxide. *Journal of Materials Science*, 49(18):6311–6320, September 2014.

[19] D. W. Litchfield, D. G. Baird, D. W. Litchfield, and D. G. Baird. The rheology of high aspect ratio nano- particle filled liquids. *Rheology Reviews*, 2006:1–60, 2006.

[20] H. A. Barnes, J. F. Hutton, and K. Walters. *An Introduction to Rheology*. Number 3 in Rheology Series. Elsevier, Amsterdam, 6. impr edition, 1998.

[21] G. Filippone and M. Salzano de Luna. A unifying approach for the linear viscoelasticity of polymer nanocomposites. *Macromolecules*, 45(21):8853–8860, November 2012.

[22] H. P. Grace. Dispersion phenomena in high viscosity immiscible fluid systems and application of static mixers as dispersion devices in such systems. *Chemical Engineering Communications*, 14(3-6):225–277, March 1982.

[23] H. Schiessel and A. Blumen. Hierarchical analogues to fractional relaxation equations. *Journal of Physics A: Mathematical and General*, 26(19):5057–5069, October 1993.

[24] B. W. Soh and P. S. Doyle. Deformation response of catenated DNA networks in a planar elongational field. *ACS Macro Letters*, 9(7):944–949, July 2020.

[25] E. Brito-de la Fuente, M. Turcanu, O. Ekberg, and C. Gallegos. Rheological Aspects of Swallowing and Dysphagia: Shear and Elongational Flows. In O. Ekberg, editor, *Dysphagia*, pages 687–716. Springer International Publishing, Cham, 2017.

[26] V. Sharma, S. J. Haward, J. Serdy, B. Keshavarz, A. Soderlund, P. Threlfall-Holmes, and G. H. McKinley. The rheology of aqueous solutions of ethyl hydroxy-ethyl cellulose (EHEC) and its hydrophobically modified analogue (hmEHEC): Extensional flow response in capillary break-up, jetting (ROJER) and in a cross-slot extensional rheometer. *Soft Matter*, 11(16):3251–3270, 2015.

[27] H. Zhang, Q. Zhen, Y. Liu, R. Liu, and Y. Zhang. One-step melt blowing process for PP/PEG micro-nanofiber filters with branch networks. *Results in Physics*, 12:1421–1428, March 2019.

[28] G. Park, J. Yun, C. Lee, and H. W. Jung. Effect of material parameter of viscoelastic giesekus fluids on extensional properties in spinline and draw resonance instability in isothermal melt spinning process. *Polymers*, 13(1):139, January 2021.

[29] J. Du, H. Ohtani, C. E. Owens, L. Zhang, K. Ellwood, and G. H. McKinley. An improved Capillary Breakup Extensional Rheometer to characterize weakly rate-thickening fluids: Applications in synthetic automotive oils. *Journal of Non-Newtonian Fluid Mechanics*, 291:104496, May 2021.

[30] A. E. Likhtman and T. C. McLeish. Quantitative theory for linear dynamics of linear entangled polymers. *Macromolecules*, 35(16):6332–6343, 2002.

[31] R. Prabhakar, S. Gadkari, T. Gopesh, and M. J. Shaw. Influence of stretching induced self-concentration and self-dilution on coil-stretch hysteresis and capillary thinning of unentangled polymer solutions. *Journal of Rheology*, 60(3):345–366, 2016.

[32] J. Dinic and V. Sharma. Power laws dominate shear and extensional rheology response and capillarity-driven pinching dynamics of entangled hydroxyethyl cellulose (HEC) solutions. *Macromolecules*, 53(9):3424–3437, 2020.

[33] G. Santagiuliana. Preparation, characterisation, and modelling of graphene-based polymer nanocomposites with enhanced mechanical and electrical properties. 2019.

[34] T. C. B. Kwan, N. J. Woo, and E. S. G. Shaqfeh. An experimental and simulation study of dilute polymer solutions in exponential shear flow: Comparison to uniaxial and planar extensional flows. *Journal of Rheology*, 45(2):321–349, March 2001.

[35] G. H. McKinley. Visco-elasto-capillary thinning and break-up of complex fluids. *Rheology Reviews*, 3:1–48, 2005.

[36] The 2019 EPA Automotive Trends Report: Greenhouse Gas Emissions, Fuel Economy, and Technology since 1975. Technical Report EPA-420-R-20-006, United States Environmental Protection Agency, March 2020.

[37] A. Elmarakbi and W. Azoti. 1 - State of the Art on Graphene Lightweighting Nanocomposites for Automotive Applications. In F. Marotti de Sciarra and P. Russo, editors, *Experimental Characterization, Predictive Mechanical and Thermal Modeling of Nanostructures and Their Polymer Composites*, Micro and Nano Technologies, pages 1–23. Elsevier, January 2018.

[38] M. Baglione, M. Duty, and G. Pannone. Vehicle system energy analysis methodology and tool for determining vehicle subsystem energy supply and demand. SAE Technical Paper 2007-01-0398, SAE Technical Paper, Warrendale, PA, April 2007.

[39] R. B. Carlson, J. Wishart, and K. Stutenberg. On-road and dynamometer evaluation of vehicle auxiliary loads. *SAE International Journal of Fuels and Lubricants*, 9(2016-01-0901):260–268, April 2016.

[40] K. Rhodes, D. Kok, P. Sohoni, E. Perry, M. Kraska, and M. Wallace. Estimation of the effects of auxiliary electrical loads on hybrid electric vehicle fuel economy. In *WCX™ 17: SAE World Congress Experience*, pages 2017–01–1155, March 2017.

[41] J. Thomas. Drive cycle powertrain efficiencies and trends derived from EPA vehicle dynamometer results. *SAE International Journal of Passenger Cars - Mechanical Systems*, 7(2014-01-2562):1374–1384, October 2014.

[42] M. Pervaiz, S. Panthapulakkal, B. Kc, M. Sain, and J. Tjong. Emerging trends in automotive lightweighting through novel composite materials. *Materials Sciences and Applications*, 07(01):26–38, 2016.

[43] C. Nwosu, M. Iliut, and A. Vijayaraghavan. Graphene and water-based elastomer nanocomposites–a review. *Nanoscale*, 2021.

[44] J. Agarwal, S. Sahoo, S. Mohanty, and S. K. Nayak. Progress of novel techniques for lightweight automobile applications through innovative eco-friendly composite materials: A review. *Journal of Thermoplastic Composite Materials*, 33(7):978–1013, July 2020.

[45] J. R. Potts, D. R. Dreyer, C. W. Bielawski, and R. S. Ruoff. Graphene-based polymer nanocomposites. *Polymer*, 52(1):5–25, 2011.

[46] T. Hassan, A. Salam, A. Khan, S. U. Khan, H. Khanzada, M. Wasim, M. Q. Khan, and I. S. Kim. Functional nanocomposites and their potential applications: A review. *Journal of Polymer Research*, 28(2):36, February 2021.

[47] P. P. Das and V. Chaudhary. Application of Graphene-Based Biopolymer Nanocomposites for Automotive and Electronic Based Components. In B. Sharma and P. Jain, editors, *Graphene Based Biopolymer Nanocomposites*, Composites Science and Technology, pages 311–323. Springer, Singapore, 2021.

[48] H. V. Madhad, N. S. Mishra, S. B. Patel, S. S. Panchal, R. A. Gandhi, and D. V. Vasava. Graphene/graphene nanoplatelets reinforced polyamide nanocomposites: A review. *High Performance Polymers*, page 09540083211011216, 2021.

[49] Cell Phones, Sporting Goods, and Soon, Cars: Ford Innovates with "Miracle" Material, Powerful Graphene for Vehicle Parts.

https://media.ford.com/content/fordmedia/fna/us/en/news/2018/10/09/ford-innovates-with-miracle-material-powerful-graphene-for-vehicle-parts.html.

[50] R. Kandasamy. Recent advances in graphene based nano-composites for automotive and off-highway vehicle applications. *Current Graphene Science*, 03, November 2019.

[51] The Role of Nanomaterials in the Automotive Industry. https://www.azom.com/article.aspx?ArticleID=19222, 2020-04-21T11:36:00.0000000-04:00.

[52] K.-Y. Shin, J.-Y. Hong, S. Lee, and J. Jang. Evaluation of anti-scratch properties of graphene oxide/polypropylene nanocomposites. *J. Mater. Chem.*, 22:7871–7879, March 2012.

[53] A. Woo, B. Fidan, and W. W. Melek. Localization for Autonomous Driving. In *Handbook of Position Location*, chapter 29, pages 1051–1087. John Wiley & Sons, Ltd, 2018.

[54] E. D'Elia, S. Barg, N. Ni, V. G. Rocha, and E. Saiz. Self-healing graphene-based composites with sensing capabilities. *Advanced Materials*, 27(32):4788–4794, 2015.

[55] R. Moriche, M. Moreno-Avilés, A. Jiménez-Suárez, S. Prolongo, and A. Ureña. Graphene nanoplatelets electrical networks as highly efficient self-heating materials for glass fiber fabrics. *Journal of Industrial Textiles*, page 1528083720931482, June 2020.

[56] L. Pan, Z. Liu, O. kızıltaş, L. Zhong, X. Pang, F. Wang, Y. Zhu, W. Ma, and Y. Lv. Carbon fiber/poly ether ether ketone composites modified with graphene for electro-thermal deicing applications. *Composites Science and Technology*, 192:108117, May 2020.

[57] J. Seyyed Monfared Zanjani, B. Saner Okan, P.-N. Pappas, C. Galiotis, Y. Z. Menceloglu, and M. Yildiz. Tailoring viscoelastic response, self-heating and deicing properties of carbon-fiber reinforced epoxy composites by graphene modification. *Composites Part A: Applied Science and Manufacturing*, 106:1–10, March 2018.

[58] S. Dul, L. G. Ecco, A. Pegoretti, and L. Fambri. Graphene/Carbon Nanotube Hybrid Nanocomposites: Effect of Compression Molding and Fused Filament Fabrication on Properties. *Polymers*, 12(1):101, January 2020.

[59] C. Aumnate, A. Pongwisuthiruchte, P. Pattananuwat, and P. Potiyaraj. Fabrication of ABS/Graphene Oxide Composite Filament for Fused Filament Fabrication (FFF) 3D Printing. *Advances in Materials Science and Engineering*, 2018:1–9, November 2018.

[60] A. Patel and M. Taufik. *Nanocomposite Materials for Fused Filament Fabrication*. April 2021.

[61] R. Wagener and T. J. G. Reisinger. A rheological method to compare the degree of exfoliation of nanocomposites. *Polymer*, 44(24):7513–7518, November 2003.

[62] H. Kim, A. A. Abdala, and C. W. Macosko. Graphene/Polymer nanocomposites. *Macromolecules*, 43(16):6515–6530, August 2010.

[63] P. Berki, K. László, N. T. Tung, and J. Karger-Kocsis. Natural rubber/graphene oxide nanocomposites via melt and latex compounding: Comparison at very low graphene oxide content. *Journal of Reinforced Plastics and Composites*, 36(11):808–817, June 2017.

[64] J. Du. Rheological characterization of lubricants in automotive industries through development of a novel capillary breakup extensional rheometer. Master's thesis, Massachusetts Institute of Technology, 2018.

[65] T. S. Ghanta, S. Aparna, N. Verma, and D. Purnima. Review on nano-and microfiller-based polyamide 6 hybrid composite: Effect on mechanical properties and morphology. *Polymer Engineering & Science*, 60(8):1717–1759, 2020.

[66] A. F. Carvalho, B. Kulyk, A. J. S. Fernandes, E. Fortunato, and F. M. Costa. A review on the applications of graphene in mechanical transduction. *Advanced Materials*, page 2101326, July 2021.

[67] W. Zhang, J. Cui, C.-a. Tao, Y. Wu, Z. Li, L. Ma, Y. Wen, and G. Li. A strategy for producing pure single-layer graphene sheets based on a confined self-assembly approach. *Angewandte Chemie International Edition*, 121(32):5978–5982, 2009.

[68] S. J. Chae, F. Güneş, K. K. Kim, E. S. Kim, G. H. Han, S. M. Kim, H.-J. Shin, S.-M. Yoon, J.-Y. Choi, and M. H. Park. Synthesis of large-area graphene layers on poly-nickel substrate by chemical vapor deposition: Wrinkle formation. *Advanced Materials*, 21(22):2328–2333, 2009.

[69] C.-D. Kim, B.-K. Min, and W.-S. Jung. Preparation of graphene sheets by the reduction of carbon monoxide. *Carbon*, 47(6):1610–1612, 2009.

[70] N. Li, Z. Wang, K. Zhao, Z. Shi, Z. Gu, and S. Xu. Large scale synthesis of N-doped multi-layered graphene sheets by simple arc-discharge method. *Carbon*, 48(1):255–259, 2010.

[71] A. Dato, V. Radmilovic, Z. Lee, J. Phillips, and M. Frenklach. Substrate-free gas-phase synthesis of graphene sheets. *Nano Letters*, 8(7):2012–2016, July 2008.

[72] K. S. Novoselov, A. K. Geim, S. V. Morozov, D. Jiang, Y. Zhang, S. V. Dubonos, I. V. Grigorieva, and A. A. Firsov. Electric field effect in atomically thin carbon films. *Science*, 306(5696):666–669, 2004.

[73] Y. Hernandez, V. Nicolosi, M. Lotya, F. M. Blighe, Z. Sun, S. De, I. T. McGovern, B. Holland, M. Byrne, Y. K. Gun'Ko, J. J. Boland, P. Niraj, G. Duesberg, S. Krishnamurthy, R. Goodhue, J. Hutchison, V. Scardaci, A. C. Ferrari, and J. N. Coleman. High-yield production of graphene by liquid-phase exfoliation of graphite. *Nature Nanotechnology*, 3(9):563–568, September 2008.

[74] N. Liu, F. Luo, H. Wu, Y. Liu, C. Zhang, and J. Chen. One-step ionic-liquid-assisted electrochemical synthesis of ionic-liquid-functionalized graphene sheets directly from graphite. *Advanced Functional Materials*, 18(10):1518–1525, 2008.

[75] M. S. Dresselhaus and G. Dresselhaus. Intercalation compounds of graphite. *Advances in Physics*, 30(2):139–326, 1981.

[76] G. Chen, W. Weng, D. Wu, and C. Wu. PMMA/graphite nanosheets composite and its conducting properties. *European Polymer Journal*, 39(12):2329–2335, December 2003.

[77] J. H. Lee, D. W. Shin, V. G. Makotchenko, A. S. Nazarov, V. E. Fedorov, Y. H. Kim, J.-Y. Choi, J. M. Kim, and J.-B. Yoo. One-step exfoliation synthesis of easily soluble graphite and transparent conducting graphene sheets. *Advanced Materials*, 21(43):4383–4387, 2009.

[78] S. Wang, M. Tambraparni, J. Qiu, J. Tipton, and D. Dean. Thermal expansion of graphene composites. *Macromolecules*, 42(14):5251–5255, 2009.

[79] L. R. Bunnell. Method for producing thin graphite flakes with large aspect ratios, February 1993.

[80] K. Kalaitzidou, H. Fukushima, and L. T. Drzal. A new compounding method for exfoliated graphite–polypropylene nanocomposites with enhanced flexural

properties and lower percolation threshold. *Composites Science and Technology*, 67(10):2045–2051, 2007.

[81] B. Z. Jang and A. Zhamu. Processing of nanographene platelets (NGPs) and NGP nanocomposites: A review. *Journal of Materials Science*, 43(15):5092–5101, August 2008.

[82] S. Park and R. S. Ruoff. Chemical methods for the production of graphenes. *Nature Nanotechnology*, 4(4):217–224, 2009.

[83] A. Buchsteiner, A. Lerf, and J. Pieper. Water dynamics in graphite oxide investigated with neutron scattering. *The Journal of Physical Chemistry B*, 110(45):22328–22338, November 2006.

[84] D. A. Dikin, S. Stankovich, E. J. Zimney, R. D. Piner, G. H. B. Dommett, G. Evmenenko, S. T. Nguyen, and R. S. Ruoff. Preparation and characterization of graphene oxide paper. *Nature*, 448(7152):457–460, July 2007.

[85] S. Stankovich, D. A. Dikin, R. D. Piner, K. A. Kohlhaas, A. Kleinhammes, Y. Jia, Y. Wu, S. T. Nguyen, and R. S. Ruoff. Synthesis of graphene-based nanosheets via chemical reduction of exfoliated graphite oxide. *Carbon*, 45(7):1558–1565, June 2007.

[86] X. Li, H. Wang, J. T. Robinson, H. Sanchez, G. Diankov, and H. Dai. Simultaneous nitrogen doping and reduction of graphene oxide. *Journal of the American Chemical Society*, 131(43):15939–15944, 2009.

[87] Z. Fan, K. Wang, T. Wei, J. Yan, L. Song, and B. Shao. An environmentally friendly and efficient route for the reduction of graphene oxide by aluminum powder. *Carbon*, 48(5):1686–1689, 2010.

[88] H. C. Schniepp, J.-L. Li, M. J. McAllister, H. Sai, M. Herrera-Alonso, D. H. Adamson, R. K. Prud'homme, R. Car, D. A. Saville, and I. A. Aksay. Functionalized single graphene sheets derived from splitting graphite oxide. *The Journal of Physical Chemistry B*, 110(17):8535–8539, May 2006.

[89] M. J. Allen, V. C. Tung, and R. B. Kaner. Honeycomb carbon: A review of graphene. *Chemical Reviews*, 110(1):132–145, 2010.

[90] L. Staudenmaier. Verfahren zur darstellung der graphitsäure. *Berichte der Deutschen Chemischen Gesellschaft*, 31(2):1481–1487, 1898.

[91] W. S. Hummers and R. E. Offeman. Graphene oxide. *Journal of the American Chemical Society*, 80:1339, 1958.

[92] D. R. Dreyer, S. Park, C. W. Bielawski, and R. S. Ruoff. The chemistry of graphene oxide. *Chemical Society Reviews*, 39(1):228–240, 2010.

[93] A. Siklitskaya, E. Gacka, D. Larowska, M. Mazurkiewicz-Pawlicka, A. Malolepszy, L. Stobiński, B. Marciniak, A. Lewandowska-Andrałojć, and A. Kubas. Lerf–Klinowski-type models of graphene oxide and reduced graphene oxide are robust in analyzing non-covalent functionalization with porphyrins. *Scientific Reports*, 11(1):7977, December 2021.

[94] M. Herrera-Alonso, A. A. Abdala, M. J. McAllister, I. A. Aksay, and R. K. Prud'homme. Intercalation and stitching of graphite oxide with diaminoalkanes. *Langmuir*, 23(21):10644–10649, 2007.

[95] D. R. Dreyer, R. S. Ruoff, and C. W. Bielawski. From conception to realization: An historial account of graphene and some perspectives for its future. *Angewandte Chemie International Edition*, 49(49):9336–9344, 2010.

[96] C. Gómez-Navarro, M. Burghard, and K. Kern. Elastic properties of chemically derived single graphene sheets. *Nano Letters*, 8(7):2045–2049, 2008.

[97] H. A. Becerril, J. Mao, Z. Liu, R. M. Stoltenberg, Z. Bao, and Y. Chen. Evaluation of solution-processed reduced graphene oxide films as transparent conductors. *ACS Nano*, 2(3):463–470, 2008.

[98] S. Park, J. An, I. Jung, R. D. Piner, S. J. An, X. Li, A. Velamakanni, and R. S. Ruoff. Colloidal suspensions of highly reduced graphene oxide in a wide variety of organic solvents. *Nano Letters*, 9(4):1593–1597, April 2009.

[99] G. Williams, B. Seger, and P. V. Kamat. TiO2-graphene nanocomposites. UV-assisted photocatalytic reduction of graphene oxide. *ACS Nano*, 2(7):1487–1491, 2008.

[100] D. R. Dreyer, H.-P. Jia, and C. W. Bielawski. Graphene oxide: A convenient carbocatalyst for facilitating oxidation and hydration reactions. *Angewandte Chemie International Edition*, 49(38):6686–6686, 2010.

[101] D. W. Boukhvalov and M. I. Katsnelson. Modeling of graphite oxide. *Journal of the American Chemical Society*, 130(32):10697–10701, 2008.

[102] D. R. Dreyer, S. Murali, Y. Zhu, R. S. Ruoff, and C. W. Bielawski. Reduction of graphite oxide using alcohols. *Journal of Materials Chemistry*, 21(10):3443–3447, 2011.

[103] S. Stankovich, D. A. Dikin, G. H. Dommett, K. M. Kohlhaas, E. J. Zimney, E. A. Stach, R. D. Piner, S. B. T. Nguyen, and R. S. Ruoff. Graphene-based composite materials. *Nature*, 442(7100):282–286, 2006.

[104] J. W. Suk, R. D. Piner, J. An, and R. S. Ruoff. Mechanical properties of monolayer graphene oxide. *ACS Nano*, 4(11):6557–6564, 2010.

[105] Y. Zhu, S. Murali, M. D. Stoller, A. Velamakanni, R. D. Piner, and R. S. Ruoff. Microwave assisted exfoliation and reduction of graphite oxide for ultracapacitors. *Carbon*, 48(7):2118–2122, 2010.

[106] S. Naficy, R. Jalili, S. H. Aboutalebi, R. A. Gorkin III, K. Konstantinov, P. C. Innis, G. M. Spinks, P. Poulin, and G. G. Wallace. Graphene oxide dispersions: Tuning rheology to enable fabrication. *Materials Horizons*, 1(3):326–331, 2014.

[107] F. Del Giudice and A. Q. Shen. Shear rheology of graphene oxide dispersions. *Current Opinion in Chemical Engineering*, 16:23–30, 2017.

[108] Y. Matsuo, K. Hatase, and Y. Sugie. Preparation and Characterization of Poly(vinyl alcohol)- and $Cu(OH)_2$-Poly(vinyl alcohol)-Intercalated Graphite Oxides. *Chemistry of Materials*, 10(8):2266–2269, August 1998.

[109] S. Barwich, J. N. Coleman, and M. E. Möbius. Yielding and flow of highly concentrated, few-layer graphene suspensions. *Soft Matter*, 11(16):3159–3164, 2015.

[110] H.-B. Zhang, W.-G. Zheng, Q. Yan, Y. Yang, J.-W. Wang, Z.-H. Lu, G.-Y. Ji, and Z.-Z. Yu. Electrically conductive polyethylene terephthalate/graphene nanocomposites prepared by melt compounding. *Polymer*, 51(5):1191–1196, 2010.

[111] Y.-X. Pan, Z.-Z. Yu, Y.-C. Ou, and G.-H. Hu. A new process of fabricating electrically conducting nylon 6/graphite nanocomposites via intercalation polymerization. *Journal of Polymer Science Part B: Polymer Physics*, 38(12):1626–1633, 2000.

[112] H. Zois, L. Apekis, and M. Omastova. Electrical properties and percolation phenomena in carbon black filled polymer composites. In *10th International Symposium on Electrets (ISE 10). Proceedings (Cat. No.99 CH36256)*, pages 529–532, September 1999.

[113] G. Pinto, C. López-gonzález, and A. Jiménez-martín. Polymer composites prepared by compression molding of a mixture of carbon black and nylon 6 powder:

Polymer composites prepared by compression molding. *Polymer Composites*, 20(6):804–808, December 1999.

[114] M. M. Rueda, M. C. Auscher, R. Fulchiron, T. Périé, G. Martin, P. Sonntag, and P. Cassagnau. Rheology and applications of highly filled polymers: A review of current understanding. *Progress in Polymer Science*, 66:22–53, 2017.

[115] E. T. Thostenson and T.-W. Chou. Aligned multi-walled carbon nanotube-reinforced composites: Processing and mechanical characterization. *Journal of Physics D: Applied Physics*, 35(16):L77–L80, August 2002.

[116] S. B. Kharchenko, J. F. Douglas, J. Obrzut, E. A. Grulke, and K. B. Migler. Flow-induced properties of nanotube-filled polymer materials. *Nature Materials*, 3(8):564–568, 2004.

[117] J. Obrzut, J. F. Douglas, S. B. Kharchenko, and K. B. Migler. Shear-induced conductor-insulator transition in melt-mixed polypropylene-carbon nanotube dispersions. *Physical Review B*, 76(19):195420, 2007.

[118] L. F. Drummy, Y. C. Wang, R. Schoenmakers, K. May, M. Jackson, H. Koerner, B. L. Farmer, B. Mauryama, and R. A. Vaia. Morphology of layered silicate-(NanoClay-) polymer nanocomposites by electron tomography and small-angle x-ray scattering. *Macromolecules*, 41(6):2135–2143, 2008.

[119] T. Fornes and D. Paul. Modeling properties of nylon 6/clay nanocomposites using composite theories. *Polymer*, 44(17):4993–5013, August 2003.

[120] P. Steurer, R. Wissert, R. Thomann, and R. Mülhaupt. Functionalized graphenes and thermoplastic nanocomposites based upon expanded graphite oxide. *Macromolecular Rapid Communications*, 30(4-5):316–327, 2009.

[121] H. Kim, Y. Miura, and C. W. Macosko. Graphene/polyurethane nanocomposites for improved gas barrier and electrical conductivity. *Chemistry of Materials*, 22(11):3441–3450, 2010.

[122] K. A. Mkhoyan, A. W. Contryman, J. Silcox, D. A. Stewart, G. Eda, C. Mattevi, S. Miller, and M. Chhowalla. Atomic and electronic structure of graphene-oxide. *Nano Letters*, 9(3):1058–1063, March 2009.

[123] A. M. Philippe, C. Baravian, M. Imperor-Clerc, J. De Silva, E. Paineau, I. Bihannic, P. Davidson, F. Meneau, P. Levitz, and L. J. Michot. Rheo-SAXS investigation of shear-thinning behaviour of very anisometric repulsive disc-like clay suspensions. *Journal of Physics Condensed Matter*, 23(19), 2011.

[124] D. R. Paul and L. M. Robeson. Polymer nanotechnology: Nanocomposites. *Polymer*, 49(15):3187–3204, 2008.

[125] M. S. Spector, E. Naranjo, S. Chiruvolu, and J. A. Zasadzinski. Conformations of a tethered membrane: Crumpling in graphitic oxide? *Physical Review Letters*, 73(21):2867–2870, November 1994.

[126] X. Wen, C. W. Garland, T. Hwa, M. Kardar, E. Kokufuta, Y. Li, M. Orkisz, and T. Tanaka. Crumpled and collapsed conformation in graphite oxide membranes. *Nature*, 355(6359):426–428, January 1992.

[127] Y. Song and Q. Zheng. Linear rheology of nanofilled polymers. *Journal of Rheology*, 59(1):155–191, 2015.

[128] Q. Zhang, F. Fang, X. Zhao, Y. Li, M. Zhu, and D. Chen. Use of dynamic rheological behavior to estimate the dispersion of carbon nanotubes in carbon nanotube/polymer composites. *The Journal of Physical Chemistry B*, 112(40):12606–12611, 2008.

[129] A. Zosel. Rheological properties of disperse systems at low shear stresses. *Rheologica Acta*, 21(1):72–80, 1982.

[130] S. K. Kumar and R. Krishnamoorti. Nanocomposites: Structure, phase behavior, and properties. *Annual Review of Chemical and Biomolecular Engineering*, 1(1):37–58, 2010.

[131] J. Ren, B. F. Casanueva, C. A. Mitchell, and R. Krishnamoorti. Disorientation kinetics of aligned polymer layered silicate nanocomposites. *Macromolecules*, 36(11):4188–4194, 2003.

[132] M. J. Solomon, A. S. Almusallam, K. F. Seefeldt, A. Somwangthanaroj, and P. Varadan. Rheology of polypropylene/clay hybrid materials. *Macromolecules*, 34(6):1864–1872, March 2001.

[133] H. H. G. Song, R. T. Rumma, C. K. Ozaki, E. R. Edelman, and C. S. Chen. Vascular tissue engineering: Progress, challenges, and clinical promise. *Cell Stem Cell*, 22(3):340–354, March 2018.

[134] W.-H. Shih, W. Y. Shih, S.-I. Kim, J. Liu, and I. A. Aksay. Scaling behavior of the elastic properties of colloidal gels. *Physical Review A*, 42(8):4772–4779, October 1990.

[135] W. H. Herschel and R. Bulkley. Konsistenzmessungen von gummi-benzollösungen. *Kolloid-Zeitschrift*, 39(4):291–300, 1926.

[136] R. B. Bird, R. C. Armstrong, and O. Hassager. *Dynamics of Polymeric Liquids. Vol. 1: Fluid Mechanics*. 1987.

[137] A. Einstein and R. Brown. *Investigations on the Theory of the Brownian Movement*. Dover Publ, New York, one thousand, nine hundred twenty-sixth edition, 1967.

[138] G. K. Batchelor. The stress generated in a non-dilute suspension of elongated particles by pure straining motion. *Journal of Fluid Mechanics*, 46(4):813–829, April 1971.

[139] I. M. Krieger and T. J. Dougherty. A mechanism for non-newtonian flow in suspensions of rigid spheres. *Transactions of the Society of Rheology*, 3(1):137–152, 1959.

[140] J. J. Stickel and R. L. Powell. Fluid mechanics and rheology of dense suspensions. *Annual Review of Fluid Mechanics*, 37(1):129–149, 2005.

[141] G. Romeo, G. Filippone, A. Fernández-Nieves, P. Russo, and D. Acierno. Elasticity and dynamics of particle gels in non-Newtonian melts. *Rheologica Acta*, 47(9):989–997, December 2008.

[142] R. Pal. Complex shear modulus of concentrated suspensions of solid spherical particles. *Journal of Colloid and Interface Science*, 245(1):171–177, January 2002.

[143] G. Filippone, G. Romeo, and D. Acierno. Viscoelasticity and structure of polystyrene/fumed silica nanocomposites: Filler network and hydrodynamic contributions. *Langmuir*, 26(4):2714–2720, February 2010.

[144] K.-M. Jäger and S. S. Eggen. Scaling of the viscoelasticity of highly filled carbon black polyethylene composites above the melting point. *Polymer*, 45(22):7681–7692, October 2004.

[145] Y. Song, Q. Zheng, and Q. Cao. On time-temperature-concentration superposition principle for dynamic rheology of carbon black filled polymers. *Journal of Rheology*, 53(6):1379–1388, November 2009.

[146] M. Fang, K. Wang, H. Lu, Y. Yang, and S. Nutt. Single-layer graphene nanosheets with controlled grafting of polymer chains. *Journal of Materials Chemistry*, 20(10):1982–1992, 2010.

[147] D. Chen, H. Zhu, and T. Liu. In situ thermal preparation of polyimide nanocomposite films containing functionalized graphene sheets. *ACS Applied Materials & Interfaces*, 2(12):3702–3708, 2010.

[148] B. Das, K. E. Prasad, U. Ramamurty, and C. N. R. Rao. Nano-indentation studies on polymer matrix composites reinforced by few-layer graphene. *Nanotechnology*, 20(12):125705, 2009.

[149] X. Zhao, Q. Zhang, D. Chen, and P. Lu. Enhanced mechanical properties of graphene-based poly (vinyl alcohol) composites. *Macromolecules*, 43(5):2357–2363, 2010.

[150] H. B. Lee, A. V. Raghu, K. S. Yoon, and H. M. Jeong. Preparation and characterization of poly (ethylene oxide)/graphene nanocomposites from an aqueous medium. *Journal of Macromolecular Science, Part B*, 49(4):802–809, 2010.

[151] Y. Cao, J. Feng, and P. Wu. Preparation of organically dispersible graphene nanosheet powders through a lyophilization method and their poly (lactic acid) composites. *Carbon*, 48(13):3834–3839, 2010.

[152] E.-Y. Choi, T. H. Han, J. Hong, J. E. Kim, S. H. Lee, H. W. Kim, and S. O. Kim. Noncovalent functionalization of graphene with end-functional polymers. *Journal of Materials Chemistry*, 20(10):1907–1912, February 2010.

[153] B. Zhang, Y. U. Chen, X. Zhuang, G. Liu, B. Yu, E.-T. Kang, J. Zhu, and Y. Li. Poly (N-vinylcarbazole) chemically modified graphene oxide. *Journal of Polymer Science Part A: Polymer Chemistry*, 48(12):2642–2649, 2010.

[154] S. H. Lee, D. R. Dreyer, J. An, A. Velamakanni, R. D. Piner, S. Park, Y. Zhu, S. O. Kim, C. W. Bielawski, and R. S. Ruoff. Polymer brushes via controlled, surface-initiated atom transfer radical polymerization (ATRP) from graphene oxide. *Macromolecular Rapid Communications*, 31(3):281–288, 2010.

[155] F. d. C. Fim, J. M. Guterres, N. R. Basso, and G. B. Galland. Polyethylene/graphite nanocomposites obtained by in situ polymerization. *Journal of Polymer Science Part A: Polymer Chemistry*, 48(3):692–698, 2010.

[156] Z. Gu, L. Zhang, and C. Li. Preparation of highly conductive polypyrrole/graphite oxide composites via in situ polymerization. *Journal of Macromolecular Science, Part B*, 48(6):1093–1102, October 2009.

[157] P. Liu, K. Gong, P. Xiao, and M. Xiao. Preparation and characterization of poly (vinyl acetate)-intercalated graphite oxide nanocomposite. *Journal of Materials Chemistry*, 10(4):933–935, 2000.

[158] Y. R. Lee, A. V. Raghu, H. M. Jeong, and B. K. Kim. Properties of waterborne polyurethane/functionalized graphene sheet nanocomposites prepared by an in situ method. *Macromolecular Chemistry and Physics*, 210(15):1247–1254, 2009.

[159] H. Shioyama. Polymerization of isoprene and styrene in the interlayer spacing of graphite. *Carbon*, 35(10-11):1664–1665, 1997.

[160] R. Prud'Homme, B. Ozbas, I. Aksay, R. Register, and D. Adamson. Functional graphene-rubber nanocomposites, June 2010.

[161] S. S. Ray and M. Okamoto. Polymer/layered silicate nanocomposites: A review from preparation to processing. *Progress in Polymer Science*, 28(11):1539–1641, 2003.

[162] S. Kim, I. Do, and L. T. Drzal. Thermal stability and dynamic mechanical behavior of exfoliated graphite nanoplatelets-LLDPE nanocomposites. *Polymer Composites*, 31(5):755–761, 2010.

[163] K. Kalaitzidou, H. Fukushima, and L. T. Drzal. Mechanical properties and morphological characterization of exfoliated graphite–polypropylene nanocomposites. *Composites Part A: Applied Science and Manufacturing*, 38(7):1675–1682, 2007.

[164] X. Jiang and L. T. Drzal. Multifunctional high density polyethylene nanocomposites produced by incorporation of exfoliated graphite nanoplatelets 1: Morphology and mechanical properties. *Polymer Composites*, 31(6):1091–1098, 2010.

[165] A. Magrez, S. Kasas, V. Salicio, N. Pasquier, J. W. Seo, M. Celio, S. Catsicas, B. Schwaller, and L. Forró. Cellular toxicity of carbon-based nanomaterials. *Nano Letters*, 6(6):1121–1125, June 2006.

[166] B. J. Panessa-Warren, J. B. Warren, S. S. Wong, and J. A. Misewich. Biological cellular response to carbon nanoparticle toxicity. *Journal of Physics: Condensed Matter*, 18(33):S2185, 2006.

[167] V. Pandey and J. M. Maia. Extension-dominated improved dispersive mixing in single-screw extrusion. Part 1: Computational and experimental validation. *Journal of Applied Polymer Science*, 138(4):49716, 2021.

[168] K. Wakabayashi, C. Pierre, D. A. Dikin, R. S. Ruoff, T. Ramanathan, L. C. Brinson, and J. M. Torkelson. Polymer-Graphite Nanocomposites: Effective Dispersion and Major Property Enhancement via Solid-State Shear Pulverization. *Macromolecules*, 41(6):1905–1908, March 2008.

[169] S. O. Carson, J. A. Covas, and J. M. Maia. A new extensional mixing element for improved dispersive mixing in twin-screw extrusion, part 1: Design and computational validation. *Advances in Polymer Technology*, 36(4):455–465, 2017.

[170] D. Bourry, R. E. Khayat, L. A. Utracki, F. Godbille, J. Picot, and A. Luciani. Extensional flow of polymeric dispersions. *Polymer Engineering & Science*, 39(6):1072–1086, June 1999.

[171] J. Rondin, M. Bouquey, R. Muller, C. A. Serra, G. Martin, and P. Sonntag. Dispersive mixing efficiency of an elongational flow mixer on PP/EPDM blends: Morphological analysis and correlation with viscoelastic properties. *Polymer Engineering & Science*, 54(6):1444–1457, May 2014.

[172] S. O. Carson, J. M. Maia, and J. A. Covas. A new extensional mixing element for improved dispersive mixing in twin-screw extrusion, part 2: Experimental validation for immiscible polymer blends. *Advances in Polymer Technology*, 37(1):167–175, 2018.

[173] M. Bouquey, C. Loux, R. Muller, and G. Bouchet. Morphological study of two-phase polymer blends during compounding in a novel compounder on the basis of elongational flows. *Journal of Applied Polymer Science*, 119(1):482–490, 2011.

[174] R. Ibarra-Gómez, R. Muller, M. Bouquey, J. Rondin, C. A. Serra, F. Hassouna, Y. E. Mouedden, V. Toniazzo, and D. Ruch. Processing of nanocomposites PLA/graphite using a novel elongational mixing device. *Polymer Engineering & Science*, 55(1):214–222, 2015.

[175] K. Friedrich and A. A. Almajid. Manufacturing aspects of advanced polymer composites for automotive applications. *Applied Composite Materials*, 20(2):107–128, April 2013.

[176] A. Jaishankar and G. H. McKinley. Power-law rheology in the bulk and at the interface: Quasi-properties and fractional constitutive equations. *Proceedings of the Royal Society A: Mathematical, Physical and Engineering Sciences*, (1989):1–21, 2012.

[177] A. Jaishankar and G. H. McKinley. A fractional K-BKZ constitutive formulation for describing the nonlinear rheology of multiscale complex fluids. *Journal of Rheology*, 58(6):1751–1788, 2014.

[178] G. H. McKinley and T. Sridhar. Filament stretching rheometry of complex fluids. *Annual Review of Fluid Mechanics*, 34(1):375–415, January 2002.

[179] S. L. Anna, C. Rogers, and G. H. McKinley. On controlling the kinematics of a filament stretching rheometer using a real-time active control mechanism. *Journal of Non-Newtonian Fluid Mechanics*, 87(2):307–335, November 1999.

[180] H. Münstedt. New universal extensional rheometer for polymer melts. Measurements on a polystyrene sample. *Journal of Rheology*, 23(4):421–436, 1979.

[181] J. Meissner, T. Raible, and S. E. Stephenson. Rotary clamp in uniaxial and biaxial extensional rheometry of polymer melts. *Journal of Rheology*, 25(1):1–28, 1981.

[182] R. K. Gupta and T. Sridhar. Elongational rheometers. In *Rheological Measurement*, pages 516–549. Springer, 1998.

[183] M. L. Sentmanat. Miniature universal testing platform: From extensional melt rheology to solid-state deformation behavior. *Rheologica Acta*, 43(6):657–669, 2004.

[184] V. Tirtaatmadja and T. Sridhar. A filament stretching device for measurement of extensional viscosity. *Journal of Rheology*, 37(6):1081–1102, 1993.

[185] M. I. Kolte, H. K. Rasmussen, and O. Hassager. Transient filament stretching rheometer. *Rheologica Acta*, 36(3):285–302, 1997.

[186] A. V. Bazilevsky, V. M. Entov, and A. N. Rozhkov. Liquid filament microrheometer and some of its applications. In *Third European Rheology Conference and Golden Jubilee Meeting of the British Society of Rheology*, pages 41–43. Springer, 1990.

[187] L. Campo-Deaño and C. Clasen. The slow retraction method (SRM) for the determination of ultra-short relaxation times in capillary breakup extensional rheometry experiments. *Journal of Non-Newtonian Fluid Mechanics*, 165(23-24):1688–1699, 2010.

[188] D. Sachsenheimer, B. Hochstein, H. Buggisch, and N. Willenbacher. Determination of axial forces during the capillary breakup of liquid filaments – the tilted CaBER method. *Rheologica Acta*, 51(10):909–923, October 2012.

[189] P. Schümmer and K. H. Tebel. A new elongational rheometer for polymer solutions. *Journal of Non-Newtonian Fluid Mechanics*, 12(3):331–347, 1983.

[190] B. Keshavarz, V. Sharma, E. C. Houze, M. R. Koerner, J. R. Moore, P. M. Cotts, P. Threlfall-Holmes, and G. H. McKinley. Studying the effects of elongational properties on atomization of weakly viscoelastic solutions using Rayleigh Ohnesorge Jetting Extensional Rheometry (ROJER). *Journal of Non-Newtonian Fluid Mechanics*, 222:171–189, 2015.

[191] J. Dinic, Y. Zhang, L. N. Jimenez, and V. Sharma. Extensional relaxation times of dilute, aqueous polymer solutions. *ACS Macro Letters*, 4(7):804–808, 2015.

[192] G. Juarez and P. E. Arratia. Extensional rheology of DNA suspensions in microfluidic devices. *Soft Matter*, 7(19):9444–9452, 2011.

[193] P. K. Kundu and L. M. Cohen. Fluid Mechanics, 638 pp. *Academic, Calif*, 1990.

[194] B. Keshavarz and G. H. McKinley. Micro-scale extensional rheometry using hyperbolic converging/diverging channels and jet breakup. *Biomicrofluidics*, 10(4):043502, 2016.

[195] S. J. Haward, M. S. Oliveira, M. A. Alves, and G. H. McKinley. Optimized cross-slot flow geometry for microfluidic extensional rheometry. *Physical Review Letters*, 109(12):128301, 2012.

[196] R. G. Larson and P. S. Desai. Modeling the rheology of polymer melts and solutions. *Annual Review of Fluid Mechanics*, 47(1):47–65, January 2015.

[197] E. Narimissa and M. H. Wagner. Review on tube model based constitutive equations for polydisperse linear and long-chain branched polymer melts. *Journal of Rheology*, 63(2):361–375, 2019.

[198] Q. Huang, O. Mednova, H. K. Rasmussen, N. J. Alvarez, A. L. Skov, K. Almdal, and O. Hassager. Concentrated polymer solutions are different from melts: Role of entanglement molecular weight. *Macromolecules*, 46(12):5026–5035, 2013.

[199] D. Sachsenheimer, C. Oelschlaeger, S. Müller, J. Küstner, S. Bindgen, and N. Willenbacher. Elongational deformation of wormlike micellar solutions. *Journal of Rheology*, 58(6):2017–2042, 2014.

[200] O. Arnolds, H. Buggisch, D. Sachsenheimer, and N. Willenbacher. Capillary breakup extensional rheometry (CaBER) on semi-dilute and concentrated polyethyleneoxide (PEO) solutions. *Rheologica Acta*, 49(11):1207–1217, 2010.

[201] L. E. Rodd, T. P. Scott, J. J. Cooper-White, and G. H. McKinley. Capillary break-up rheometry of low-viscosity elastic fluids. *Applied Rheology*, 15(1):12–27, 2005.

[202] H. C.-H. Ng, A. Corker, E. García-Tuñón, and R. J. Poole. GO CaBER: Capillary breakup and steady-shear experiments on aqueous graphene oxide (GO) suspensions. *Journal of Rheology*, 64(1):81–93, 2020.

[203] L. Martinie, H. Buggisch, and N. Willenbacher. Apparent elongational yield stress of soft matter. *Journal of Rheology*, 57(2):627–646, 2013.

[204] S. H. Sadek, H. H. Najafabadi, and F. J. Galindo-Rosales. Capillary breakup extensional magnetorheometry. *Journal of Rheology*, 64(1):55–65, November 2019.

[205] P. Moschopoulos, A. Syrakos, Y. Dimakopoulos, and J. Tsamopoulos. Dynamics of viscoplastic filament stretching. *Journal of Non-Newtonian Fluid Mechanics*, 284(February):104371, 2020.

[206] K. Niedzwiedz, H. Buggisch, and N. Willenbacher. Extensional rheology of concentrated emulsions as probed by capillary breakup elongational rheometry (CaBER). *Rheologica Acta*, 49(11):1103–1116, 2010.

[207] D. T. Papageorgiou. On the breakup of viscous liquid threads. *Physics of Fluids*, 7(7):1529–1544, 1995.

[208] V. M. Entov and E. J. Hinch. Effect of a spectrum of relaxation times on the capillary thinning of a filament of elastic liquid. *Journal of Non-Newtonian Fluid Mechanics*, 72(1):31–53, 1997.

[209] R. B. Bird, C. F. Curtiss, R. C. Armstrong, and O. Hassager. *Dynamics of Polymeric Liquids. Vol. 2: Kinetic Theory*. Wiley, 1987.

[210] G. H. McKinley and A. Tripathi. How to extract the Newtonian viscosity from capillary breakup measurements in a filament rheometer. *Journal of Rheology*, 44(3):653–670, May 2000.

[211] C. Clasen, J. P. Plog, W.-M. Kulicke, M. Owens, C. Macosko, L. E. Scriven, M. Verani, and G. H. McKinley. How dilute are dilute solutions in extensional flows? *Journal of Rheology*, 50(6):849–881, November 2006.

[212] V. Tirtaatmadja, G. H. McKinley, and J. J. Cooper-White. Drop formation and breakup of low viscosity elastic fluids: Effects of molecular weight and concentration. *Physics of Fluids*, 18(4):043101, 2006.

[213] M. K. Tiwari, A. V. Bazilevsky, A. L. Yarin, and C. M. Megaridis. Elongational and shear rheology of carbon nanotube suspensions. *Rheologica Acta*, 48(6):597–609, 2009.

[214] C. McIlroy and O. G. Harlen. Modelling capillary break-up of particulate suspensions. *Physics of Fluids*, 26(3):33101, 2014.

[215] S. J. Haward, V. Sharma, C. P. Butts, G. H. McKinley, and S. S. Rahatekar. Shear and extensional rheology of cellulose/ionic liquid solutions. *Biomacromolecules*, 13(5):1688–1699, 2012.

[216] M. Torres, B. Hallmark, and D. Wilson. Effect of concentration on shear and extensional rheology of guar gum solutions. *Food Hydrocolloids*, 40:85–95, October 2014.

[217] L. N. Jimenez, C. D. Martínez Narváez, and V. Sharma. Capillary breakup and extensional rheology response of food thickener cellulose gum (NaCMC) in salt-free and excess salt solutions. *Physics of Fluids*, 32(1):012113, 2020.

[218] L. N. Jimenez, C. D. V. Martínez Narváez, C. Xu, S. Bacchi, and V. Sharma. The rheologically-complex fluid beauty of nail lacquer formulations. *Soft Matter*, page 10.1039.D0SM02248A, 2021.

[219] S. A. E. International. Engine oil viscosity classification. *Tribology International*, 10(2):77–80, 1977.

[220] N. Canter. Special report: Additive challenges in meeting new automotive engine specifications. *Tribology and Lubrication Technology*, 62(9):10–19, 2006.

[221] M. Smeeth, H. Spikes, and S. Gunsel. Boundary film formation by viscosity index improvers. *Tribology Transactions*, 39(3):726–734, January 1996.

[222] N. Canter. How does ZDDP function? *Tribology and Lubrication Technology*, 61(6):20–26, 2005.

[223] N. J. Mosey and T. K. Woo. Finite temperature structure and dynamics of zinc dialkyldithiophosphate wear inhibitors: A density functional theory and ab initio molecular dynamics study. *Journal of Physical Chemistry A*, 107(25):5058–5070, 2003.

[224] N. J. Mosey, M. H. Müser, and T. K. Woo. Molecular mechanisms for the functionality of lubricant additives. *Science*, 307(5715):1612–1615, 2005.

[225] L. R. Rudnick. *Lubricant Additives: Chemistry and Applications*. CRC press, 2017.

[226] M. Ratoi, V. B. Niste, and J. Zekonyte. WS2 nanoparticles-potential replacement for ZDDP and friction modifier additives. *RSC Advances*, 4(41):21238–21245, 2014.

[227] N. Nunn, Z. Mahbooba, M. G. Ivanov, D. M. Ivanov, D. W. Brenner, and O. Shenderova. Tribological properties of polyalphaolefin oil modified with nanocarbon additives. *Diamond and Related Materials*, 54(1):97–102, 2015.

[228] N. G. Demas, R. A. Erck, C. Lorenzo-Martin, O. O. Ajayi, and G. R. Fenske. Experimental evaluation of oxide nanoparticles as friction and wear improvement additives in motor oil. *Journal of Nanomaterials*, 2017, 2017.

[229] A. B. Vipper. Antioxidant properties of engine oil detergent additives. *Lubrication Science*, 9(1):61–70, 1996.

[230] O. P. Parenago, A. B. Vipper, and G. N. Kuz'mina. Zinc and molybdenum dithiocarbamates - antioxidant additives. *Lubrication Science*, 13(2):113–124, 2001.

[231] S. Tarasov, A. Kolubaev, S. Belyaev, M. Lerner, and F. Tepper. Study of friction reduction by nanocopper additives to motor oil. *Wear*, 252(1-2):63–69, 2002.

[232] J. Mewis and N. J. Wagner. *Colloidal Suspension Rheology*. Cambridge University Press, Cambridge ; New York, 1st edition edition, January 2012.

[233] J. F. Morris. A review of microstructure in concentrated suspensions and its implications for rheology and bulk flow. *Rheologica Acta*, 48(8):909–923, 2009.

[234] H. A. Barnes. Rheology of emulsions—a review. *Colloids and Surfaces A: Physicochemical and Engineering Aspects*, 91:89–95, 1994.

[235] K. Ohsawa, S. Kiyama, Y. Nakamura, Y. Ochiai, S. Nakagawa, T. Oda, and Y. Miyauchi. Visualization study on lubricant oil film behavior around piston skirt. SAE Technical Paper 2011-01-2119, SAE Technical Paper, Warrendale, PA, August 2011.

[236] T. W. Bates, B. Williamson, J. A. Spearot, and C. K. Murphy. The importance of oil elasticity. *Industrial Lubrication and Tribology*, 40(6):4–19, 1988.

[237] C. Clasen, J. Eggers, M. A. Fontelos, J. Li, and G. H. McKinley. The beads-on-string structure of viscoelastic threads. *Journal of Fluid Mechanics*, 556:283–308, 2006.

[238] A. Sequeira. *Lubricant Base Oil and Wax Processing*. CRC press, 1994.

[239] V. H. Weßlau. Die molekulargewichtsverteilung einiger niederdruckpolyäthylene. *Die Makromolekulare Chemie*, 20(1):111–142, 1956.

[240] B. Debbaut and M. J. Crochet. Extensional effects in complex flows. *Journal of Non-Newtonian Fluid Mechanics*, 30(2-3):169–184, 1988.

[241] H.-C. Tseng. A revisitation of generalized Newtonian fluids. *Journal of Rheology*, 64(3):493–504, 2020.

[242] A. Savitzky and M. J. Golay. Smoothing and differentiation of data by simplified least squares procedures. *Analytical Chemistry*, 36(8):1627–1639, 1964.

[243] D. C. Vadillo, W. Mathues, and C. Clasen. Microsecond relaxation processes in shear and extensional flows of weakly elastic polymer solutions. *Rheologica Acta*, 51(8):755–769, 2012.

[244] C. Wagner, L. Bourouiba, and G. H. McKinley. An analytic solution for capillary thinning and breakup of FENE-P fluids. *Journal of Non-Newtonian Fluid Mechanics*, 218:53–61, April 2015.

[245] J. Dinic and V. Sharma. Flexibility, extensibility, and ratio of Kuhn length to packing length govern the pinching dynamics, coil-stretch transition, and rheology of polymer solutions. *Macromolecules*, 53(12):4821–4835, 2020.

[246] K. A. Marshall and T. W. Walker. Investigating the dynamics of droplet breakup in a microfluidic cross-slot device for characterizing the extensional properties of weakly-viscoelastic fluids. *Rheologica Acta*, 58(9):573–590, 2019.

[247] N. S. Suteria, S. Gupta, R. Potineni, S. K. Baier, and S. A. Vanapalli. eCapillary: A disposable microfluidic extensional viscometer for weakly elastic polymeric fluids. *Rheologica Acta*, 58(6-7):403–417, 2019.

[248] I. Nahringbauer. Dynamic surface tension of aqueous polymer solutions, I: Ethyl(hydroxyethyl)cellulose (BERMOCOLL cst-103). *Journal of Colloid and Interface Science*, 176(2):318–328, December 1995.

[249] J. M. Dealy and R. G. Larson. *Molecular Structure and Rheology of Molten Polymers*. 2006.

[250] J. Eggers and T. F. Dupont. Drop formation in a one-dimensional approximation of the Navier–Stokes equation. *Journal of Fluid Mechanics*, 262:205–221, October 1994.

[251] L. A. Slobozhanin and J. M. Perales. Stability of liquid bridges between equal disks in an axial gravity field. *Physics of Fluids A: Fluid Dynamics*, 5(6):1305–1314, 1993.

[252] M. Renardy. Some comments on the surface-tension driven break-up (or the lack of it) of viscoelastic jets. *Journal of Non-Newtonian Fluid Mechanics*, 51(1):97–107, 1994.

[253] I. S. Gradshteyn, I. M. Ryzhik, A. Jeffrey, and D. Zwillinger. *Table of Integrals, Series, and Products, Sixth Edition*. Academic Press, San Diego, 6th edition edition, August 2000.

[254] J. Eggers. Universal pinching of 3D axisymmetric free-surface flow. *Physical Review Letters*, 71(21):3458, 1993.

[255] M. P. Brenner, J. R. Lister, and H. A. Stone. Pinching threads, singularities and the number 0.0304... *Physics of Fluids*, 8(11):2827–2836, 1996.

[256] G. Schwarz. Estimating the dimension of a model. *The Annals of Statistics*, 6(2):461–464, 1978.

[257] D. Sachsenheimer, B. Hochstein, and N. Willenbacher. Experimental study on the capillary thinning of entangled polymer solutions. *Rheologica Acta*, 53(9):725–739, 2014.

[258] S. L. Anna and G. H. McKinley. Elasto-capillary thinning and breakup of model elastic liquids. *Journal of Rheology*, 45(1):115–138, 2001.

[259] T. C. McLeish. Tube theory of entangled polymer dynamics. *Advances in Physics*, 51(6):1379–1527, 2002.

[260] E. Narimissa, Q. Huang, and M. H. Wagner. Elongational rheology of polystyrene melts and solutions: Concentration dependence of the interchain tube pressure effect. *Journal of Rheology*, 64(1):95–110, 2020.

[261] P.-G. de Gennes. Reptation of a polymer chain in the presence of fixed obstacles. *The Journal of Chemical Physics*, 55(2):572–579, 1971.

[262] P. C. Hiemenz and T. P. Lodge. *Polymer Chemistry*. CRC press, 2007.

[263] M. Doi and S. Edwards. Dynamics of concentrated polymer systems. Part 1.—Brownian motion in the equilibrium state. *Journal of the Chemical Society, Faraday Transactions 2: Molecular and Chemical Physics*, 74:1789–1801, 1978.

[264] J. M. Dealy, D. J. Read, and R. G. Larson. *Structure and Rheology of Molten Polymers: From Structure to Flow Behavior and Back Again*. Hanser Publishers, Cincinnati, 2nd edition edition, 2018.

[265] J. Oberhauser. Non-Newtonian fluid mechanics for polymeric liquids: A status report. *Korea-Australia Rheology Journal*, 12(1):1–25, 2000.

[266] G. Marrucci and N. Grizzuti. The free energy function of the Doi-Edwards theory: Analysis of the instabilities in stress relaxation. *Journal of Rheology*, 27(5):433–450, 1983.

[267] R. S. Graham, A. E. Likhtman, T. C. B. McLeish, and S. T. Milner. Microscopic theory of linear, entangled polymer chains under rapid deformation including chain stretch and convective constraint release. *Journal of Rheology*, 47(5):1171–1200, 2003.

[268] A. E. Likhtman and R. S. Graham. Simple constitutive equation for linear polymer melts derived from molecular theory: Rolie-Poly equation. *Journal of Non-Newtonian Fluid Mechanics*, 114(1):1–12, 2003.

[269] B. J. Geurts and R. J. Jongschaap. A new reptation model for the rheological properties of concentrated polymer solutions and melts. *Journal of Rheology*, 32(4):353–365, 1988.

[270] D. Pearson, E. Herbolzheimer, N. Grizzuti, and G. Marrucci. Transient behavior of entangled polymers at high shear rates. *Journal of Polymer Science Part B: Polymer Physics*, 29(13):1589–1597, December 1991.

[271] A. Cohen. A Padé approximant to the inverse Langevin function. *Rheologica Acta*, 30(3):270–273, 1991.

[272] W. Mathues, S. Formenti, C. McIlroy, O. G. Harlen, and C. Clasen. CaBER vs ROJER—Different time scales for the thinning of a weakly elastic jet. *Journal of Rheology*, 62(5):1135–1153, 2018.

[273] G. Marrucci. Dynamics of entanglements: A nonlinear model consistent with the Cox-Merz rule. *Journal of Non-Newtonian Fluid Mechanics*, 62(2-3):279–289, 1996.

[274] P. K. Bhattacharjee, J. P. Oberhauser, G. H. McKinley, L. G. Leal, and T. Sridhar. Extensional rheometry of entangled solutions. *Macromolecules*, 35(27):10131–10148, 2002.

[275] D. S. Pearson, A. D. Kiss, L. J. Fetters, and M. Doi. Flow-induced birefringence of concentrated polyisoprene solutions. *Journal of Rheology*, 33(3):517–535, 1989.

[276] S. Ravindranath, S.-Q. Wang, M. Olechnowicz, and R. P. Quirk. Banding in Simple Steady Shear of Entangled Polymer Solutions. *Macromolecules*, 41(7):2663–2670, April 2008.

[277] C. Clasen. Capillary breakup extensional rheometry of semi-dilute polymer solutions. *Korea-Australia Rheology Journal*, 22(4):331–338, 2010.

[278] G. Wypych. *Handbook of Polymers*. Elsevier, 2016.

[279] J. E. Mark. *Physical Properties of Polymers Handbook*, volume 1076. Springer, 2007.

[280] Polyethylene Glycol Density and Length Affects Nanoparticle Uptake by Cancer Cells. page 6, 2014.

[281] B. H. Cao and M. W. Kim. Molecular weight dependence of the surface tension of aqueous poly(ethylene oxide) solutions. *Faraday Discussions*, 98(0):245–252, January 1994.

[282] E. J. Hinch and L. G. Leal. Time-dependent shear flows of a suspension of particles with weak Brownian rotations. *Journal of Fluid Mechanics*, 57(4):753–767, 1973.

[283] N. M. P. Bocken, E. A. Olivetti, J. M. Cullen, J. Potting, and R. Lifset. Taking the circularity to the next level: A special issue on the circular economy. *Journal of Industrial Ecology*, 21(3):476–482, June 2017.

[284] E. A. Olivetti and J. M. Cullen. Toward a sustainable materials system. *Science*, 360(6396):1396–1398, 2018.

[285] P. Wang, B. Barnes, Z. Huang, Z. Wang, M. Zheng, and Y. Wang. Beyond Color: The New Carbon Ink. *Advanced Materials*, n/a(n/a):2005890.

[286] B. J. Collier, M. Dever, S. Petrovan, J. R. Collier, Z. Li, and X. Wei. Rheology of lyocell solutions from different cellulose sources. *Journal of Polymers and the Environment*, 8(3):151–154, 2000.

[287] A. J. Sayyed, N. A. Deshmukh, and D. V. Pinjari. A critical review of manufacturing processes used in regenerated cellulosic fibres: Viscose, cellulose acetate, cuprammonium, LiCl/DMAc, ionic liquids, and NMMO based lyocell. *Cellulose*, 26(5):2913–2940, 2019.

[288] U. Henniges, M. Kostic, A. Borgards, T. Rosenau, and A. Potthast. Dissolution behavior of different celluloses. *Biomacromolecules*, 12(4):871–879, 2011.

[289] R. P. Swatloski, S. K. Spear, J. D. Holbrey, and R. D. Rogers. Dissolution of cellulose with ionic liquids. *Journal of the American Chemical Society*, 124:4974–4975, 2002.

[290] M. J. Earle, J. M. S. S. Esperança, M. A. Gilea, J. N. C. Lopes, L. P. N. Rebelo, J. W. Magee, K. R. Seddon, and J. A. Widegren. The distillation and volatility of ionic liquids. *Nature*, 439(7078):831–834, 2006.

[291] C. Maton, N. De Vos, and C. V. Stevens. Ionic liquid thermal stabilities: Decomposition mechanisms and analysis tools. *Chemical Society reviews*, 42(13):5963–77, July 2013.

[292] X. Yuan and G. Cheng. From cellulose fibrils to single chains: Understanding cellulose dissolution in ionic liquids. *Physical Chemistry Chemical Physics*, 17(47):31592–31607, 2015.

[293] M. J. Kamlet and R. Taft. The solvatochromic comparison method. I. The ß-Scale of solvent hydrogen-bond acceptor (HBA) basicities. *Journal of the American Chemical Society*, pages 377–383, 1975.

[294] N. Sun, H. Rodriguez, M. Rahman, and R. D. Rogers. Where are ionic liquid strategies most suited in the pursuit of chemicals and energy from lignocellulosic biomass? *Chemical Communications*, 47(5):1405–1421, 2011.

[295] A. Brandt, J. Gräsvik, J. P. Hallett, and T. Welton. Deconstruction of lignocellulosic biomass with ionic liquids. *Green Chemistry*, 15(3):550, 2013.

[296] B. Lindman, G. Karlström, and L. Stigsson. On the mechanism of dissolution of cellulose. *Journal of Molecular Liquids*, 156(1):76–81, 2010.

[297] P. B. Sánchez, S. Tsubaki, A. A. H. Pádua, and Y. Wada. Kinetic analysis of microwave-enhanced cellulose dissolution in ionic solvents. *Physical Chemistry Chemical Physics*, 22:1003–1010, 2020.

[298] A. Michud, M. Hummel, S. Haward, and H. Sixta. Monitoring of cellulose depolymerization in 1-ethyl-3-methylimidazolium acetate by shear and elongational rheology. *Carbohydrate Polymers*, 117:355–363, 2015.

[299] A. Michud, M. Hummel, and H. Sixta. Influence of molar mass distribution on the final properties of fibers regenerated from cellulose dissolved in ionic liquid by dry-jet wet spinning. *Polymer*, 75:1–9, 2015.

[300] R. De Silva, K. Vongsanga, X. Wang, and N. Byrne. Cellulose regeneration in ionic liquids: Factors controlling the degree of polymerisation. *Cellulose*, 22(5):2845–2849, 2015.

[301] Y. Ahn, S. Y. Kwak, Y. Song, and H. Kim. Physical state of cellulose in BmimCl: Dependence of molar mass on viscoelasticity and sol-gel transition. *Physical Chemistry Chemical Physics*, 18(3):1460–1469, 2016.

[302] M. Hummel, A. Michud, M. Tanttu, S. Asaadi, Y. Ma, L. K. J. Hauru, A. Parviainen, A. W. T. King, I. Kilpeläinen, and H. Sixta. Ionic liquids for the production of man-made cellulosic fibers: Opportunities and challenges. *Cellulose Chemistry and Properties: Fibers, Nanocelluloses and Advanced Materials*, 271:133–168, 2015.

[303] H. Ouaer and M. Gareche. The rheological behaviour of a water-soluble polymer (HEC) used in drilling fluids. *Journal of the Brazilian Society of Mechanical Sciences and Engineering*, 40(8):380, August 2018.

[304] C. D. V. Martínez Narváez, J. Dinic, X. Lu, C. Wang, R. Rock, H. Sun, and V. Sharma. Rheology and Pinching Dynamics of Associative Polysaccharide Solutions. *Macromolecules*, June 2021.

[305] D. M. Binding. An approximate analysis for contraction and converging flows. *Journal of Non-Newtonian Fluid Mechanics*, 27(2):173–189, 1988.

[306] M. Renardy. A numerical study of the asymptotic evolution and breakup of Newtonian and viscoelastic jets. *Journal of Non-Newtonian Fluid Mechanics*, 59(2-3):267–282, 1995.

[307] H. Bai, C. Li, X. Wang, and G. Shi. A pH-sensitive graphene oxide composite hydrogel. *Chemical Communications*, 46(14):2376–2378, 2010.

[308] Y. Q. Li, T. Yu, T. Y. Yang, L. X. Zheng, and K. Liao. Bio-Inspired nacre-like composite films based on graphene with superior mechanical, electrical, and biocompatible properties. *Advanced Materials*, 24(25):3426–3431, 2012.

[309] J. Liang, Y. Huang, L. Zhang, Y. Wang, Y. Ma, T. Cuo, and Y. Chen. Molecular-level dispersion of graphene into poly(vinyl alcohol) and effective reinforcement of their nanocomposites. *Advanced Functional Materials*, 19(14):2297–2302, 2009.

[310] S. Morimune, T. Nishino, and T. Goto. Poly(vinyl alcohol)/graphene oxide nanocomposites prepared by a simple eco-process. *Polymer Journal*, 44(10):1056–1063, 2012.

[311] L. Jiang, X.-P. Shen, J.-L. Wu, and K.-C. Shen. Preparation and characterization of graphene/poly (vinyl alcohol) nanocomposites. *Journal of Applied Polymer Science*, 118(1):275–279, 2010.

[312] Y. Xu, W. Hong, H. Bai, C. Li, and G. Shi. Strong and ductile poly (vinyl alcohol)/graphene oxide composite films with a layered structure. *Carbon*, 47(15):3538–3543, 2009.

[313] M. R. Haider and P. K. Singh. Mechanical and Thermal Properties of Graphene based Hybrid Polymer Nanocomposites-A Review. In *IOP Conference Series: Materials Science and Engineering*, volume 1116, page 012038. IOP Publishing, 2021.

[314] M. Hareesha, B. Yogesha, L. L. Naik, and D. Saravanabavan. Development on graphene based polymer composite materials and their applications—A recent review. In *AIP Conference Proceedings*, volume 2316, page 030016. AIP Publishing LLC, 2021.

[315] C. J. Dimitriou and G. H. McKinley. A comprehensive constitutive law for waxy crude oil: A thixotropic yield stress fluid. *Soft Matter*, 10(35):6619–6644, 2014.

[316] H. A. Barnes. Thixotropy—a review. *Journal of Non-Newtonian Fluid Mechanics*, 70(1):1–33, May 1997.

[317] M. Klüppel. The role of disorder in filler reinforcement of elastomers on various length scales. *Filler-reinforced elastomers scanning force microscopy*, pages 1–86, 2003.

[318] A. Bonfanti, J. L. Kaplan, G. Charras, and A. Kabla. Fractional viscoelastic models for power-law materials. *Soft Matter*, 16(26):6002–6020, 2020.

[319] L.-I. Palade, V. Verney, and P. Attané. A modified fractional model to describe the entire viscoelastic behavior of polybutadienes from flow to glassy regime. *Rheologica Acta*, 35(3):265–273, 1996.

[320] A. Takeh and S. Shanbhag. A computer program to extract the continuous and discrete relaxation spectra from dynamic viscoelastic measurements. *Applied Rheology*, 23(2), 2013.

[321] M. H. Wagner. Analysis of time-dependent non-linear stress-growth data for shear and elongational flow of a low-density branched polyethylene melt. *Rheologica Acta*, 15(2):136–142, February 1976.

[322] V. H. Rolón-Garrido and M. H. Wagner. The damping function in rheology. *Rheologica Acta*, 48(3):245–284, April 2009.

[323] P. R. Soskey and H. H. Winter. Large step shear strain experiments with parallel-disk rotational rheometers. *Journal of Rheology*, 28(5):625–645, 1984.

[324] D. Doraiswamy, A. N. Mujumdar, I. Tsao, A. N. Beris, S. C. Danforth, and A. B. Metzner. The Cox–Merz rule extended: A rheological model for concentrated suspensions and other materials with a yield stress. *Journal of Rheology*, 35(4):647–685, May 1991.

[325] G. Ianniruberto and G. Marrucci. On compatibility of the Cox-Merz rule with the model of Doi and Edwards. *Journal of Non-Newtonian Fluid Mechanics*, 65(2):241–246, August 1996.

[326] R. H. Colby and M. Rubinstein. Polymer physics. In *Polymer International*. Oxford University Press, Oxford, 3rd edition, 2004.

[327] N. Sivashinsky, A. T. Tsai, T. J. Moon, and D. S. Soong. Some new transient test results from a parallel-plate rheometer. *Journal of Rheology*, 28(3):287–301, June 1984.

[328] S. R. Doshi and J. M. Dealy. Exponential shear: A strong flow. *Journal of Rheology*, 31(7):563–582, October 1987.

[329] B. Zülle, J. J. Linster, J. Meissner, and H. P. Hürlimann. Deformation hardening and thinning in both elongation and shear of a low density polyethylene melt. *Journal of Rheology*, 31(7):583–598, October 1987.

[330] J. Neergaard, K. Park, D. C. Venerus, and J. D. Schieber. Exponential shear flow of linear, entangled polymeric liquids. *Journal of Rheology*, 44(5):1043–1054, September 2000.

[331] R. S. Graham, T. C. B. McLeish, and O. G. Harlen. Using the pom-pom equations to analyze polymer melts in exponential shear. *Journal of Rheology*, 45(1):275–290, January 2001.

[332] D. C. Venerus. Exponential shear flow of branched polymer melts. page 9.

[333] A. S. Lodge and J. Meissner. Comparison of network theory predictions with stress/time data in shear and elongation for a low-density polyethylene melt. *Rheologica Acta*, 12(1):41–47, 1973.

[334] G. Taylor. The viscosity of a fluid containing small drops of another fluid. *Proceedings of the Royal Society of London. Series A, Containing Papers of a Mathematical and Physical Character*, 138(834):41–48, October 1932.

[335] W. Milliken and L. Leal. Deformation and breakup of viscoelastic drops in planar extensional flows. *Journal of Non-Newtonian Fluid Mechanics*, 40(3):355–379, November 1991.

[336] J. Dai, G. Wang, L. Ma, and C. Wu. Study on the surface energies and dispersibility of graphene oxide and its derivatives. *Journal of Materials Science*, 50(11):3895–3907, June 2015.

[337] P. T. Callaghan. Rheo-NMR: Nuclear magnetic resonance and the rheology of complex fluids. *Reports on Progress in Physics*, 62(4):599–670, January 1999.

[338] M. A. Calabrese and N. J. Wagner. New insights from Rheo-SANS. page 30.